Dynamics of Long Flexible Cylinders at
High-Mode Number in Uniform and Sheared Flows

by

Susan B. Swithenbank

B.S. Mechanical Engineering (2000)
Carnegie Mellon University

Submitted to the Department of Mechanical Engineering
in Partial Fulfillment of the Requirements for the Degree of
Doctor of Philosophy in Ocean Engineering

at the

Massachusetts Institute of Technology

February 2007

Signature of Author……
Department of Mechanical Engineering
January 30, 2007

Certified by……
J. Kim Vandiver
Professor of Mechanical and Ocean Engineering
Thesis Supervisor

Accepted by……...
Lallit Anand
Chairman, Department Committee on Graduate Students

Dynamics of Long Flexible Cylinders at
High-Mode Number in Uniform and Sheared Flows

By

Susan B. Swithenbank

Submitted to the Department of Mechanical Engineering
on January 30, 2007 in partial fulfillment of the
requirements for the Degree of Doctor of Philosophy in
Ocean Engineering

ABSTRACT

The primary objective of this thesis is to characterize the response of risers at high-mode numbers in sheared and uniform ocean currents. As part of this thesis work, three separate experiments have been planned and executed. The objective of these tests was to create a set of model tests at high-mode numbers, the first test was in uniform currents and the other tests in sheared currents.

In the experiments, Vortex-Induced Vibrations (VIV) happened at one frequency at one time, rather than at many frequencies simultaneously. The single VIV frequency varied with time, but the VIV frequencies did not co-exist. The major impact of time-sharing frequencies is that it increases the damage rate and fatigue of the pipe.

The high density of the sensors on the pipe allowed for analysis that had not previously been done. Two methodologies are presented to locate the area of the power-in region. Once the region where the vibration originated has been found, the different phenomena that effect the location of the power-in region that were discovered are shown. Four different factors are presented that effect the locations of the power-in region: the incidence angle of the current, the gradient of the current direction, the current profile, and the end effects at high mode number.

Two dimensionless parameters are presented which help in the prediction of VIV given a current profile. The first is the power-in determination factor which predicts the region where the power-in occurs using a combination of the current velocity and the power-in length. The second parameter, the time sharing parameter, helps to determine whether the riser will respond with a single frequency, or switch between frequencies in time.

Thesis Supervisor: J. Kim Vandiver
Title: Professor of Mechanical and Ocean Engineering

Table of Contents

Chapter 1: Introduction

Vortex-induced vibrations (VIV) have been a long standing problem for mooring lines and drilling risers in ocean-current fields. During the last 20 years, the prediction of VIV has greatly improved by using data collected in laboratory tests and information from risers in the field. Multiple VIV prediction programs have been written to help engineers predict VIV and help in the design of future underwater applications.

The natural resources that are being developed today are in deeper water with stronger currents. The design with respect to VIV becomes more important because of the increased risk of fatigue failure.

Present modeling programs were designed and proven using data on shorter risers and from laboratory experiments at low-mode numbers. With the move from risers in shallow water to those in deep water comes the need to validate these programs at high-mode number.

The objectives of this thesis are four-fold:

- Help design and complete a set of tests to investigate VIV at high-mode numbers in uniform and sheared flow
- Determine when single-frequency and multi-frequency VIV responses are observed
- Define dimensionless parameters to help predict the dynamics of long cylinders at high-mode numbers
- Determine under what conditions of current shear separable cross-flow and in-line responses are observed

In the last two years, three separate scaled-model tests have been designed and completed by Prof. Vandiver's research group to investigate high-mode number VIV: two Miami Gulf Stream Tests and the Lake Seneca Test.

The first test was conducted at the Naval Acoustic Test Facility at Lake Seneca, New York. The Lake Seneca facility presented a controlled environment where uniform flow velocity and uni-directional cases could be investigated. At Lake Seneca a 400 ft long pipe with a diameter of 1.3 inches was instrumented with 25 tri-axial accelerometers to measure the VIV.

The Lake Seneca experiment was a controlled experiment conducted in a lake. The flow was virtually uniform over the span of the pipe, and the direction of the current was known. The in-line and cross-flow responses are evident in both the amplitude and the spectrum of the cases at Lake Seneca.

In comparison, the second and third tests, which were conducted in the Gulf Stream off the coast of Miami, had sheared currents and multi-directional flow. The Gulf Stream allowed for a greater variety of current profiles. Different types of sheared currents were seen in the Gulf Stream. In the two Miami experiments, an approximately 500 ft long pipe was instrumented with 70 fiber optic strain gauges in each of four quadrants.

The tests were designed to produce responses at high-mode numbers. The model was scaled so that high-mode numbers would be excited, where high-mode numbers are defined as those greater than the 10^{th} mode.

Results

The results of the four objectives are shown in different chapters throughout the thesis. The test design and results from the tests are shown in Chapter 3 and Appendix G. Chapter 3 shows the overall test design, whereas Appendix G shows the accelerometer placement algorithm in detail.

In the experiments, Vortex-Induced Vibrations (VIV) happened at one frequency at one time, rather than at many frequencies simultaneously. The single VIV frequency varied with time, but the VIV frequencies did not co-exist. The major impact of time-sharing frequencies is the impact upon the damage rate and fatigue of the pipe. The discussion of time-sharing of frequencies is presented in Chapter 5.

Chapter 6 presents two methodologies for finding the source of the VIV. One methodology is based on the reduced velocity and has been used before. The second methodology uses the signal processing technique called coherence to locate the source of the vibrations.

Using the results of the techniques discussed in Chapter 6, the effects of different factors on the location of the source region were examined. Factors such as the angle of incidence of the current, the gradient of the current direction, the reduced velocity

bandwidth and the proximity to the boundary were all factors in where the source region was located.

Chapter 9 presents the derivation of two dimensionless parameters that help predict the behavior of cylinders at high-mode numbers. The first parameter predicts the center of the source region. The second parameter determines whether the vibrations will be single frequency or switch between frequencies.

Chapter 2: Test Description

Introduction

The tests at Lake Seneca were conducted in the summer of 2004 and focused on the measurement of VIV in uniform flow at high-mode number for a bare pipe and for the same pipe with complete strake coverage. In comparison, the Gulf Stream tests were conducted in October 2004 and October 2006 and focused on bare pipe, partial strake coverage, and partial fairing coverage with sheared flow. Both tests are part of a larger VIV-testing program developed by DEEPSTAR, a joint industry technology development consortium.

As oil exploration and drilling moves into deeper water, understanding the dynamics of long pipes, vibrating at high mode numbers in sheared currents, becomes important. Additionally, understanding how strakes affect the dynamics of bare pipe is also important. The main objectives of the Gulf Stream Test were:

- To gather vortex-induced vibration response data using a densely instrumented circular pipe at high-mode numbers
- To measure mean drag coefficients (C_D) at high-mode numbers and improve drag-coefficient prediction formulas.
- To test the efficacy of helical strakes at high-mode numbers.
- To obtain statistics on the distribution of single-mode vs. multi-mode response to VIV.
- To determine the relative contribution to damage rate, arising from in-line and cross-flow VIV.
- To improve knowledge of damping factors on risers equipped with helical strakes.

Lake Seneca Experiment Description

The Lake Seneca test facility was selected as the testing site, because it is a fully equipped field-test station moored in calm, deep water. It was ideal for conducting a controlled test on a long circular pipe in uniform flow. This was accomplished by towing a vertical, composite pipe with a suspended bottom weight to produce the desired tension.

The length, diameter, and tension of the pipe were chosen so as to permit cross-flow excitation of up to the 25th mode. The maximum speed possible with the system at Lake Seneca was limited by the maximum allowable deflection angle of the pipe. Typical

towing speeds were approximately 1.0 to 3.5 ft/s, (0.3 to 1.1m/s). Vandiver and Marcollo, [2003], provide an analysis of the design tradeoffs when attempting to achieve high-mode numbers. This is done in terms of tension, length, diameter, and top angle.

The pipe was constructed in 100 foot segments which were then joined together. The depth of Lake Seneca limited the total pipe length to a maximum of 450 ft. During the experiment, total lengths of 201 and 401 feet (61.26 and 122.23 m) were tested. The properties of the pipe are shown in Table 1.

Table 1- Mechanical Properties of the Fiberglass Model Riser Used in the Lake Seneca Tests

Outer diameter	1.310 in.(0.0333m)
Inner diameter including liner	0.980 in.(0.0249m)
Lengths tested	201 & 401 feet(61.26 & 122.23m)
Effective tension	805 lbs submerged bottom weight (3581N)
Modulus of elasticity (E)	1805.0 ksi (1.276E10 N/sq m)
Moment of inertia (I)	3.994E-06 ft^4 (3.447E-8 m^4)
EI	149489.3 [lb-in^2](429.0 N-m^2)
Mass / displaced mass of water	1.35
Weight per unit length in air	0.79 [lb/ft](11.53 N/m),(1.176 kg/m)

Each 100 foot long section of pipe contained six evenly spaced tri-axial accelerometers. These accelerometers were sampled by analog-to-digital converters and micro-processors located locally at each accelerometer unit. The units were connected to a digital serial network, which had two parallel branches for redundancy. Half of the accelerometers used one network branch and half used the other. In this way, if one branch failed, half of the data would still be retrieved. The networks were controlled by a surface computer, which set the sampling rate and downloaded the data from each accelerometer unit. The surface data acquisition system was designed and built by BMT Scientific Marine Services Inc.

The sampling rate used in these experiments was 60 Hz for every accelerometer. The same serial network was used to sample the tension and tilt-measuring devices located very close to the top universal-joint connection.

Towing speed was measured by two mechanical current meters. One was suspended underneath the towed weight and the other was hung over the side of the towing vessel. The current meters were cup anemometer devices, with a magnetically activated reed switch which detected the rotation of the spinning multi-cup rotor. One

pair of wires ran the full length of the pipe from the bottom current meter to the data acquisition system on the surface.

In total, the pipe had ten conductors of wires which ran the full length. Two pairs of wires were used to support the serial networks. One pair carried power to all accelerometers. One pair was used for the bottom current meter and one pair was a spare. A ten-conductor waterproof connector was made up between each 100-foot long pipe section. The pipe was filled with a flexible epoxy compound to exclude water and to hold the wires in place.

At the top of the pipe, a load cell and tilt meter were attached. This additional instrumentation allowed the measurement of the tension in the pipe and the top angle of inclination.

The experimental set-up can be seen in Figure 1.

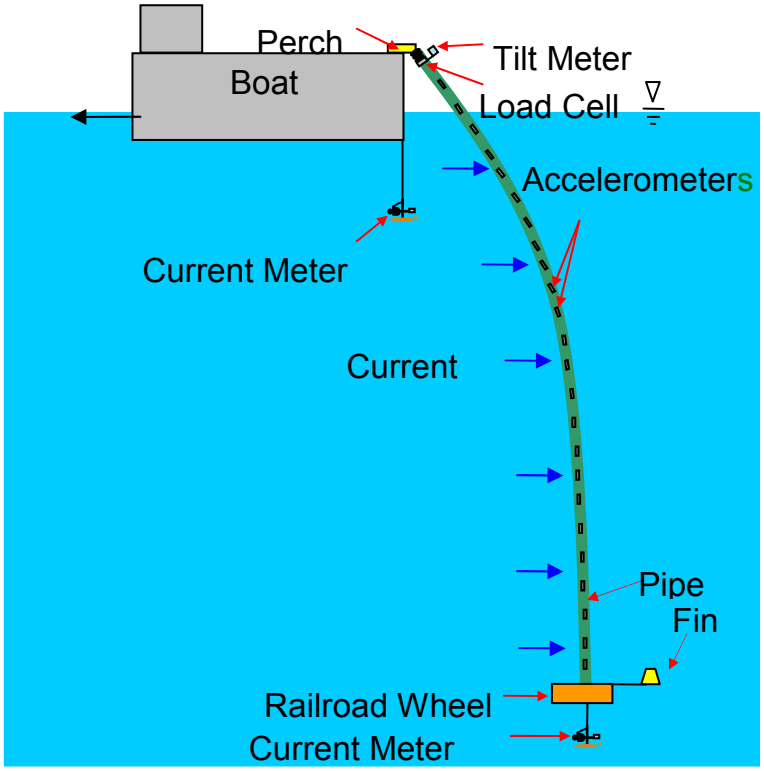

Figure 1 - Experimental Setup

The pipe was first assembled and deployed using a crane on the moored barge in Lake Seneca. The pipe was then transferred by crane from the perch on the barge to a perch on the bow of a supply boat. The supply boat was driven in reverse. In reverse, the slow speeds needed for the experiment could be more easily controlled. A railroad wheel

was connected to the bottom end to provide tension. Fins mounted on the railroad wheel prevented it from pitching and rotating. Great care was taken to design the towed weight so that it would have dynamic-response characteristics which would not interfere with the desired VIV. In particular, the pitch and roll natural frequencies of the weight were approximately 0.8 Hz and lower than the lowest VIV response frequency of interest.

Accelerometer Design

The placement of instrumentation on a riser can be crucial to later analysis of the data. If the sensors are not placed correctly, certain types of analysis such as modal analysis are impossible. With incorrectly placed instruments, the modes could be misidentified as other modes through aliasing, or missed entirely. The purpose of the sensor placement algorithm is to find the optimal placement for instrumentation on a riser that will avoid these problems.

An algorithm for placement is shown in Appendix G; this algorithm of the placement of sensors uses assumed mode shapes. Since mode shapes are orthogonal, the dot product of any two different modes should be zero. In the case of an instrumented riser, the mode shapes are discretely sampled only at the locations of the instrumentation. If the sampling of the mode shapes is poorly chosen, then the dot product of two different modes will not be zero. This algorithm considers the dot product of all the mode shapes when discretely sampled at the specified sensor locations and tries to minimize the dot products by locating the sensors in the optimal position.

Gulf Stream Test Description

The 2004 Gulf Stream test was conducted on the Research Vessel F. G. Walton Smith, operated by the University of Miami. The composite pipe was 485.3 feet long and 1.4 inches in diameter. The pipe was instrumented with embedded fiber optic strain gauges to monitor the vibration.

The 2006 Gulf Stream test was also conducted on the Research Vessel F. G. Walton Smith, operated by the University of Miami. The composite pipe was 504.5 feet long and 1.41 inches in diameter. The pipe was also instrumented with embedded fiber optic strain gauges to monitor the vibration. The experiment setup is show in Figure 2.

For both tests, the pipe was spooled on a drum that was mounted on the aft portion of the boat. The pipe was un-spooled and lowered into the water using a hydraulic motor. At the bottom end was a railroad wheel assembly which included a current meter, a center spool and U-joint. The assembly weighed 836 lbs in air and approximately 725 lbs in water, and was attached to the bottom of the pipe to provide tension. The weight of the pipe in water was 0.12 lb/ft. With additional drag forces on the pipe, the mean total top-end tension was 820 lb. The pipe was attached to the stern of the boat on a perch. About six feet of pipe were above the waterline. A variety of current profiles with significant variation in speed and direction were achieved by steering the vessel at numerous headings, while in the Gulf Stream.

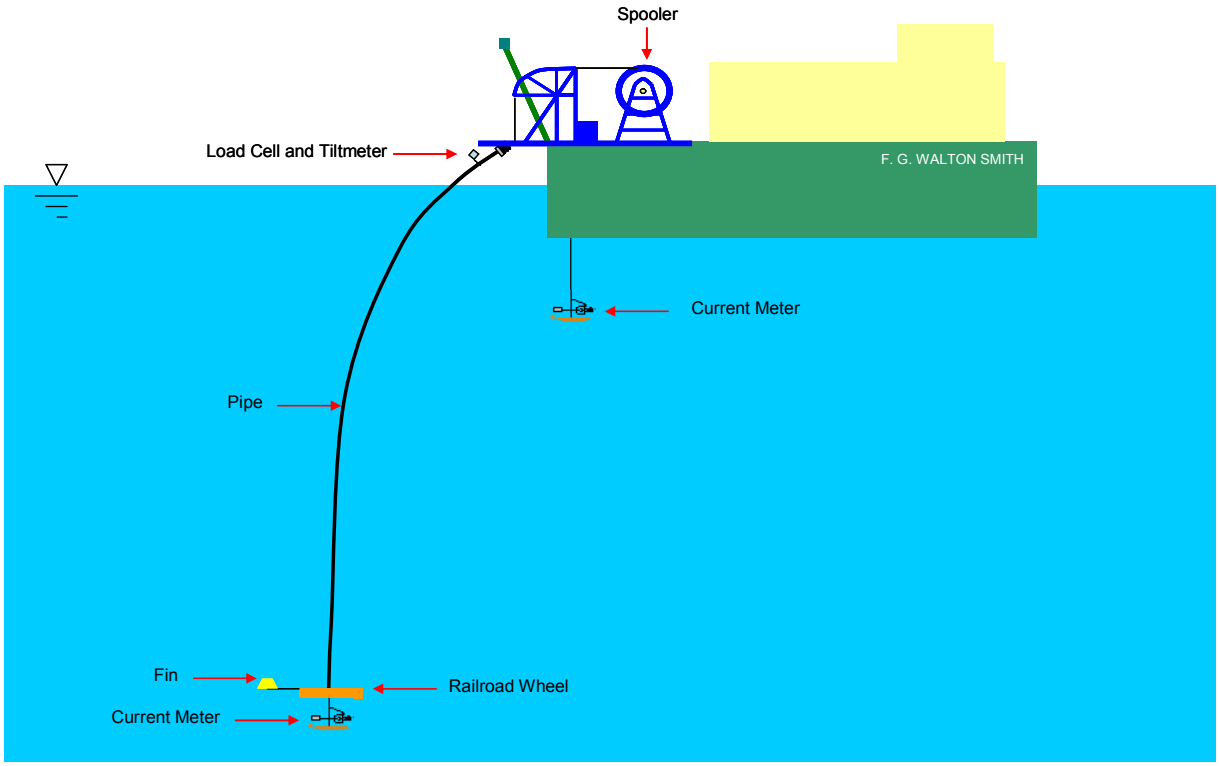

Figure 2 – Experiment setup for the Gulf Stream Test

Eight optical fibers were embedded under the outer layer of the pipe during manufacture. Each fiber contained 35 strain gauges, spaced fourteen feet apart. Two fibers were located in each of the four quadrants of the pipe, as see in Figure 3.

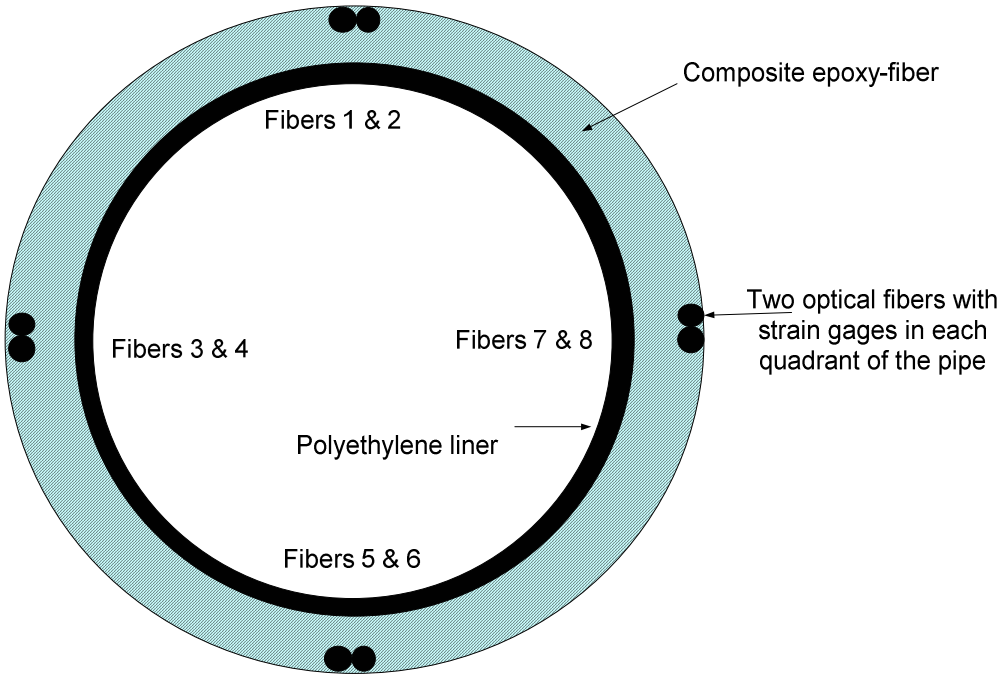

Figure 3 - Cross-Section of the Pipe from the Gulf Stream Test

The gauges in one fiber of a pair were not placed at the same axial position as the gauges in the adjacent fiber. Instead they were offset axially from one another by seven feet, as seen in Figure 4. When both fibers are functioning, a spatial resolution of seven feet was achieved. By merging the data from both fibers, an effective resolution was achieved with seventy total strain gauges per quadrant.

During the experiments, the exact orientation of the four quadrants was not known. This is due in part to a residual twist over the total length of the pipe of approximately 60 degrees, which was introduced in the fabrication process. There was a fin on the wheel, which was intended to orient the wheel in the current. However, the exact current direction at the wheel is not known because the depth of the wheel varies with changes in the drag force. It is known that within the same quadrant, the orientation of the optical fibers varies slowly. The conclusions reached in this paper do not depend on knowing the exact orientation of the strain gauges with respect to the boat. This is not a significant limitation in understanding the efficacy of strakes. It will be shown that there is very little difference in RMS amplitude and frequency content between gauges located in different quadrants.

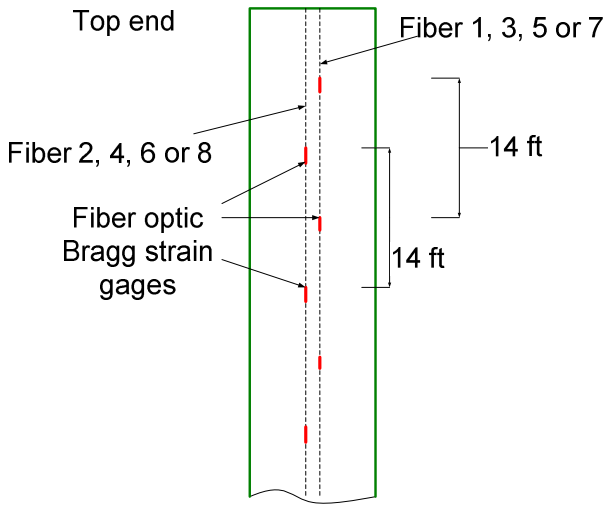

Figure 4 - Side View of the Pipe from the Gulf Stream Test

The pipe properties are found in Table 2 for the 2004 experiment and Table 3 for the 2006 experiment.

Table 2 –2004 Gulf Stream Pipe Properties

Inner diameter	1.05 in. (0.0267 m)
Outer diameter	1.40 in.(0.0356 m)
Optical fiber diameter	1.30 in.(0.033 m)
EI	1.7e5 lb.in^2 (488 Nm^2)
Modulus of elasticity (E)	2.30e6 lb./in^2 (1.586e10 N/m^2)
EA	8.5e5 lb. (3.78e6 N)
Weight in seawater	0.12 lb./ft. (flooded in Seawater) (1.75 N/m)
Weight in air, w/trapped water	0.83 lb./ft. (12.11 N/m)
Density	0.053 lb/in^3 (1.47 g./cc).
Material	Carbon fiber –epoxy
Length	485.3 ft (147.3 m) (U-joint to U-joint)
Roughness (k/D)	0.002

Table 3 – 2006 Gulf Stream Pipe Properties

Inner Diameter	0.98 inch (0.0249 m)
Outer Diameter	1.43 inch (0.0363 m)
EI	1.483e3 lb ft^2 (613 N m^2)
EA	7.468e5 lb (3.322e6)
Weight in Seawater	0.1325 lb/ft (0.1972 kg/m)
Weight in air	0.511 lb/ft (0.760 kg/m)
Density	86.39 lb/ft^3 (1383 kg/m^3)
Effective Tension	725 lb
Material	Glass fiber epoxy composite

Length	500.4 ft (152.524 m)
Manufactured by	FiberSpar Inc

An Acoustic Doppler Current Profiler (ADCP) was used to record the current along the length of the pipe. An ADCP uses acoustic sound waves to measure current speed and direction. The ADCP sends out an acoustic ping and waits for the return sound. Based on the time the ping takes to return and the Doppler shift in frequency, the ADCP obtains an estimate of the current speed as a function of depth.

The R/V F. G. Walton Smith has high and low frequency ADCPs. The broadband (600 kHz) ADCP is used to obtain a greater resolution and accuracy at the shallow depths, whereas the narrowband (150 kHz) ADCP is used for deeper depths. During the Gulf Stream testing both ADCPs were used to gather data.

Additional instrumentation included a tilt meter to measure the inclination of the top of the pipe, a load cell to measure the tension at the top of the pipe, and two mechanical current meters to measure current speed at the top and the bottom of the pipe.

Strake Properties

The strakes, used for both the Lake Seneca and the Gulf Stream experiments, were of a triple helix design made of polyethylene, with a pitch of 17.5 times the diameter of the pipe. This represents a typical design for strakes in the industry. The properties of the strakes are shown in Table 4. The strakes had a slit down the side that allowed them to be snapped over the outside of the pipe, and secured to the pipe using tie wraps. The strakes were manufactured by AIMS International.

Table 4 - Strake Properties

Material	Polyethylene
Length	26.075 in. (0.66 m)
Shell OD	1.49 in.(0.038 m), includes the strake height
Shell ID	1.32 in. (0.0335 m)
Strake height	0.375 in. (0.009 m) (about 25% of shell diameter)
Wall thickness	0.09 in.(0.0022 m)
Pitch	17.5 times the Diameter
Weight/length in air	0.11 lb/ft ±10% (1.6 N/m ±10%)

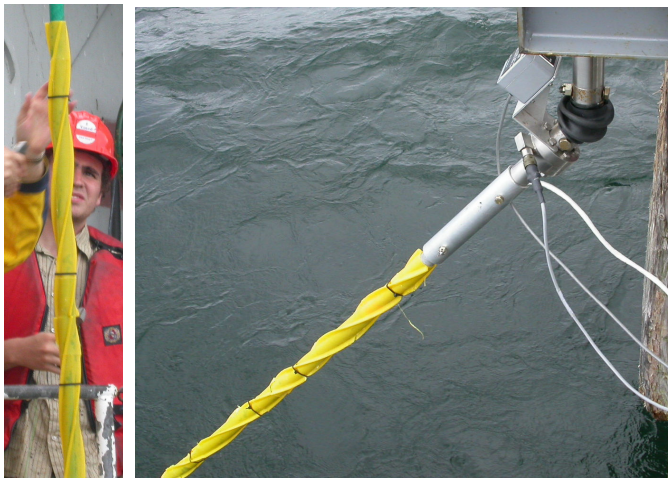

Figure 5 - Strakes Attached to the Pipe at Lake Seneca

Fairing Properties

A new fairing, designed and fabricated by AIMS International, was tested. The properties of the fairings are shown in Figure 6. The fairings used a split design, which allowed them to be snapped over the outside of the pipe, and were secured to the pipe using rubber bands (Figure 6). The fairings were attached in groups of five. Between each group a thrust collar was attached to the pipe with a tie wrap. The collar prevented the fairing from sliding up or down the pipe, which could have caused the fairings to interfere with free rotation and alignment. The fairings were manufactured and donated by AIMS International.

Table 5 - Fairing Properties

Material	Polyethylene
Length(inches)	14.96 in (38 cm)
Shell Thickness (inches)	0.132 in (3.35 mm)
Shell ID(inches)	1.38 in (3.51 mm)
Weight/length in air(lbs/ft)	0.764 lb (0.341 g)
Length of Fairings (in/mm)	9.15 in (3.6 mm)

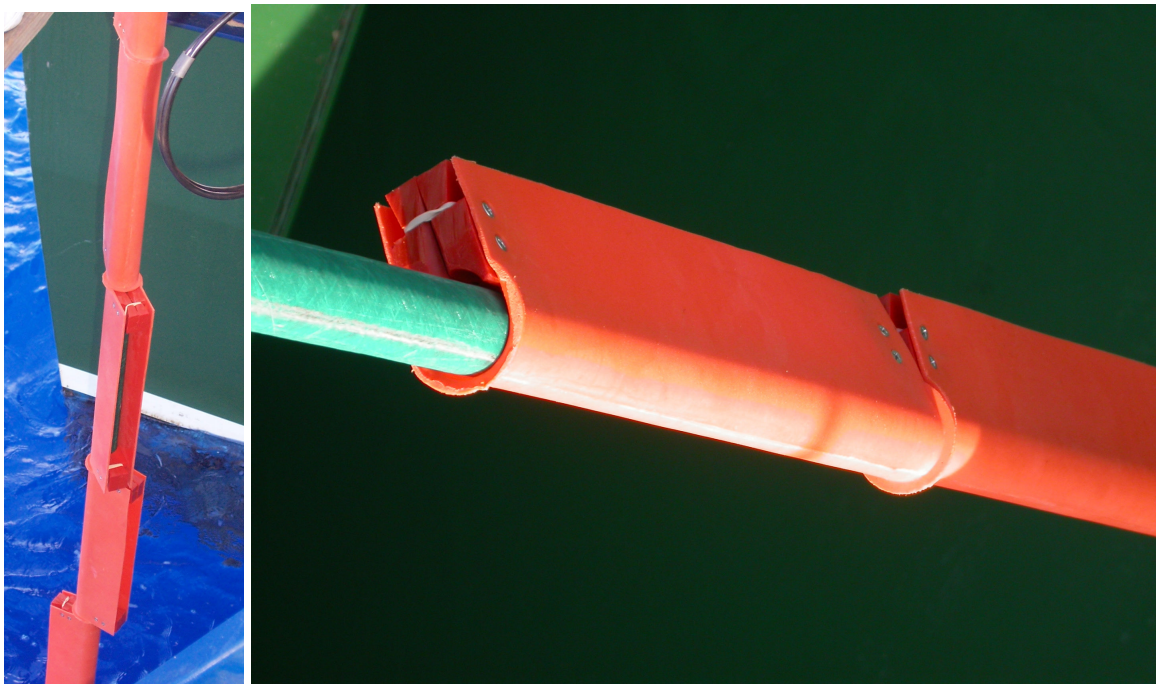

Figure 6 - Fairings attached to pipe during the second Gulf Stream experiment

Results from Lake Seneca

As stated above, the current profiles at Lake Seneca were essentially uniform with the only variation caused by the angle of the pipe with the vertical. Figure 7 shows the cross-flow acceleration Power Spectral Density (PSD) for a Lake Seneca test. The PSDs in the figure correspond to points located at 75 ft (x/L = 0.19) and 309 ft (x/L = 0.77) from the top end. The odd harmonics were seen in the cross-flow spectrum while the in-line spectrum captures the even harmonics. As mentioned earlier, this paper focuses on the cross-flow components and therefore the odd harmonics.

The PSD of the acceleration response at Lake Seneca shows that the frequency content was sharply peaked, indicating that the excitation was a quite narrow band at the fundamental excitation frequency. Although the magnitudes of the PSDs at the two different locations were different, the frequency content was the same at both points, indicating that the same fundamental VIV frequency was excited along the whole length of the pipe. Figure 7 also shows that there was significant energy in the cross-flow spectrum at the three-time frequency. The three-time harmonic is consistent with the results of Jauvtis and Williamson [2004].

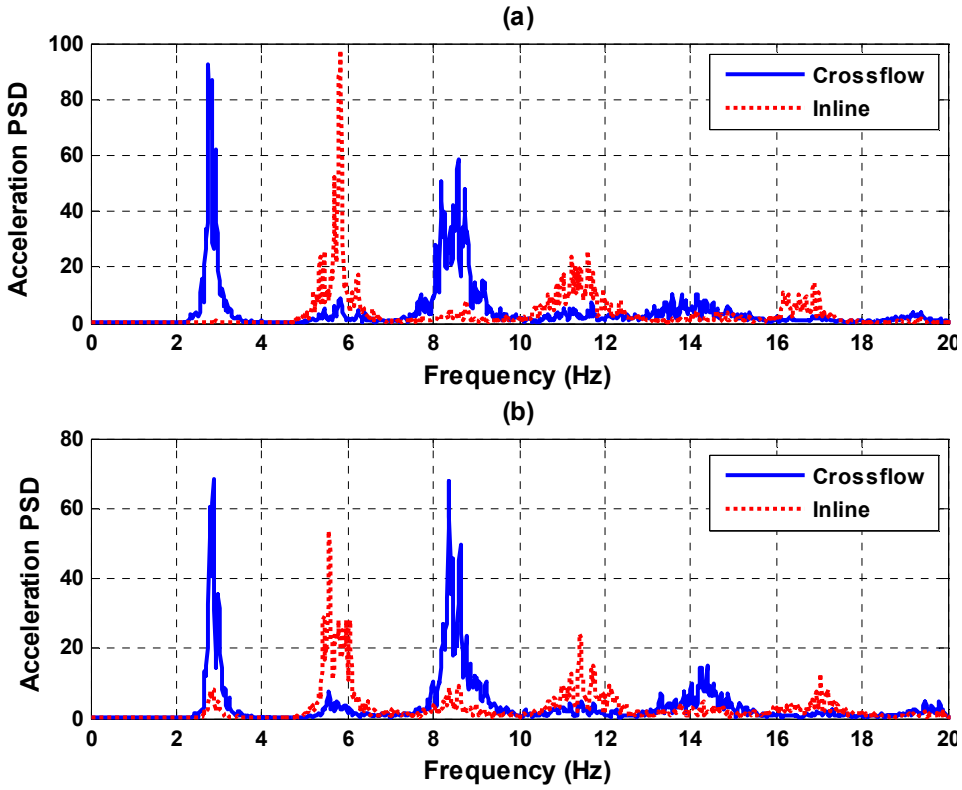

Figure 7 – Cross-flow and in-line acceleration PSDs showing the lack of spatial variation in frequency content in the Lake Seneca experiments. 1.76 ft/s = U_n, 5.5 = V_{r_i} (a) At x/L = 0.19 from top end, (b) At x/L = 0.77 from top end. The units of both (a) and (b) are $(m/s^2)^2/Hz$

Results from the 2004 Gulf Stream Test

An example comparing the different tests scenarios and strake configurations from the Gulf Stream tests is shown in Figure 8. One test case from each of the test configurations is shown: bare, 40% coverage at the bottom, and 70% staggered coverage. The cases were chosen to have similar current profiles so the results can be more easily compared. In the cases shown, the stronger currents are at the bottom of the pipe. The sheared profiles vary from approximately 2.4 ft/s to 3.2 ft/s.

Figure 9 shows the RMS strain measured for the second quadrant for each of the three strake configurations. The total strain as measured at any strain gauge is made up of contributions from bending as well as tension variations in the test pipe. To estimate true bending strain, one must subtract in the time domain the strain measured in one quadrant from that measured in the quadrant on the opposite side of the pipe. This computation results in common tension contributions in both fibers canceling one another, but allows common bending strains to add.

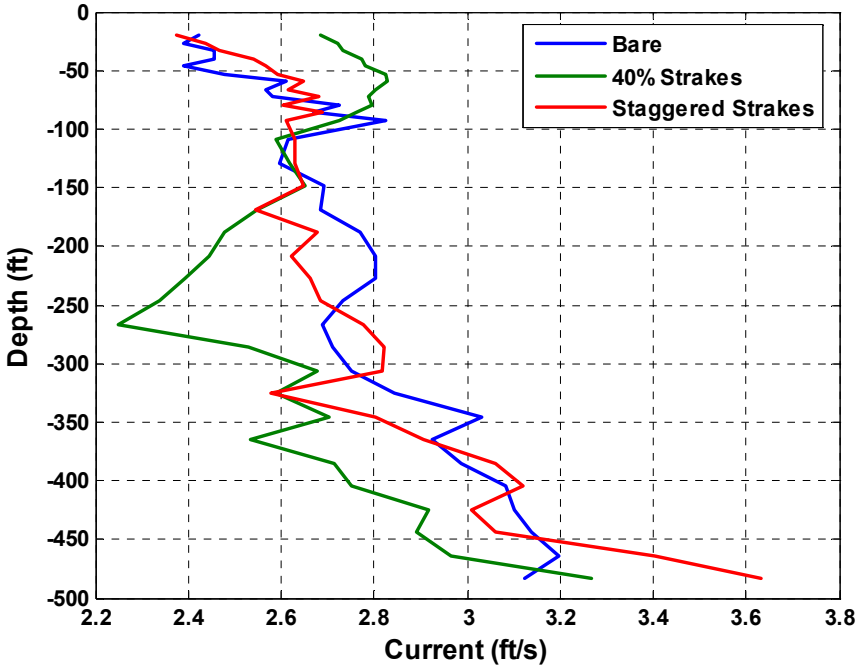

Figure 8 - Current Profiles for Comparison of the Bare Pipe Response to that with 40% and 70% Strake Coverage

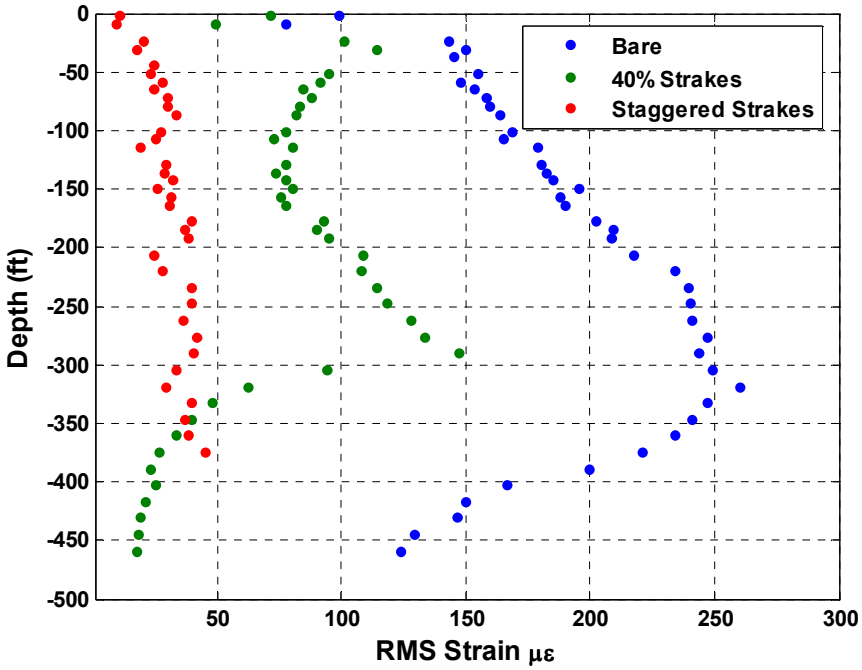

Figure 9 - RMS Strain in the Second Quadrant for Pipe with and without Strakes

In this study, fiber optic-mechanical failures greatly reduced the number of paired strained gauges, which were on opposite sides of the pipe. It was rarely possible to

evaluate true bending. In order to salvage useful information from single-fiber measurements, the data was filtered to eliminate the low-frequency tension variations caused by vessel motion. Vessel heave, pitch and roll periods were in excess of 2 seconds and waves large enough to affect vessel motion had periods in excess of three seconds. In order to isolate bending energy from the tension variations due to vessel motion, the data was high pass filtered at 1.0 Hz. VIV frequencies of interest were at 2 Hz and above. All data shown here has been high pass filtered.

Most of the dynamic strain data presented in this paper has been extracted from single-gauge measurements because, due to fiber failures, it was frequently not possible to take the difference between measurements from strain gauges on opposite sides of the pipe. Though disappointing, this was not entirely unexpected. The use of fiber-optic strain gauges in this application was pushing the state of the art in the use of such gauges. A significant amount of valuable data was obtained, including gaining experience with a new measurement technology.

When comparing the RMS strain from a single fiber for the various coverage scenarios the bare case has the highest response, as expected.

The case with 40% strake coverage shows the previously described stress concentration at the point of reflection. For this particular case, the RMS single-fiber strain is about half the RMS single-fiber strain for the bare case at all locations, including the point of the stress concentration. The RMS single-fiber strain for the staggered strake coverage is less than one-fifth that of the bare coverage case, and does not exceed 50 micro-strain ($\mu\varepsilon$) at any point on the pipe. The stress concentration is highlighted in Figure 10.

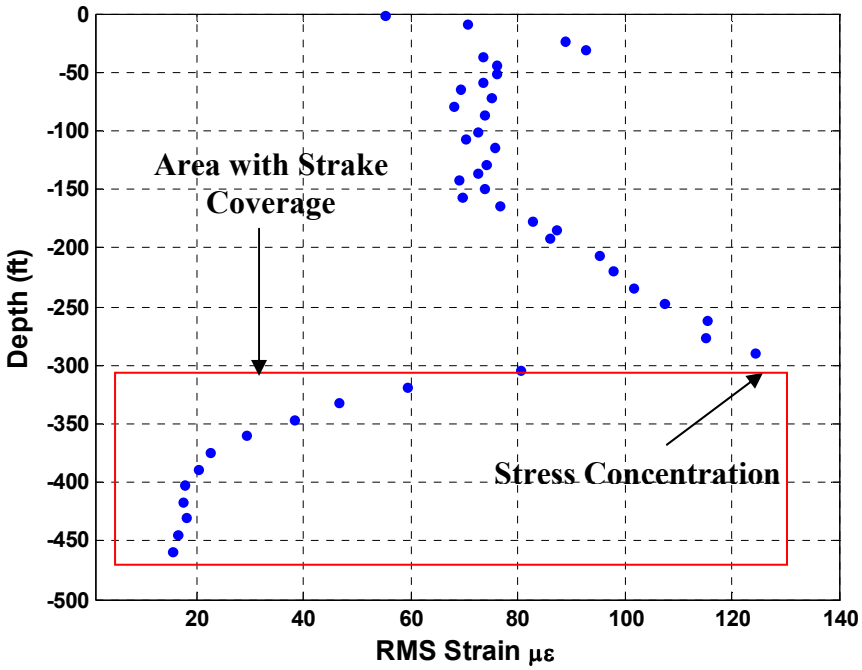

Figure 10 – RMS strain from 40% strake coverage at the bottom showing the stress concentration at 300 ft below the top universal joint.

The impact of the strakes can be seen not only in a reduction of RMS strain, but also in a change in frequency content. Figure 11 shows the PSD for each of the different strake configurations at an axial position 306 feet from the top. This depth is just inside the region with strakes in the 40% case and is in a region without strakes for the 70% strake coverage case.

The dominant VIV frequency for the bare case (the blue curve in Figure 11) is 4.48 Hz. There is also a prominent two-time harmonic peak and a broad peak which includes significant energy at three-time the dominant VIV frequency.

The dominant VIV frequency for the 40% straked coverage case is 3.32 Hz. This is the green curve in Figure 11. There is also a small three-time peak. The frequency content of the response is changed by the strakes. The bare pipe case contains frequencies up to 25 Hz with significant energy up to 20 Hz. When 40% strakes are applied, the frequency content is limited to approximately 20Hz with significant energy up to 12 Hz. With 70% staggered strake coverage, the frequency content of the pipe is limited to 6 Hz at the location of this strain gauge with no visible two-time and three-time components.

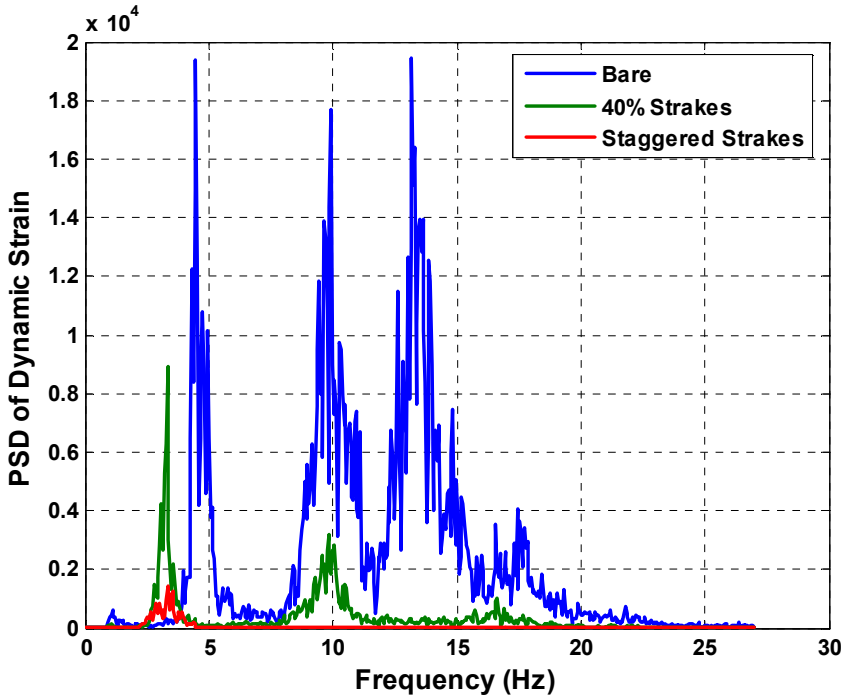

Figure 11 - PSD of the three configurations at 306 feet from the top

Chapter 3: Literature Review

Introduction

This chapter introduces important parameters that affect Vortex-Induced Vibrations (VIV). Various parameters control whether or not VIV cause large-amplitude vibrations that could fatigue a structure. The parameters are both structural and hydrodynamic.

Flow around a Cylinder

When flow passes a bluff body, such as a cylinder, the boundary layer on both sides of the cylinder separates, creating two shear layers that bound the wake. Within the shear layer, the flow at the surface of the structure approaches zero velocity, forming vortices in the wake of the cylinder. These vortices, formed by the separating shear layer, are periodic and apply forces on the cylinder. Figure 12 shows the vortex-wake pattern for a cylinder in laminar flow.

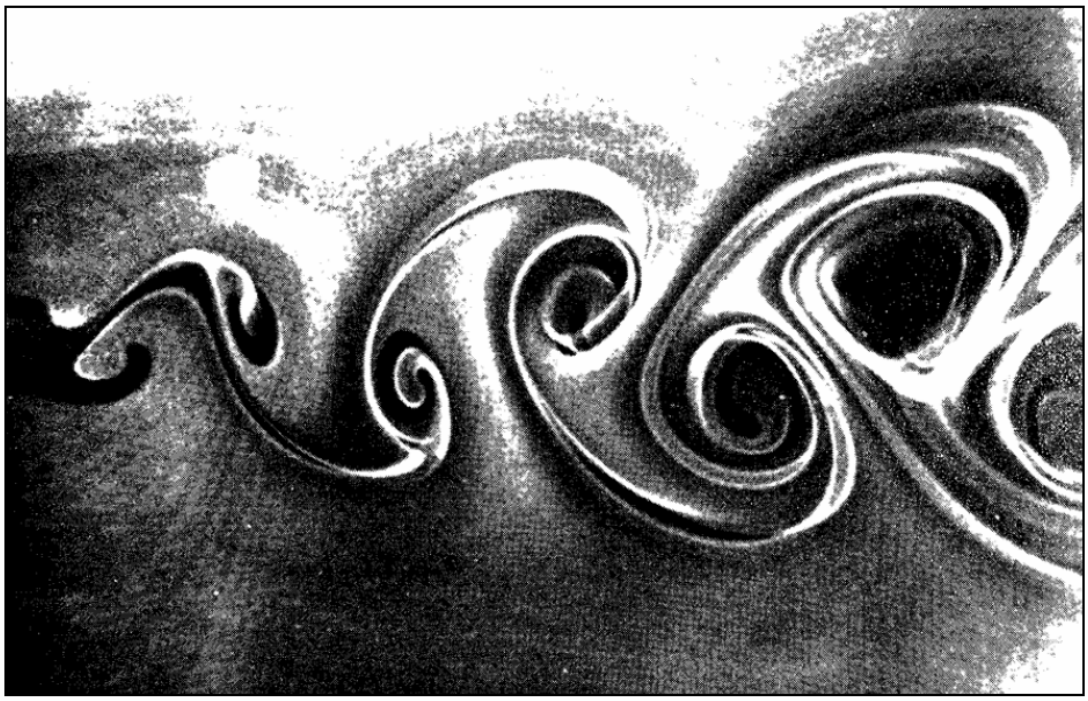

Figure 12 – Vortex-wake pattern from an oscillating cylinder [Griffen and Ramberg 1974]

The frequency with which vortices shed is a function of the current velocity, U. One parameter used to characterize vortex shedding from stationary cylinders is the Strouhal number:

$$St = \frac{f_n D}{U} \tag{3.1}$$

where U is the free stream current velocity, D is the diameter, and f_n is the natural frequency of the n^{th} mode.

The Reynolds number is important in VIV. The vortex wake changes depending on the Reynolds number, defined as:

$$\mathrm{Re} = \frac{UD}{\nu} \tag{3.2}$$

where ν is the kinematic viscosity of the fluid.

Figure 13 shows the relationship between the Strouhal number and the Reynolds Number as shown for a stationary cylinder [Blevins, 2001].

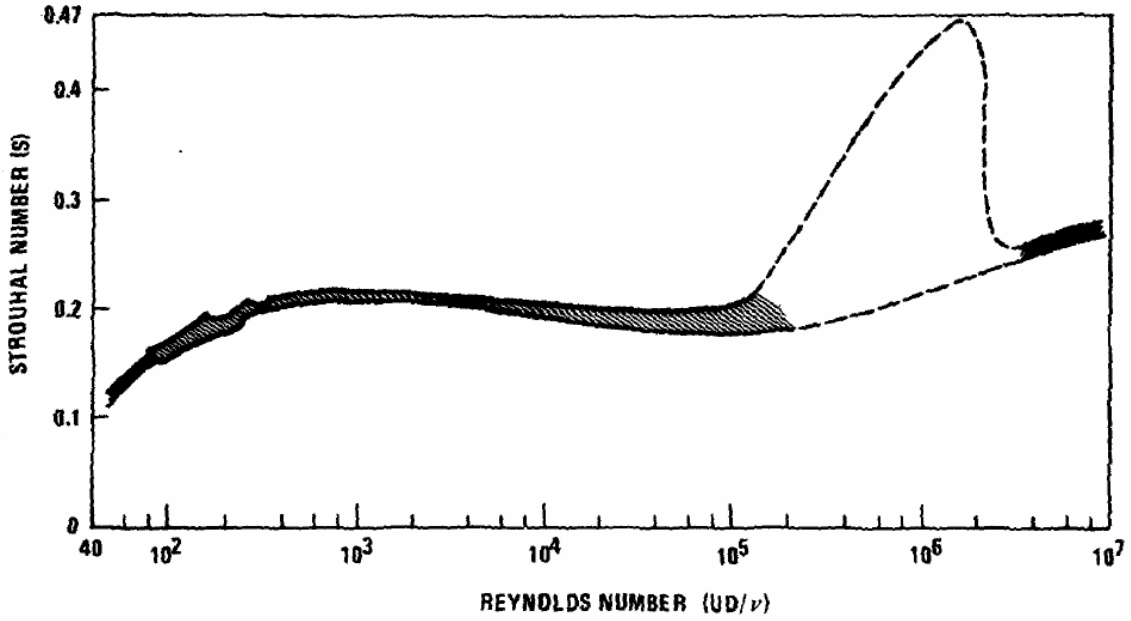

Figure 13 –The Relationship between Strouhal Number and Reynolds Number, [Blevins 2001]

The vortex shedding wake responds differently depending on the regime that the Reynolds number is in. Laminar flow is from a Reynolds number of 0 to ~350. Sub-critical turbulent flow happens at Reynolds numbers from ~350 to ~100k. The critical regime is from ~100k to ~6M. The super-critical regime is Reynolds numbers greater than 6M. Vortex shedding can happen in all the regimes of the Reynolds number, but the pattern of the shedding will differ.

The roughness of the pipe can vary the Reynolds number governing the transition from sub-critical to critical. The rougher the pipe, the lower the Reynolds number needed to enter the critical regime. [Achenbach and Heinecke 1981]

For most offshore platforms, the Reynolds number is in the critical regime (~100k < Re < 6M). The Lake Seneca and Gulf Stream experiments were in the sub-critical regime (~350 < Re < ~100k).

When discussing vibrating cylinders, a second parameter called the reduced velocity is often used instead of the Strouhal number. The reduced velocity can be defined two different ways. The first is:

$$V_r = \frac{U_n}{f_v D} \tag{3.3}$$

where f_v is the frequency of vibration.

Additionally the reduced velocity can be defined as

$$V_{rn} = \frac{U_n}{f_n D} \tag{3.4}$$

where f_n is the natural frequency of the cylinder at a specific condition .

The main difference between V_r and V_{rn} is that the frequency of vibration can be any range of frequencies depending on the current, whereas the natural frequency, as used in V_{rn}, is a fixed value.

Vortices can be shed at any reduced velocity, but the amplitude of vibration is often dependant on the value of the reduced velocity. At reduced velocities of less than four, few vibrations are seen. The largest amplitude of vibrations is seen at reduced velocity of $5 < V_r < 7$ for sub-critical Reynolds numbers. .

Normal-Incident Current

The setup of the Gulf Stream and Lake Seneca tests had the top end of the pipe inclined due to drag force. Since the pipe is inclined, the current is not normal to the pipe. This inclination angle is important when considering the vibrations. Only the component that is normal to the pipe is considered when calculating vibration of the pipe. Figure 14 shows the current divided into normal and tangential component vectors.

Therefore:

$$U_n = U \cos\phi \tag{3.5}$$

where Φ is the incidence angle of the pipe with the vertical.

For the Gulf Stream tests, the inclination angle can be as great at 60°. This can reduce the current by up to 50%.

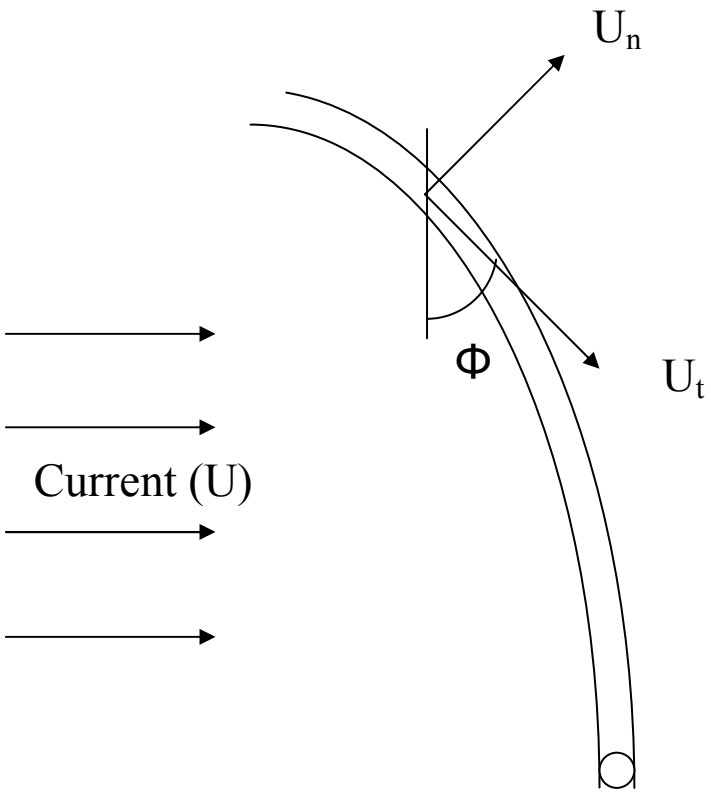

Figure 14 - The pipe showing normal incident current

Speed of Propagation and Natural Frequency

The speed of propagation and the natural frequency are proportional. With the speed of propagation equal to:

$$c = f\lambda \tag{3.6}$$

a pipe under tension has a speed of propagation that may be frequency dependant. At low frequencies, the pipe is dominated by tension effects and reacts like a tensioned string with a constant speed of propagation of:

$$c = \sqrt{\frac{T}{m}} \tag{3.7}$$

where c is the speed of propagation, T is the tension, and m is the mass per unit length including the added mass.

At high frequencies, the speed of propagation is controlled by the bending stiffness of the pipe. The speed of propagation therefore is:

$$c^2 = \omega\sqrt{\frac{EI}{m}} \tag{3.8}$$

where E is the Young's modulus, I the moment of inertia, and A is the cross-sectional area.

In between, the pipe will react as a combination of the tensioned string and the beam with pinned-pinned connections. The speed of propagation is:

$$c = \left(\frac{T}{m} + \left(\frac{n\pi}{L}\right)^2 \frac{EI}{m}\right)^{1/2} \tag{3.9}$$

where L is the length and n is the mode number.

Subsequently, the natural frequencies for the string and the beam are:

$$f_{n,string} = \frac{n}{2L}\sqrt{\frac{T}{m}} \tag{3.10}$$

$$f_{n,beam} = \frac{n^2\pi}{2L^2}\sqrt{\frac{EI}{m}} \tag{3.11}$$

The natural frequency of a string is proportional to the mode number n, whereas the natural frequency of a beam is proportional to the mode number squared. Therefore, the naturally frequency of a tensioned beam is:

$$f_n = \sqrt{f_{n,string}^2 + f_{n,beam}^2} \tag{3.12}$$

Resonance and "Lock-In" Behavior

The periodic shedding of the vortices has two major effects on the cylinder. In the cross-flow direction, a lift force and the corresponding cross-flow vibrations are transverse to the flow. In the in-line direction, a drag force and corresponding in-line vibration are parallel to the flow.

The cross-flow vibration occurs at or near the vortex-shedding frequency, whereas the in-line vibration occurs at twice the cross-flow vibration frequency. In the cross-flow direction, a vortex is shed when the cylinder is near either the maxima or the

minima of cross-flow motion. In the in-line direction, the pressure drag increases every time a vortex is shed whether at a maximum or a minimum. Thus, the frequency of the in-line is twice that of the cross-flow.

When the frequency of the vortex shedding closely matches the natural frequency of the structure, a resonance or "lock-in" behavior can occur. When the lock-in phenomenon occurs, the structure responds coherently and the vortices correlate along a segment that can be up to the length of the pipe. At lock-in, the pipe can respond with displacement of up to one and a half times the diameter of the pipe. Lock-in can occur over a wide range of frequencies near the natural frequency of the pipe because of added mass. Added mass is a function of the reduced velocity and allows the natural frequency to increase with flow velocity. This effect is most significant at low mass ratios, where the mass ratio is defined as:

$$m^* = \frac{m}{\rho_f D^2} \tag{3.13}$$

Various experiments have shown that the RMS amplitude divided by the diameter is a function of the reduced velocity. The displacement and the range of reduced velocities are affected by the mass ratio, [Chung 1987]. Figure 15 shows experimental data with the RMS amplitudes/diameter for various mass ratios plotted versus reduced velocity (V_{rn}).

Added mass is an additional complication that results from working in a hydrodynamic environment. When doing VIV calculations in air, added mass is not an issue. Because of the density of the water being displaced by the vibrations, the mass of the water must be taken into account when calculating the mass per unit length of the pipe. The added mass is given by:

$$m_a = \frac{\pi}{4} C_a \rho_f D^2 \tag{3.14}$$

where C_a is the added mass coefficient.

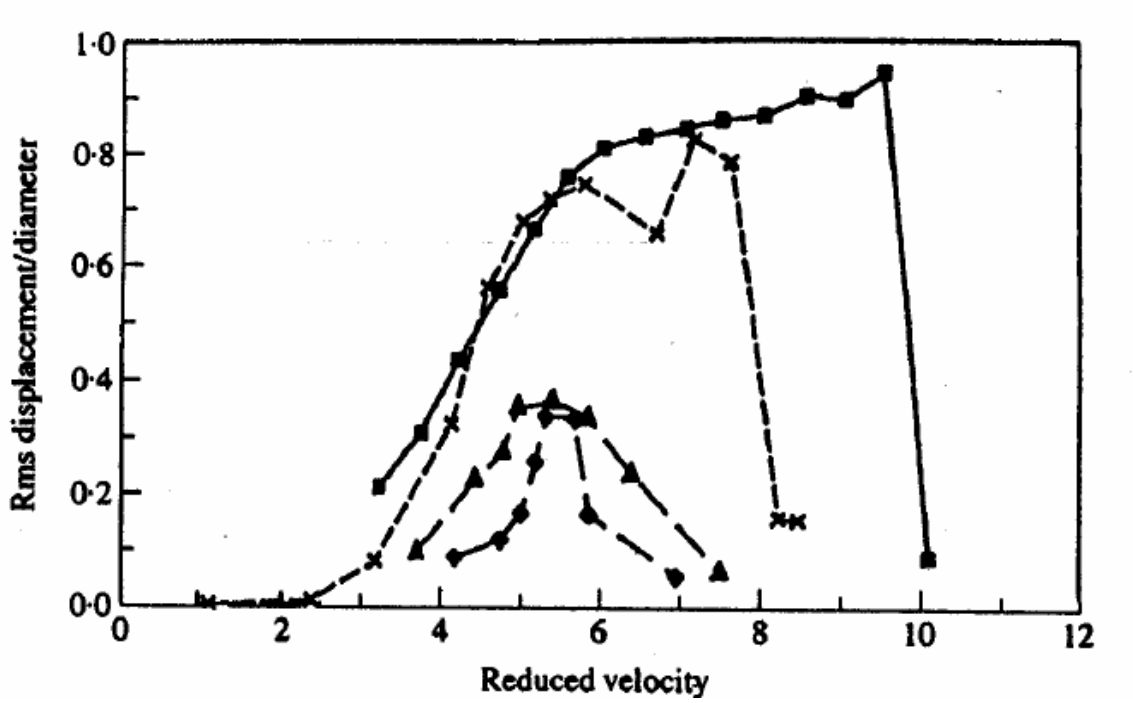

Figure 15 –RMS displacement versus reduced velocity (V_{rn}) for various mass ratios. [Chung 1987]: □ m*=0.78; x m*=1.77; Δ m* = 3.8; ◊m*=34

Power-In Region

The section of the pipe over which the wake is correlated is known as the power-in region. The correlated wake equates to a correlated input force, thus over this section of the pipe power is entering the system. The length of this power-in region is defined as L_{in}. The wake is correlated and therefore has a single frequency of input.

The current speed may change over the length of the power-in region; since the frequency is constant across the entire length, the reduced velocity changes proportionally to the change in current speed.

The percentage change in velocity over the power-in region is known as the reduced velocity bandwidth, and is defined as:

$$dV_r = \frac{V_{r,\max} - V_{r,\min}}{V_{r,mean}} = \frac{\frac{U_{\max}}{fD} - \frac{U_{\min}}{fD}}{\frac{U_{mean}}{fD}} = \frac{U_{\max} - U_{\min}}{U_{mean}} \qquad (3.15)$$

Modal Response and Damping

In laboratory experiments and on short span risers at low-mode number, standing wave behavior can be seen in these tests. The entire riser responds regardless of whether the forcing function is at a single point or distributed down the length of the riser.

The opposite response to the standing wave behavior is the response seen in an infinite string. In the infinite string response, a section of the string is excited and has large amplitude response. Outside the area of large response, the waves travel away from the source and are damped by the structural and hydrodynamic damping.

The Lake Seneca and Gulf Stream experiments had a large length-to-diameter ratio and high enough currents that standing wave behavior was not recorded. In real time experiments, infinite string behavior is never seen because of reflections from the ends of the riser and other factors. Therefore, for the Lake Seneca and Gulf Stream experiments, the responses are between the two extremes of standing wave and infinite string.

Whether or not the cable responds as an infinite string or with standing wave behavior largely depends on the hydrodynamic damping. The parameter of $n\zeta_n$, (Vandiver 1993), where n is the mode number and ζ is the total structural and hydrodynamic damping, is useful in determining how the pipe will respond. When $n\zeta_n$ is less than 0.2, clear standing wave behavior is expected over the entire length of the pipe. When $n\zeta_n$ is greater than 2.0, an infinite cable response is seen. For $0.2 < n\zeta_n < 2.0$, the behavior of the pipe is a combination of standing wave behavior and infinite cable response.

In sheared flow, the hydrodynamic damping can often be greater than the structural damping and must be considered when calculating $n\zeta_n$. The hydrodynamic damping model used in the program SHEAR7 has three empirical terms [Vikestad et al. (2000)]. SHEAR7 is an industry program used to predict VIV of risers. These terms are given below.

The low reduced velocity damping model:

$$r_h(z) = r_{sw} + C_{rl}\rho DV \tag{3.16}$$

where r_{sw} is the still water contribution and C_{rl} is an empirical coefficient taken for the present to be 0.18.

The still water contribution is given by:

$$r_{sw} = \frac{\omega \pi \rho D^2}{2}\left[\frac{2\sqrt{2}}{\sqrt{\mathrm{Re}_\omega}} + C_{sw}\left(\frac{A}{D}\right)^2\right] \tag{3.17}$$

where $\mathrm{Re}_w = \omega D^2 / v$, a vibration Reynolds number. v is the kinematic viscosity of the fluid and ω is the vibration frequency. C_{sw} is the coefficient of still water damping; the coefficient may be varied to produce more or less still water damping.

The high reduced velocity damping model:

$$r_h = C_{rh}\rho V^2 / \omega \tag{3.18}$$

where C_{rh} is another empirical coefficient which at present is taken to be 0.2. ρ is the fluid density.

In comparison, the structural damping constant is given by:

$$r_s = 2\zeta_s \omega m \tag{3.19}$$

where r_s is the structural damping per unit length and ξ_s is the measured damping ratio.

High-Mode Number Prediction

Many experiments have been done at low mode number using spring-mounted rigid cylinders, flexible cylinders, and real risers.

The Gulf Stream and Lake Seneca tests were designed to produce responses at high-mode numbers. The model was scaled so that high-mode numbers would be excited, where high-mode numbers is defined as greater than 10^{th} mode.

The length to diameter (L/D) ratio is an important factor when determining the scaling of the achievable mode numbers. In equation (3.20), [Vandiver and Marcollo 2003], the maximum mode number is seen to be a function of the current profile and physical parameters but is dependant on the L/D ratio and the angle the top end of the pipe makes with vertical, Φ.

$$n_{\max}^2 = \frac{2\pi \cdot St^2}{C_D} \cdot \sin\phi \cdot \frac{U_{\max}^2}{\langle U^2 \rangle} \cdot \left(\frac{\rho}{\rho_f} + C_a\right) \cdot \frac{L}{D} \tag{3.20}$$

where $\langle U^2 \rangle$ is the mean-squared velocity, and ρ/ρ_f is the ratio of the density of the structure to the density of the fluid.

The test setups used at Lake Seneca and in the Gulf Stream allowed for the fundamental transverse mode to be between 10^{th} and 35^{th} mode for the current profiles in each test.

Shear Parameter

The simplest method of quantifying the amount of shear in a current profile is:

$$\beta = \frac{U_{\max} - U_{\min}}{U_{\max}} = \frac{\Delta U}{U_{\max}} \tag{3.21}$$

For a uniform flow, this shear factor would be equal to 0. A shear factor of close to zero favors a single-frequency response, whereas if the shear factor is one, it indicates a highly sheared flow. The number of possible participating modes is N_s. For a uniform flow, N_s is usually equal to 1, whereas for highly sheared flows, N_s can be much greater.

A more refined parameter was introduced by Vandiver (1993).

$$\beta = \frac{D}{U(x)} \frac{dU}{dx} \tag{3.22}$$

where U(x) is the local velocity of the flow at position x. This shear parameter gives more localized information which may be useful in predicting power-in regions.

Vandiver at al. (1996) presented a categorization based on the shear factor in Equation(3.18), which suggested when single mode versus multi-mode responses might be expected. This categorization was based on model tests done in uniform and shear flow. Vandiver et al. observed that under highly sheared conditions some single-mode behavior was seen, Figure 16.

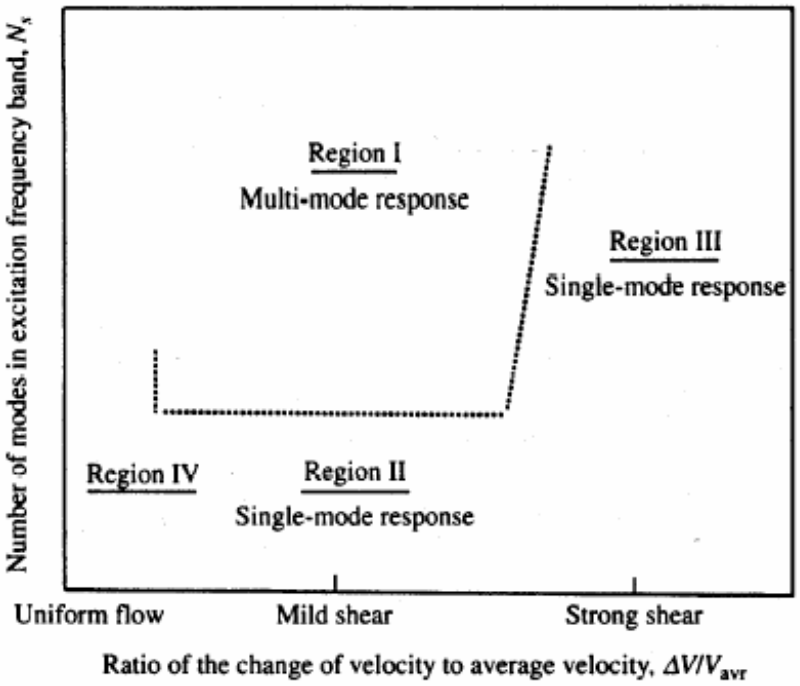

Figure 16 - Identification of multi-mode and single mode response regions. Vandiver et al. (1996)

Higher Harmonics

Higher harmonic VIV response has been discussed in the offshore engineering literature for over twenty-five years. In-line vibration at twice the cross-flow vibration frequency is common knowledge and has been associated with figure-eight motions since the early 1980s [Vandiver 1983; Vandiver and Jong 1987]. The third and fifth harmonics were noticed in accelerometer measurements described in the late 1980s [Vandiver and Chung 1988], but were not considered to be of significant concern when making fatigue life estimates. This was because the response at the frequency of the third and fifth harmonics was quite small in these early experiments on flexible cylinders at low-mode number in uniform and sheared flows.

These experiments were primarily at low-mode number: second, third, or perhaps fourth mode. In the recent experiments, the twentieth to thirtieth modes were excited at the vortex shedding frequencies and large response was observed at higher harmonics of the vortex-shedding frequency.

In the early experiments, the low-mode number and low modal density did not favor the occurrence of resonance between the third harmonic of the lift force and a pipe

natural frequency. In the recent experiments, the third harmonic corresponds to approximately the 60th modal natural frequency. Adjacent natural frequencies are very close together and significant response is always possible. A frequency shift of less than 2% moves the mode number from fifty-ninth to the sixtieth.

Recently, Jauvtis and Williamson [2004] studied VIV for spring mounted cylinders having relatively low mass ratios (<6) and two degrees of freedom. They found the excitation at the 3x harmonic is associated with the shedding of three vortices in the wake behind the cylinder during each VIV half cycle. They call this the '2T' mode of vortex shedding. They report that the switch to the 2T mode happens around reduced velocities of 5 and persists until reduced velocities of 8. They observed large A_y/D_o ratios associated with the 2T mode and call it the SuperUpper (SU) region in the plot of A_y/D_o versus reduced velocity. The 2T mode is associated with a relatively large third harmonic lift force component in the cross-flow direction.

Figure 17 shows Jauvtis' and Williamson's A_y/D_o versus reduced velocity data. This plot has been constructed from data shared by Williamson. The horizontal axis is V_r reduced velocity based on the observed vibration frequency. The data is the same as that presented in Jauvtis and Williamson [2004], in which the data was plotted using a reduced velocity based on the still-water natural frequency. In order to compare the Jauvtis and Williamson data to the observations from the Gulf Stream and Lake Seneca experiments, the reduced velocity must be expressed in terms of observed response frequency, as in Figure 17. The region labeled as SU is the response branch associated with a strong 3x harmonic force component.

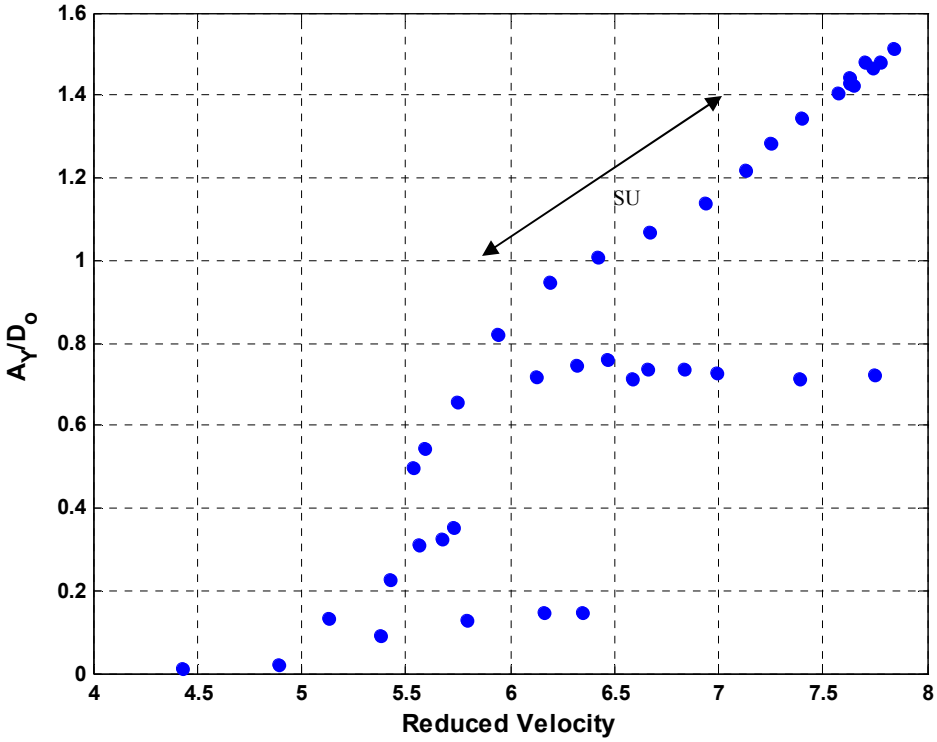

Figure 17 - The SuperUpper (SU) region where the '2T' mode of vortex shedding is found [Jauvtis and Williamson 2004] using the Reduced Velocity (V_{rn})

Chapter 4: Time Sharing of Dominant VIV Frequencies

Introduction

A long-discussed question in VIV is when does a single-frequency response happen and when does a multi-frequency response happen. The Lake Seneca tests were uniform-flow tests and single-frequency response was expected. The Lake Seneca tests can be used as a baseline for studying the difference in single- and multi-frequency responses.

The Gulf Stream tests provided a perfect opportunity to investigate the difference between single-frequency and multi-frequency behavior. After close examination of the data, it appears that single-frequency response happens all the time, but in sheared flows the single dominant frequency changes quickly in time. Using Maximum Entropy Method (MEM) analysis, [Burg 1968], the data could be analyzed on small time scales. When looking at short time segments, only one frequency dominated at any one time, but the frequency changed quickly in time.

Modal Behavior

A large number of tests have been done on cylinders at low mode number both in the laboratory and in the field. In these tests, single-frequency response is associated with a modal response. The RMS response shows clear nodes and anti-nodes. Figure 18 shows an example of this modal behavior for an instrumented riser. At these low-mode number cases, single-frequency behavior is controlled by a single mode.

At high mode number, the dynamics of the riser are different. The riser has more behavior of the infinite string than the finite length pinned-pinned string. Therefore, standing mode behavior is not seen at high-mode number. Instead, a single frequency response is seen. The modal behavior with nodes and anti-nodes is not seen at high mode numbers; instead, fairly uniform RMS response is seen in the power-in region with a damped decay outside the power-in region. Therefore, it is inaccurate to discuss singe-mode behavior at high-mode number; instead, the system is dominated by a single frequency response.

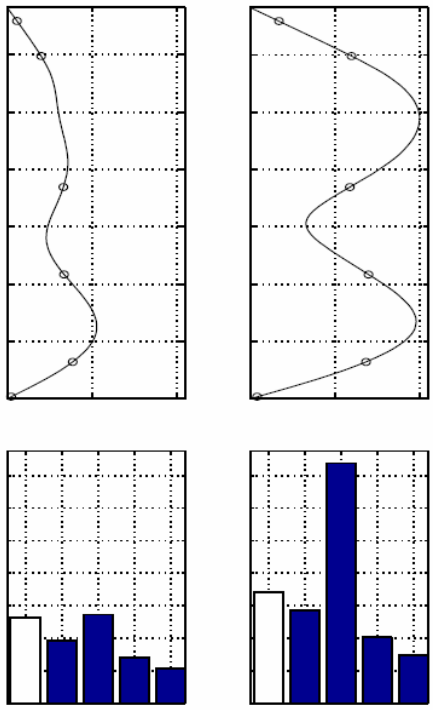

Figure 18 – RMS Profiles of riser displacement and modal weight factors from an NDP drilling riser test [Kaasen et al 2000]

Resonant Behavior at High Mode Number

At low-mode number, resonant behavior is associated with modal behavior. When the frequency of vibration is close to a natural frequency of the cylinder, the vibrations are amplified or they "lock-in". For high-mode numbers, resonant behavior is more associated with large amplitude response that is caused by coherent narrowband forcing lift forces. The resulting motion at the same frequency is sufficiently large to prevent vortex formation at competing frequencies. The vibrations interact with the wake formation so as to amplify, not dampen the response.

Current prediction programs, such as SHEAR7, allow multiple excitation frequencies to co-exist. This method allows different frequencies to have different non-overlapping power-in regions that abut one another. This new concept of single-frequency behavior, says that the frequencies share in time rather than space. This concept only holds true for resonant behavior, where resonant behavior is when large amplitude vibrations occur over an extended region of the pipe.

Local small amplitude vibrations can occur outside of a region with large amplitude response. These vibrations are localized to a small area, are caused by the local

current velocity, and are only slightly larger amplitude than the background noise. The vibrations are damped before they can travel to other areas of the pipe. Local small vibrations appear to be precluded from the areas that have a resonant behavior

Uniform Flow Cases

The Lake Seneca tests had uniform and uni-directional flow. Since the lake was still water, the flow was created by dragging the pipe through the water, [Vandiver et al, 2004]. This created known current speed and flow in only a single direction. The speed of the test was controlled by the speed of the boat that was towing the pipe. The speed control of the boat was not particularly precise, and the current speed varied somewhat over the course of the approximately 2.5 minute runs.

Figure 19 shows the Power Spectral Density (PSD) of a typical constant speed run at Lake Seneca. Because the towing speed was fairly constant and uniform, a single-frequency response is expected. The dominant VIV response is narrow-banded, with components that are harmonics of the dominant VIV frequency also contributing to the spectrum.

In Figure 20, a set of spectra is shown. Each spectrum is from 8.5 seconds of data. The spectra are in time sequential order, with the top spectrum being the first. There is no overlap in time between the spectra. The frequency is stationary, but amplitude varies, especially that of the third harmonic.

To look at the data on a longer time scale, a waterfall spectrum can be used. Burg MEM analysis was used to create Figure 21. Each increment contains 17 seconds of data, with 95% overlap. By looking at the dominant VIV frequency, one sees that only one frequency dominates at any one time. The change in frequency is likely caused by small variations in the current.

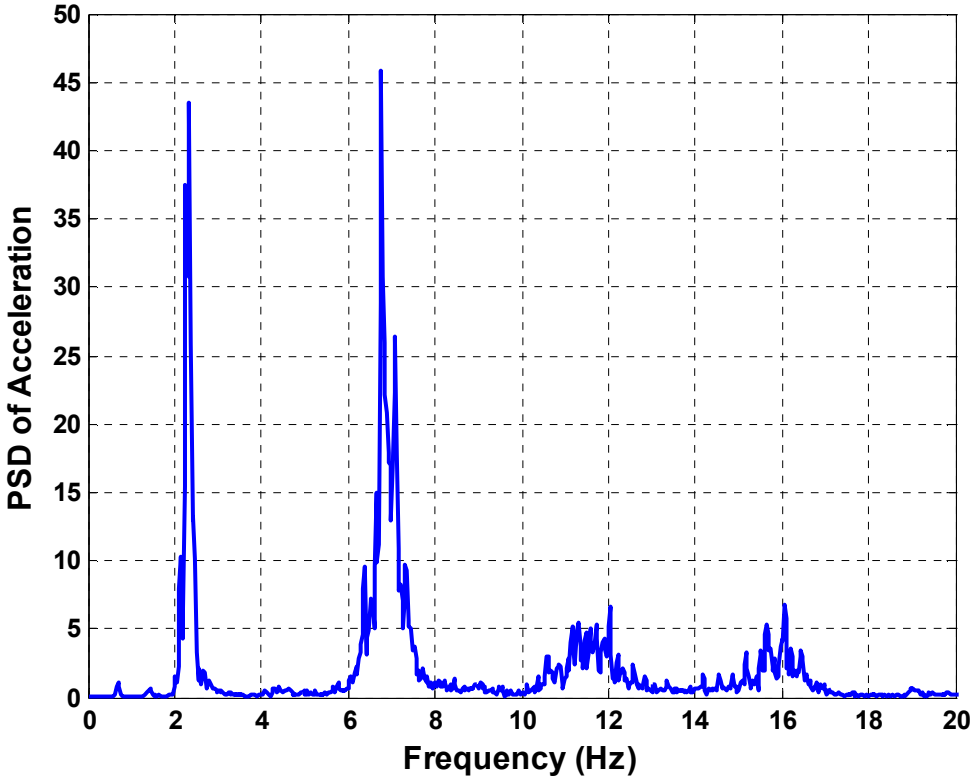

Figure 19 – Spectrum of 138 seconds of data from the Lake Seneca test.

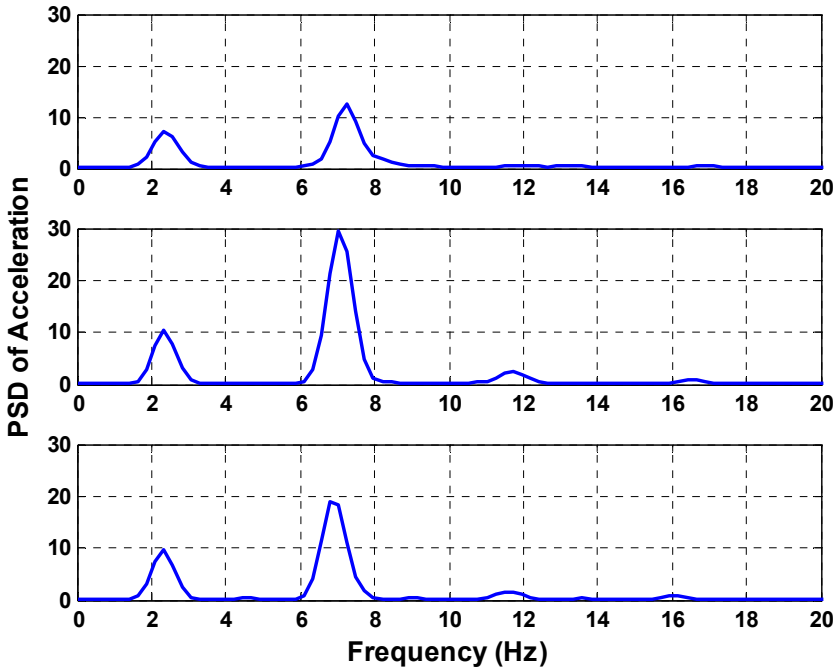

Figure 20 - A series of spectra in time increments of 8.5 seconds showing the dominant VIV frequency and the three-time harmonic component.

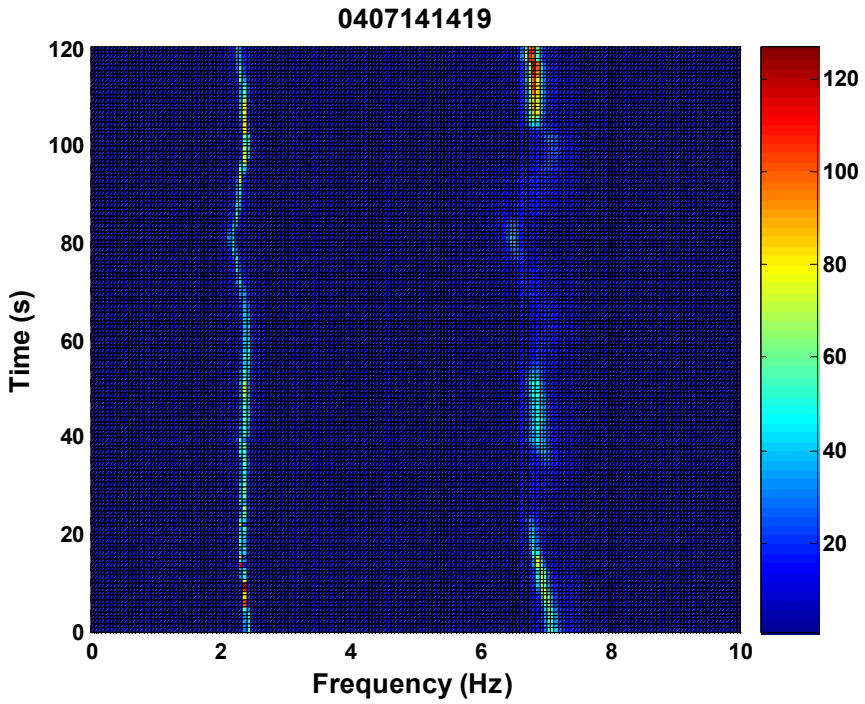

Figure 21 – Waterfall spectra for a base case from Lake Seneca. Each time step used 4.2 seconds of data with 95% overlap

Sheared-Current Time Sharing

When a Power Spectral Density (PSD) is taken over one minute, up to 6 dominant frequencies may have happened in that time, and would all appear in the FFT. When the data is broken into very small time increments and analyzed, single-frequency response becomes more evident.

Figure 22 shows the spectra taken over two minutes for one strain gauge. The dominant VIV frequency shows multi-frequency participation. In Figure 23, the same time series is broken into 10-second intervals. The first two intervals show single-frequency resonant behavior. The second two intervals show the transition from one dominant frequency to another dominant frequency. The vibration at the original frequency loses energy as the second frequency builds up energy in vibration.

The existence of time-sharing does not prevent all multi-frequency behavior. Multi-frequency behavior happens at two different scenarios. The first scenario is seen in Figure 23, in the final two ten-second intervals. There is multi-frequency behavior as the vibrations change from one frequency to another. One frequency will be dominant, then another frequency will begin to gain energy, and the first frequency will lose energy.

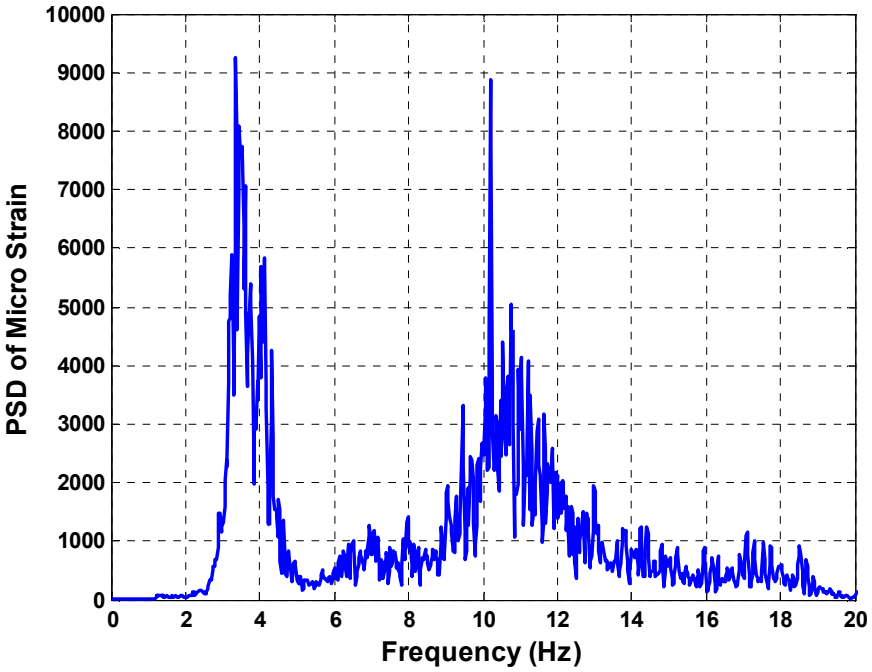

Figure 22 - Spectrum of 134 seconds of data from the Gulf Stream Bare Test

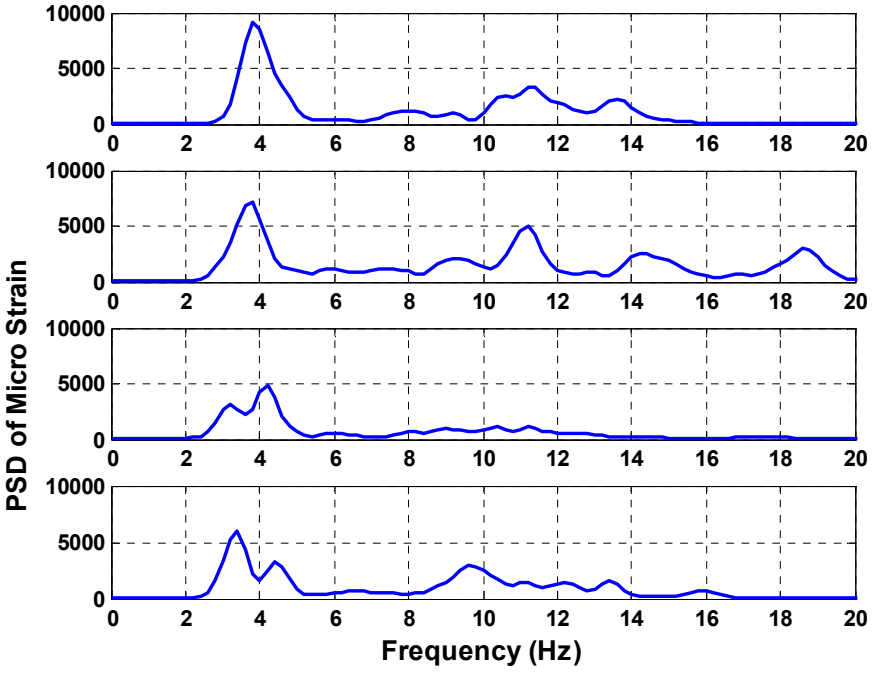

Figure 23 - A set of incremental time series with 10 second windows.

Multiple frequencies can exist at the same time in the Gulf Stream and Lake Seneca data. When this phenomenon occurs the amplitudes of the vibrations are small. When multi-frequency behavior is apparent, the amplitude of the spectral peak is less than 30% of the amplitude at resonant behavior.

The apparent behavior of the riser exhibits small locally generated vibrations that are damped before they travel more than one wavelength. When a resonance occurs, local vibrations are prevented by the coherent vortex shedding at the resonance frequency. The resonant-behavior vibrations are damped as they travel away from the region with a coherent wake. At sufficient distance from the excitation region, locally generated vibrations may be seen again.

Figure 24 is a waterfall spectrum of the same case. The dominant VIV frequency is seen to be about 4 Hz. When the amplitude of the vibration is at less than 1e4 εμ/Hz, some smeared behavior of multi-frequency participating is seen, but when the amplitude is large only one dominant frequency is apparent.

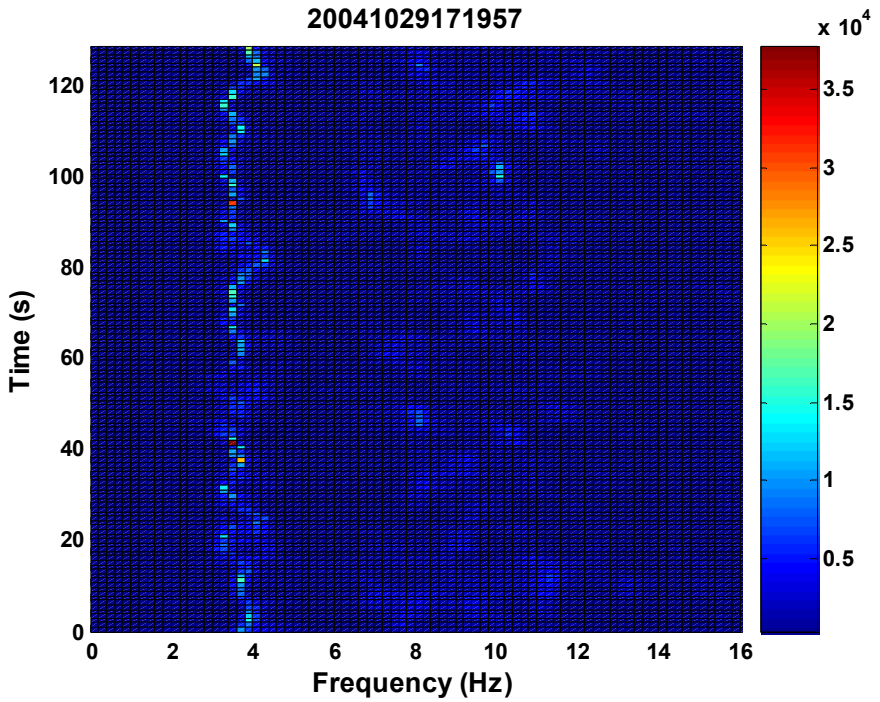

Figure 24 - Waterfall spectra of the strain gauge from the Gulf Stream Bare Case. Each spectrum was calculated using MEM analysis with a 5 second window and 80% overlap.

Figure 25 shows the same waterfall spectrum, but each time step has been normalized such that the maximum value is one. This shows that for most time steps that

no other dominant VIV frequency is greater than 50% of the magnitude of the dominant VIV frequency.

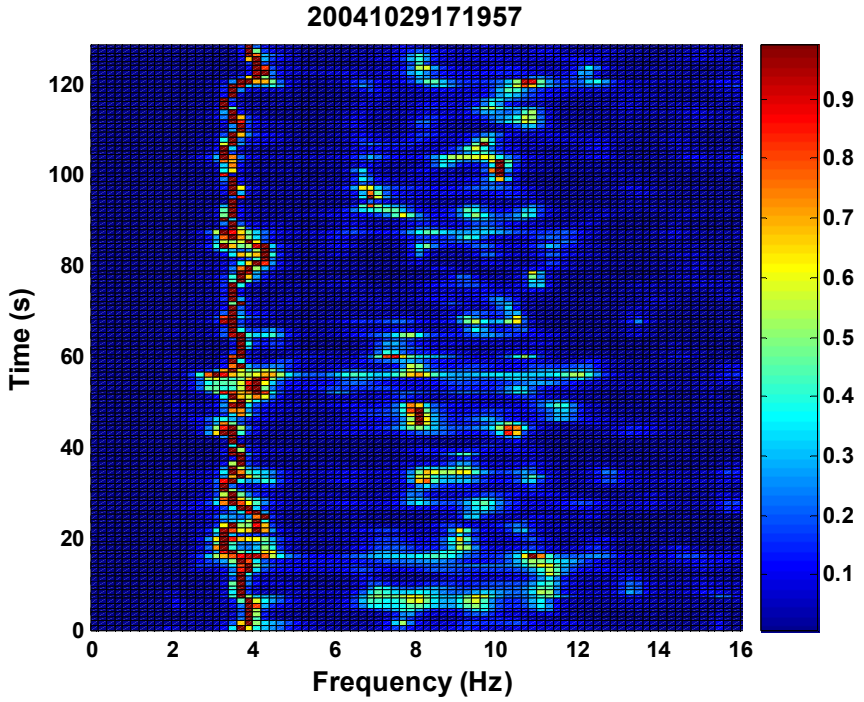

Figure 25 - Waterfall spectra of the strain gauge from the Gulf Stream Bare Case. Each time step is normalized to the largest peak. Each spectrum was calculated using MEM analysis with a 5 second window and 80% overlap.

Impact

The largest impact of time sharing is on the result of fatigue calculations. The calculations of the damage rate for a narrow-banded process, such as single frequency response are different from those for broad-banded or multi-frequency responses.

Common industry practice for the estimation of fatigue damage of risers is to use S-N curves. The fatigue curve for the riser is characterized by the equation $NS^b=C$, where N being the number of cycles to failure, S is the RMS stress range, and b and C are parameters that best fit the data for a given material. When the time history of the stress is a constant stress range sinusoidal process, the damage rate, D_r, is given by:

$$D_r = \frac{\omega_n T_{yr}}{2\pi C}\left(\sqrt{2}S\right)^b \qquad (4.1)$$

If the stress history is a narrow-banded Gaussian random process, then the damage rate is, [Vandiver and Li 2003]:

$$D_r = \frac{\omega_n T_{yr}}{2\pi C}\left(\sqrt{2}\, S_{rms}\right)^b \Gamma\left(\frac{b+2}{2}\right) \qquad (4.2)$$

Equation (4.1) is based on a sinusoidal distribution. Since VIV is rarely a constant amplitude sinusoidal function even with single frequency, Equation (4.2) is a better approximation of the damage. The damage caused by a single-frequency constant-amplitude sinusoidal input is the greatest damage. With single frequency time sharing, the damage rate is higher than it would be for a multi-frequency response, because the damage rate for a single frequency response is higher than the damage rate for a multi-frequency response. Unfortunately, there is no simple equation to describe the damage rate of a broadband spectrum. [Dirlick 1985].

Conclusions

The concept of time-sharing of dominant frequencies as opposed to multiple frequencies participating simultaneously is based on the data from the Gulf Stream and Lake Seneca tests. Single-frequency, time-shared response happens when significant zones of the riser are excited by spatially coherent single frequency forces. Multi-frequency response can happen with small amplitude locally generated waves. Time-sharing of single-frequency responses, as opposed to multi-frequency responses, has an effect on the damage rate of the riser.

Chapter 5: Finding the Power-In Region

Introduction

When looking at the current profile's effect on a pipe, questions of which section of the pipe will allow power to enter the system, known as the power-in region, and which areas of the pipe act to damp the structure become important.

On short pipes at low-mode number, standing wave responses are seen. In the Lake Seneca and Gulf Stream experiments, the length-to-diameter ratio is greater than 3500. Additionally the pipes are responding at modes greater than 10^{th}. At these mode numbers standing wave behavior over the entire pipe is not observed. Instead, a finite power-in region is observed with traveling waves leaving the power-in region and propagating to other regions.

Presented here are two methods of finding the power-in region, the reduced velocity method and the coherence mesh. The first method uses the local reduced velocity to determine whether points are in the power-in region. Reduced velocities from 5 to 8 are traditionally associated with large VIV response at sub-critical Reynolds number.

The second method uses a coherence calculation to find the range over which the vibrations are linearly dependant. The large amplitude waves that are generated in the power-in region will be coherent over a large range, whereas the local small vibrations will not be coherent over a large range.

Reduced Velocity Method

In the Lake Seneca and Gulf Stream experiments, reduced velocities from approximately 3 to 7 were observed by correlating the largest RMS strain response to the reduced velocity. Reduced velocities of 4.5 to 6.5 are observed in the regions with the largest RMS strain response.

Figure 26(a) shows the normal incidence current profile for a run from the Gulf Stream test with both speed (blue) and direction (green). The current profile is sheared from 1.5 ft/s to 3.0 ft/s. Figure 26(b) shows the total RMS strain (blue) and the RMS strain filtered to only contain the dominant VIV frequency (green).

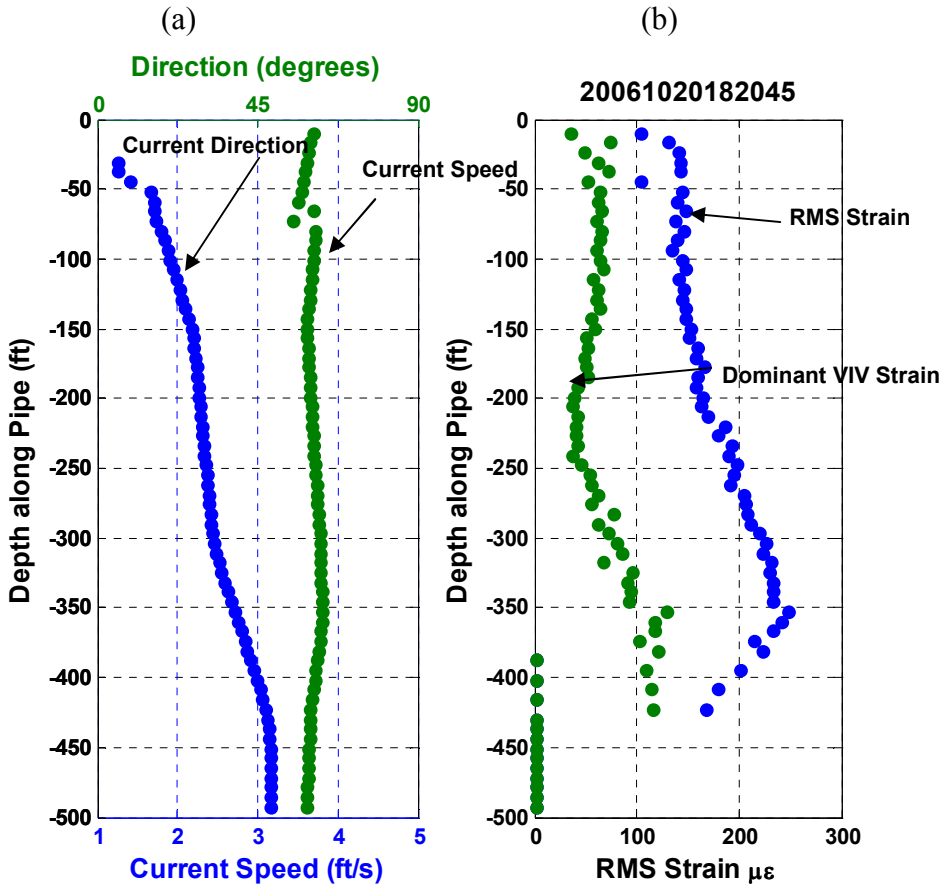

Figure 26 – Gulf Stream bare case (a) Current Speed (blue) and current direction (green); (b) RMS strain (blue) and RMS strain filtered to only show the contribution of the dominant VIV frequency.

Figure 27(a) shows the same current profiles as Figure 26. Figure 27(b) shows the dominant VIV frequencies for each location. The frequency that dominates for the most time is shown with the blue vertical line. The error bars show the variation of the dominant VIV frequency during the total record. In the power-in region, the variation in the frequency is seen to be similar and fairly constant.

Figure 27(c) shows the reduced velocity, calculated using the frequency of vibration. As the frequencies change with time sharing, the reduced velocities change at each location. The reduced velocities are also shown with error bars to show the shift in reduced velocity caused by the shift in frequency over the entire time history.

At the top of the pipe, the variation in reduced velocity is larger. The top of the pipe is an area with low RMS strain and is unlikely to be the power-in region. In this areas, traveling waves from the power-in region will sometimes dominate, which would cause the frequency to appear to be the same as in the power-in region. At other times,

locally generated small amplitude waves that are caused by local currents will dominate. This causes for much greater variation in the frequency, because the local current speed and the current speed in the power-in region can be significantly different from each other.

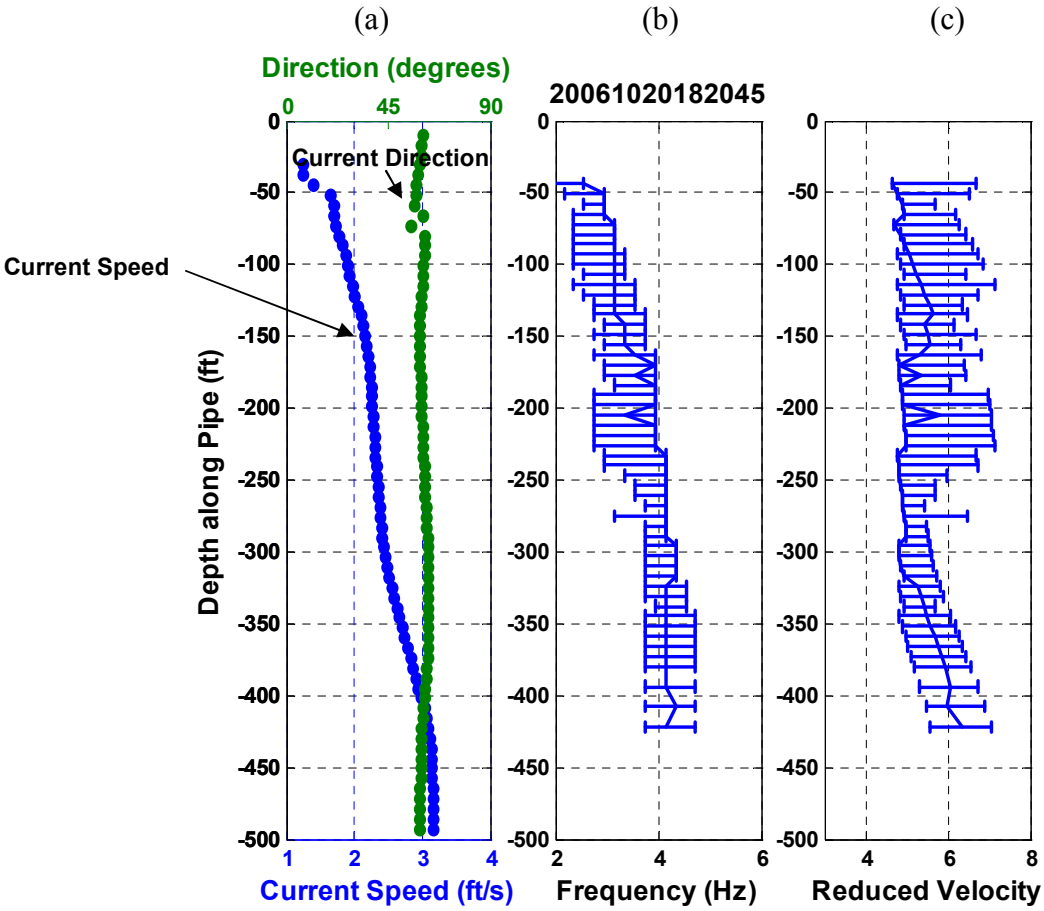

Figure 27 – Gulf Stream bare case (a) Current speed (blue) and the current direction (green); (b) Dominant VIV frequency, showing the most common frequency with the vertical line and the varying frequencies due to time sharing; (c) the reduced velocity, using dominant VIV frequency, the variance is due to the variation in frequency with time shifting.

Coherence Mesh

This method involves calculating the coherence from one sensor in a quadrant to every other sensor in the same quadrant. Coherence is a commonly used signal processing tool that shows linear dependence between to signals and is defined as:

$$C_{xy}(f) = \frac{\left|P_{xy}(f)^2\right|}{P_{xx}(f)P_{yy}(f)} \qquad (5.1)$$

The first step in creating the coherence mesh is to find the distance over which the waves are coherent from each point. Starting with one sensor, the coherence is calculated from that sensor to every sensor point on the pipe. The distance range is defined at the sum of the distance both up and down the pipe over which the coherence is greater than 0.7. A distance range is calculated for every frequency for this original sensor. This process is then repeated for every other sensor, until a distance range has been calculated for every sensor for every frequency. Figure 28 shows an example of the distance ranges from each sensor for an example from the Gulf Stream test.

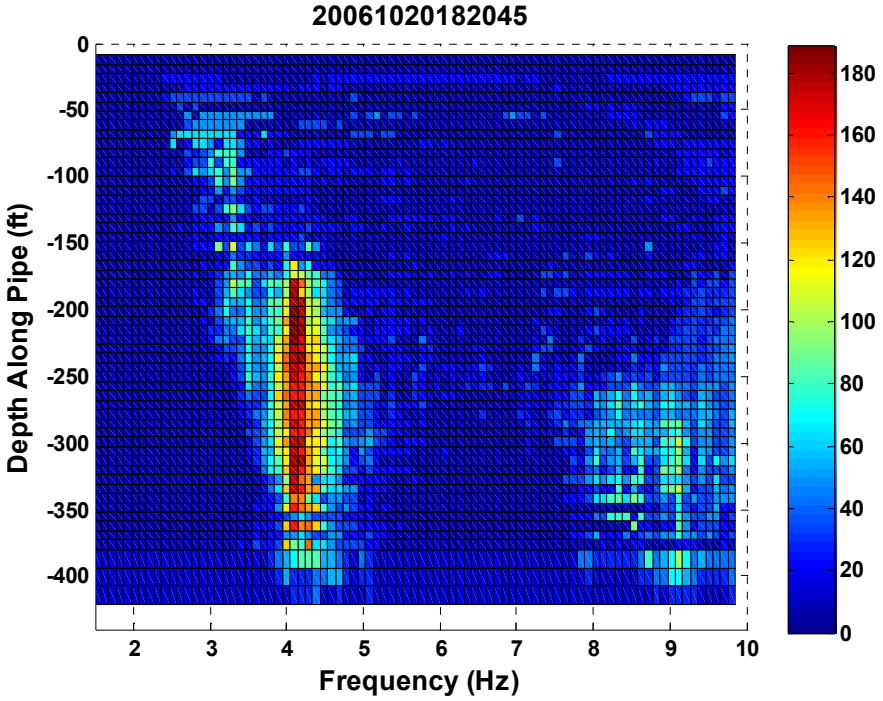

Figure 28 – Gulf Stream bare case coherence mesh showing the distance range from every point over which there is coherence of greater than 0.7

The blue colors represent sensors and frequencies that are coherent over less than 50 ft. Therefore, these waves have little energy and do not travel much distance. The yellow and red tones represent waves that are traveling up to 200 ft. By looking at the frequency 4.2 Hz, it shows that at that frequency waves are traveling over a significant distance. The sensors from 175 ft to 375 ft all show significant coherence over a large distance at a frequency of approximately 4 Hz.

Similar phenomena can be seen at approximately twice the frequency, this would represent the power-in region for the in-line. Due to a sample rate issue with the data [See

Appendix A], the coherence is not as good at this frequency and can not be seen as clearly. Additionally the orientation of this fiber is not known with respect to the flow, and the sensor may be oriented in the cross-flow direction.

More than one frequency can be seen to be coherent; this is because of time sharing. For the coherence calculation to be accurate, a number of averages must be taken. Each average contains 10 seconds of data with 50% overlap between averages. For this coherence mesh, 60 seconds of data was used, indicating that approximately 10 averages were used in the mesh. The more averages reduces error from noise. Unfortunately because of time sharing, the frequencies were not constant and shifted in this example.

To find the power-in region, the point that has the largest total range, as calculated by the coherence mesh, is found. Then any point that has at least 70% of the range of the maximum point is considered part of the power-in region. Figure 29 shows the coherence mesh after the cut-off has been applied. The red points represent the power-in region, where blue points represent the sensors and frequencies that are not adding power to the system.

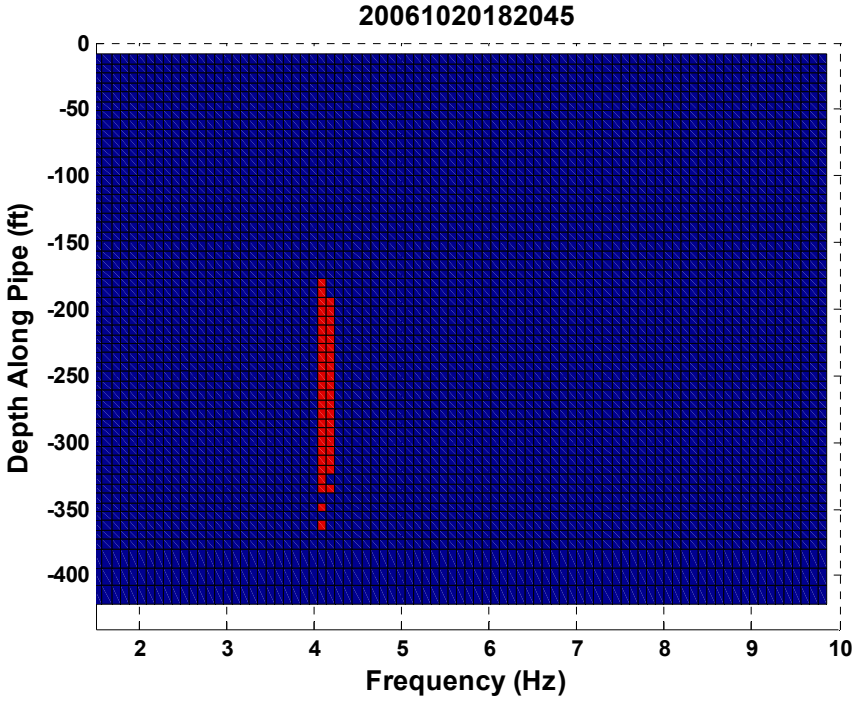

Figure 29 – Coherence mesh after the cut-off has been applied. The power-in region is shown in red.

Conclusions

The coherence mesh is a useful tool for predicting the area of the power-in region. The coherence mesh does have limitations. It can only be used on long cylinders at high mode number. When standing wave behavior is seen in the test data, the coherence mesh does not work.

For a more in-depth analysis of the abilities and limitations of the coherence mesh, including multiple power-in regions and using the coherence mesh with strakes, refer to Appendix H.

Chapter 6: Investigation of the Power-In Region

Introduction

Using both the reduced velocity method and the coherence mesh to identify the power-in region of the pipe allows for further investigation of what factors other than current velocity affect the formation of a power-in region.

Factors such as incident angle of the pipe, the direction of the current, the reduced velocity bandwidth, and the end effects of the pipe are investigated to see their effects of the formation and length of the power-in region.

Reduced Velocity Bandwidth

The reduced velocity bandwidth is defined as:

$$dV_r = \frac{U_{\max} - U_{\min}}{U_{\text{mean}}} \qquad (4.1)$$

where U_{max} is the maximum velocity in the power-in region, U_{min} is the minimum velocity in the power-in region, and U_{mean} is the mean velocity in the power-in region.

For each of the bare Gulf Stream cases, the reduced velocity bandwidth can be calculated for the power-in region found by the coherence mesh. The reduced velocity bandwidths varied from 0.15 to 0.44 for all the cases. The cases with lower reduced velocities had power-in regions that were limited by outside factors such as the angle of incidence of the current or the gradient of the direction of the current. When the power-in region was not limited by incidence angle or direction of the current or other outside factors, the reduced velocity bandwidth in the power-in region found by the coherence mesh was 0.40 ± 10%.

Incident Angle of the Current

For all the steady bare pipe cases from the Gulf Stream test, the maximum incident angle where a dominant power-in region exists is 47 degrees. The Lake Seneca experiment never saw incident angles greater than 47 degrees for the bare pipe; therefore this phenomenon would not affect the Seneca data. This number was derived by looking at all the cases from Miami to find the maximum incidence angle sustainable in a power-in region. Figure 30 and Figure 31 show an example from the Gulf Stream.

Figure 30 shows a case from the Gulf Stream test with the current and RMS Strain.

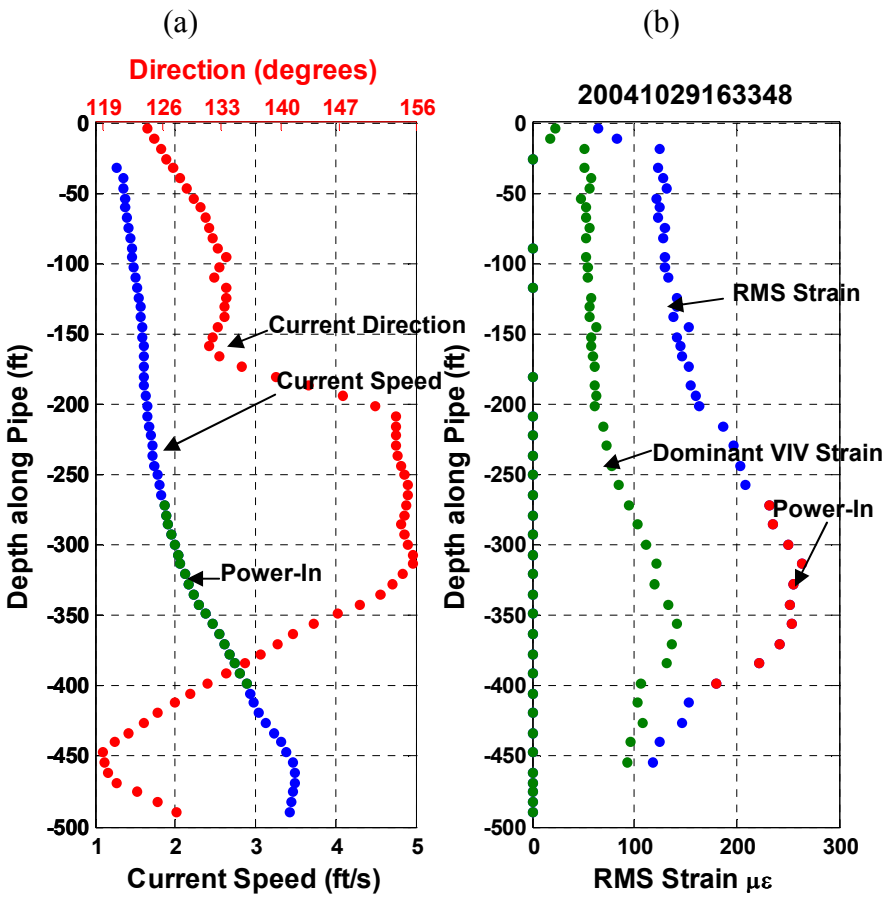

Figure 30 – Gulf Stream bare case (a) Current speed (blue), current direction (red), and power-in region (green); (b) RMS strain (blue) and RMS strain filtered to only show the contribution of the dominant VIV frequency. The power-in region found using the coherence method is shown on both graphs; (a) green and (b) red.

Figure 31 shows the incident angle of the pipe versus depth. Note that this is not the shape of the pipe, but rather the angle of tilt at each location. Zero degrees is a vertical pipe. The dominant power-in region is shown in green. For the dominant power-in region the tilt angle with respect to the current is not great than 40 degrees.

It is impossible to decouple whether it is the incident angle to the current or the change in tilt angle of the pipe that is preventing the dominant power-in region to form in this inclined region. In this test, the pipe's high incident angles occurred at the location of the high gradient of change in the tilt angle. Further investigation will be needed to discover why dominant power-in region cannot form in the curved region of the pipe.

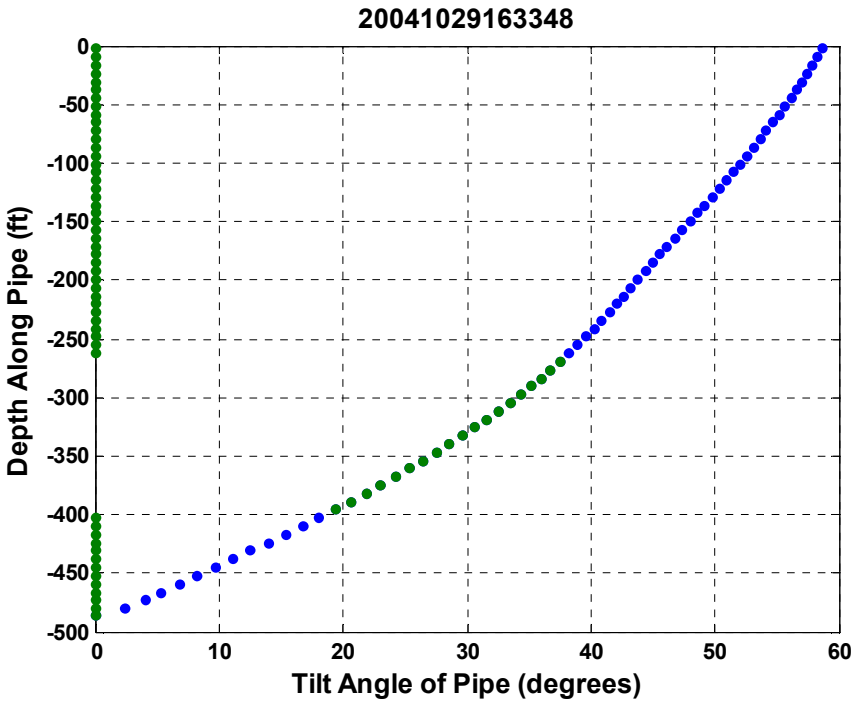

Figure 31 - Incident angle of the pipe shown versus depth for the case of two power-in regions, showing the angle of incidence (blue) and the angle of incidence in the power-in region (green). A second power-in region is from 50 ft to 100 ft, but in this power-in region no large amplitude vibrations are seen.

The Gradient of the Direction of the Current

The gradient of the direction of the current is important to the length of the power-in region. If the direction changes too rapidly over a section of the pipe, the power-in region cannot be sustained there. A rapid change in the direction of the current would prevent coherent vortex shedding.

Figure 32(a) shows the current profile (blue) and direction (red). The power-in region is overlaid on the current profile (green). The current direction varies 35 degrees over the 150 ft with a gradient of 0.24 degree/ft. At the bottom of the power-in region, the direction gradient goes to 0.75 degree/ft. After analyzing each of the steady state runs, it was observed that the power-in region could not be sustained in an area with a large directional gradient. The large change in direction over a short span would prevent a coherent wake from forming in a single direction.

Using the same current profile shown in Figure 32, Figure 33 shows the current direction (red) overlaid with the power-in region (green). Additionally, the gradient of the

current is shown in red. Over the power-in region, the gradient of the direction can be seen as between -0.5 degree/ft and 0 degree/ft.

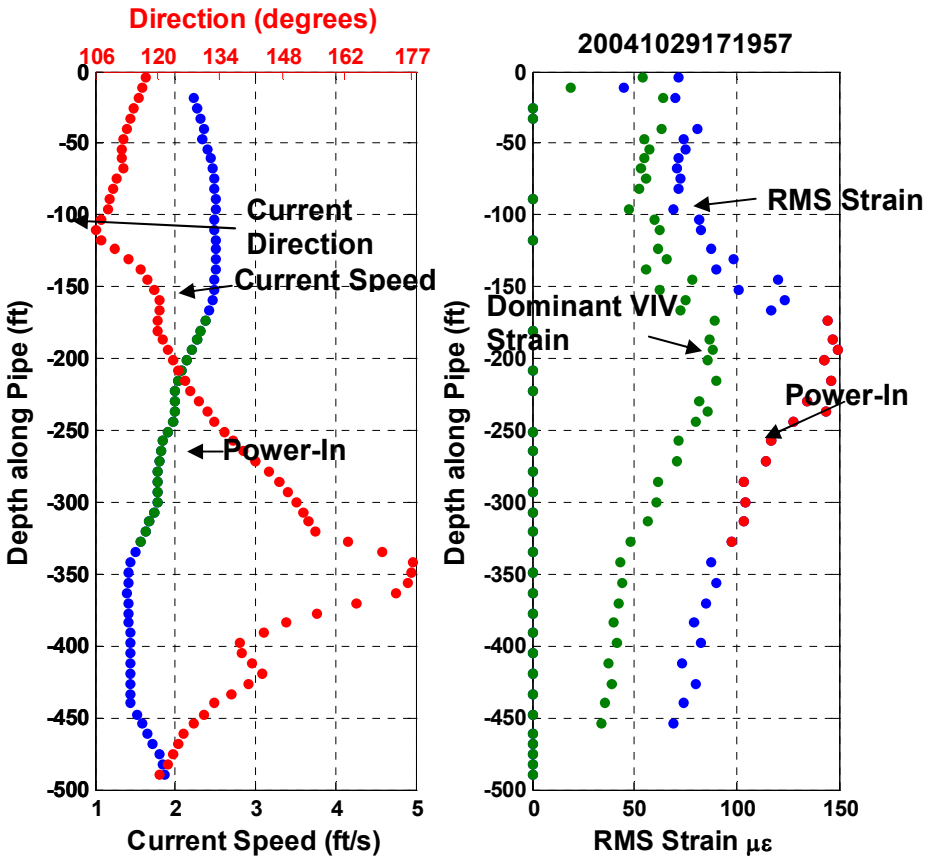

Figure 32 – Gulf Stream bare case (a) Current speed (blue), current direction (red), and power-in region (green); (b) RMS strain (blue) and RMS strain filtered to only show the contribution of the dominant VIV frequency. The power-in region found using the coherence method is shown on both graphs; (a) green and (b) red.

Over all the stationary runs from the Gulf Stream, the maximum allowable direction gradient within a power in region is ±0.5 degree/ft. Further investigation is needed to establish a more exact value.

Likely, the gradient of the current that is allowed in the power-in region is not a fixed number but rather is determined by the structure of the pipe, and may actually be (0.5 degrees/ft)*(the diameter). For the Gulf Stream test, this would be 0.05 degrees allowed per diameter. Another factor that could affect the gradient of the current direction is the wavelength of the vibration, where the factor would be (0.5 degrees/ft)*(the wavelength).

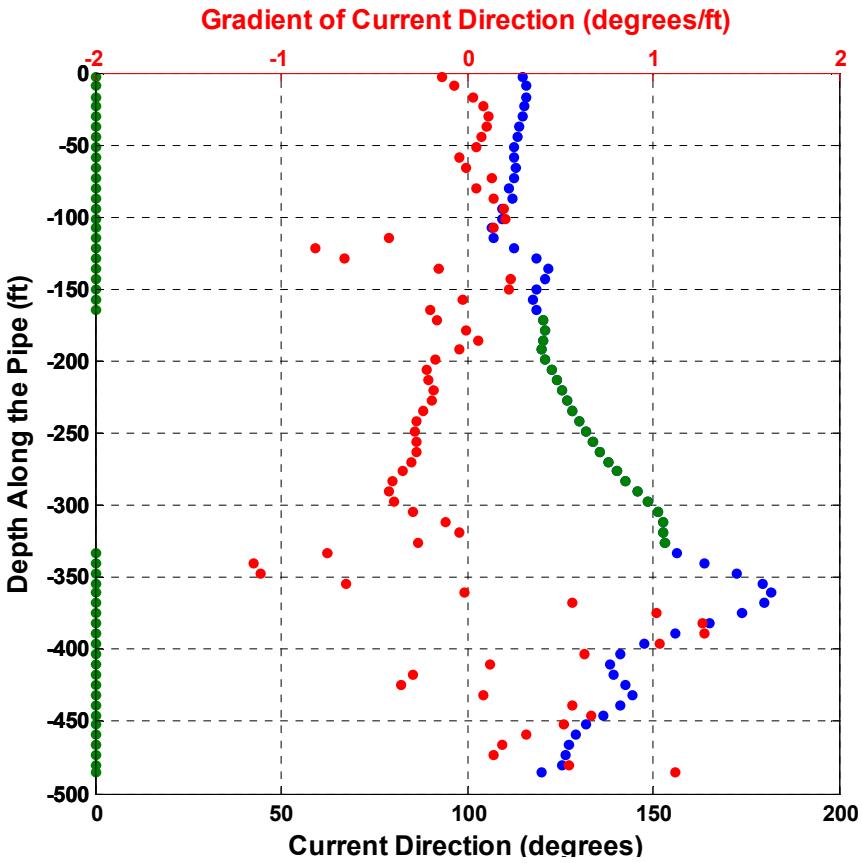

Figure 33 – Gulf Stream bare case; Current direction (blue) overlaid with the power-in region (green) found with the coherence mesh; The gradient of the current direction (red)

End Effects

While analyzing all the Lake Seneca and Gulf Stream data, one anomaly was that the power-in region was never found in the bottom 75-100 ft. One potential reason for this is the presence of the boundary that is established as waves propagating down the pipe are reflected at the end. A large drop in the RMS strain can be seen in the bottom 75 feet.

Figure 34 shows a typical strain measurement from the second Gulf Stream experiment. Figure 34(a) shows the strain from each quadrant, and Figure 34(b) is the current profile, the red and green dots indicate the mechanical current meters at the top and bottom. The power-in region is from approximately 300 to 400 ft. Below the power-in region, there is a significant drop off in the strain measurement. The profile is most uniform at the bottom and because of the normal incident angle the current profile is the fastest. Therefore previous understanding would have predicted this to be the power-in region.

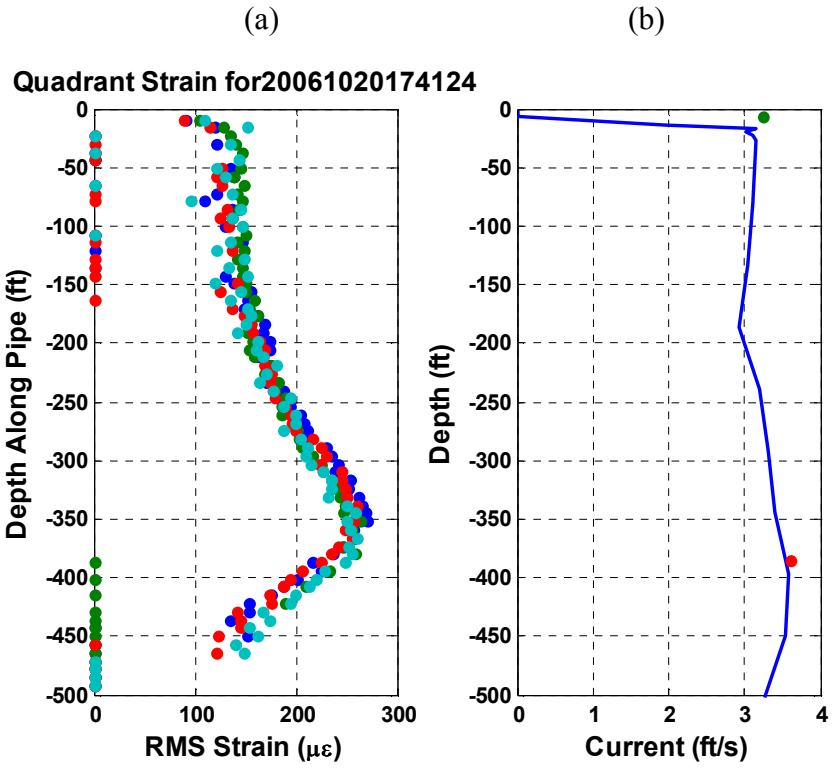

Figure 34 – (a) The quadrant strain for a bare test from the second Gulf Stream experiment. (b) the normal incidence current profile.

One possible explanation for this phenomenon is hydrodynamic. The reflections may interfere with the formation of the wake. Computational fluid dynamics models have shown that n low-mode standing-wave cases the vortex sheets separate from the cylinder all at once. In longer high-mode number cases, the vortex sheets separate at a continuous rate, where the separation point travels down the pipe. This leads to the vortex sheets being diagonal to the cylinder.

The same set-up using the railroad wheel and universal joint on the end was tested at shorter lengths of approximately 200 ft. This test was designed to use the same bottom boundary condition but have a shorter length to diameter ratio. This test was attempting to see whether the same end effects were seen at shorter length to diameter ratios.

At the shorter lengths the end effects were not seen. Therefore this end effect is not likely a product of the set-up of the experiment, and is instead will likely be seen in other VIV experiments on long flexible cylinders at high mode numbers.

During the second Gulf Stream experiment, a set of runs were conducted to force the power-in region into the bottom 125 ft. The experiment used strake coverage over the

center 50% of the pipe. Strakes covered from 125 ft to 375 ft on the pipe. The top end was unlikely to become a power-in region because of the high normal incident angle of the pipe.

In Figure 35, the RMS strain and the current profile are shown for a typical run from these cases. The strain is seen to have a large peak at 375 ft, which is a typical stress concentration for the beginning of the strakes region. [Vandiver et al. 2005]

(a) (b)

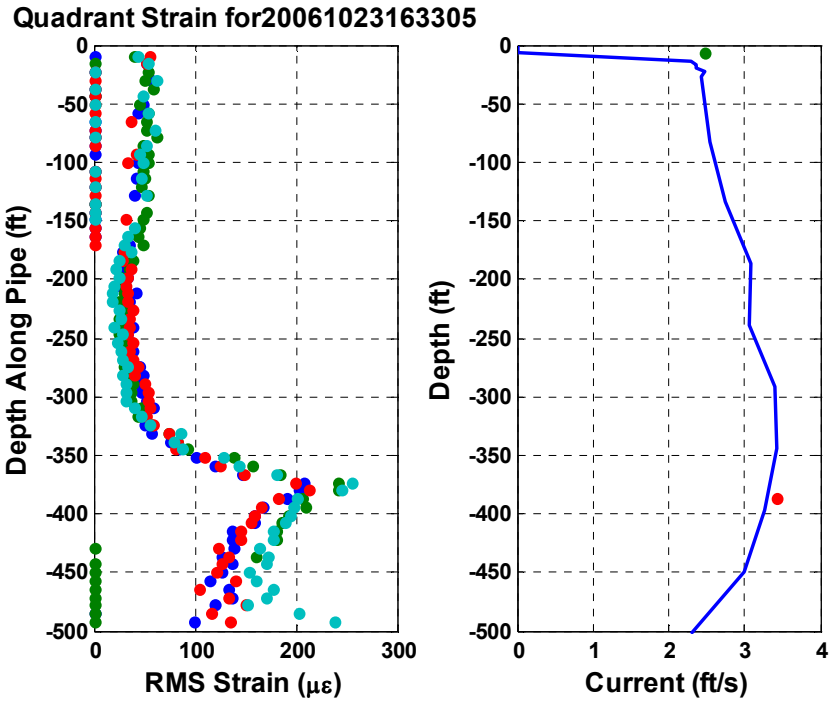

Figure 35 – (a) The individual quadrant strain for a run using 50% strake coverage in the middle. (b) the current profile.

Conclusions

Four influences to the location of the power-in region are shown here, current profile, end effects, pipe curvature. and current directional gradient. The most important of these is the current profile. The power-in region will be dictated by the current, unless either the gradient of the current direction is greater than 0.5 degree/ft or the current's incidence angle to the pipe is greater than 45 degrees. Additionally no power-in will be found in the bottom 75 ft because of the boundary conditions potentially caused by hydrodynamic effects.

When the power-in region was not limited by incidence angle or direction of the current or other outside factors, the reduced velocity bandwidth in the power-in region found by the coherence mesh was 0.40 ± 10%.

Recommendations

All of these conclusions are based solely on the data from the Gulf Stream and Lake Seneca tests. Various sets of tests could be conducted to help reduce the error from these tests and to more fully understand the different factors that affect the location and length of the power-in region.

A set of tests in which the gradient of the current can be controlled and varied would help to determine the exact gradient of the current which can sustain a power-in region and over what length that gradient needs to be sustained. Additionally, being able to vary the diameter of the pipe and the natural frequency of the pipe for these tests would be useful. The number 0.5 degrees/ft is only useful for the Gulf Steam pipe. Because the gradient of the current direction with respect to the pipe can interfere with the vortex wake formation, this is most likely a hydrodynamic phenomenon. Therefore, the change in the gradient of current may not be a steady number such as 0.5 degrees/ft, but instead may be dependant on the diameter of the pipe. Additionally, by being able to vary the natural frequency of the pipe, future research could determine whether or not the wavelength of the vibrations is an influential factor.

Further investigation should be done using the data from the second Gulf Stream experiment and during which run in uniform flow at increasing speeds were conducted. The increasing speeds would vary the top angle of the pipe and therefore the incidence angle of the current. By doing a slowly increasing test, the incidence angles that do not favor a power-in region could be found. The tests at Lake Seneca only reached approximately 30 degrees which did not greatly effect the formation of the power-in region, whereas the Gulf Stream tests saw incidence angles that adversely affected the formation of a dominant power-in region. Further investigation in a controlled environment could help with the design of SCRs and other off-shore catenaries.

A test that involved a linear shear could help to expand understanding of the phenomena of modal shifting in time, and would be useful in the power-in calculations as

well. A linear shear with little current variation would help to determine whether or not the power-in region moves greatly when the mode shifts.

Lastly, further investigation of the end effect phenomenon should be done to determine whether this is a hydrodynamic effect or something else controlling the dynamics. Tools such as flow visualization may be used for both these last two experiments to understand the hydrodynamic forces and wake synchronization.

Chapter 7: Discerning In-Line and Cross-Flow Vibrations

Introduction

In uni-directional flow, finding the in-line and cross-flow direction is simple because the one-time and three-time vibrations align perpendicular to the flow. When the directions of the flows vary, the direction or even existence of separable in-line and cross-flow vibrations is a topic for further research. Using the Lake Seneca experiment as a baseline, the Gulf Stream experiments are a good example to use to investigate the effects of the direction of current on the in-line and cross-flow vibrations.

Rotation of Sensors

When looking for the in-line and cross-flow directions in the Lake Seneca and Gulf Stream experiments, it is easiest to align the sensors nominally in the direction of the cross-flow and in-line directions.

For the Lake Seneca experiment, the orientation of the sensors was found before the experiment, [Vandiver et al. 2005]. Therefore, the vector components of the response could be rotated to align them with the direction of the flow.

The orientation of the sensors for the Gulf Stream test was initially unknown and varies down the length of the pipe, [See Test Description]. Spectra of the two vector components are taken, and then the two orthogonal directions have been rotated to maximize the peak of the dominant VIV frequency. A simple rotation matrix was used to perform this rotation:

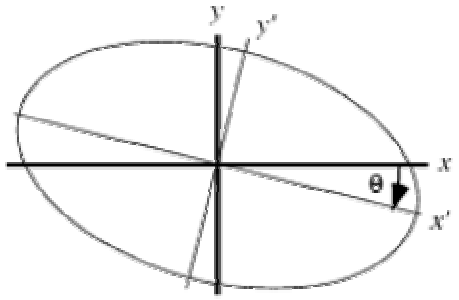

Figure 36 - An illustration of the effects of a rotation matrix

$$\begin{bmatrix} x' \\ y' \end{bmatrix} = \begin{bmatrix} \cos\theta & \sin\theta \\ -\sin\theta & \cos\theta \end{bmatrix} \begin{bmatrix} x \\ y \end{bmatrix} \tag{7.1}$$

Figure 36 is an illustration of the effects of the rotation matrix, where x and y are the original orientation of the sensors and x' and y' are the orientation of the estimated cross-flow and in-line directions.

The graphs in this chapter have all been rotated to maximize the dominant VIV frequency.

Uniform and Uni-Directional Results

Since the flow was from a single direction, in-line and cross-flow directions are easily discernable. Figure 37 shows an example steady-state bare case at a current speed of 2.1 ft/s from Lake Seneca. The Power Spectral Density (PSD) shows the cross-flow (blue) and in-line (green) components of the flow. The response is composed of a cross-flow component at the odd harmonics and an in-line component at the even harmonics. The spectra have been taken for the entire 2.5 minute test run, leading to the broad-banded nature of some of the peaks.

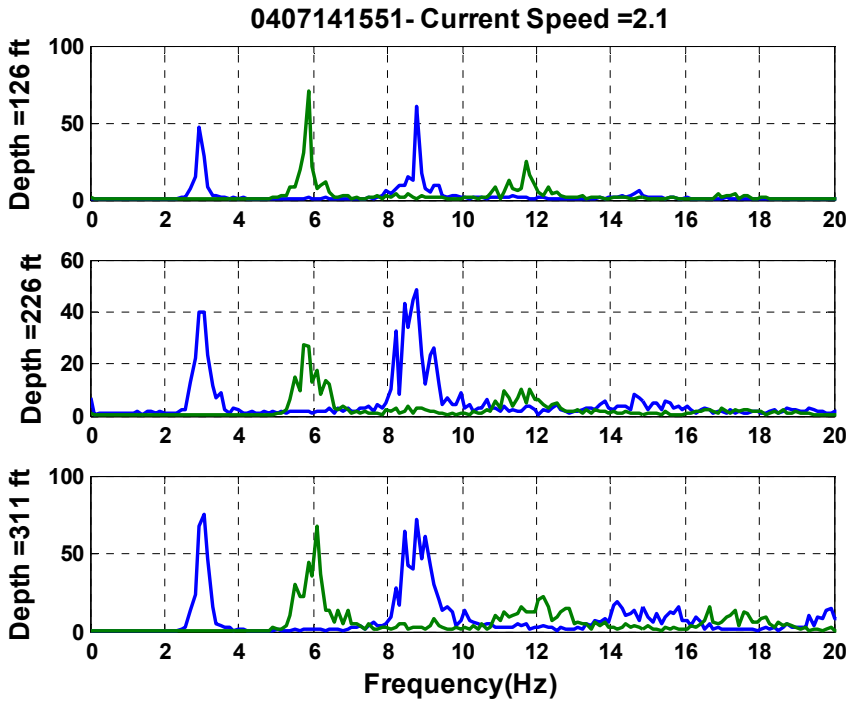

Figure 37 – Cross-flow (blue) and in-line (green) PSDs from a Lake Seneca bare test at depths of 126, 226, and 311 ft over the course of a 2.5 minute test.

Another example from the Lake Seneca test, with a current speed of 1.6 ft/s, is shown in Figure 38. The cross-flow (blue) and in-line (green) components are again

clearly discernable. The Lake Seneca uni-directional flows gave the expected results and were similar to the results from laboratory tests.

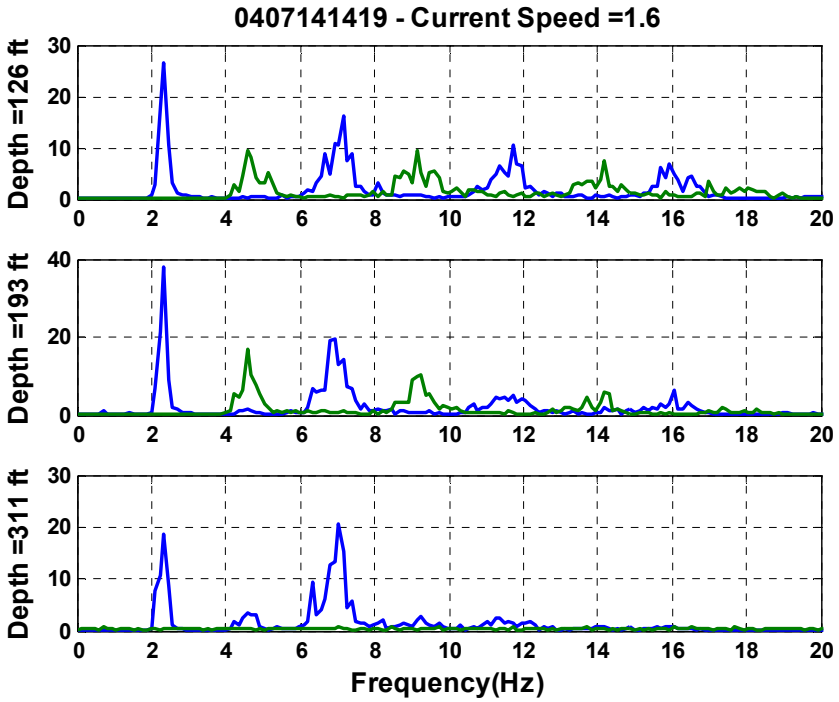

Figure 38 - Cross-flow (blue) and in-line (green) PSDs from a Lake Seneca bare test at depths of 126, 226, and 311 ft over the course of a 2.5 minute test.

Sheared Flow Multi-Directional Flow

The Gulf Stream tests allow analysis to see whether discernable in-line and cross-flow vibrations exist in multi-directional flow.

Similar to Figure 38, Figure 39 shows the spectra from three different locations along the length of the pipe, 102.9 ft, 243.5 ft, and 384 ft, for a 100 second period of time. At 243.5 ft, in-line and cross-flow vibrations are discernable though both are very broadband.

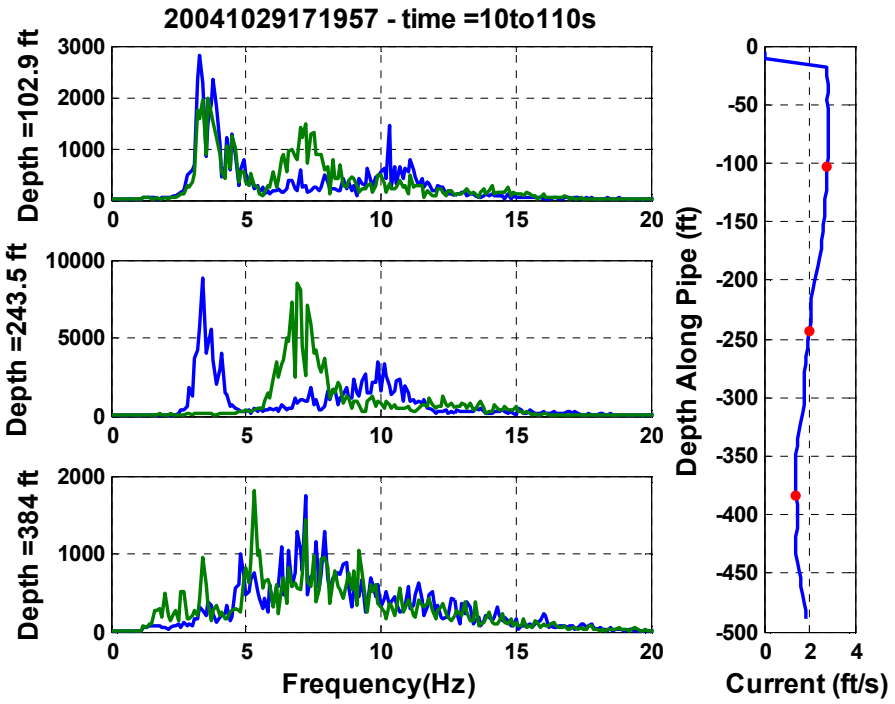

Figure 39 - Cross-flow (blue) and in-line (green) PSDs from a Gulf Stream bare test at depths of 102.9, 243.5, and 384 ft over the course of approximately 100 seconds. On the right hand side, the current profile is shown, corrected for incidence angle and showing the location of the three PSDs.

By looking at the power-in region found in Chapter 5 for this case, the power-in region extends from approximately 200 to 325 ft. At 102.9 ft, the dominant VIV frequency is visible in both the in-line and cross-flow component and is broadband in nature. At 384 ft, no discernable in-line and cross-flow components can be found. The amplitude of the vibrations is also approximately 20% of the amplitude of the dominant VIV frequency in the power-in region. On the right-hand side, the current profile, corrected for incidence angle, is shown with the location of the three spectra marked in red.

By breaking the test run down into smaller sections of time and looking at a time when only a single frequency dominates is be seen in Figure 40. Sharp peaks correlating to the dominant VIV frequency and the two-time component are prominent in the PSD at 234.5 ft. At 102.9 ft, the same dominant VIV frequency is seen, though at a smaller amplitude. The two-time component is smaller. This is expected as the higher frequency components will attenuate faster outside the power-in region. The peaks seen in the 384 ft. spectrum have no correlation to the dominant VIV frequency. The peaks are at one-fifth the amplitude of the dominant VIV frequency and are likely locally generated.

Figure 41 shows another time block in the same run. This block is a time of transition between dominant VIV frequencies. In the power-in region, the amplitude of the VIV frequency is about half that seen in Figure 40. A second VIV frequency is also attempting to compete with the VIV frequency. The multiple low-amplitude VIV frequencies are mirrored in the spectra at 102.9 ft. At 384 ft, signal-to-noise ratio is almost 1. No clear vibration frequencies can be seen above the noise.

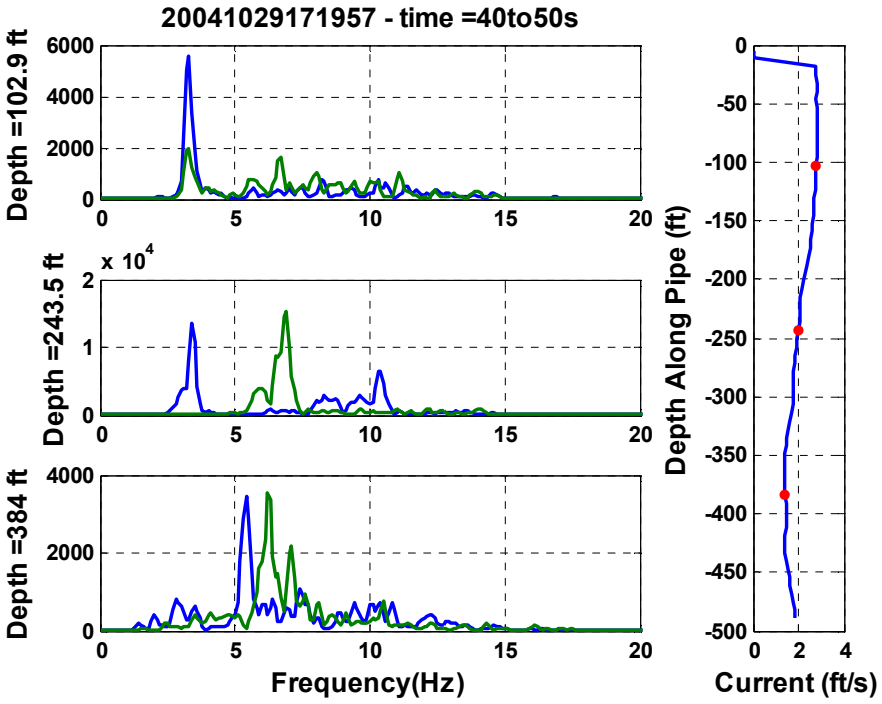

Figure 40 - Cross-flow (blue) and in-line (green) PSDs from a Gulf Stream bare test at depths of 102.9, 243.5, and 384 ft over the course of approximately 100 seconds. On the right hand side, the current profile is shown, corrected for incidence angle and showing the location of the three PSDs.

When looking at the cases with multiple power-in regions, the difference in dominant VIV frequencies can be seen. From Chapter 5, the power-in regions for Gulf Stream test 20041029163348 are from 275 ft to 400 ft for the dominant power-in region and from 75 ft to 150 ft for the other power-in region.

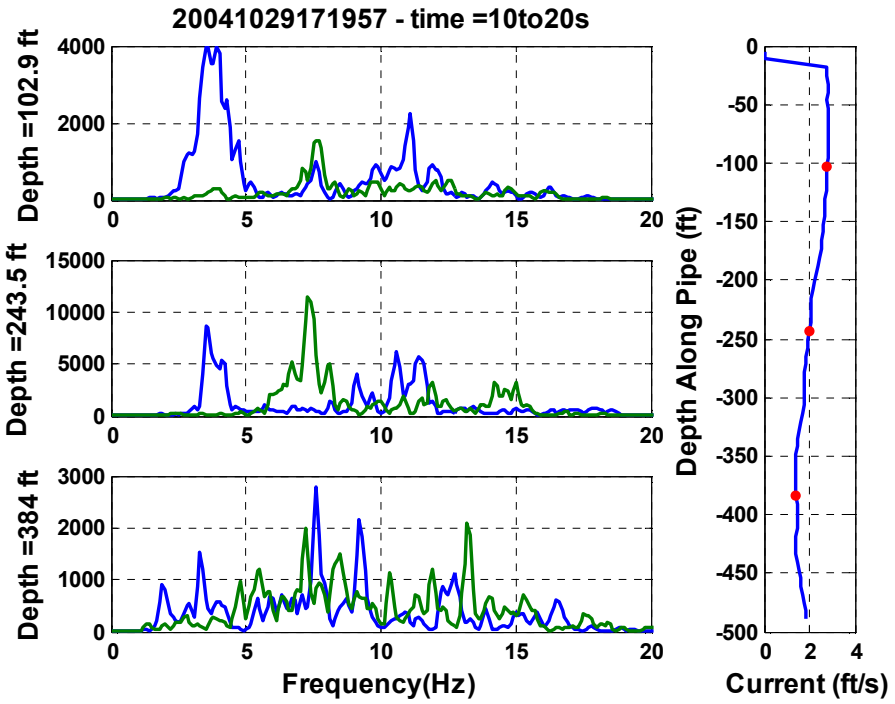

Figure 41 - Cross-flow (blue) and in-line (green) PSDs from a Gulf Stream bare test at depths of 102.9, 243.5, and 384 ft over the course of approximately 100 seconds. On the right hand side, the current profile is shown, corrected for incidence angle and showing the location of the three PSDs.

In Figure 42, the bottom spectrum is in the dominant power-in region; this spectrum shows clear characteristics of in-line and cross-flow behavior. The peaks are broadband because the spectrum is taken over 100 seconds. The top spectrum is in the upper power-in region. A broadband dominant VIV frequency is located between 3 and 4 Hz. Because the upper power-in region is not dominant, not much energy is associated with this power-in region and therefore, the signal-to-noise ratio is not large. Because the signal-to-noise ratio is not large, the higher frequencies appear very broadband in nature without any dominant frequencies. The middle spectrum shows the dominant VIV frequency of the lower power-in region, but the signal has attenuated, the signal-to-noise ratio is lower, and the spectrum is broadband. The current profile, showing the location of the three spectra, is on the right-hand side of the figure.

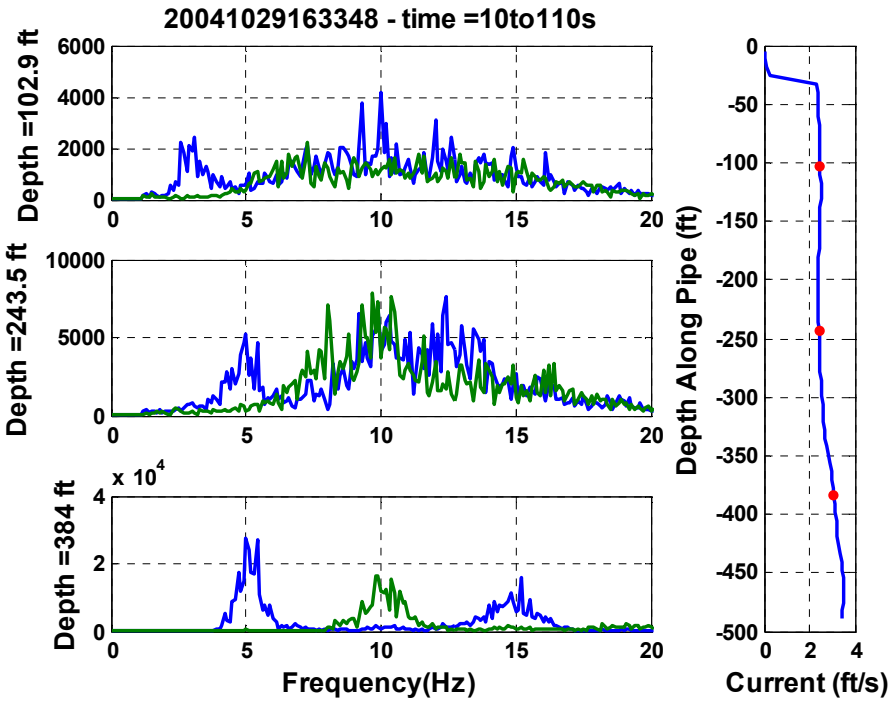

Figure 42 - Cross-flow (blue) and in-line (green) PSDs from a Gulf Stream bare test at depths of 102.9, 243.5, and 384 ft over the course of approximately 100 seconds. On the right hand side, the current profile is shown, corrected for incidence angle and showing the location of the three PSDs.

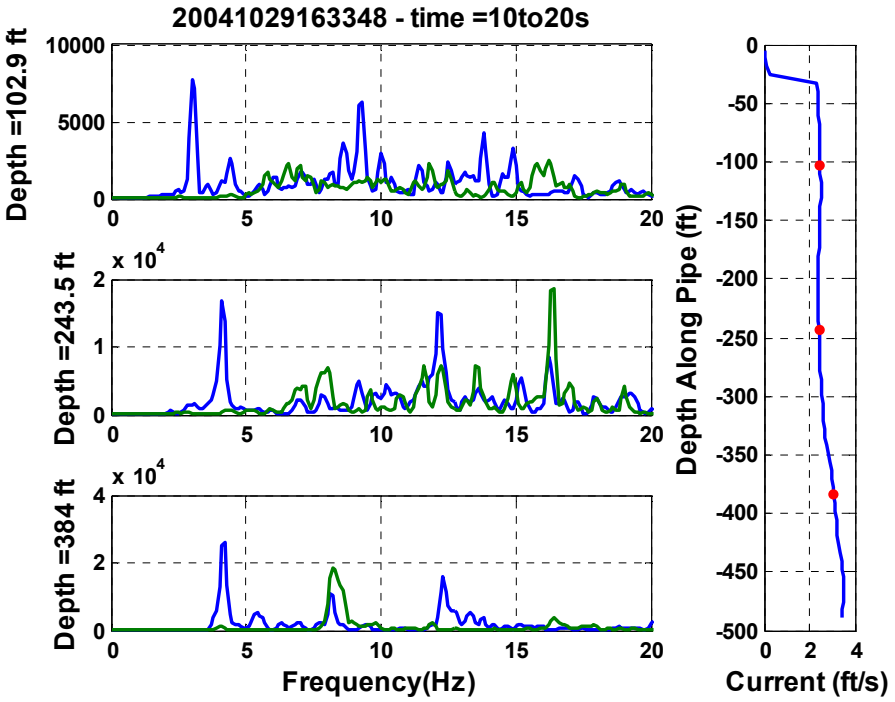

Figure 43 - Cross-flow (blue) and in-line (green) PSDs from a Gulf Stream bare test at depths of 102.9, 243.5, and 384 ft over the course of approximately 100 seconds. On the right hand side, the current profile is shown, corrected for incidence angle and showing the location of the three PSDs.

By dividing the time into sections as done before, the in-line and cross-flow become more evident. Figure 43 shows a ten-second segment of time. The spectra at depths of 384 ft and 243.5 ft. show clear cross-flow and in-line vibration. The spectrum at 243.5 ft is about two-thirds the amplitude of the spectrum at 384 ft. The spectrum at 102.9 ft shows a very different dominant VIV frequency, which correlates to the current at that depth. Both the dominant and the three-time harmonics can be seen in the 102.9 ft spectrum.

Figure 44 shows another segment of time from the case with two power-in regions. While the lower power-in region has grown in energy, as seen in the lowest spectrum, the in-line and cross-flow vibrations are separate. The upper power-in region has less energy. The signal-to-noise ratio is significantly lower and the in-line and cross-flow vibrations are difficult to discern from the noise.

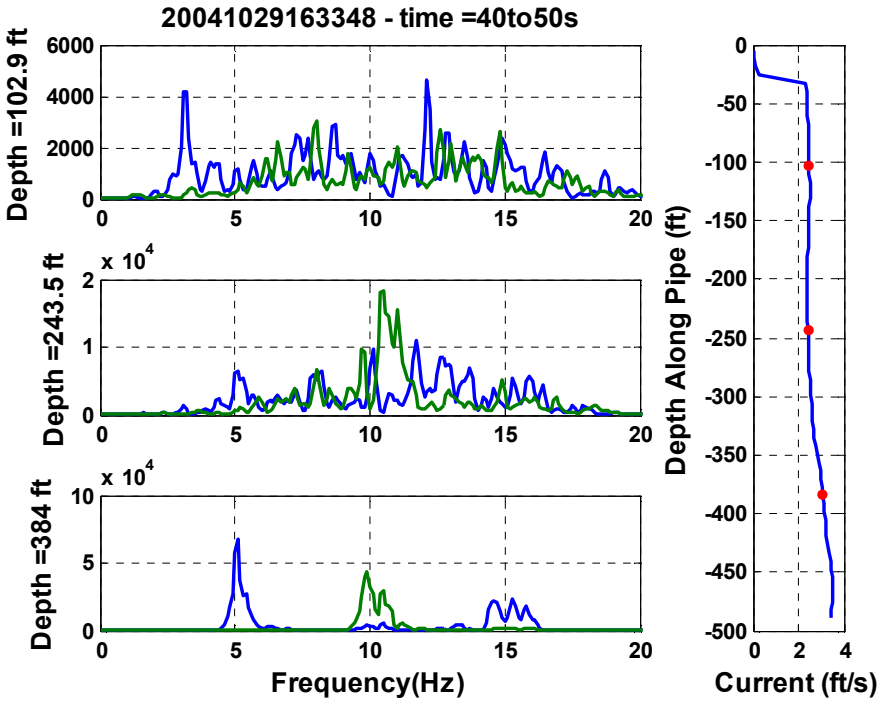

Figure 44 - Cross-flow (blue) and in-line (green) PSDs from a Gulf Stream bare test at depths of 102.9, 243.5, and 384 ft over the course of approximately 100 seconds. On the right hand side, the current profile is shown, corrected for incidence angle and showing the location of the three PSDs.

Conclusion and Recommendations

In the power-in region, the in-line and cross flow vibrations are separable. Outside the power-in region, if locally generated waves become larger than the traveling waves from the power-in region, then the in-line and cross-flow directions are no longer discernable.

Additionally, as the signal-to-noise ratio becomes close to one, the cross-flow and in-line directions are not separable.

Tests, like the Lake Seneca experiment with uni-directional and uniform flow, show a good baseline similar to laboratory tests. The Gulf Stream experiments show the other extreme with multi-directional flow and cases where locally generated waves prevent the coherent formation of in-line and cross-flow vibrations.

A future test of interest would be a uni-directional shear flow. The Gulf Stream tests supplied sheared, multi-directional flow which clearly showed the presence of multi-frequency components and smaller power-in regions. The addition of other frequencies and hydrodynamic noise prevent clear cross-flow and in-line components from being discernable over the length of the pipe.

Additionally, knowing the direction of the sensors in the sheared multi-directional flow would determine whether the cross-flow component is in a single plane or changes with the direction of the current. Also, this would help determine whether the in-line flow is orthogonal to the cross-flow direction.

The uni-directional, uniform flows at Lake Seneca did not allow for other frequencies to be introduced that degrade the signal, and therefore, the same in-line and cross-flow components are seen all along the pipe. Therefore, a uni-directional shear test would define the behavior between these two extremes.

Chapter 8: Parameters Used in the Prediction of VIV at High-Mode Number

Introduction

Many dimensionless parameters are used in the prediction of VIV, such as the Strouhal number, the Reynolds number, and the reduced-velocity bandwidth. The Gulf Stream and Lake Seneca tests give an opportunity to look into two different parameters that help in the prediction of VIV. These parameters are only useful in risers that are at high-mode numbers and do not respond with a standing-wave behavior.

The first parameter is a power-in factor which can be used to help predict the power-in region on long risers. The second parameter is a time-sharing parameter which indicates whether single-frequency response is likely or time-sharing of frequencies is likely.

The Power-In Factor

One of the problems with predicting VIV is finding the power-in region. Knowing only the current profile, a power-in factor, α, can be calculated for each point on the riser. The point with the largest power-in factor is the most probable power-in region. The power-in factor is the product of the cubed ratio of the local current velocity to the maximum current velocity and the ratio of the length of the power-in region available to the length of the pipe.

The region which dominates the VIV shedding response occurs at the location where the maximum power is available which is dependant on the current speed and the length of the power-in region. In [Vandiver 2002], Vandiver gave a modal explanation for the significance of the current cubed as the controlling parameter. Current ratio cubed is combined here with a length ratio to define the power-factor:

$$\alpha = \left(\frac{U_c}{U_{\max}} \right)^3 \left(\frac{L_{in}}{L} \right) \tag{8.1}$$

Other factors can influence the determination of the power-in region. If the gradient of the current direction is greater than 0.5 degrees/ft, (for the Gulf Stream and Lake Seneca pipes), then alpha is zero. Additionally, if the incidence angle between the flow and the pipe is less than 45º, then alpha is zero. Lastly at the bottom of the pipe for

the Gulf Stream tests, no power-in region was found in the bottom 75 ft. This may be caused by reflections interfering with the formation of a correlated vortex wake or other end effects. Therefore for the Gulf Stream tests, alpha for the bottom 75 ft was set to zero. This effect should be further investigated.

After calculating the power-in factor for each point, and taking in to account the other factors mentioned above, the location of the largest power-in factor is used to predict the center of the power-in region. Therefore the power-in factor is:

$$\alpha = \left(\frac{U_c}{U_{\max}}\right)^3 \left(\frac{L_{in}}{L}\right) f(\theta) g(\phi) h(z) \qquad (8.2)$$

where f(θ) is a factor that is 0 or 1 depending on the inclination angle at that point; g(Φ) is a factor that is 0 or 1 depending on the local current direction gradient; h(z) is a factor that is 0 or 1 depending on the proximity to the boundary.

Figure 45 and Figure 46 show examples from the Gulf Stream test. For each figure, (a) is the RMS strain for each quadrant shown; (b) is a plot of the normal incidence current; (c) is the power-in factor, α including the effects of the current gradient, the incidence angle, and the boundary effects; and (d) is the length of the power-in region assuming that the location is the center of the power-in region. A reduced-velocity bandwidth of 0.4 is used to determine the length of the region about the center point.

In Figure 45, the area over which the power-in factor is highest coincides with the region of highest RMS strain. The ends of the pipe can be seen to have little power-in available because the length of the power-in region is limited by the inclination at the top and unexplained boundary effects at the bottom.

Similarly in Figure 46, the high incidence angle of the pipe at the top and a high directional current limit the available power-in region. The power-in region found by the power-in factor corresponds to the region of highest RMS strain.

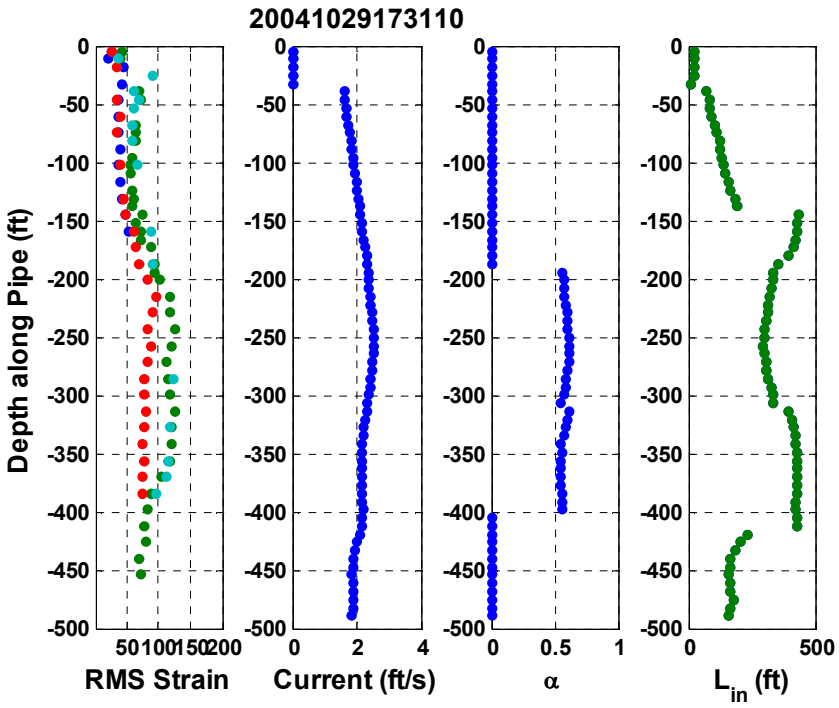

Figure 45 – (a) RMS Strain in each of the four quadrants; (b) The normal incidence current profile (ft/) (c) The Power-in Factor, α, (d) The Length of the power-in region assuming that each point is at the center velocity of the power-in region for test case 20041029173110

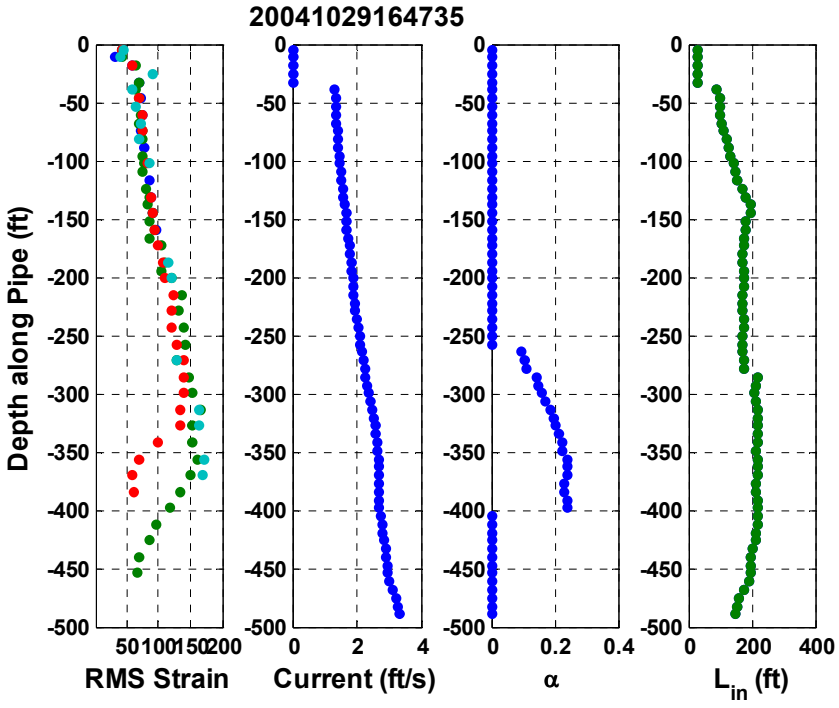

Figure 46 - (a) RMS strain in each of the four quadrants; (b) The normal incidence current profile (ft/) (c) The power-in factor, α, (d) The length of the power-in region assuming that each point is at the center velocity of the power-in region for test case 20041029164735

Time-Sharing

Since the natural frequency of a tensioned beam is:

$$f_{n,tension\_beam} = \sqrt{f_{n,string}^2 + f_{n,beam}^2} = \sqrt{\left(\frac{n}{2L}\sqrt{\frac{T}{m}}\right)^2 + \left(\frac{n^2\pi}{2L^2}\sqrt{\frac{EI}{m}}\right)^2} \tag{8.3}$$

solving for the mode number leads to a quadratic equation, (8.4).

$$n^4\frac{\pi^2 EI}{L^2} + n^2 T - 4f_n^2 L^2 m = 0 \tag{8.4}$$

Thus solving for the mode number and taking the positive real root, n is:

$$n = L\left(\frac{\left(T^2 + 16f_n^2 m\pi^2 EI\right)^{1/2} - T}{2\pi^2 EI}\right)^{1/2} \tag{8.5}$$

By using equation (8.5) and setting the tension equal to zero, the mode number for a given frequency of vibration for the beam only can be found:

$$n_{beam}^2 = \frac{2f_n}{\pi}\sqrt{\frac{mL^4}{EI}} \tag{8.6}$$

Similarly, using equations (8.4) and setting EI equal to zero, the mode number for the tension dominated case is:

$$n_{string} = 2f_n L\sqrt{\frac{m}{T}} \tag{8.7}$$

Vandiver [1993] defined the parameters Ns as the number of modes possible. From equation (8.5), N_s is:

$$\begin{aligned} N_{s,in} = n_{in,\max} - n_{in,\min} = & L\left(\frac{\left(T^2 + 16f_{in,\max}^2 m\pi^2 EI\right)^{1/2} - T}{2\pi^2 EI}\right)^{1/2} \\ & - L\left(\frac{\left(T^2 + 16f_{in,\min}^2 m\pi^2 EI\right)^{1/2} - T}{2\pi^2 EI}\right)^{1/2} \end{aligned} \tag{8.8}$$

The natural frequency can be expressed in terms of the current:

$$f_n = \frac{St * U}{D} \tag{8.9}$$

Using Equation (8.9) in Equation (8.8), and using the maximum and minimum velocities for the power-in region will result in the number of modes possible in the power-in region, $N_{s,in}$.

$$N_{s,in} = n_{in,\max} - n_{in,\min} = L\left(\frac{\left(T^2 + 16\left(\frac{StU_{in,\max}}{D}\right)^2 m\pi^2 EI\right)^{1/2} - T}{2\pi^2 EI}\right)^{1/2} - L\left(\frac{\left(T^2 + 16\left(\frac{StU_{in,\min}}{D}\right)^2 m\pi^2 EI\right)^{1/2} - T}{2\pi^2 EI}\right)^{1/2} \quad (8.10)$$

Results

A large-scale model test of a tensioned steel riser was conducted at Hangøytangen, Norway in 1997. The riser had a length of 90 m and a diameter of 0.03 m. The current profiles were linear shears, with the maximum velocity at the top and zero velocity at the bottom. The maximum velocity was varied from 0.16 to 1.96 m/s.

In Figure 47, the power-in factor is plotted against the number of participating modes. When plotted this way, the data shows an indication as to when single-frequency behavior is likely to occur and when time sharing is likely to occur.

The power-in factor takes into consideration the magnitude of the current speed, and therefore the mode number of operation, as well as the length of the power-in region, can affect how many modes are excited. These two factors can largely influence on whether or not time-sharing will occur. Thus the power-in factor is an indication of whether or not time sharing will occur.

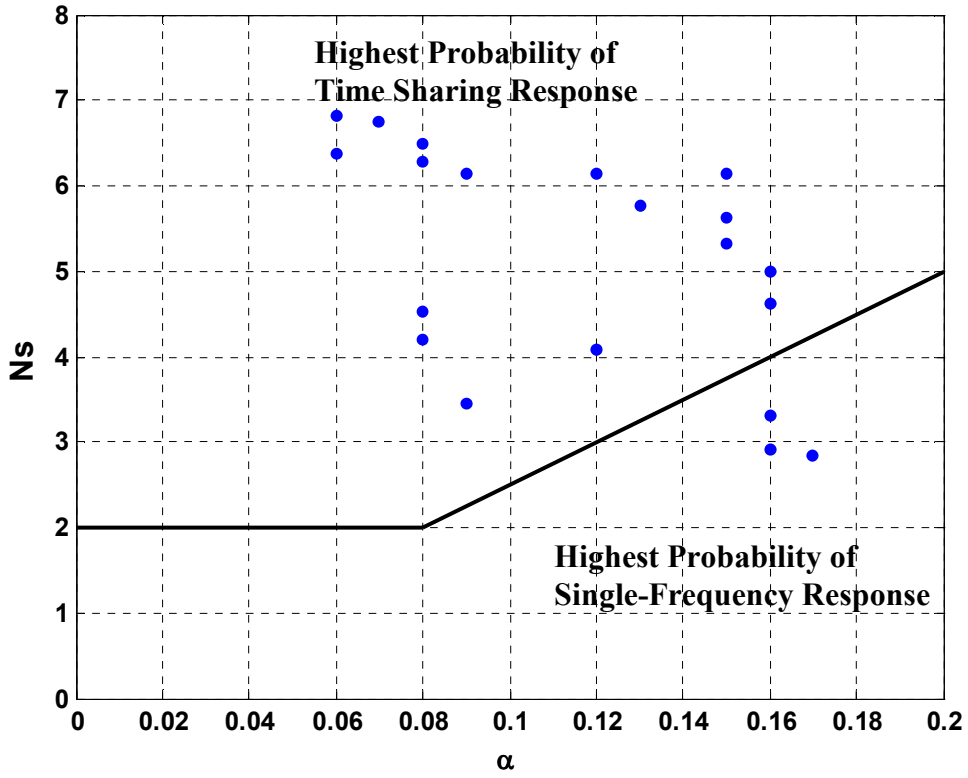

Figure 47 - The results from the Hangøytangen tests showing when single-mode response is probable and when time sharing is likely to happen.

Vandiver, Allen and Li [1996] found a similar distribution of single-mode and multi-mode behavior, except they saw a single-frequency response at high shear. Only one example from the Hangøytangen test exhibited a similar response, at the most highly sheared case.

On closer inspection of the highest shear case, using a waterfall plot, the frequency did shift. The shift is with in a tighter range of frequencies. When looking at the waterfall plot in Figure 48, one peak from 4-6 seconds is twice as large as any of the other peaks. In general the magnitude of the peaks was significantly higher than at lower frequencies, up to 30 times the magnitude.

The multiple peaks at the lower frequencies were distinct and could be seen. Because of the magnitude of the spectral peaks at higher shear and the reduced change in frequency range, the multiple peaks appeared to be a single peak, and were not distinguishable until a waterfall plot was done.

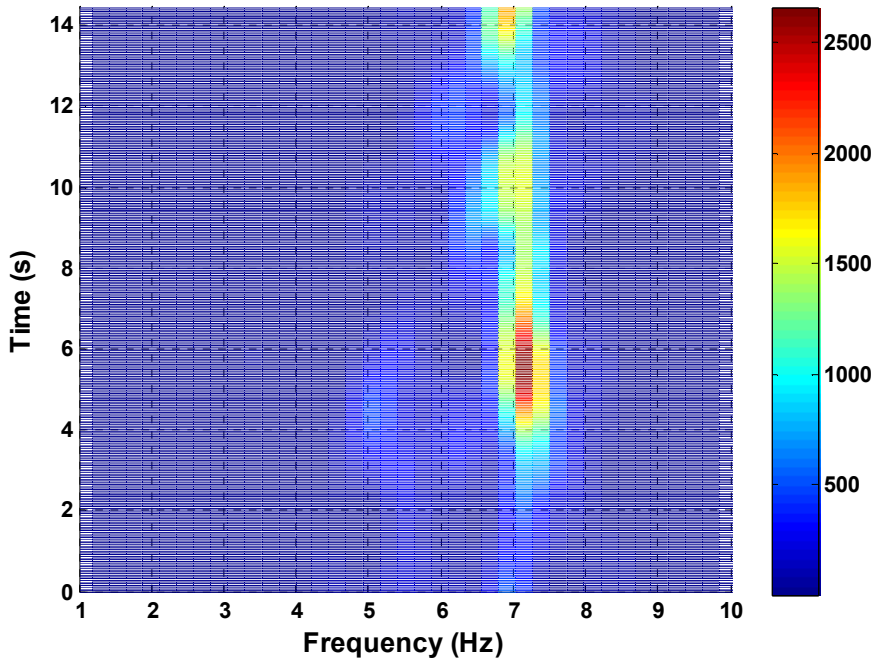

Figure 48 – Waterfall spectra from Hangoytangon, showing the time sharing and shifting frequencies.

Chapter 9: Conclusions

The Lake Seneca and Gulf Stream experiments were designed to test pipes at high-mode numbers, specifically looking at in-line and cross-flow vibrations, single-frequency and multi-frequency vibrations, drag coefficients, strake performance and damping factors. The tests yielded many interesting insights into the behavior of pipes at high-mode numbers.

The concept of frequencies sharing in time rather than in space, as many prediction programs use, is presented. This concept of single frequencies sharing in time can be used for large amplitude vibrations that cause contribute largely to the fatigue of a pipe. Small-amplitude, non-resonance local vibrations can co-exist. The major impact of time-sharing frequencies is the impact to the damage rate and fatigue.

The density of the sensors on the pipe allowed for analysis that has not been done previously. Both the reduced velocity and the coherence mesh presented use the high density of instruments to locate the area of the power-in region. Though the exact location of the power-in region is not known, the area in which the waves are created can be found. The power-in region may shift as the frequency shifts with time sharing, and therefore the exact power-in region is difficult to find unless the case is single-frequency and stable for a period of greater than about 10 averages of the coherence calculation. This length will vary depending on the number of points in the coherence calculation.

Once the region where the vibration originated has been found, the different phenomena that effect the location of the power-in region were discovered. Four different factors are presented that effect the locations of the power-in region, the incidence angle of the current, the gradient of the current direction, the current profile, and the end effects at high mode number.

In the power-in region, the in-line and cross flow vibrations indications appear to be separable. Outside the power-in region, if locally generated waves become larger than the traveling waves from the power-in region, then the in-line and cross-flow directions are no longer discernable. Additionally, as the signal-to-noise ratio becomes close to one, the cross-flow and in-line directions are not separable.

A dimensionless parameter has been presented which helps in the prediction of VIV given a current profile. The first is the power-in determination factors which will

determine the most probable power-in region using a combination of the current velocity and the power-in length available at each point. This same parameter can be used to help determine whether the riser will respond with a single frequency, or switch between frequencies in time.

There are two major issues with using the data from Lake Seneca and the Gulf Stream to predict full scale riser behavior. The first is that the tests do not have prototypical Reynolds numbers. These tests were done at sub-critical Reynolds numbers, where as risers typically are at critical Reynolds numbers. The wake structure at critical Reynolds numbers is different than at sub-critical which could effect the forcing function and the resulting vibration.

The second is that the Lake Seneca and Gulf Stream tests are purely in the tension dominated regime of the natural frequency. Some investigation by Baarhom et al [2006], showed that the fatigue damage in the regime controlled by tension is different than the regime controlled by the bending stiffness. Baarholm et al. found that:

$$D = \begin{cases} \beta_1 U^7 & U<U_{transition} \\ \beta_2 U^4 & U \geq U_{transition} \end{cases} \qquad (9.1)$$

Therefore, these results are valid and can be used for tension dominated tensioned beams. The pipes tested at Lake Seneca and the Gulf Stream were tension dominated, and therefore the natural frequencies are evenly spaced. Further investigation should be conducted to determine whether these prediction methods and dimensionless parameters hold true when the pipe is bending stiffness dominated, which implies that the natural frequencies are not even spaced.

Recommendations

All of these conclusions are based on the data from the Gulf Stream and Lake Seneca tests. Various sets of tests could be conducted to help reduce the error from these tests and more fully understand the different factors that affect the location and length of the power-in region.

Further testing should be done to see that the results are consistent at both critical Reynolds numbers and when the natural frequency is controlled by the bending stiffness for the reasons listed above.

A set of tests in which the gradient of the current direction can be controlled and varied would help to determine the exact gradient of the current direction which can sustain a power-in region. Additionally, the length, over which that gradient needs to be sustained to prevent a power-in region, could be determined. Being able to vary the diameter of the pipe and the natural frequency of the pipe for these tests would be useful. The current directional gradient of 0.5 degrees/ft is only useful for the Gulf Steam pipe. Because the gradient of the current direction with respect to the pipe can interfere with the vortex wake formation, this is most likely a hydrodynamic phenomenon. Therefore, the change in the gradient of current may not be a steady number such as 0.5 degrees/ft, but instead may be dependant on the diameter of the pipe. Additionally, by being able to vary the natural frequency of the pipe, the wavelength of the vibrations could be seen to be a factor or not.

Additionally, knowing the direction of the sensors in the sheared multi-directional flow would determine whether the cross-flow component is in a single plane or changes with the direction of the current. Also, this would help determine whether the in-line flow is orthogonal to the cross-flow direction.

Nomenclature

a(t) – Acceleration
c – Speed of Propagation
C_a – Added Mass Coefficient
C_D – Drag Coefficient
Csw – Still Water Damping Coefficient
D – Diameter
dV_r – Reduced Velocity Bandwidth
dU/dx = Gradient of the Current
E – Young's Modulus
E_n – Energy at location n
f – Frequency
F_s – Sample Rate
f_n – Natural Frequency
$f_{s,max}$ – Maximum Shedding Frequency
f_v – Frequency of Vibration
I – Moment of Inertia
i – Square Root of -1
k – Wave Number
k_r – Complex Wave Number
j – Square Root of -1
L – Length of the Pipe
L_{in} – Length of the Power-In Region
m – Mass per Unit Length
m* – Mass Ratio
m_a – Added Mass
n – Mode Number
n_{beam} – Mode number of a beam
n_{string} – Mode number of a tensioned string
N_s – Possible number of modes participating
r – Structural Damping
r_{sw} – Still Water Damping
Re – Reynolds Number
s – Distance from End of the Pipe to Source
St – Strouhal Number
T – Tension
u(t) – Step Function
U – Current Speed
U_{max} – Maximum Current Speed
U_{mean} – Average Current Speed
U_{min} – Minimum Current Speed
U_n – Current Speed Normal to the Pipe
U_t – Current Speed Tangent to the Pipe
v(t) – Velocity
v(0) – Initial Velocity
V_r – Reduced Velocity
w – Movement of the Pipe
x – Location on the Pipe
Y_{RMS} – Transverse RMS Displacement
α – Current Weight Factor
β – Shear Parameter
δ(t) – Delta Function
ΔU- Change in Current
Φ – Incident Angle of the Pipe with the Vertical
θ – Angle of Rotation in the Horizontal Plane
λ - Wavelength
υ – Kinematic Viscosity
ρ – Density of Structure
ρ_f – Fluid Density
ξ – Damping
ξ_n – Modal Damping
ξ_h – Hydrodynamic Damping
σ_g – Specific gravity
ω – Natural Frequency
ω_r – Input Frequency

Reference

Achenbach, E. and Heinecke, E., "On vortex shedding from smooth and rough cylinders in the range of Reynolds number $6x10^3$ $5x10^6$", *Journal of Fluid Mechanics* 109, 239-252

Baarholm, G.S., Larsen, C.M., Lie, H., "On fatigue damage accumulation from in-line and cross-flow vortex-induced vibrations on risers", *Journal of Fluid and Structures* 22, 2006, pp 109-207

Blevins, R.D., *Flow-Induced Vibrations*, 2nd ed., Krieger Publishing Co. 2001, pp45-48

Burg, J.P., "Maximum entropy spectral analysis", *Modern Spectrum Analysis,* 34-48. IEEE Press, 1968

Crandall S.H., Mark W.D., *Random Vibration in Mechanical Systems*, Academic Press, New York, 1973, pgs. 44, 117

Dirlick, T, PhD Thesis, "Applications of Computers to Fatigue Analysis", Warwick University 1985

Griffen, O.M., Ramberg, S.E., "The Vortex Street Wakes of Cylinders", J. Fluid Mech., 1974, vol. 66, pp 553-576

Jauvtis, N and Williamson, C.H.K., "The effects of two degrees of freedom on vortex-induced vibrations at low mass and damping*" Journal of Fluid Mechanics* 509, pp 23-62, 2004

Jong, J-Y, Vandiver J. K., "Response Analysis of the Flow-Induced Vibration of Flexible Cylinders Tested at Castine Maine in July and August 1981", Internal MIT report, 1981

Kaasen, K, Lie, H, Solaas, F. and Vandiver J.K, "Norwegian Deepwater Project: Analysis of Vortex-Induced Vibrations of Marine Rised Based on Full-Scale Measurements" *Offshore Technology Conference*, OTC 11997, Houston, May 2000

Li, Li, "A Comparison Study of the CGreen's Function and Mode Superposition Techniques and Their Application to the Lock-in Response Prediction of Cylinders in Currents", Internal MIT paper, 1993

Misiti, Oppenheim, Poggi, *Wavelet Toolbox: For Use with MATLAB*, The MathWorks Inc.1996

Oppenheim, Schafer, and Buck, *Discrete-Time Signal Processing 2nd Edition*, Prentice Hall, 1999

Sherratt, F, Bishop, N.W.M., and Dirlick, T, "Predicting fatigue life from frequency-domain data: current methods", Engineering Integrity Society

Stein, Jonathan, *Digital Signal Processing: A Computer Science Perspective*, John Wiley & Sons, 2000, pp. 285-287

Strang, G. and Nguyen, T., *Wavelets and Filter Banks*, Wellesley-Cambridge Press, 1997

Vandiver, J. K., "Drag Coefficients of Long Flexible Cylinders", *Proc. 1983 Offshore Technology Conference,* Paper No. 4490, Houston, May 1983.

Vandiver, J.K., "Dimensionless parameters important to the prediction of vortex-induced vibration of long-flexible cylinders in ocean currents", *Journal of Fluids and Structures*, 1993, pp 423-455

Vandiver, J.K., "A Universal Reduced-Damping Parameter for Prediction of Vortex-Induced Vibrations", *Proc. of Offshore and Artic Engineering Conference*, Oslo 2002

Vandiver, J.K, Allen, D, and Li, L., "The Occurrence of Lock-In Under Highly Sheared Conditions", *Journal of Fluids and Structures* 10, 1996, pp 555-561.

Vandiver, J.K., and Chung, T-Y., "Predicted and Measured Response of Flexible Cylinders in Sheared Flow" *Proc., ASME Winter Annual Meeting Symposium on Flow-Induced Vibration*, Chicago, December 1988.

Vandiver, J.K. and Jong, J. Y., "The Relationship Between In-line and Cross-flow Vortex-induced Vibration of Cylinders", *Journal of Fluids and Structures*, pp. 381-399, 1987.

Vandiver, J. K., Lee, L., "SHEAR7 Version 4.3 Theory Manual", MIT, September 2003.

Vandiver, J. Kim and Marcollo, Hayden, "High Mode Number VIV Experiments" IUTAM Symposium on Integrated Modeling of Fully Coupled Fluid Structure Using Analysis, Computations, and Experiments, June 2003

Vandiver, Marcolo, Fantone, Jaiswel, Jhingran, Peoples, Swithenbank, "DeepStar 6402 – Lake Senesca Testing Final Report" MIT Report to DeepStar, 2005

Vandiver, Marcolo, Fantone, Jaiswel, Jhingran, Swithenbank, "DeepStar 7402 – Miami2004 Riser Report" MIT Report to DeepStar, 2005

Venugopal, M, "Damping Response of a Flexible Cylinder in a Current", PhD Thesis, Dept. of Ocean Engineering, MIT 1996

Vikestad, K., Larson, C.M., and Vandiver J.K, "Damping of Vortex-Induced Vibrations", *Proc. Of Offshore Technology Conference* Houston TX May 1-4 2000, OTC 11998

Acknowledgements

I would like to thank my advisor Prof J. Kim Vandiver, and my committee, Prof. Michael Triantafyllou, Prof. Eduardo Kausel, and Dr. Hayden Marcollo for their advise, support, and expertise.

I would also like to thank the Professors and Researchers at NTNU and Marintek in Trondheim Norway for their time and support of my data analysis, specifically Dr. Elizabeth Passano, Dr. Halvor Lie, Dr. Karl Erik Kaasen, and Prof Carl Martin Larsen. I would also like to thank Sheila McNary for support above and beyond anything I could have asked for.

This research was funded but the Office of Naval Research and the SHEAR7 JIP. The support of the experiments was funded by DeepStar, a joint-industry project.. Special thanks to Dr. Owen Oakley at DeepStar for his continued support. I thank Nork Hydro for supplying the Hangøytongen.

To my parents, a large thank you goes, for feeding me, housing me, grammer checking every sentence I wrote, and fluffing me up when needed. Thank you to Dr. Ben Henty without your support, guidance, and MATLAB abilities this thesis would not be half what it is. Lastly, thank you to all of my friends and family for putting up with me over the last 5 years; you have done everything from reading my entrance essay to keeping me mostly sane through this process.

Appendix A: Analysis of Sampling Rate Issues

Introduction

Halvor Lie of Marintek was analyzing the data from the first Gulf Stream experiment and discovered when looking at the coherence between two consecutive strain gauges located on the same fiber (i.e. 14 ft apart), the coherence was on average greater than 0.5. He also noticed that the coherence between two consecutive strain gauges in the same quadrant (i.e. 7 ft apart), was on average less than 0.3.

Figure 49 and Figure 50 show the layout of the pipe. Figure 49 is the side view of the pipe, which shows the multiple fibers in each quadrant as well as the staggering of the fibers. Figure 50 is the cross-section of the pipe. This shows the different locations of the fiber in the pipe.

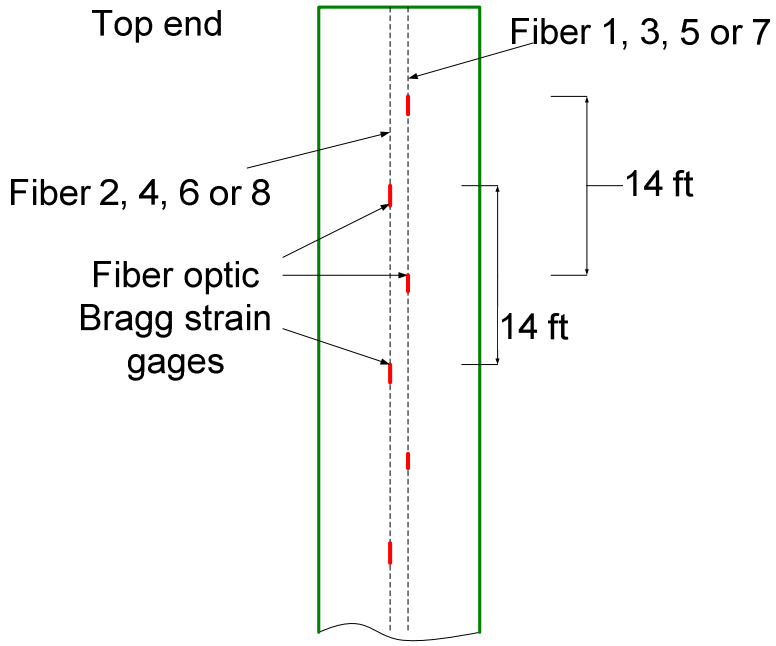

Figure 49 - Side View of the Pipe Showing the Staggered Strain Gauge Locations on the Different Fibers

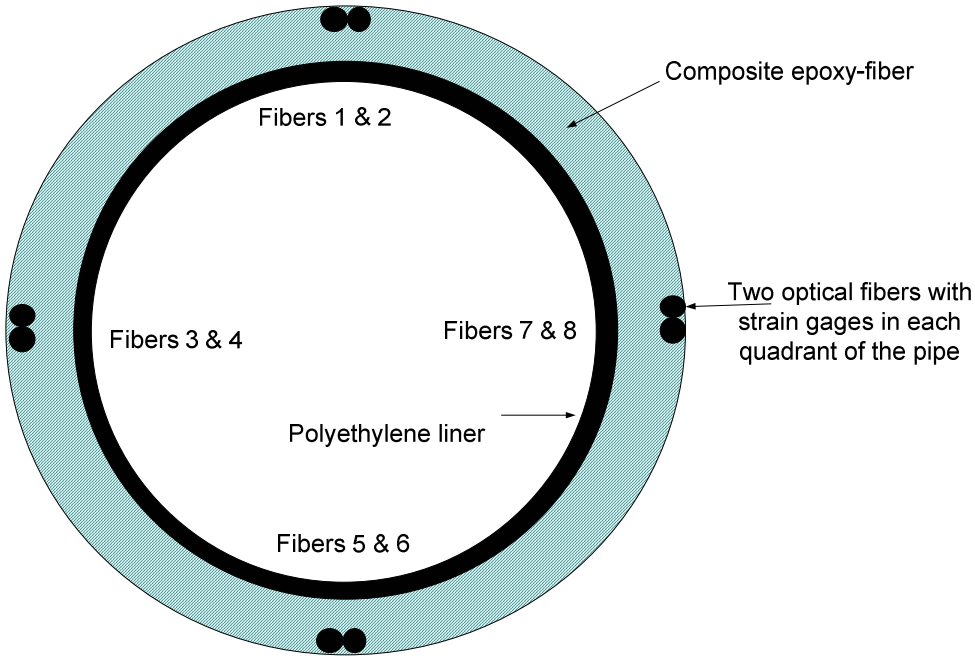

Figure 50 - Cross-Section of the Pipe Showing the Locations of the Fibers.

In Figure 51, the blue line shows the coherence for the second and fourth strain gauges from the top, which are on the same fiber. The coherence is lower at some frequencies because there is no excitation at these frequencies. The green line shows the coherence between the first and the second strain gauges, which are not on the same fiber. The green line shows that there is no coherence at any frequency.

The problem with low coherence between sensors on different fibers was tracked to a difference in sampling rates on the different fiber optic strain gauges. Each of the eight fiber optic lines was recorded by a different FSI unit. Due to a firmware problem with the FSI units, each fiber was recorded with a different sampling rate.

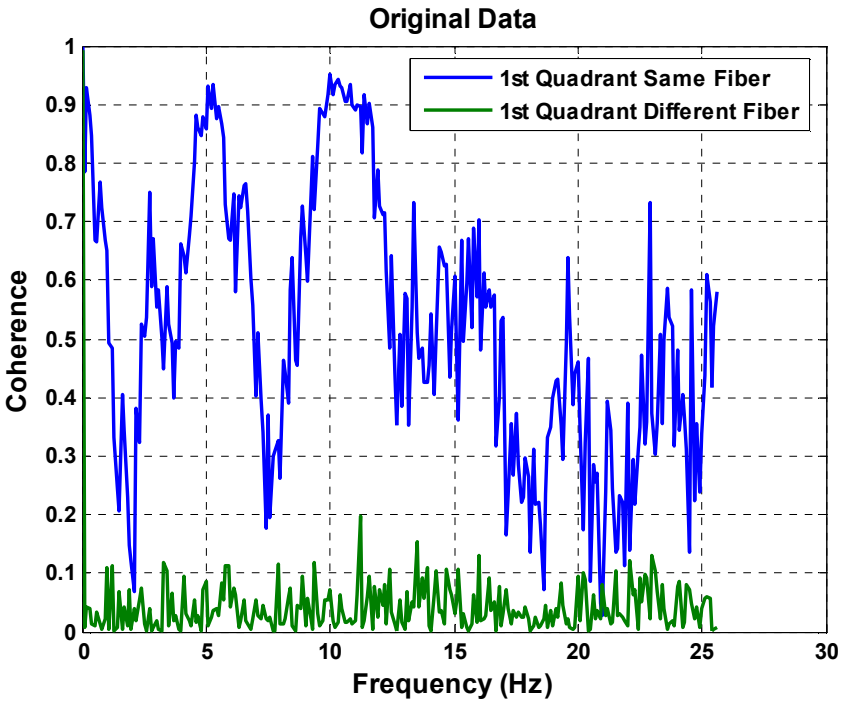

Figure 51 - Coherence on Quadrant 1 between Two Gauges on the Same Fiber (blue) and Two Gauges on Different Fibers (green)

Methodology

The data had a common low-frequency signal caused by tension fluctuations from the vessel motion. The tension signal and the strain signals were low-pass filtered at 0.5 Hz, so that only the vessel motion remained. The filter used was a fifth-order elliptical filter with a pass band frequency of 0.5 Hz, a stop band frequency of 1 Hz and attenuation of 40 dB with 0.1 dB ripple in the transition. Additionally, the data was filtered such that there was no phase shift in the data caused by the filter. [Oppenheim et al. 1999]

The signals were all normalized such that the greatest magnitude was one. This allowed the different types of signals, tension, and strain to be compared.

The tension signal had a known sample rate as it was acquired with a different data acquisition system than the fiber-optic strain gauge data. The strain signal was resampled to a new sampling rate then cut to the same number of samples as the tension signal.

Since the data had been filtered to include only the vessel motion, the two signals should have been virtually identical. Therefore, the area under the curve of each signal should be the same. Thus, the absolute value of both samples was integrated; then the

error between these two areas was compared. The process was then repeated with a different sampling rate. The goal of this resampling was to minimize the error between the areas.

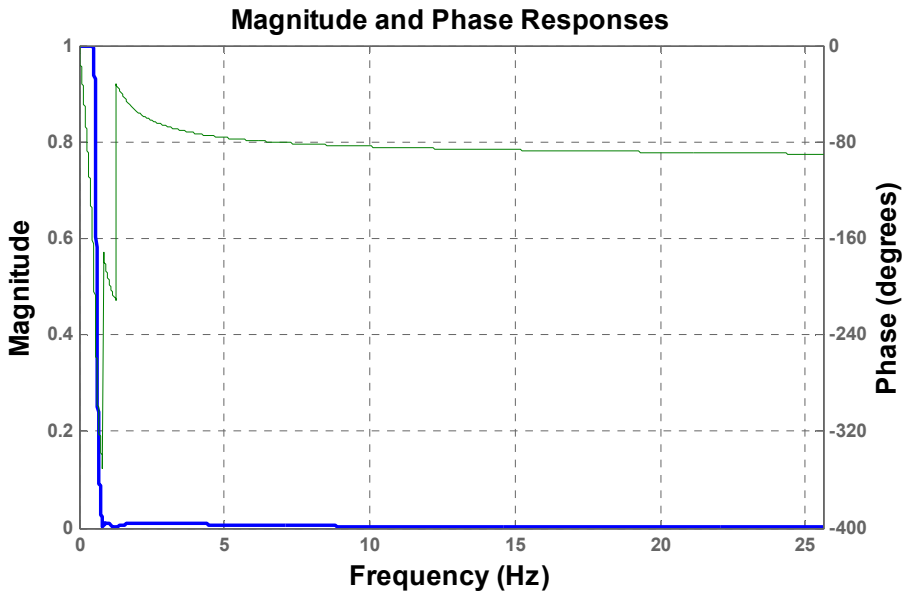

Figure 52 - Magnitude and Phase Plot for the Low-Pass Filter

The integration minimization was done for each fiber for each of seven cases. The minimization results for each case were slightly different, varying by up to 0.1 Hz. To refine the results, the data was then sampled at increments of 0.01 Hz over the entire span indicated by the minimization process. At each, step the coherence between the two signals was calculated. The increment with the maximum average coherence was considered the best sampling rate.

This analysis was done on the top two strain sensors because they were closest to the top and therefore were most affected by the tension fluctuations caused by the vessel motion. Therefore, these were the most highly correlated to the tension seen by the load cell.

Results

Using the methodology described above, each individual strain gauge was optimized and resampled. The results of October 29th bare case testing are shown in Table 6. The

results of the 40% straked case are shown in Table 7. The sample rates for the 70% staggered cases are in Table 8.

Table 6 - Sampling Rates for Bare Cases

Fiber	Sampling Rate (Hz)
1	57.33
2	61.36
3	51.36
4	54.49
5	55.71
7	54.99
8	54.61

Table 7 –Sampling Rates for the 40% Strakes

Fiber	Sampling Rate (Hz)
1	57.33
2	61.36
3	51.36
4	54.49
5	55.71
7	54.99
8	54.61

Table 8 – Sampling Rate for the 70% Staggered Strake

Fiber	Sampling Rate (Hz)
1	57.33
2	62.05
3	54.51
4	51.01
5	55.76
7	65.50
8	55.43

In the left side graph of Figure 53, the original vessel motion signals from Fibers 1, 3, 5, and 7 are plotted. On the right side of the figure, the signals after resampling are shown. These strain gauges were located 2.68 ft from the top end of the pipe. The tension fluctuations measured by these strain gauges were highly correlated with the tension fluctuations measured by the load cell.

Figure 54 shows the same graphs for Fibers 2, 4, 6, and 8. Fiber 6 was broken and no data was recorded. The data from Fibers 2, 4, and 8 also do not appear to line up.

Fibers 2, 4, and 8 were located 9.48 ft from the top end of the pipe. The magnitude of the strain caused by the tension variation was significantly smaller. By looking at the zero crossings and the general shape of the signals, the fibers have similar characteristics.

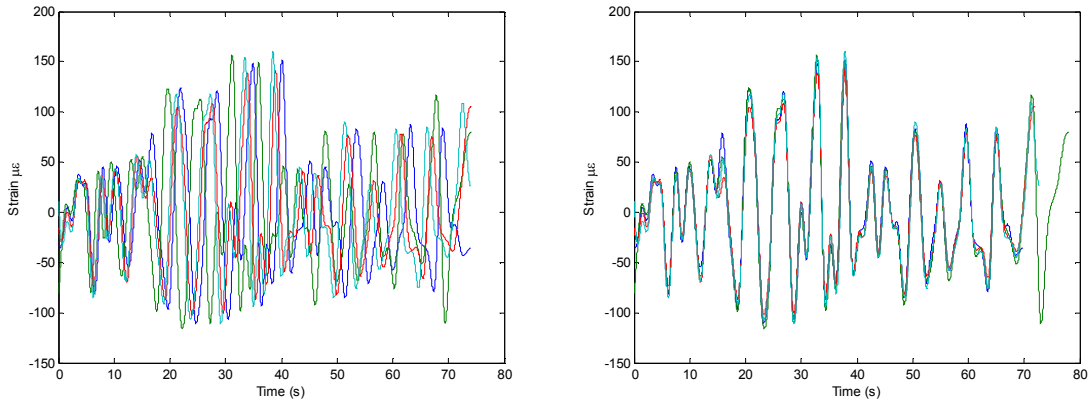

Figure 53 - Fibers 1, 3, 5, 7: Before resampling (left); After resampling (right): Case 20041029170336

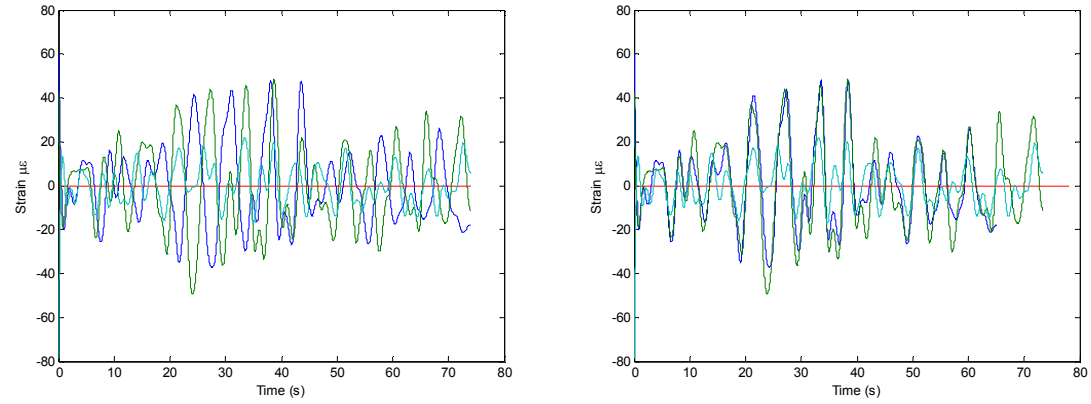

Figure 54 - Fibers 2, 4, 6, 8: Before resampling (left); After resampling (right): Case 20041029170336

Figure 55 shows the overlay of the normalized tension signal with the resampled data that has been filtered to only show the vessel motion. The two signals are hard to distinguish from one another.

Figure 56 shows the spectra from the first three strain gauges in quadrant 2 from the top. The response is fairly low, as this is the top end of the pipe.

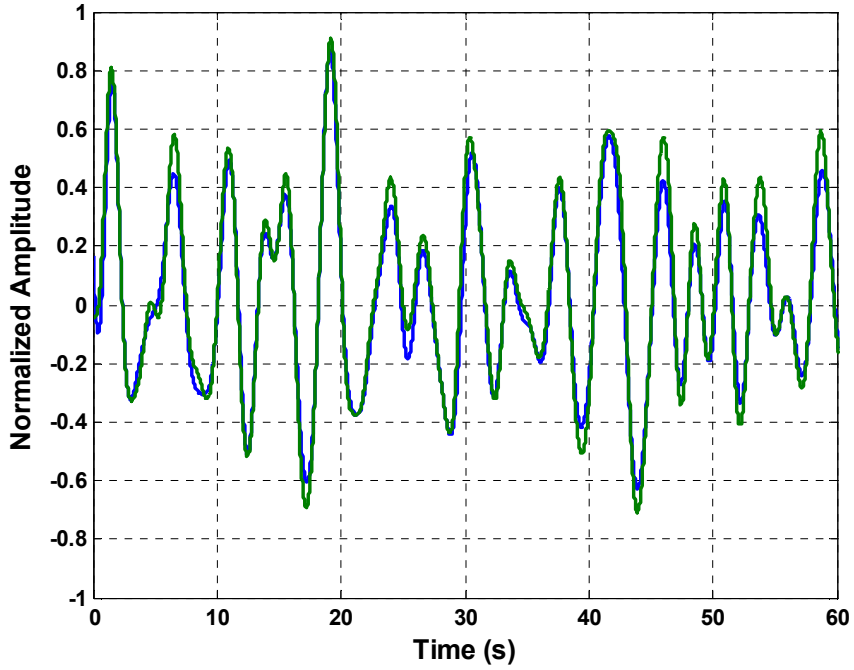

Figure 55 - Normalized Tension and Fiber 1 Overlaid After Correction

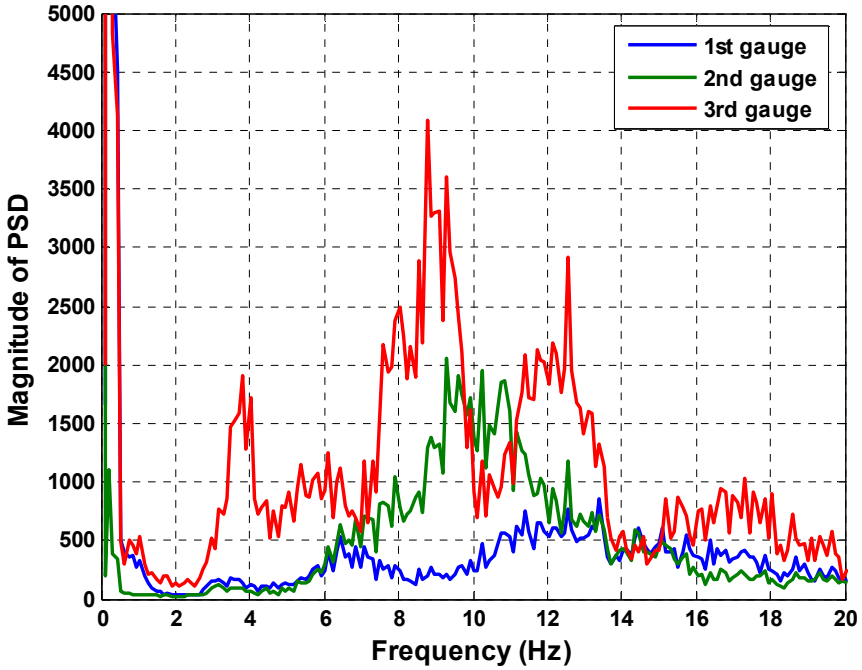

Figure 56 - Spectra of Quadrant 2, 1st, 2nd, and 3rd Gauges

In Figure 57 and Figure 58, the left side graph shows the coherence on the same fiber in blue and on different fibers in the same quadrant in green for the original data for

quadrants 1 and 2 respectively. In the right side graph, the same coherence calculations are shown but for the resampled data.

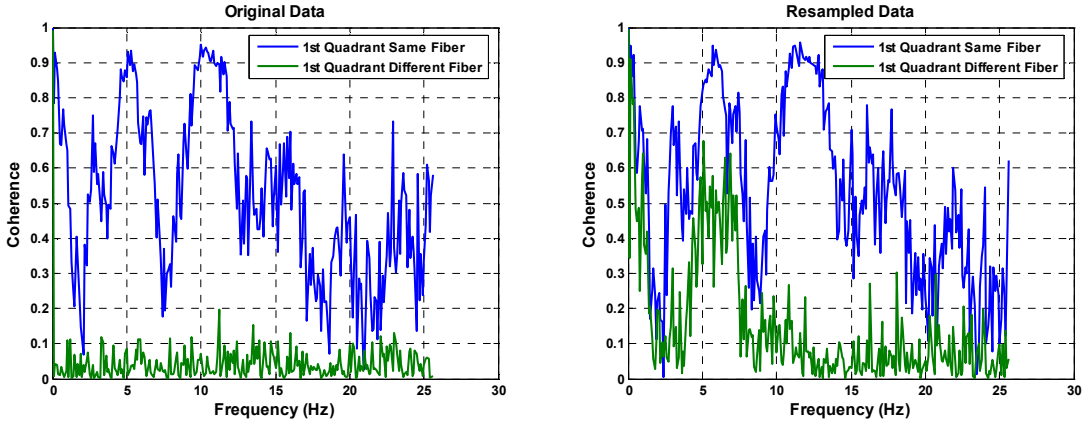

Figure 57 - Coherence Before and After Resampling For Quadrant 1 (Sensors 1, 2, 3)

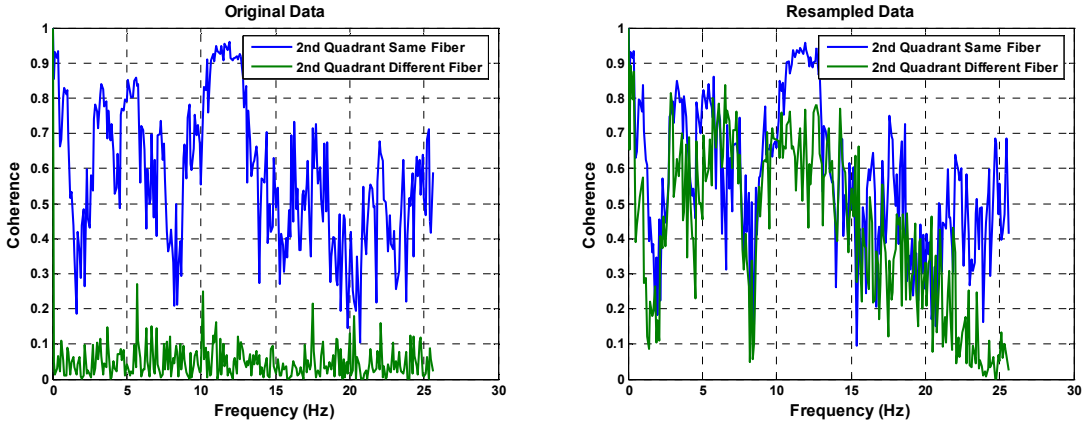

Figure 58 - Coherence Before and After Resampling For Quadrant 2 (Sensors 1, 2 ,3)

Figure 59 shows the same analysis as Figure 57 and Figure 58 but for a set of sensors located about 140 ft. from the top end.

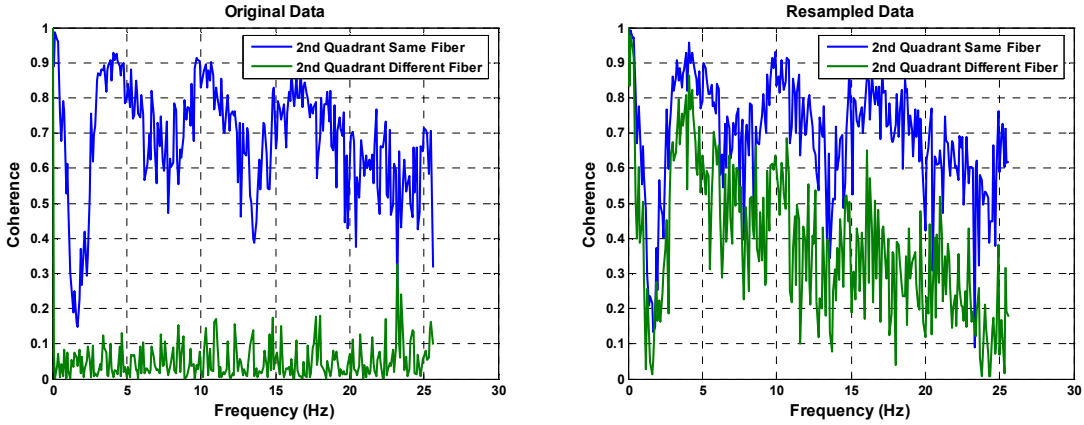

Figure 59 – Coherence Before and After Resampling For Quadrant 2 (Sensors 20, 21, 22)

Conclusions

The sampling rates reported in this report can be used for most analysis. The analysis has increased the coherence of the data. Some fibers had a greater increase in coherence than other fibers. Attempts to refine the sample rates further were not fruitful because the noise in the data created too much error and there was not good agreement at a finer increment between different test runs.

Appendix B: SHEAR7 Input File

```
SHEAR7 data file for coil tubing (English units)
File Name: 1.38" OD, 400 ft long, 1500 lb tension
*** BLOCK 1. unit system ***
      1              flag for units  0-SI  1=english
*** BLOCK 2. structural and hydrodynamic data ***
      1              flag for structural model (nmodel)
    400.000          total length of the structure (ft)
    400              number of spatial segments
    1777.00          modulus of elasticity (ksi)
    64.000           volume weight of the fluid (lbf/ft**3)
    0.0000145000     kinematic viscosity of the fluid (ft**2/s)
   0.00300           structural damping coefficient:
    1500.0           effective tension at origin (lbf)
      1              no. of zones to define sectional property
    0.0000   1.0000                zone start and end point in x/L
    1.38   1.380   1.234    hydro, strength, inside strength diameter(in)
   3.096E-06  0.843 .178  inertia(ft^4)mass(lb/ft) sbmg wt(lb/ft)
   1.000   .18000  1.0    Ca, St code, Cl reduction factor
*** BLOCK 3. current data ***
     2  0.100E+01   100   no. of profile data pts probability profile ID
   0.000   1.0          location (x/L) and velocity (ft/s)
   1.0     2.675        location (x/L) and velocity (ft/s)
*** BLOCK 4. s-n and scf data ***
      1                 no. of S-N curve segments
      0.0000              cut-off stress range (ksi)
   0.4010E+01  0.1000E+09  stress range (ksi) cycles to failure
   0.4700E+02  0.1000E+05  stress range (ksi) cycles to failure
   1.000                 global stress concentration factor
      0                 no. of local stress concentration positions
*** BLOCK 5. computation/output option ***
      1                 calculation option
```

```
   0.0000  1.0000  0.04000     response location definition
      0            no. of user input modes
    0.0             gravitational acceleration
  0.4  0.2          two-sided bandwidth multi-mode bandwidth
    0.5             cutoff for eliminating unimportant modes
   0.0  0.0  0.0    3 coefficients in damping model (use of 0.0=default)
      0             flag for importing nodal effective tension and mass (0=no;1=yes)
      1             flag for MATLAB animation data output (1=yes;0=no)
*** BLOCK 6. supplemental data ***

if nmodel =  6 (pinned-pinned tensioned beam w/two rot springs)
provide rotational stiffness at each end (see example "beam1.dat" for input format)
if nmodel =  9 (free-pinned (w/spring) beam w/varying tension  origin at free end)
provide translational stiffness at x = L (see example "beam6.dat" for input format)
if nmodel = 19 (free-pinned (w/spring) beam w/o tension  origin at free end)
provide translational stiffness at x = L (see example "beam9.dat" for input format)
if nmodel = 33 (inclined cable)
provide chord inclination (angle) (see example "scr3.dat" for input format)
```

Appendix C: Integration of Signal from Acceleration to Displacement

Introduction

One of the objectives of the Lake Seneca experiment was to estimate the displacement of a pipe that is undergoing vortex induced vibrations. For this experiment, accelerometers were used to measure the acceleration of the pipe. Since acceleration is the second derivative of position, the signal must be integrated twice to transform an acceleration time signal to a displacement time signal.

The data integration must be done carefully using a series of de-trending, windowing, and filtering functions. The use of these functions will prevent low frequency noise expansion, which can be caused by the integration, and problems with the DC offset, which introduces low-frequency noise.

Removing Trends from the Data

Trends, such as DC offsets and offsets due to gravitational changes, can cause the integration to exponentially increase [Jong and Vandiver 1981]. Therefore, these trends must be removed before the time series is integrated. For this experiment, a linear trend was removed from the data.

When integrating, the initial velocity is an important component. The velocity, v(t), is the initial velocity plus the integration of the acceleration, a(t):

$$v(t) = v(0) + \int_0^t a(t')dt' \qquad (13.1)$$

Since the initial velocity, v(0), of each data set is unknown, a bounded displacement is desired. To obtain a bounded displacement, there must be no linear trends in the velocity; then v(0) can be set to zero. Once the trends have been removed, equation (1.1) can be rewritten as:

$$v(t) = a(t) * u(t) \qquad (13.2)$$

where u(t) is the step function, which is defined as zero before time zero and one at all time after that, and * is the convolution integral. By then taking the Fourier transform, where V(ω) is the Fourier transform of v(t) and A(ω)is the Fourier transform of a(t) and δ(t) is the delta function, the velocity can be expressed as:

$$V(\omega) = A(\omega)\left(\pi\delta(\omega) + \frac{1}{i\omega}\right) = A(0)\pi + \frac{A(\omega)}{i\omega} \qquad (13.3)$$

The delta function, δ(t), is defined as zero at all time except time equaling zero.

$$A(0) = \int_{-\infty}^{\infty} a(t)dt \qquad (13.4)$$

The term A(0) can be removed by using a straight-line fit to a(t). This removes the linear trends and DC offsets in the acceleration a(t).

The same procedure can be used for integrating from the velocity function to the displacement function, with one exception. The zero mean offset assumption does not hold true for this integration. Since the dynamics component is the response of concern in this experiment, d(0) can be set arbitrarily.

Filter Choice

Before and after each of the integrations, the data needed to be high-pass filtered because the low frequency noise expansion can cause problems when integrating in time. A high pass Infinite Impulse Response (IIR) filter is used to remove low frequency noise. If the data is integrated with the low-frequency noise, the noise expansion can dominate the new time series and give inaccurate results.

The high-pass filter must be constructed to remove the noise without attenuating the time-series data. Therefore, the filter characteristics and coefficients are important. Not only must the correct filter cut-off frequencies be chosen, but also the correct type of filter must be selected.

The choice of filter was based on the different characteristics of the filters. Since the filter is being used for time integration, only an IIR may be used [Stein 2000]. Four types of IIR filters were considered: Butterworth, Chebyshev Type I, Chebyshev Type II, and Elliptical. Phase shift was not considered as a factor, since by filtering the data twice the phase shift will be eliminated; see below for explanation.

The Butterworth filter had the smoothest transition, but the transition band in the filter was too large. To get a sharp enough transition, the order of the filter needed to be quite large. Since the order of the filter is doubled when the data is double filtered to remove the phase shift, the Butterworth filter is not ideal.

The Chebyshev Type 1 filter allows ripple in the pass band and has no ripple in the stop band, whereas the Chebyshev Type II filter allows ripple in the stop band but not in the pass band. Since the pass band is more important in the integration, the Chebyshev Type I filter was not chosen. The elliptical filter allows ripple in both the pass and stop bands, but has the advantage of having the sharpest transition region.

In this experiment, the data contains frequencies as low as 1.5 Hz. This is low in comparison to the Nyquist frequency of 30 Hz. Therefore, the high-pass filter must have a very sharp transition, such that the low-frequency noise can be removed without attenuation of the data. The ripple of the elliptical filter was constrained to 0.1 dB with attenuation in the stop band of 40 dB. These filter characteristics minimized the ripple and allowed the desired sharp transition. Since the pass band ripple could be minimized and the elliptical filter had a sharper transition, the elliptical filter was a better choice than the Chebyshev Type II for this experiment.

For the Lake Seneca experiment, the stop band is from 0 to 0.75 Hz; the pass band begins at 1.5 Hz, resulting in a fifth-order elliptical filter. The order of the filter is doubled because the data will be filtered twice to eliminate the phase shift; see explanation below. These cut-off values were chosen after review of the data to determine that this would minimize the large low-frequency values that are caused by the integration, without attenuating the data. The resulting filter can be seen in Figure 60.

In Figure 61, the displacement of an integrated time series can be seen when a high-pass filter was not used. The low-frequency noise dominates the time series, giving displacements that are over one hundred times greater than the diameter of the pipe.

Figure 62a and Figure 62b show the power spectral density (PSD) of the acceleration and the velocity of a typical case from the Lake Seneca experiment. The filter is only affecting the data below 1.25 Hz. From the figures, the vortex-induced vibrations are not acting at frequencies below 1.5 Hz. Thus, the filter is only affecting low-frequency noise.

Changes in the DC offset due to gravity, such as in the Lake Seneca pendulum tests, should not affect the integration because of the trend removal and the filtering used. Problems can occur if the data is dominated by white noise or other interference in the region of interest, as this can result in an inaccurate integration.

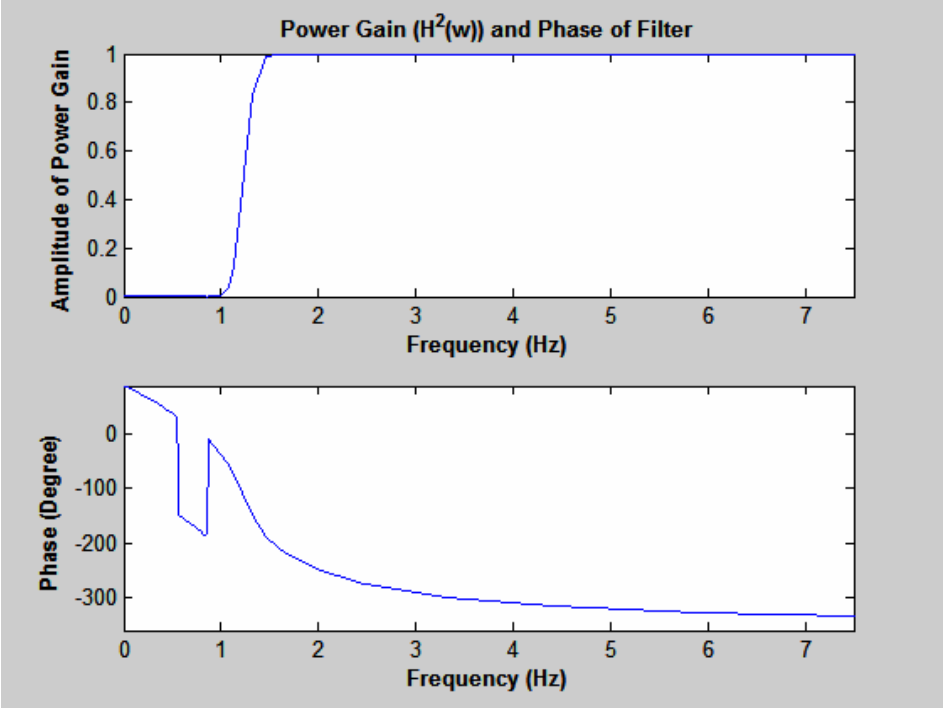

Figure 60 – 5TH order elliptical filter

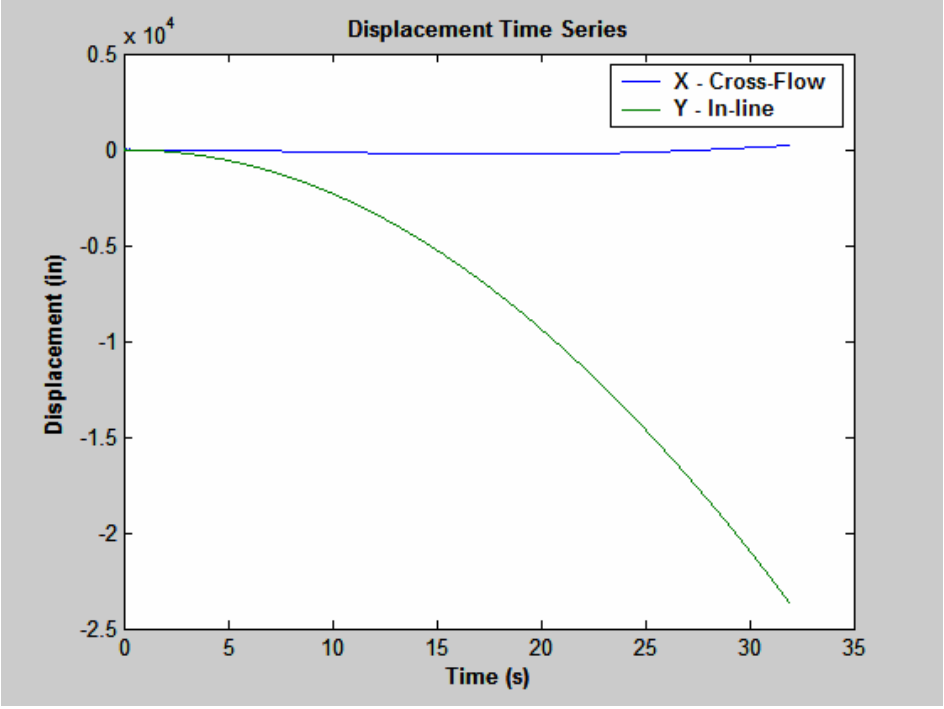

Figure 61 – Displacement time series without high-pass filtering

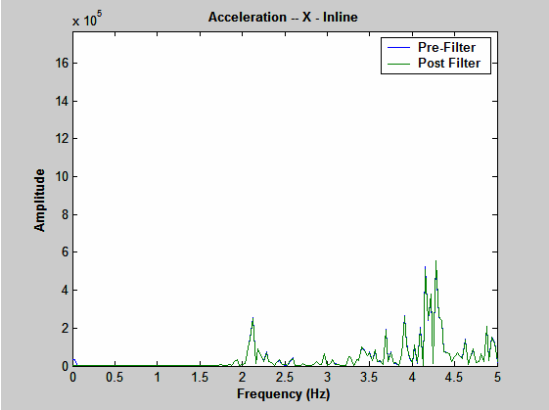

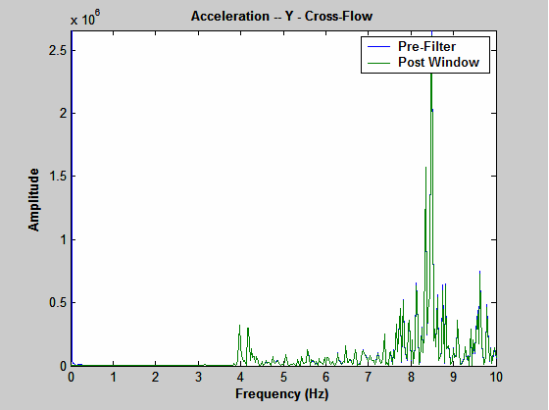

Figure 62 – PSD of the acceleration in cross-flow and in-line

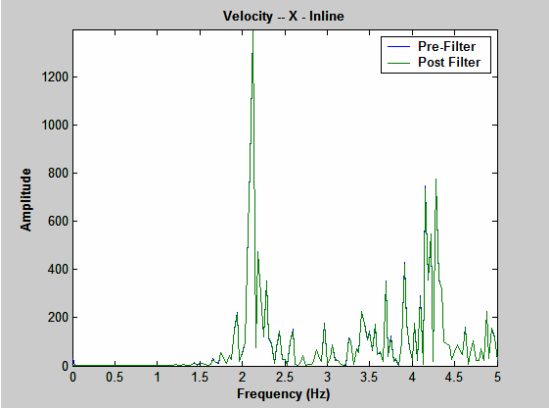

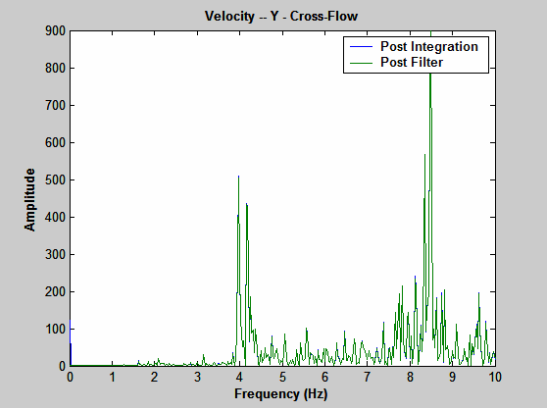

Figure 63 – PSD of velocity in cross-flow and in-line

Phase Shift

Since the phase information is important when integrating, the distortion of phase due to the filter needs to be minimized or eliminated. To achieve a zero-phase shift, a double filtering technique can be used. This filtering is acausal, and therefore can only be used in post-processing of the data. Effectively, the data is being filtered twice: once in the forward direction and once in the reverse direction to cancel out the phase shift. A graphical representation of the time domain representation of this filtering can be seen in Figure 64.

F(t) is the input signal that has been recorded; h(t) is the filter that is being used; g(t) is the filtered f(t); x(t) is the signal after g(t) has been reversed in time and then filtered again. Lastly, x(t) is reversed in time to give the final output y(t). The final output, y(t), has been filtered twice so as to negate any phase shift.

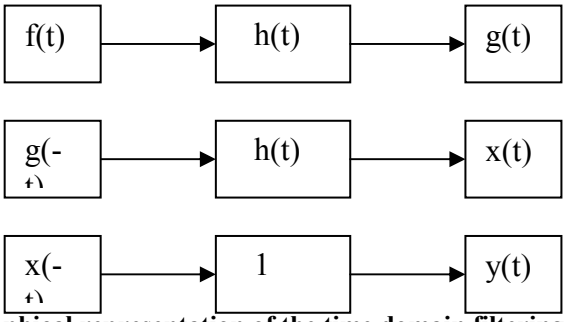

Figure 64 – A graphical representation of the time domain filtering for zero-phase shift

To more easily understand this filtering technique, a Fourier domain explanation can be used. Since filtering in the time domain is a convolution of the filter with the time series, the Fourier domain equivalent is multiplication of the Fourier transform of the time series and the filter.

$$G(\omega) = F(\omega)H(\omega) \qquad (13.5)$$

When filtering a time signal in reverse, the Fourier domain equivalent is multiplying by the complex conjugate of the Fourier transform of the time series.

$$X(\omega) = H(\omega)\overline{G}(\omega) \qquad (13.6)$$

By multiplying both sides of the equation by their complex conjugates Equation (1.6) can be transformed into equation (1.7).

$$\overline{X}(\omega) = \overline{H}(\omega)G(\omega) \qquad (13.7)$$

Since y(t) = x(-t):

$$Y(\omega) = \overline{X}(w) \qquad (13.8)$$

Lastly, by substituting equations (1.5) and (1.7) into equation (1.8), the resulting Fourier transform can be seen.

$$Y(\omega) = \overline{H}(\omega)G(\omega) = \overline{H}(\omega)H(\omega)F(w) = H^2(\omega)F(\omega) \qquad (13.9)$$

Since $H(\omega)$ and its complex conjugate $\overline{H}(\omega)$ have equal and opposite phase, the equivalent phase shift is zero. The resulting time series is the equivalent of filtering with the squared magnitude of the filter and no phase shift.

Windowing

As in all experiments, the time series is of finite length, which is effectively multiplying the time series by a rectangular window. With the time integration, the time series is not assumed to be zero outside of the time of analysis. To negate end effects and their

resulting leakage effects in the frequency domain, a windowing function attenuates the signal at the very beginning and end of the data.

For this analysis, a window was constructed such that only the first and last 50 samples were affected. For a sampling rate of 60 Hz, less than a second of data is windowed at each end. The window length was chosen to be longer than one period of the lowest frequency. The window contained a Hanning widow at each end with a boxcar window in the center. Figure 65 shows the window used for this experiment. An enlarged view of the first hundred samples is also shown to see the effect of the Hanning window.

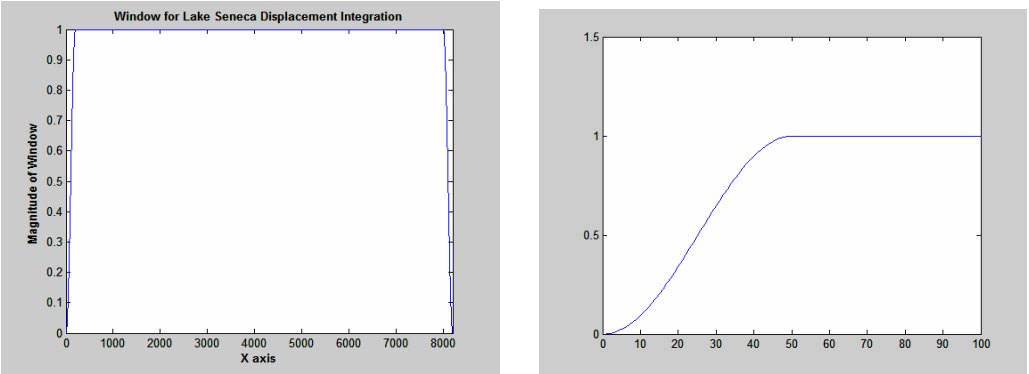

Figure 65 –Window used in the analysis (a) Entire window; (b) the beginning Hanning section of the window

In Figure 66, the effects of the lack of window can be seen. The blue lines represents expected result. The green line repesents the data that has been integrated without a windowing function. The green line can be seen to have a greatly skewed result especially at the beginning and ending of the time series. Smaller diviations exist throughout the rest of the data caused by the lack of window.

In comparison, Figure 67 shows the same signal when integrated with the windowing function. When comparing the green and blue lines, these show very little deviation except at the ends where the windowing function affects the time series.

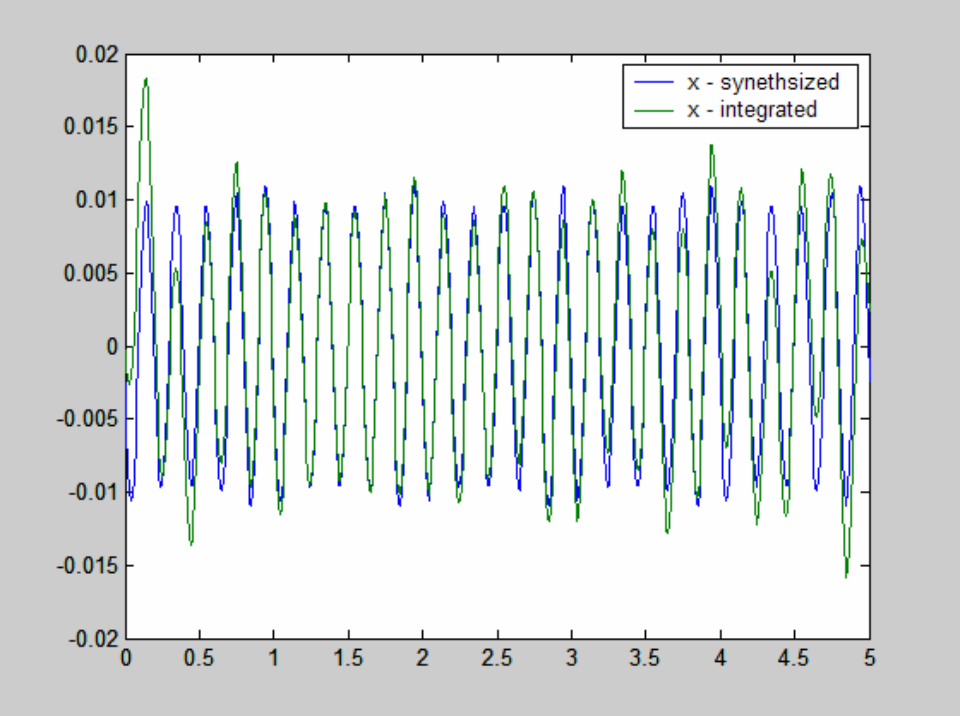

Figure 66 –Synthesized data series illustrating the effects of integration without windowing.

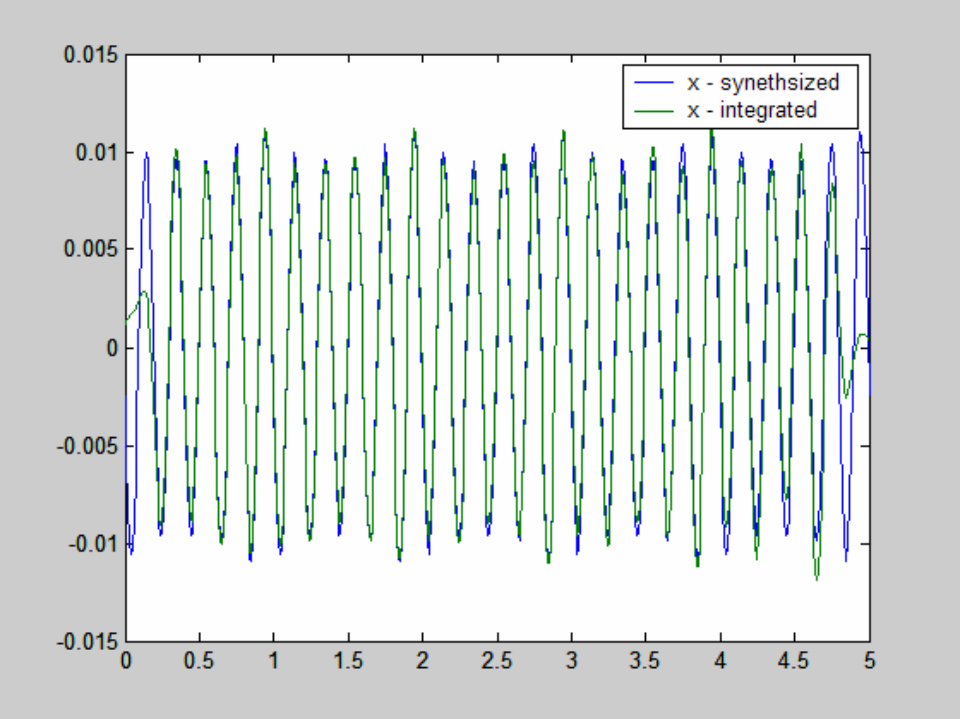

Figure 67 –Synthesized data illustrating the effects of integration with windowing.

Another way of evaluating the windowing function is to look at not only the time series but also to investigate the Fourier transforms. In Figure 68, the synthesized data can be seen to have large side lobes off of the main peaks. This is best described by

viewing this in the Fourier domain. Since the windowing function is multiplied by the time series, this is equivalent to convolving the window function and the time series in the Fourier domain.

In Figure 68, the Fourier transform of the accelerations can be seen both before (the blue line) and after the windowing (the green line).

Figure 69 shows the Fourier transform of the Windowing function used in this analysis. Since the windowing function is highly concentrated around zero, the effect of the windowing function is a blurring of the Fourier transform of the time series. This blurring is seen as widening of sharp peaks and smoothing of sharp spectral features. Figure 70 shows the times series both with and without the windowing. Only the very ends are affected by the window.

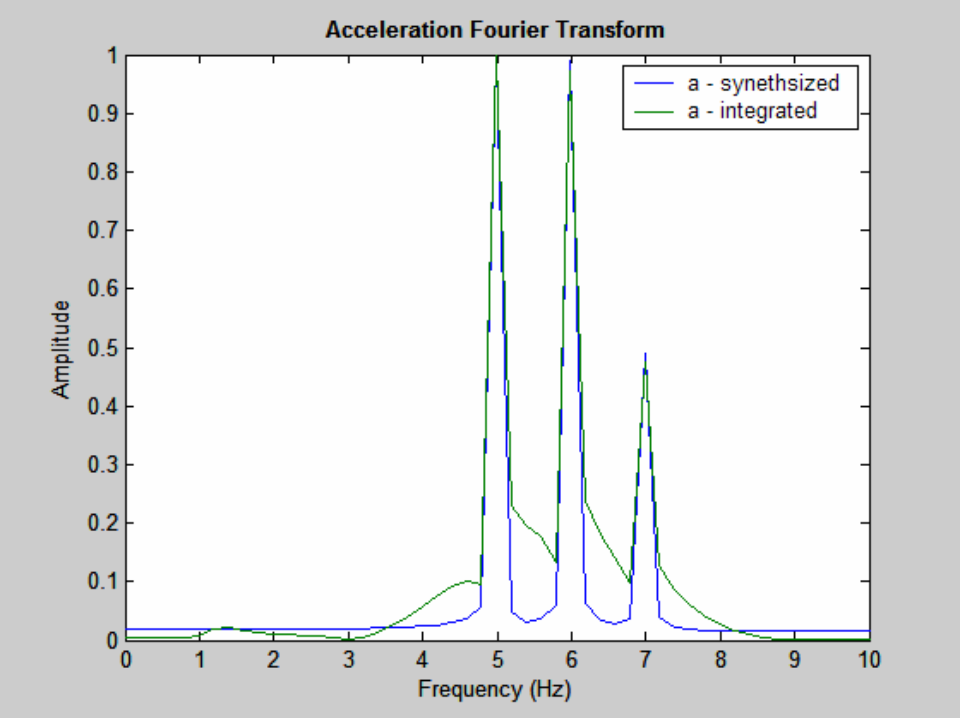

Figure 68 – Fourier transform of the acceleration time series before and after windowing

Figure 71 shows the velocity after the time integration. The blue line represents the theoretical integration, while the green line is the filtered and windowed data. The peaks of the Fourier transform are unaffected by the windowing, but the peaks are widened at the base. These side bands could potentially be a problem if there were smaller peaks that were covered by the side band. These side lobes in the Fourier domain have little effect on the time series, as can be seen in Figure 72.

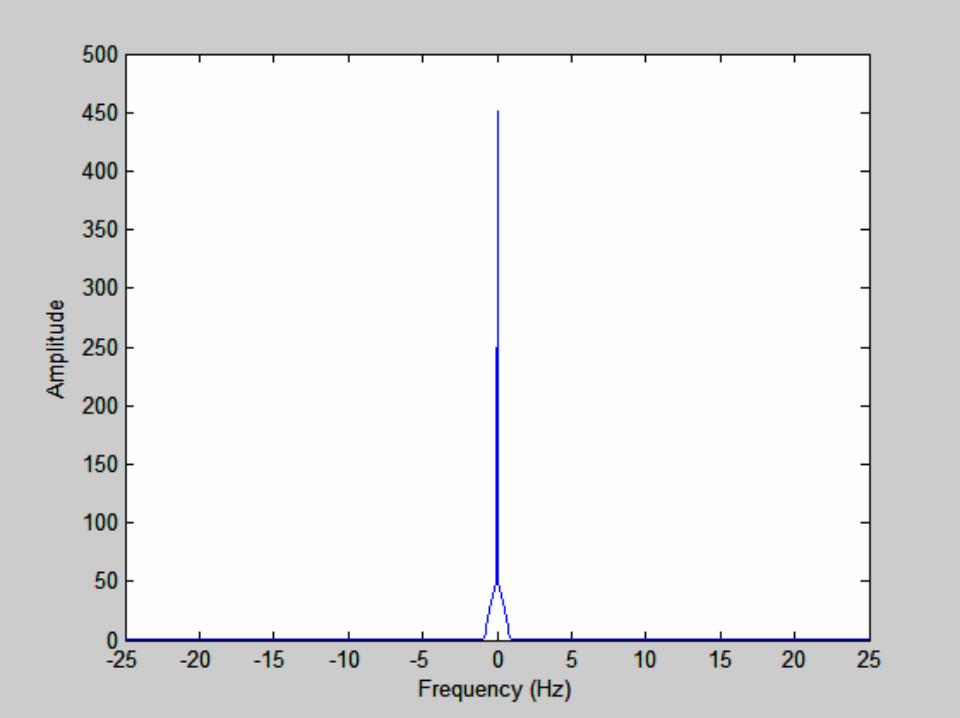

Figure 69 – Fourier transform of the windowing function

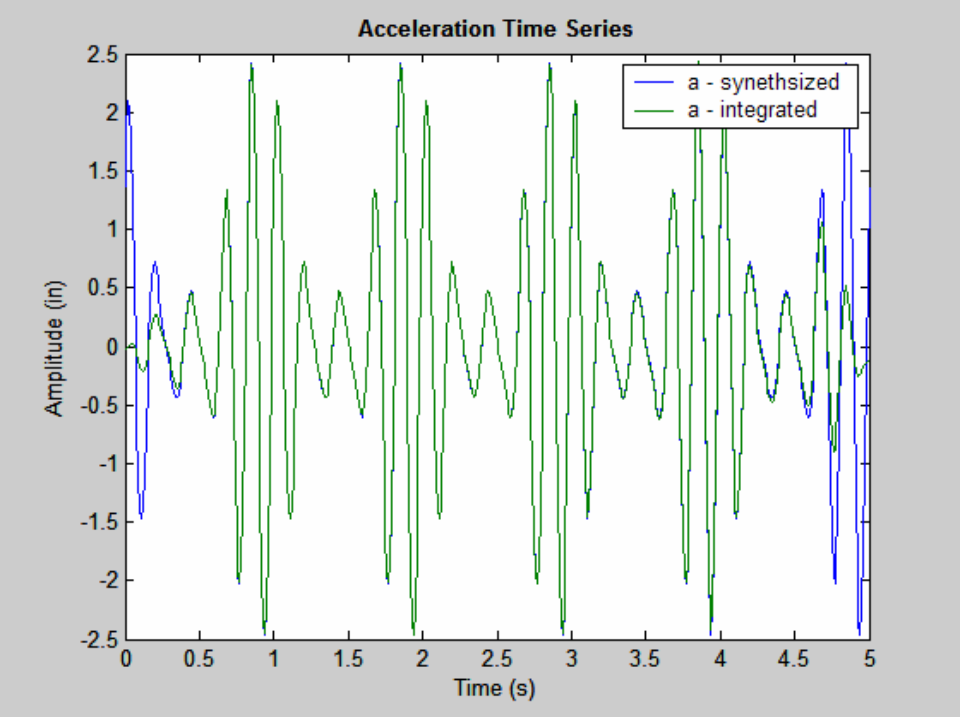

Figure 70 – Acceleration time series with and without windowing

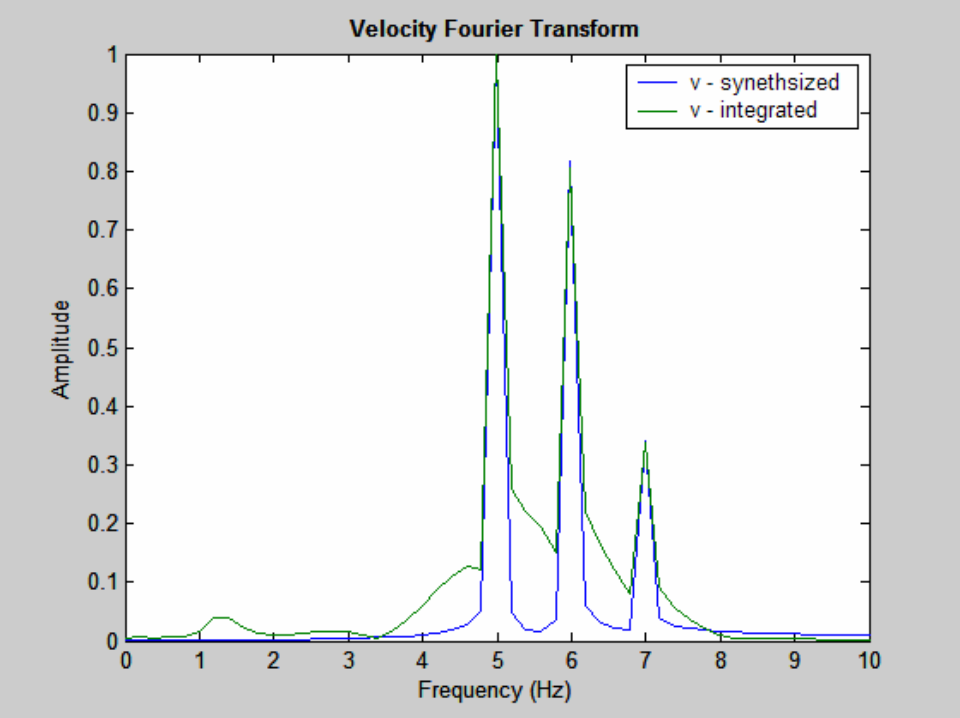

Figure 71 – Fourier transform of the synthesized velocity and the integrated velocity

Similar results can be seen when the data is double integrated to represent the displacement time series, as seen in Figure 73.

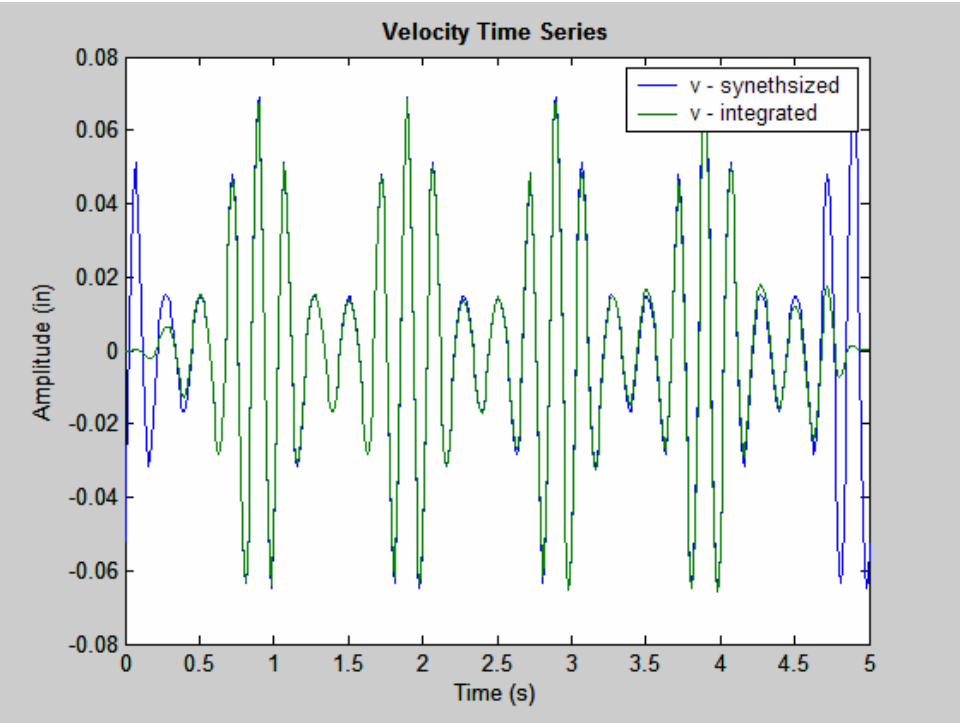

Figure 72 – Time series of the synthesized velocity and the integrated velocity

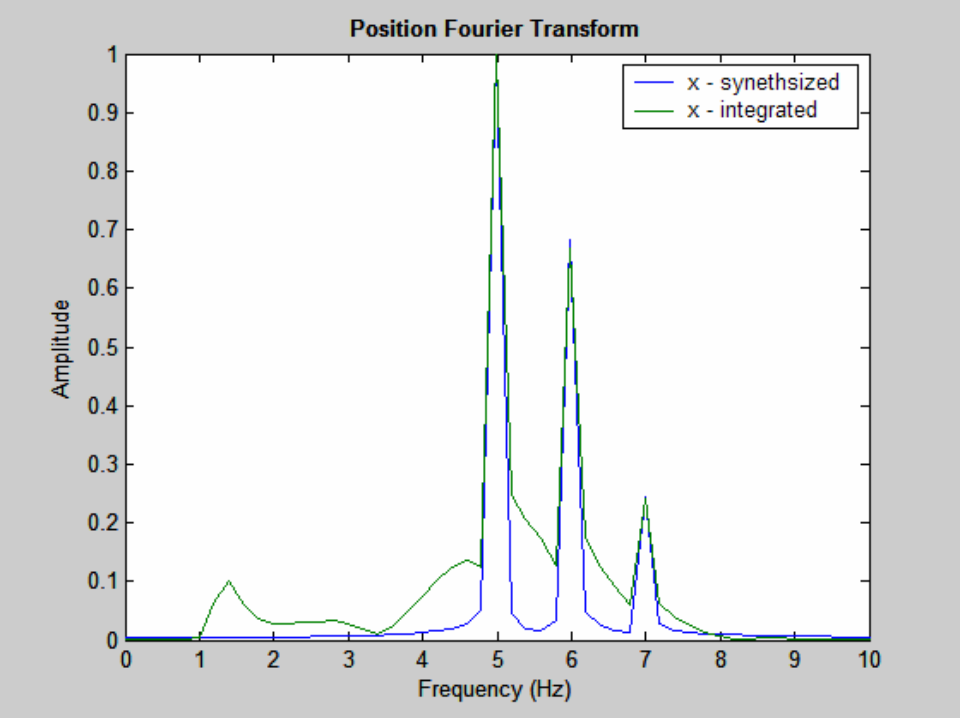

Figure 73 –Fourier transform of the synthesized displacement and the integrated displacement

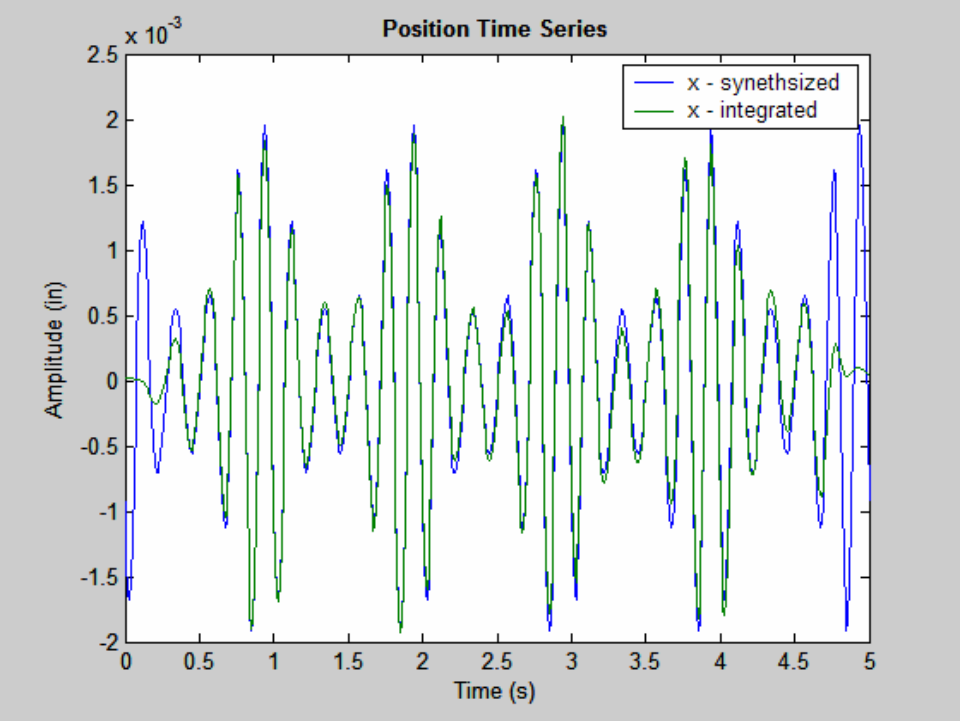

Figure 74 – Time series of the synthesized displacement and the integrated displacement

Cumulative Integration

The final step is to perform the actual integration. A trapezoidal integration was used for this application. The integration was calculated cumulatively at each point to create the time series.

Integration Methodology

To summarize the steps needed to integrate the data:

1. Remove trends from the data such as DC offsets, to prevent low-frequency noise interference from these trends in the acceleration time signals.
2. Use a high pass IIR filter to remove low-frequency noise from the acceleration time series. The filter coefficients should be chosen as not to attenuate any of the actual signals.
3. Window data to remove the effects from the ends of the acceleration times series.
4. Integrate the acceleration using a cumulative trapezoidal integration to get a velocity time series.
5. Remove trends such as DC offsets from the data, to prevent low-frequency noise interference from these trends in the velocity time signals.
6. Use a high-pass IIR filter to remove low-frequency noise from the acceleration time series. The filter coefficients should be chosen as not to attenuate any of the actual signals.
7. Window data to remove the effects of the discontinuities at the ends of the velocity times series.
8. Integrate the velocity using a cumulative trapezoidal integration to get a displacement time series.
9. Remove trends from the data such as DC offsets, to prevent low-frequency noise interference from these displacement time signals.
10. Use a high-pass IIR filter to remove low-frequency noise from the displacement time series.

This methodology works to double integrate most acceleration time series into displacement time series. The filtering and windowing coefficients must be chosen specifically for each experiment so as not to effect and attenuate the original time series.

Examples from the Lake Seneca Data

In Figure 75, the acceleration time series can be seen. In comparison, Figure 76 shows the displacement times series. The acceleration time series contains more high-frequency noise. This is expected as an integrator acts as a low-pass filter.

The low-pass filtering effects of the integrator can more easily be explained in the Fourier domain. When integrating in the Fourier domain, the Fourier transform of a time series is divided by ω. For a double integration the Fourier transform of the time series would be divided by ω^2. The higher the frequency, the greater the reduction would be of the acceleration spectrum when dividing by ω^2.

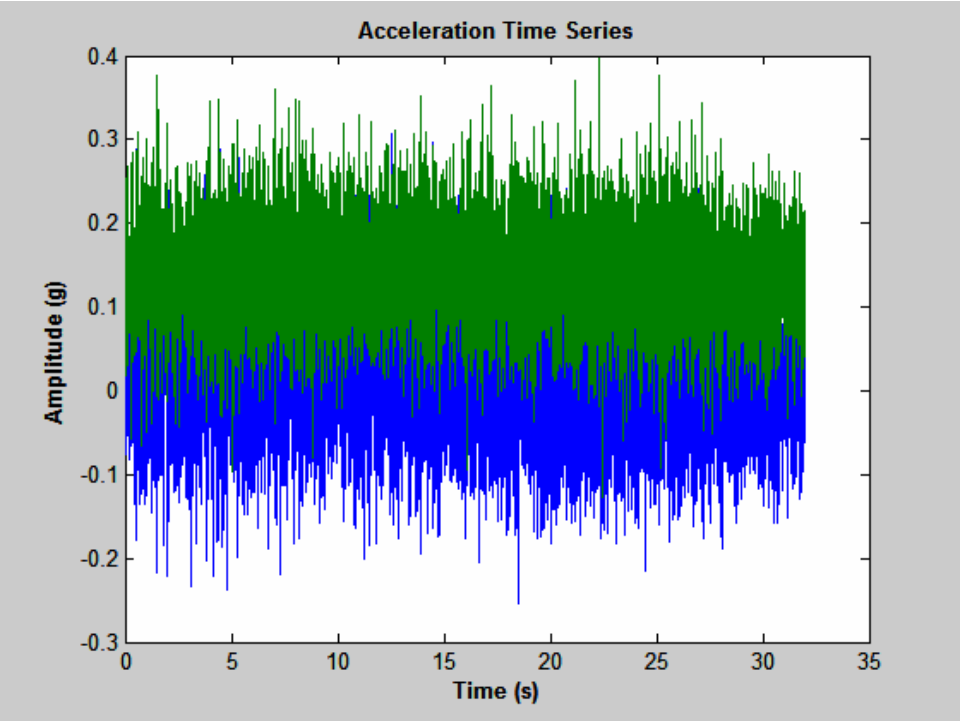

Figure 75 – Time series of the acceleration from the Lake Seneca experiment

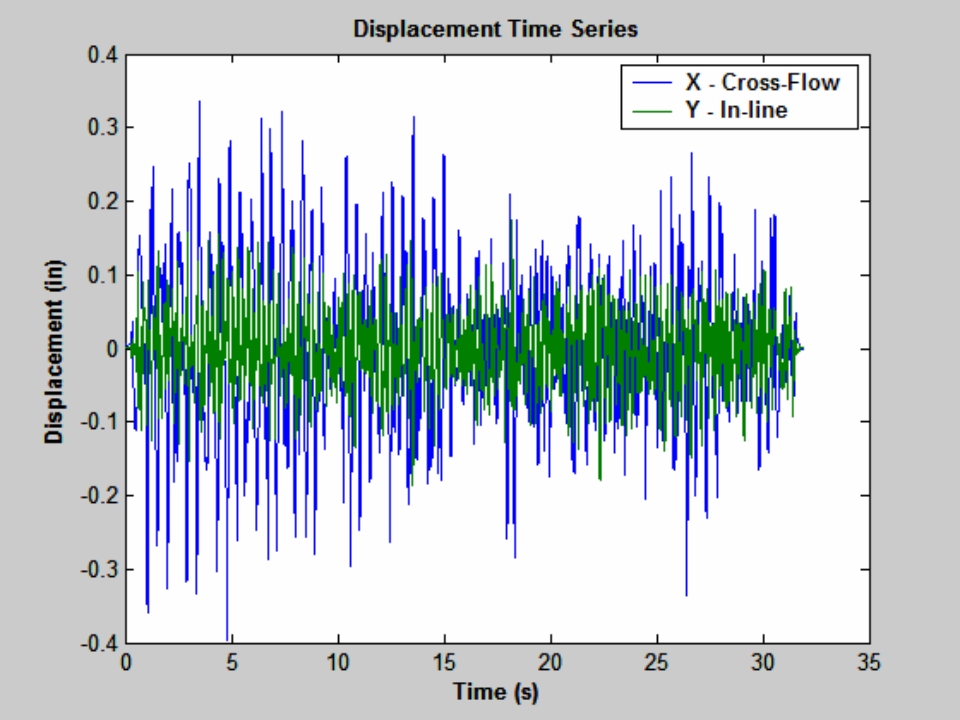

Figure 76 Integrated displacement time series from the Lake Seneca experiment

Appendix D: Damping Estimates

Introduction

One of the original goals of the Lake Seneca and Gulf Stream tests was to calculate damping parameters. Two separate methodologies of calculating damping are shown. The first calculates the still-water damping coefficients for the Lake Seneca test from the eccentric mass shaker tests. The second calculates the damping for the straked region.

Damping Estimation Using Shaker Excitation

A Green's function can be constructed for the theoretical response of a continuous system to a unit, transverse, harmonic force at a single point somewhere on the finite cylinder, as discussed in [Li 1993] and [Vandiver and Chung 1988].

The coordinate 's' is the distance from the top end of the cylinder to the input point. 'x' is the coordinate of any response location, also measured from the top of the pipe. Equation (14.1) is the Green's function for the section of pipe above the point source, and Equation (14.2) is for the section of pipe below the source.

$$G(k_r, x, s) = \frac{\sin(k_r(L-s)) * \sin(k_r x)}{k_r T \sin(k_r L)} \qquad s < x \qquad (14.1)$$

$$G(k_r, x, s) = \frac{\sin(k_r(L-x)) * \sin(k_r s)}{k_r T \sin(k_r L)} \qquad x > s \qquad (14.2)$$

The complex wave number, k_r, is given by equation (14.3). The structural damping, r, is given by equation (14.4).

$$k_r = \sqrt{\frac{\rho\omega_r^2 + jr\omega_r}{T}} \qquad (14.3)$$

$$r = 2\rho\omega_r\xi \qquad (14.4)$$

where ω_r is the input frequency of the shaker, and ξ is the damping factor.

Figure 77 is the prediction of the magnitude of the Green's function displacement for a point source 15 feet below the universal joint at an input frequency of 4.5 Hz and a linear damping ratio of 0.03. The blue line in the graph represents the displacement above the point source; the green line represents the displacement below the point source.

The Green's function takes into account the reflections of the waves off the bottom of the pipe. Therefore, the nodes are not at zero unless there is zero damping. The damping controls the height between the nodes and the anti-nodes.

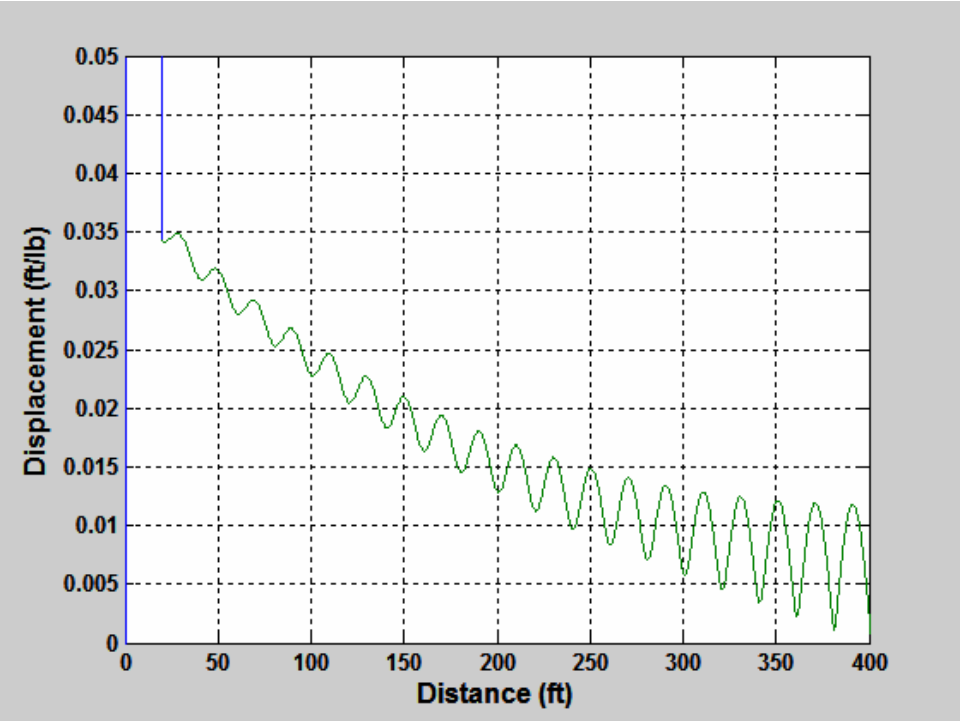

Figure 77 – Magnitude of the displacement Green's function, 3% damping and an excitation frequency of 4.5Hz.

Figure 78 is a plot of the measured RMS response overlaid with a plot of the magnitude of the Green's function. The red stars represent the magnitude of the RMS response in the plane of the shaker vibration. The Green's function has been multiplied by a constant to give it the same amplitude as the observed response.

Instead of comparing the exact amplitude of each point's measured response to the predicted response, the damping was adjusted until the decay rates of the measured response and the predicted response were approximately the same. The damping that provides the best fit is that linear equivalent damping ratio that approximates the real phenomena. This damping is the hydrodynamic damping which is the damping induced by the motion in water. Figure 79 shows the RMS response, the predicted Green's function and the two exponential decay rates.

To determine the best damping values to use in the Green's function, an exponential curve was fit to the data as well as to the Green's function. The damping factors were varied to get the exponential decay rate that best matches to the data.

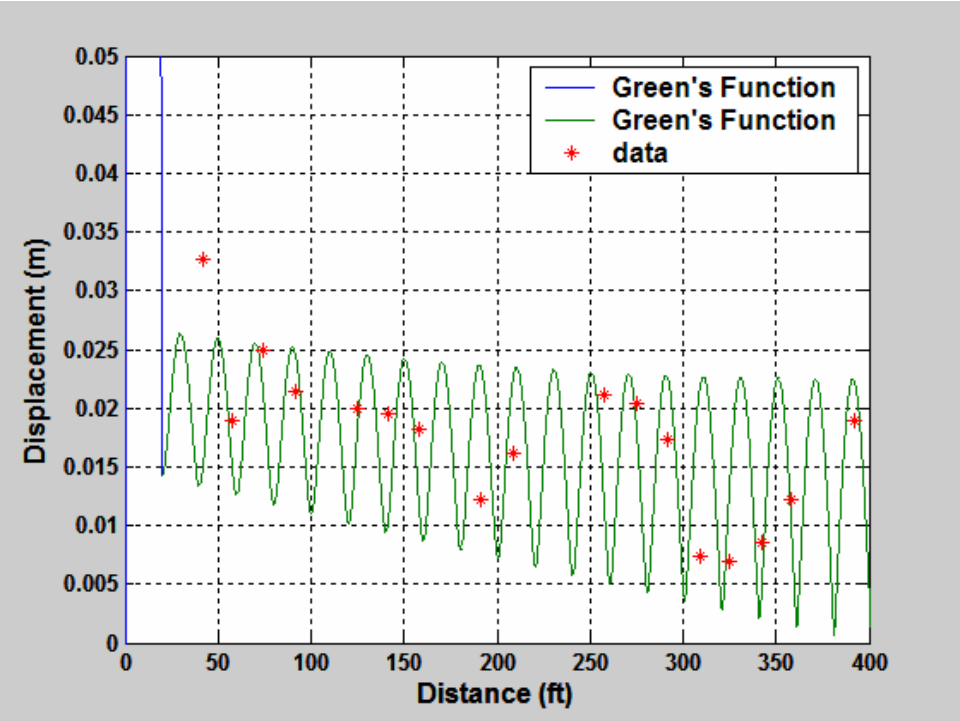

Figure 78 - Green's function prediction vs. RMS displacement

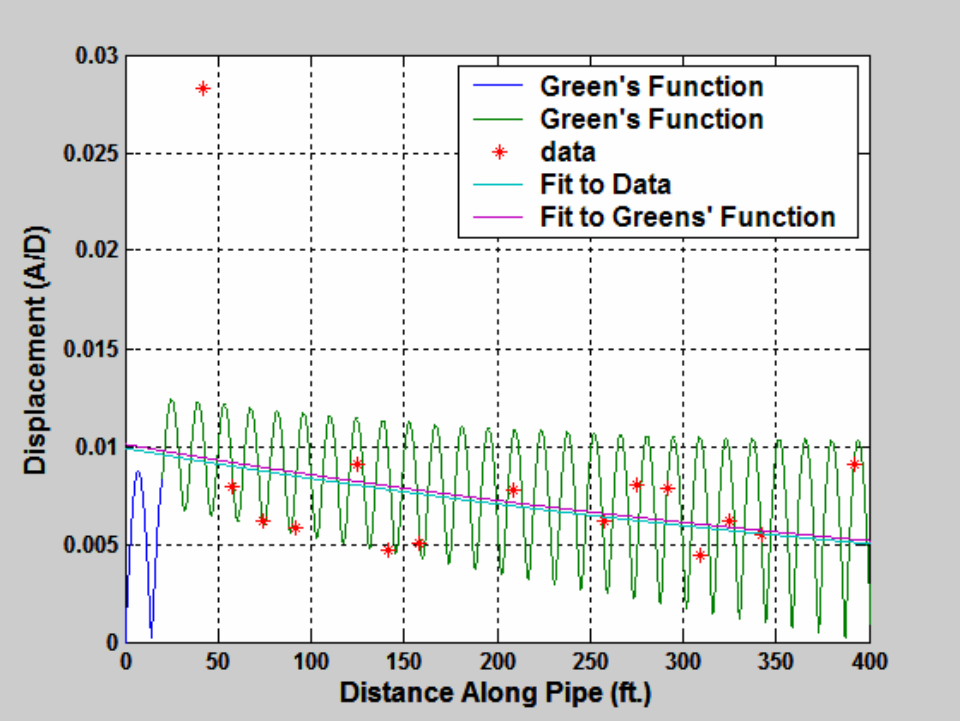

Figure 79 - Exponential fit to Green's function and data

SHEAR7 uses the still-water model for hydrodynamic damping given in Equation (14.5), as discussed in [Vandiver and Li 2003] and [Venugopal 1996].

The constant C_{sw} equals 0.2 for bare pipe. Furthermore, the term containing amplitude, (Y_{rms}/D), is negligible for small values of amplitude. In this example, Y_{rms}/D is less than 0.03. The term involving Y_{rms}/D inside the square brackets is $2*10^{-4}$. This is two orders of magnitude smaller than the $1.8*10^{-2}$ for the first term in this example.

$$r_{sw} = \frac{\rho_f \pi \omega_r D^2}{2}\left[\frac{2\sqrt{2}}{\sqrt{\omega_r D^2 / \nu}} + C_{sw}\left(\frac{Y_{RMS}}{D}\right)^2\right] \tag{14.5}$$

In Equation (14.5), ω_r is the excitation. This equation may be put in terms of the damping ratio. By neglecting the term containing Y_{rms}/D, this leads to the formula shown in Equation (14.6) for predicting still-water damping ratio:

$$\zeta = \frac{r_{sw}}{2\omega_r (m + m_a)} = \frac{\rho_f \pi D^2}{4(m + m_a)}\left[\frac{2\sqrt{2}}{\sqrt{\omega_r D^2 / \nu}}\right] = \frac{1}{\sigma_g + C_a}\left[\frac{2\sqrt{2}}{\sqrt{\omega_r D^2 / \nu}}\right] \tag{14.6}$$

where ν is the kinematic viscosity of water, m is the mass per unit length of the pipe, and *s.g.*, is the specific gravity of the pipe.

Figure 80 shows the theoretical values from SHEAR7 compared with the values found from matching the exponential decay of the Green's function to the data.

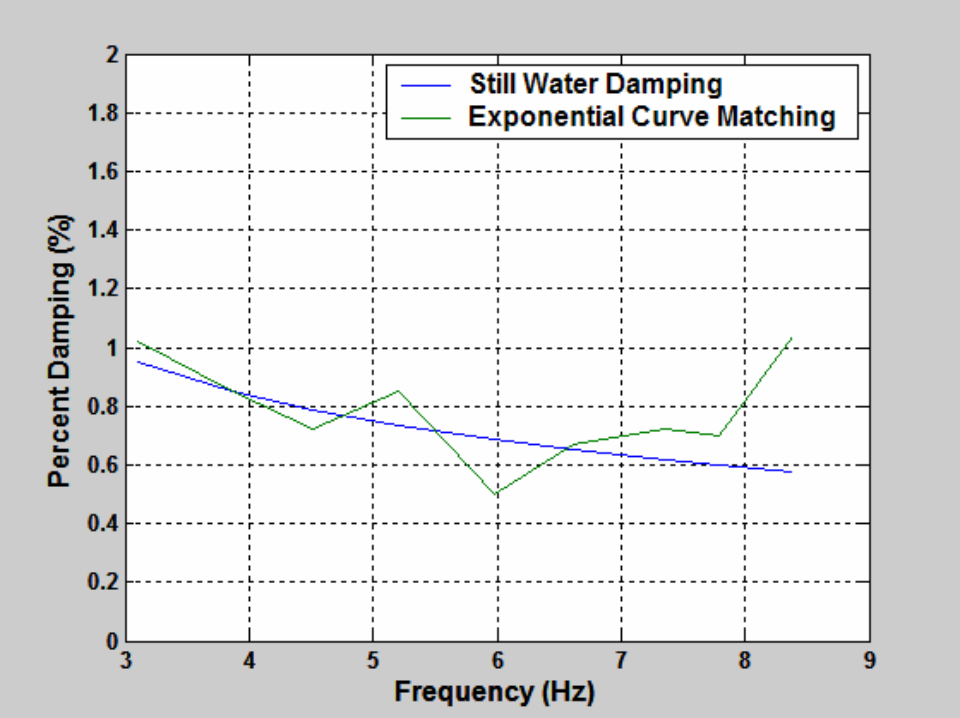

Figure 80 - Estimated still water damping factors compared with theoretical

Damping Factors for Strakes

On the second day of testing in the Gulf Stream, 40% strake coverage was applied to the bottom portion of the pipe. The bottom one hundred ninety four feet of the pipe was covered in strakes. The vibration was driven entirely by vortex shedding from the bare region of the pipe. The vibration waves generated in this region propagated into the straked region where the waves attenuated rapidly, as seen in Figure 81. The magnitude of the observed RMS single-channel strain was as high as 200 micro-strain (με) in the bare region and was reduced to less than 25 με as the waves traveled through the strake region to the bottom end of the pipe.

Figure 81 shows a single quadrant RMS strain and the corresponding current profile. The exponential decay can be seen at depths below 300 ft. Figure 82 shows the 14 steady-state 40% strake coverage cases. No matter the vibration response in the bare region, the response in the straked region has the same exponential decay characteristics.

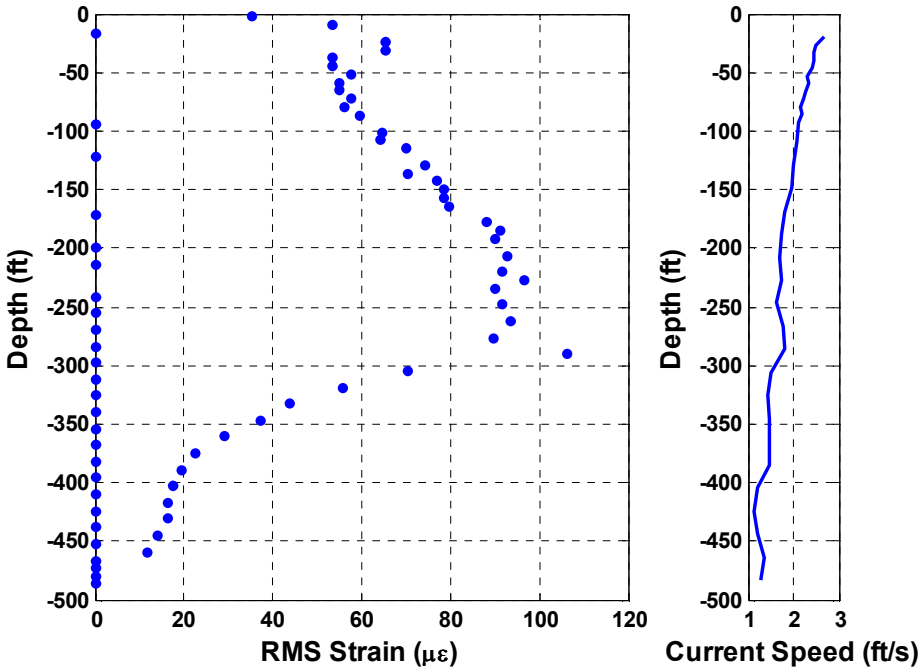

Figure 81 - Measured single fiber RMS strain for 40% strake coverage, shown with the corresponding current profile

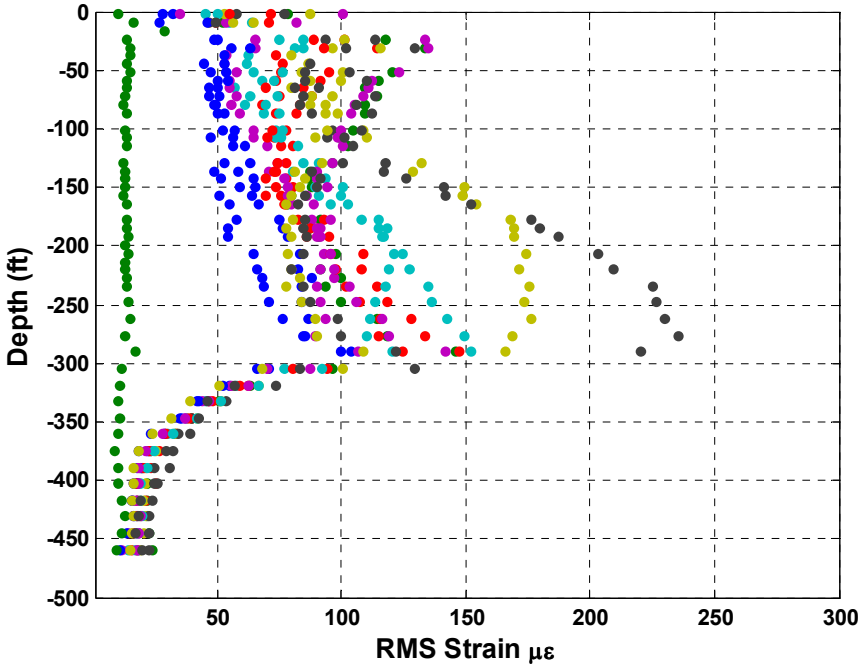

Figure 82 - RMS single channel strain for the pipe with 40% strake coverage

A problem created by the partial strake coverage is a stress concentration at the interface between the bare and straked regions. One hypothesis is that for the traveling

waves generated in the bare region the change in mass per unit length at the beginning of the straked region caused wave reflections and a local stress concentration. The stress concentration is illustrated in Figure 83.

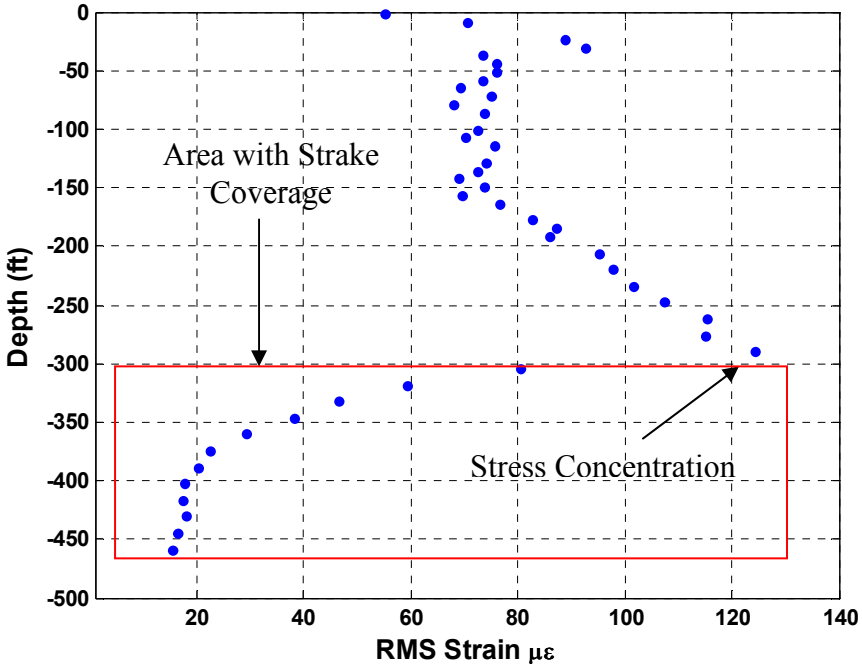

Figure 83 - Stress concentration in measured single channel strain

Figure 82 shows that the waves attenuated exponentially upon entering the straked region, as modeled in Equation 1.1.

$$y_2 = A\, e^{-\zeta k_2 \Delta x} \tag{14.7}$$

Equation (14.7) describes the amplitude of propagating waves with exponential decay due to damping, where ζ is the damping ratio, k_2 is the wave number in the straked region, and Δx is the distance between two points. By using a logarithmic fit, the rate of decay for the data shown in Figure 82 is found to be given by the following equation:

$$\zeta k_2 = 0.0114 \; {}^{1}\!/_{ft} \tag{14.8}$$

$$k_2 = \frac{\omega}{c_2} = \frac{2\pi f}{c_2} \tag{14.9}$$

$$\zeta = \frac{0.0114 c_2}{2\pi f} = \frac{0.0018 c_2}{f} = \frac{0.185}{f(Hz)} \tag{14.10}$$

for $c_2 = 102\, ft/s$

From equation (14.10), the frequency-dependant damping ratio, ζ, is plotted in Figure 84, using the measured propagation speed of 102 ft/s in the straked region.

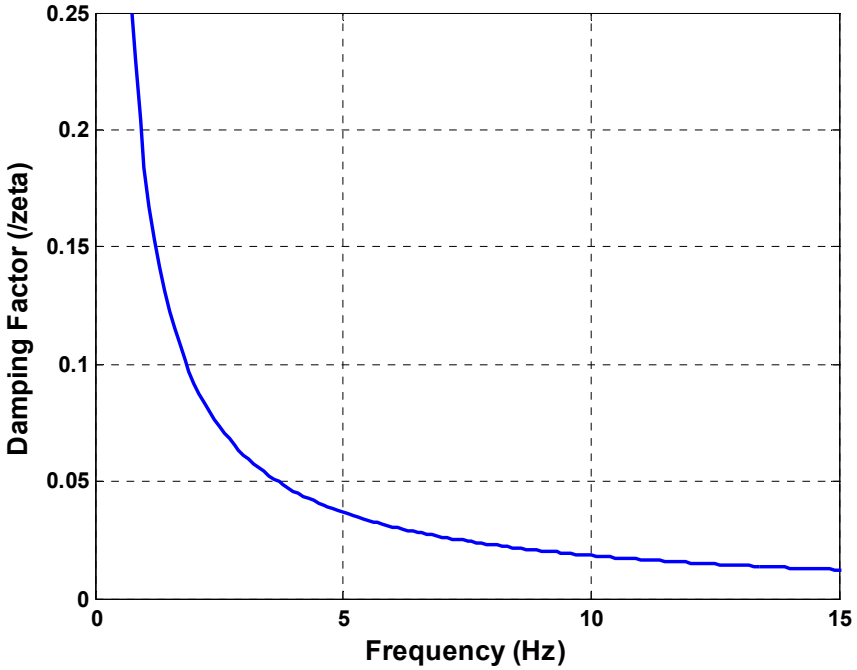

Figure 84 – Estimated damping ratio for the region with strakes

Appendix E: Finding Still-Water Damping Coefficients Using Wavelet Analysis

Introduction

All materials have three inherent properties: inertia, stiffness, and damping. In this experiment, the damping factors are calculated for a pipe being used for testing of vortex induced vibrations (VIV). Damping factors characterize the loss of energy in the system.

Damping factors can be difficult to determine because of their frequency dependence. Since this is an impact test, the duration of the data is too short to do normal frequency analysis. Therefore, either the short-time Fourier analysis or wavelet analysis is ideal for this application. Since the calculation of damping is based on the energy in the time series, wavelets are the preferred analysis tool to give both time and frequency resolution.

When estimating the effects of VIV on a pipe, damping factors are important because they affect the amplitude of the vibration. With off-shore platforms, the estimated amplitudes and frequencies of vibration correlate to the fatigue of the platform. By understanding the fatigue of the pipes and risers, these off-shore platforms can be designed for longer lives and can be built to be more cost-effectively.

Background

During the mechanical shakedown test done at Lake Seneca, a series of impact tests were performed. A hammer was used to impact the side of the pipe and impart energy into it. This impact starts a wave packet that travels the length of the pipe and then reflects off the end of the pipe and continues traveling the length of the pipe until all the energy of the wave has been damped out.

The impact test is done with a large weight impacting the pipe to create waves that vibrate in the horizontal direction. The impact of the hammer with the pipe occurred just above the water line. Figure 85 shows the setup of the impact hammer.

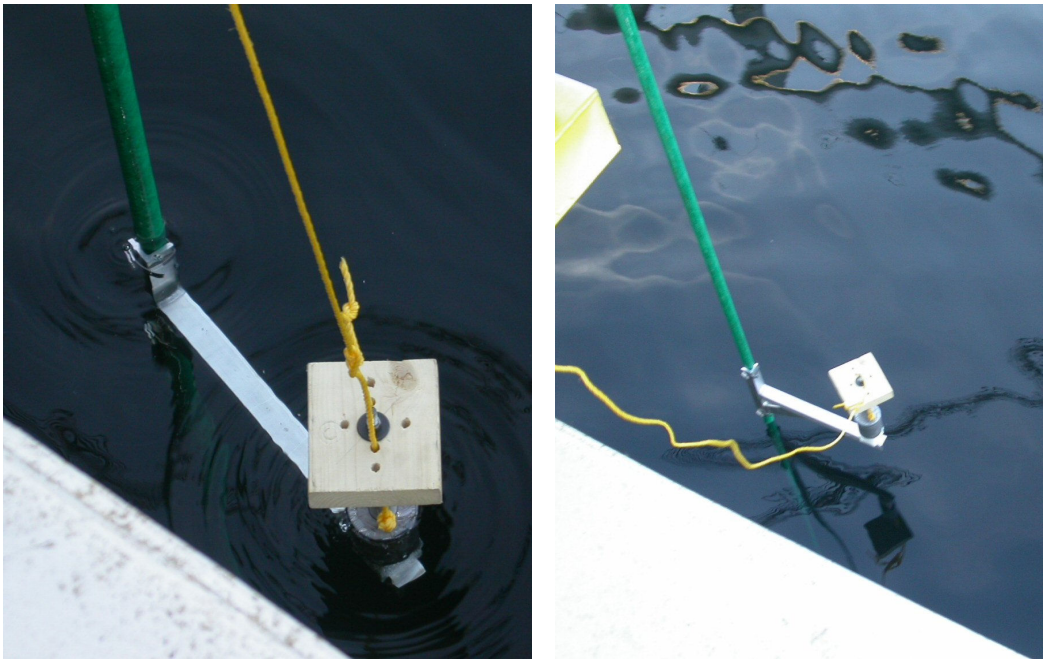

Figure 85 – The impact hammer used during the Lake Seneca still water damping tests.

Preliminary testing impact data was taken with the set of accelerometers shown in Figure 86. During the preliminary mechanical test, two accelerometers were mounted in the horizontal directions. These accelerometers were mounted above the water line and therefore very close to the top of the pipe. Figure 86 shows the accelerometers attached to the pipe.

Figure 86 – Accelerometers used in the mechanical shake-down test and the impact testing

Simulations

A computer simulation of the pipe was made by Technip Inc. to model the VIV in the pipe. This model was also used to simulate an impact test. This model provides a way to benchmark the wavelet analysis to estimate the damping, since the damping factors in the model are known. The simulated data had the same physical properties as the pipe, but a different sampling rate was used for the simulated data, 2000Hz. Figure 87 shows the simulated impact data.

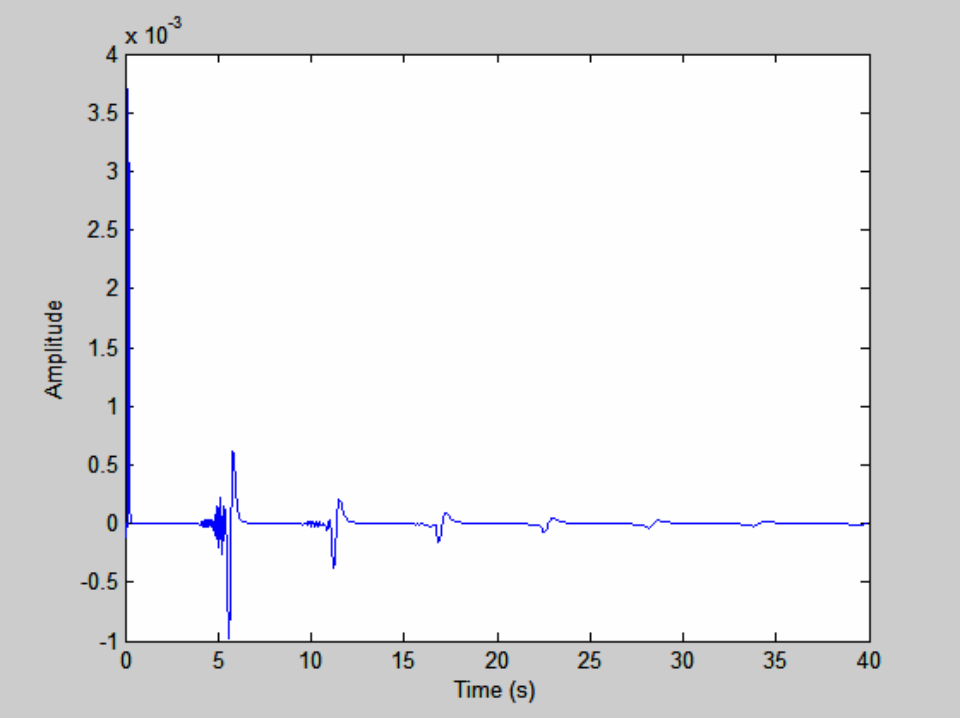

Figure 87 – An impact test from the Technip computer simulation

Calculation of Damping

In the case of the polyethylene and fiberglass material, the damping factors can be difficult to discern because they rely on the speed of sound, which is frequency dependant.

The accelerometers detect the impact just after its occurrence. The waves travel down the pipe and reflect off the end of the pipe. The accelerometers then see a "bounce" as the wave is reflected back up the pipe. This "bouncing" effect continues until the waves are completely damped out. These "bounces" can be seen in Figure 87.

Damping creates an exponential decay in the energy of the wave.

$$E_2 = E_1 e^{-2\zeta k \Delta x} \qquad (15.1)$$

Where ξ is the damping factor; Δx is the distance between the two sections. The energy, E, in each wave packet can be found by summing the time signal squared, or in the case of the wavelets, the square of the time series for each frequency range. The wave number, k, is defined as the frequency divided by the speed of propagation.

$$k(\omega) = \frac{\omega}{c(\omega)} \tag{15.2}$$

By modifying Equation (15.1)

$$\ln\left(\frac{E_1}{E_2}\right) = 2\zeta k \Delta x \tag{15.3}$$

$$\zeta(\omega) = \frac{1}{2k\Delta x}\ln\left(\frac{E_1}{E_2}\right) = \frac{c(\omega)}{2\omega\Delta x}\ln\left(\frac{E_1}{E_2}\right) \tag{15.4}$$

When using wavelets, for each band, there is a range of frequencies and the speed of propagation is an estimate over the range of frequencies. For the estimation of the damping factors, the center frequency of the band was used to calculate damping factor.

Speed of Propagation

The pipes in off-shore platforms are under tension. The bottom of the pipe is attached to the ocean floor and the platform's buoyancy places tension on the pipe. The pipes in off-shore platforms are made of steel and can be several feet in diameter. Therefore there are two different factors that control the speed of propagation in the pipe: the tension and the stiffness of the material.

At low frequencies, the pipe's motion in vibration is like a string under tension. The speed of propagation is dominated by the tension. Since the pipe is dynamically acting like a string, the pipe's motion obeys the wave equation.

$$c^2 \frac{d^2 w}{dx^2} = \frac{d^2 w}{dt^2} \tag{15.5}$$

The motion of the pipe is defined as w. The speed of propagation, c, is:

$$c = \sqrt{\frac{T}{m}} \tag{15.6}$$

T is the tension and m is the mass per unit length.

At higher frequencies, the pipe's motion is less dominated by the tension and the pipe responds to vibration more like a rod. Therefore the speed of propagation is

controlled by the stiffness of the pipe, EI (the Young's modulus multiplied by the moment of inertia).

$$c^2 \frac{d^4 w}{dx^4} = -\frac{d^2 w}{dt^2} \tag{15.7}$$

Where c is defined as:

$$c = \sqrt{\frac{EI}{m}} \tag{15.8}$$

For the majority of the frequencies, the speed of propagation is a combination of these two speeds, since the pipe is never totally controlled by either the bending or the stiffness.

In the simulated data, the speed of propagation due to tension is c = 138.9 ft/s, and the speed of propagation due to stiffness is c = 291.38 ft/s. At low frequencies, added mass is added to the mass per unit length because the movement in water will create an added mass effect at the lower frequencies. At the higher frequencies, added mass is not as much of a factor. Thus, at low frequencies, a mass per unit length of 1.365 lb./ft. is used which includes an added mass term; while as higher frequencies, the mass per unit length is 0.843 lb./ft. is used, which is the dry weight of the pipe.

To accurately predict the speed of propagation for each level of decomposition in the wavelet, the speed was measured from one impulse to the next impulse. By knowing the distance the wave traveled and the time between reflections, the speed of propagation can be calculated for each level of decomposition in the wavelet. The speed of propagation found through wavelet analysis for the simulated data can be seen in Figure 88.

Note that at very low frequencies, the speed of propagation is approximately 140 ft/s, which matches the speed of propagation in a tension-dominated system. At higher speed, the speed of propagation is a combination of the tension-dominated system and the stiffness-dominated system, but continues to increase towards the theoretical speed of propagation of ~290 ft/s.

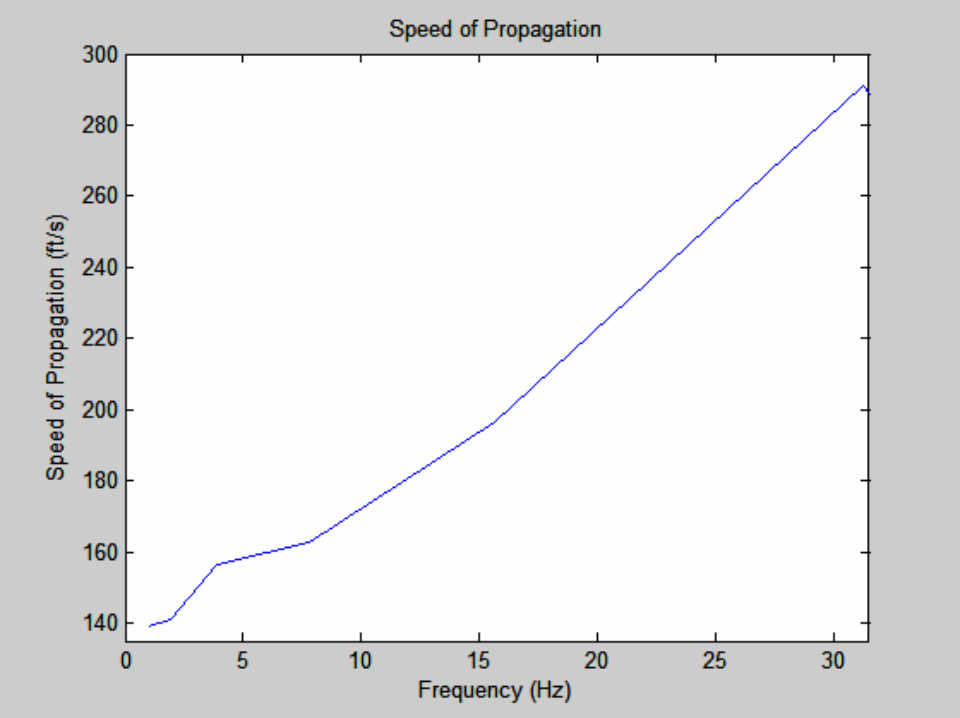

Figure 88 – Speed of propagation in the pipe as predicted using wavelet analysis.

As the wave packet travels down the pipe, the higher frequencies have a faster speed of propagation, and therefore travel faster than the lower frequencies. When looking at the wave packet after it has traveled the length of the pipe, reflected off the end, and returned to the accelerometer near the impact, the higher frequencies will return faster than the lower frequencies.

Figure 89 shows the wavelet decomposition of the time series. The different time series represent different frequency bands of the returning signal. The upper time series are the faster returning high frequency waves, whereas the lower time series are the lower frequency waves. The first wave packet is the signal as it comes from the impact hammer and has not had time to disperse. The ovals are around the reflection of the wave packet in its return to the accelerometer. The different frequencies return at different times, meaning the speed of propagation for each is different.

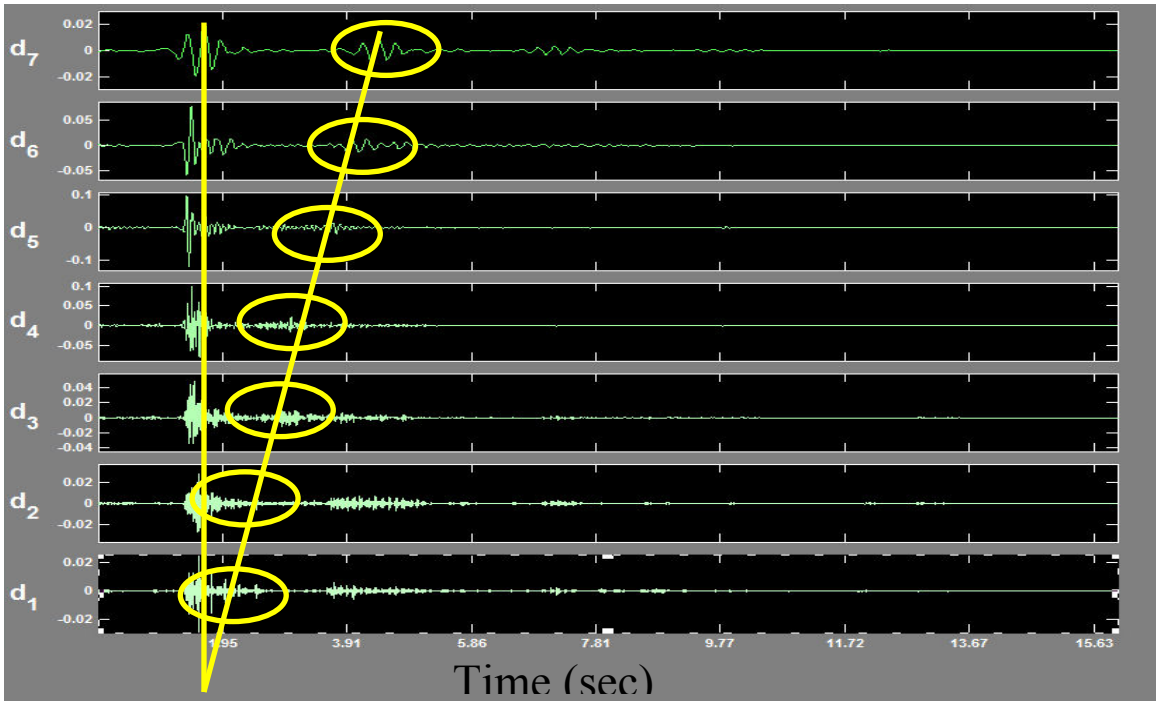

Figure 89 – Wavelet time series showing the difference in the speed of the wavelet packets for different frequencies

Wavelet Choice

For the damping calculation, energy must be preserved in each frequency range. Parseval's Theorem states that for an ortho-normal transform, the energy in the time signal is the same as the energy in the spectrum. Since Parseval's Theorem applies to any orthogonal transformation, then the energy of the wavelet coefficients will be the same as the energy of the signal as long as you use ortho-normal wavelets. For this experiment, multiple Daubechies filters were used. Figure 90 shows the two wavelets most commonly used in this experiment, the Daubechies 8 and Daubechies 16 scaling functions, which are both ortho-normal,[Strang and Nyuyen 1997] and [Misti et al. 1996].

Daubechie's filters were ideal for the impact data because the physical features are characteristics of a dispersive wave. The high-frequency waves will move to the front of the wave packet and the slower-low frequency waves will move to the back of the wave packet.

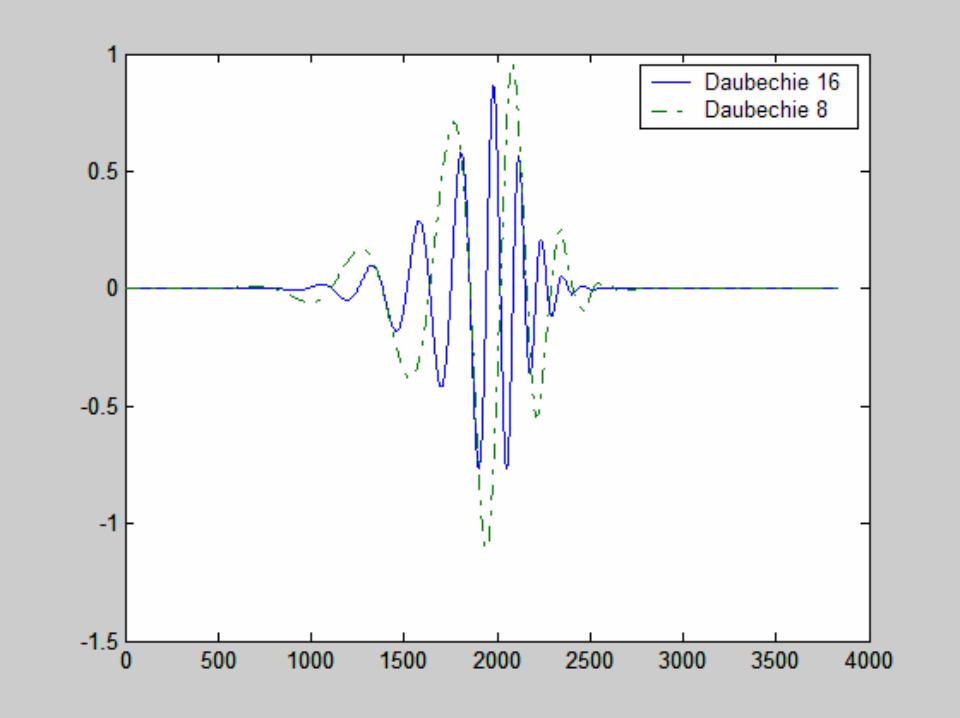

Figure 90 – Daubechie wavelet filters

Levels of Decomposition

The impact hammer only inputs energy into the system over a certain range of frequencies, dependant on the size of the hammer. Damping coefficients can only be calculated in the frequency ranges with energy from the impact hammer. Choosing the correct number of levels for the wavelet analysis is important, such that every frequency has energy.

By looking at the Fourier spectrum of the data before analyzing the data, the number of levels of decomposition can be determined. Each level has a frequency band that ranges from:

$$f = \frac{F_s}{2^n} \sim \frac{F_s}{2^{n+1}} \tag{15.9}$$

Thus, the number of levels of decomposition should be chosen such that only levels with energy will be used in the calculation.

In Figure 91, the Fourier spectrum of an impact from the Lake Seneca test is shown. Seven levels of decomposition were used in the analysis of this data; therefore the lowest level of decomposition is from 2 Hz to 4 Hz. Also in Figure 91, the energy is seen

to die out at the higher frequency. Therefore the highest level of decomposition that is usable to determine damping factors is the 16 to 32 Hz range.

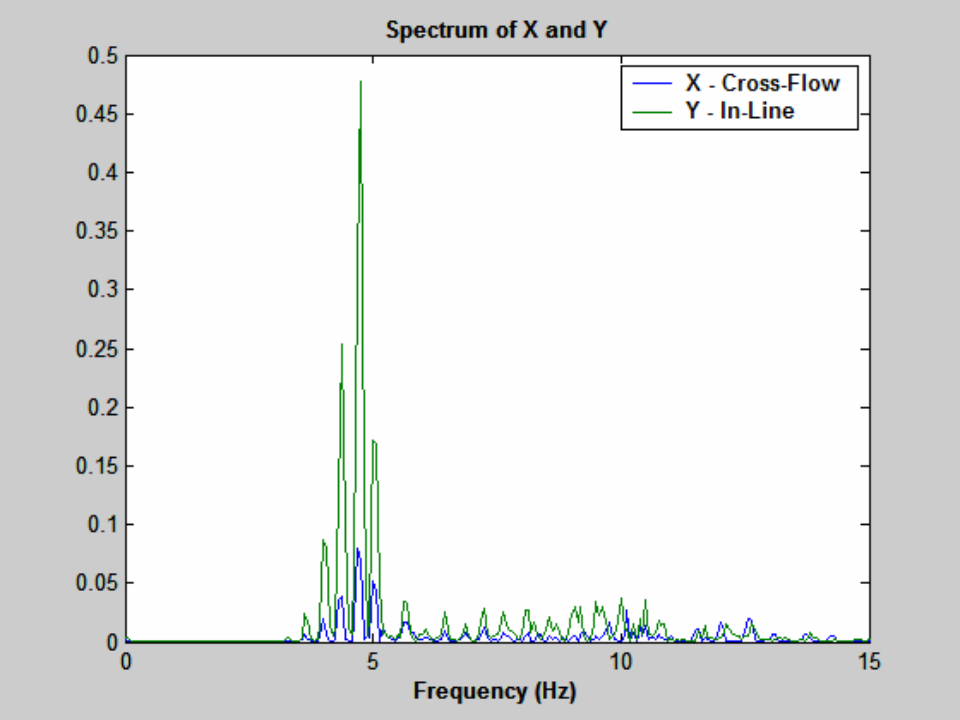

Figure 91 – Spectrum of impact

At 5 Hz, the speed of propagation is approximately 150 Hz. The length that the wave is traveling from one impact to another is approximately 400 ft. Therefore, the fundamental frequency is:

$$f_1 \approx \frac{150\,{}^{ft}\!/\!_{s}}{400\,ft} = 0.375Hz \qquad (15.10)$$

The spectrum in Figure 91 contains a large number of peaks that are approximately 0.35 Hz apart; this is consistent with the theoretical calculation.

Results

Two different sets of data were used for the analysis. First, the simulated data was used to correlate the experimental results to the known results. The energy was calculated at each frequency for each reflection. Then consecutive reflections, such as the first and second reflection, were used to calculate the damping. After the method was proved using the known data, the results were used to analyze the experimental data from the Lake Seneca testing.

The damping factors from the simulated data were estimated using a VIV prediction program supplied by Technip, and are still water damping coefficients.

$$\zeta = 4.1788\omega^{-0.3987} \qquad (15.11)$$

Different orders of Daubechies filters were used to estimate the wavelets. The lower-order Daubechies filters, such as 4 and 8, gave good correlation at low frequencies, but at higher frequencies the estimate of the damping factors was low. At higher frequencies (~30 Hz) the lower-order filters did not approximate the data well. The results, using the Daubechies 8 filter, are seen in Figure 92.

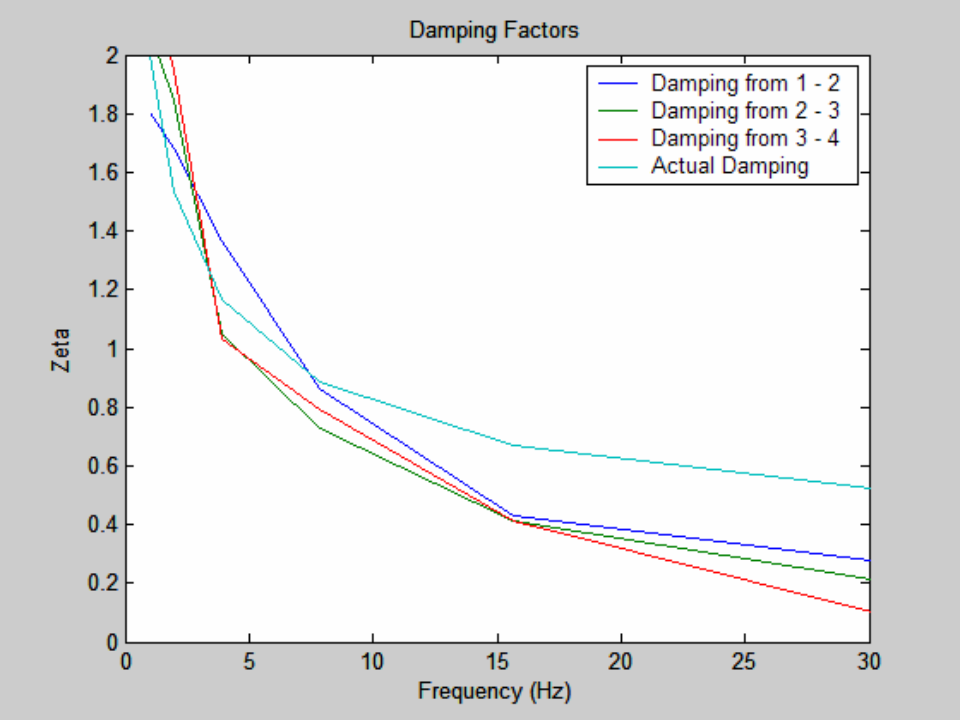

Figure 92 –Damping coefficients calculated using wavelet analysis from simulated data using a Daubechies 8 filter

Higher-order Daubechies filters, such as 16 or 20, gave results similar to those of other filters at the low frequencies, but more accurately predicted the damping factors at higher frequencies. The Daubechies 16 filter was found to give the best results. This is seen in Figure 93.

Figure 92 and Figure 93 use the data from the simulation. The line representing the "Actual Damping" is the damping that was used in this simulation and calculated using Shear7. The other lines represent the damping as calculated from the first bounce to

the second bounce, or the second bounce to the third bounce, or the third bounce to the fourth bounce.

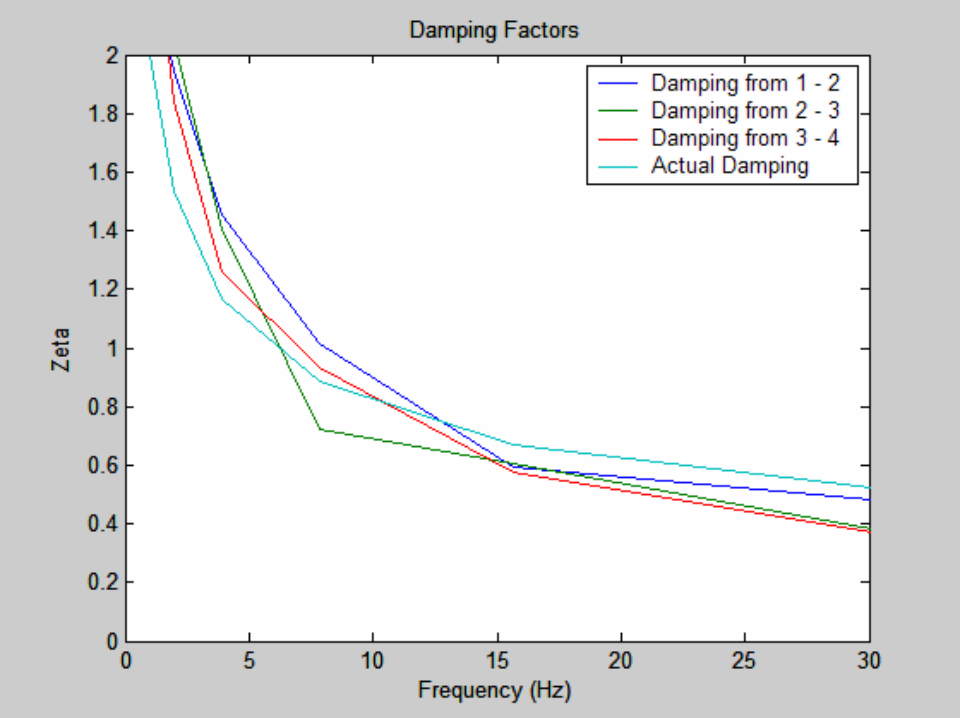

Figure 93 – Damping coefficients calculated using wavelet analysis from simulated data using a Daubechies 16 filter

Damping coefficients were only calculated for approximately 1 Hz to 32 Hz, because the impact data did not create critical amounts of energy outside of these frequency ranges. Therefore, no speed of propagation or damping factors could be calculated for those frequency ranges. The range of energy can be seen in the spectrum in Figure 91.

The frequency's band of the energy is controlled by the size of the impact hammer. The heavier the impact hammer, the lower the frequencies of the energy in the system. Also, the stiffness of the surface impacting the pipe can affect the frequencies. The lower the stiffness of the impact surface, (or the softer the impact surface) the lower the frequencies will be.

In Figure 94, the actual signal from the Lake Seneca impact testing can be seen. When the measured impact data in Figure 94 and the synthesized impact data in Figure 87 are compared, the high frequency noise is greater in Figure 94. This high-frequency

noise obscures the reflection in the data. For comparison, the synthesized data has a clear impact and each of the reflections is clear.

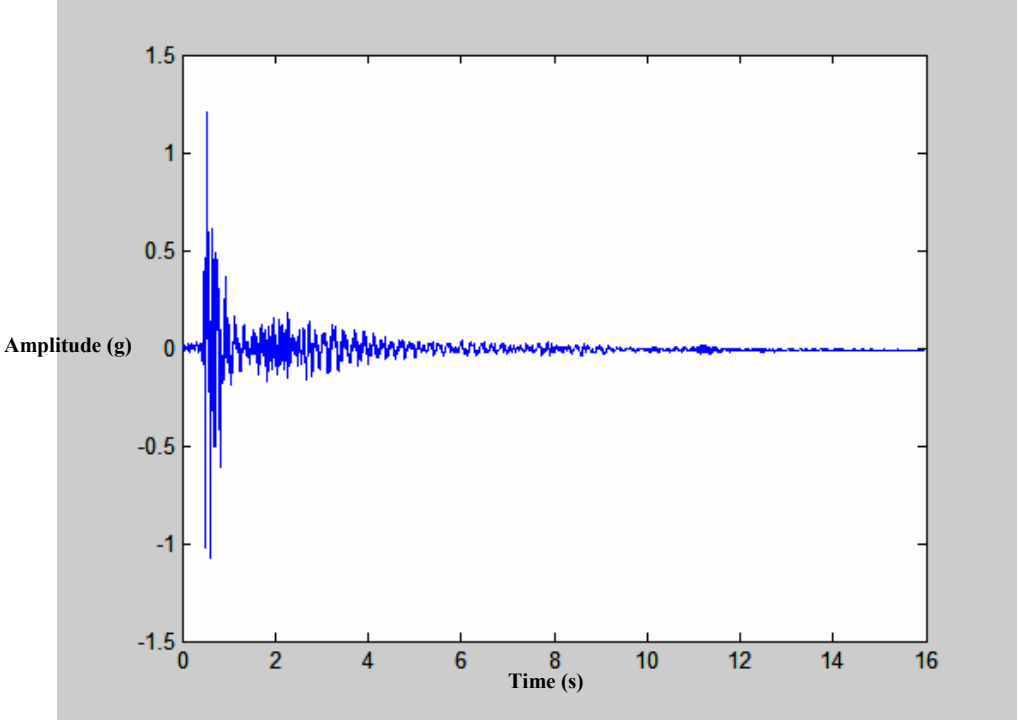

Figure 94 – Time series of impact from the accelerometer at Lake Seneca.

Figure 95 shows the seven level wavelet decomposition using a Daubechies 16 filter. The reflections become very clear at the lower frequencies once the signal has been decomposed into its wavelet coefficients. These clear reflections make the speed of sound easy to calculate.

Once the speed of propagation is established for each frequency range, the size of each packet can also be found. Establishing the correct width of the packet in the frequency range is critical since the energy for each packet must be calculated separately. For the damping calculations to be accurate, no energy from one packet can be confused with that from another packet.

In comparison, Figure 96 shows the wavelet decomposition of the synthesized signal. At the higher frequencies, the noise level is much lower; therefore the signals reflections can be seen more clearly at the higher frequencies.

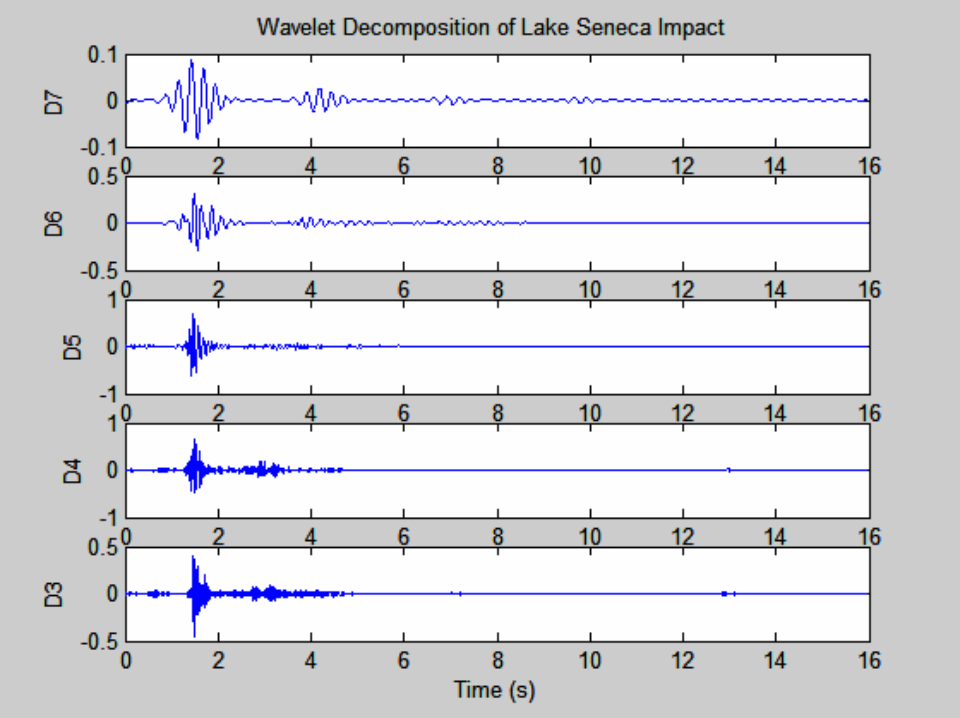

Figure 95 – Wavelet decomposition of the Lake Seneca impact experiment

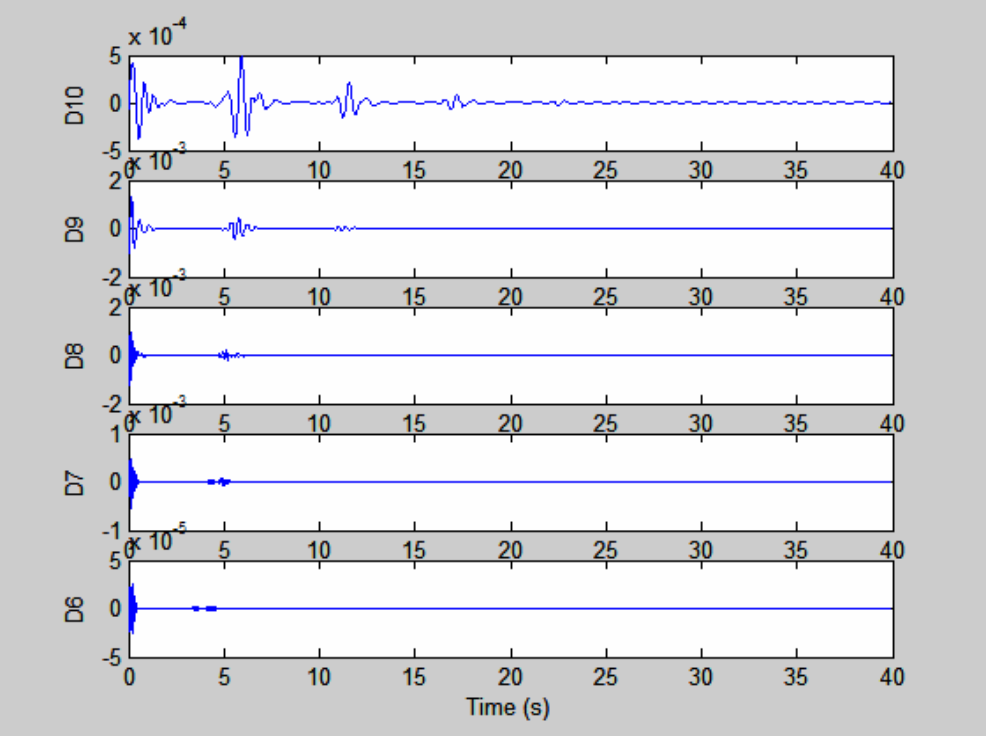

Figure 96 – Wavelet decomposition of the synthesized data.

The damping factors from the Lake Seneca testing are shown in Figure 97. The damping factors, from reflection one to reflection two, are similar to the simulated data.

The damping from two to three and from three to four can be seen to be skewed. This is most likely due to the low signal-to-noise ratio for these later reflections. The signal-to-noise ratio at the higher frequencies does not allow for accurate estimation of the energy content; thus the damping factors are inaccurate with the high signal-to-noise ratio. If a larger impact were possible at these frequency ranges, it could be possible to extract these damping factors, but with the current amplitude of vibration, the signal-to-noise ratio is too high.

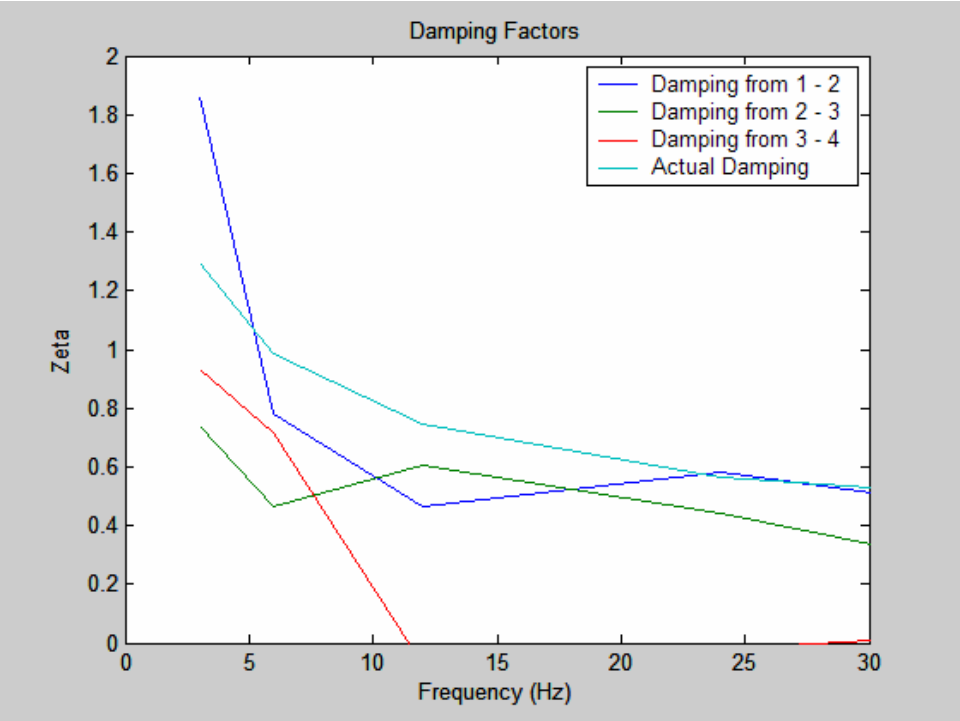

Figure 97 – Damping factors from the Lake Seneca experiment using wavelet analysis

During the Lake Seneca testing, multiple impacts were done. The damping factors from the different impacts were averaged. Averaging is commonly used in signal processing to reduce the impact of noise. Since the impacts were not all perfectly uniform and things such as the wave or current condition change between the various impacts, averaging helps to remove any anomalies in the data. The results are in Figure 98.

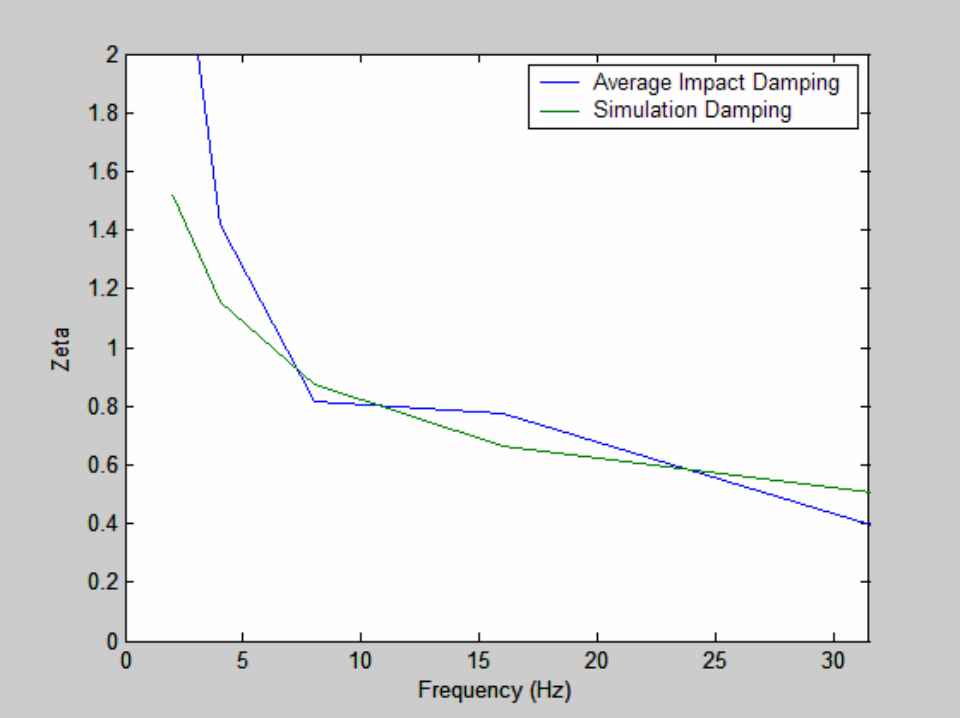

Figure 98 – Average damping coefficients from the Lake Seneca experiment using wavelet analysis

Conclusions

Using wavelets to decompose the signals into different frequency bins allows for the calculation of frequency-dependant damping factors. The speed of propagation can be extracted for each set of frequencies. Using the speed of propagation and the energy contained in each set of frequencies, the damping factors can be extracted.

Using data with low noise content, such as the synthesized data shown here, multiple reflections can be used to calculate damping factors with good correlation between the reflections' energy. This data can be correlated to the known values of damping in the system.

When using the data taken at Lake Seneca, the noise can be larger than the later reflections at the higher frequencies. Only the first and second reflections have enough energy to extract damping factors. Using averaging improves the estimates of damping in these cases with high-noise content and inconsistent inputs.

Appendix F: Impedance of a String

When considering the data from the Lake Seneca and the Gulf Stream tests, the third harmonic has a significant contribution to the spectra and the fatigue life. This analysis looks at the impedance of finite and infinite strings at resonant and non-resonant conditions.

The mechanical impedance is defined as the ratio of the force to the velocity.

$$\vec{Z} = \frac{\vec{F}(x,t)}{\vec{v}(x,t)} \tag{15.12}$$

Governing Equations

At low frequencies the pipe is tension dominated and reacts like a string. Therefore, it must obey the wave equation.

$$\frac{\partial^2 u}{\partial t^2} = c^2 \frac{\partial^2 x}{\partial t^2} \tag{15.13}$$

where c is the speed of propagation:

$$c = f\lambda = \frac{f}{k} = \sqrt{\frac{T}{m}} \tag{15.14}$$

and k is the wave number:

$$k = \frac{1}{\lambda} = 2\pi f \sqrt{\frac{m}{T}} = \frac{2\pi f}{c} \tag{15.15}$$

Infinite String

Taking the case of an infinite string that goes from negative infinity to positive infinity, with a point source at x = 0, such that:

$$F(t) = Fe^{j\omega t} \quad \text{at } x = 0 \tag{15.16}$$

Since the input is a sinusoidal function, the displacement of the rise is going to be a sinusoidal function with amplitude A:

$$y(x,t) = Ae^{j(\omega t - kx)} \tag{15.17}$$

The velocity is the first derivative in time on the displacement:

$$v(x,t) = \frac{\partial y}{\partial t} = \frac{1}{2} jA\omega e^{j(\omega t - kx)} \tag{15.18}$$

The force in the transverse direction is equal to:

$$F_y = -T\frac{\partial y}{\partial x} \text{ at } x = 0 \tag{15.19}$$

Mechanical impedance is defined as the force divided by the velocity of a particle. Therefore the mechanical impedance, Z, is:

$$Z_1 = \frac{F(x,t)}{v(x,t)} = \frac{\frac{1}{2}jTAke^{j(\omega t - kx)}}{\frac{1}{2}jA\omega e^{j(\omega t - kx)}} = \frac{Tk}{\omega} = \frac{T}{c} = mc \tag{15.20}$$

For the third harmonic, the frequency is three times the frequency of the first harmonic.

$$\omega_3 = 3\omega \tag{15.21}$$

Thus the velocity is:

$$v(x,t) = \frac{\partial y}{\partial t} = \frac{3}{2}jA\omega e^{j(3\omega t - kx)} \tag{15.22}$$

And the mechanical impedance is:

$$Z_3 = \frac{F(x,t)}{v(x,t)} = \frac{\frac{3}{2}jTAke^{j(\omega t - kx)}}{\frac{3}{2}jA\omega e^{j(\omega t - kx)}} = \frac{Tk}{\omega} = \frac{T}{c} = mc \tag{15.23}$$

The ratio of the mechanical impedance at the third harmonic to the mechanical impedance is:

$$\frac{Z_3}{Z_1} = \frac{mc}{mc} = 1 \tag{15.24}$$

Finite String

For the finite string case, a standing wave solution should be used:

$$y(x,t) = Ae^{j(\omega t - kx)} + Be^{j(\omega t + kx)} \tag{15.25}$$

With boundary conditions of:

$$y(-L,t) = y(L,t) = 0 \tag{15.26}$$

$$F_y = -T\frac{\partial y}{\partial x} \tag{15.27}$$

Using the boundary conditions to solve for the coefficients:

$$0 = Ae^{j(-kL)} + Be^{j(kL)} \tag{15.28}$$

$$F_y = Tjk\left(Ae^{j(\omega t - kx)} - Be^{j(\omega t + kx)}\right) \tag{15.29}$$

at x = 0

$$F_y = Tjk\left(A - B\right) \tag{15.30}$$

$$\begin{bmatrix} jTk & -jTk \\ e^{-jkL} & e^{jkL} \end{bmatrix}\begin{bmatrix} A \\ B \end{bmatrix} = \begin{bmatrix} F \\ 0 \end{bmatrix} \tag{15.31}$$

$$\begin{aligned} A &= \frac{-jFe^{jkL}}{Tk\left(e^{jkL} + e^{-jkL}\right)} = \frac{-jFe^{jkL}}{2Tk\cos(kL)} \\ B &= \frac{jFe^{jkL}}{Tk\left(e^{jkL} + e^{-jkL}\right)} = \frac{jFe^{jkL}}{2Tk\cos(kL)} \end{aligned} \tag{15.32}$$

Thus, the displacement is:

$$\begin{aligned} y(x,t) &= \frac{-jFe^{-jkL}}{2Tk\cos(kL)}e^{j(\omega t - kx)} + \frac{jFe^{jkL}}{2Tk\cos(kL)}e^{j(\omega t + kx)} \\ &= \frac{F}{kT}\frac{\sin(k(L-x))}{\cos(kL)}e^{j\omega t} \end{aligned} \tag{15.33}$$

At resonance $\cos(kL) = 0$:

$$Z = \frac{F}{v} = \frac{-F\dfrac{\cos(k(L-x))}{\cos(kL)}e^{j\omega t}}{\dfrac{j\omega F}{kT}\dfrac{\sin(k(L-x))}{\cos(kL)}e^{j\omega t}} = \frac{-kT}{j\omega}\cot(k(L-x)) = \frac{-jmc}{\tan(k(L-x))} \tag{15.34}$$

At the center of the string, the impedance is:

$$Z_r = \frac{-jmc}{\tan(kL)} \tag{15.35}$$

Therefore the ratio of the impedance of the third harmonic to the impedance of the first harmonic is:

$$\frac{Z_{r3}}{Z_{r1}} = \frac{\dfrac{-jmc}{\tan\left(k_3L\right)}}{\dfrac{-jmc}{\tan\left(k_1L\right)}} = \frac{\tan\left(k_1L\right)}{\tan\left(k_3L\right)} = \frac{\tan\left(f_1L/c\right)}{\tan\left(f_3L/c\right)} = \frac{\tan\left(f_1L/c\right)}{\tan\left(3f_1L/c\right)} \tag{15.36}$$

$$\frac{Z_{r3}}{Z_{r1}} = \frac{\tan\left(f_1 L/c\right)}{\tan\left(3 f_1 L/c\right)} = \frac{\tan\left(UL/DcV_r\right)}{\tan\left(3UL/DcV_r\right)} = \frac{\sin\left(UL/DcV_r\right)\cos\left(3UL/DcV_r\right)}{\cos\left(UL/DcV_r\right)\sin\left(3UL/DcV_r\right)}$$
$$= \frac{\sin\left(4UL/DcV_r\right)+\sin\left(2UL/DcV_r\right)}{\sin\left(4UL/DcV_r\right)-\sin\left(2UL/DcV_r\right)} \qquad (15.37)$$

Results

The Gulf Stream test is used here as an example. The pipe has a length of 500 ft, a diameter of 1.4 in. and a speed of propagation, c, of 150 ft/s. Assume a fixed reduced velocity of 7, which was the reduced velocity found to have the maximum third harmonic response found by Jauvtis and Williamson [2004]. The current velocity was varied from 0 to 10 ft/s in increments of 0.001 ft/s. The results can be seen in Figure 99.

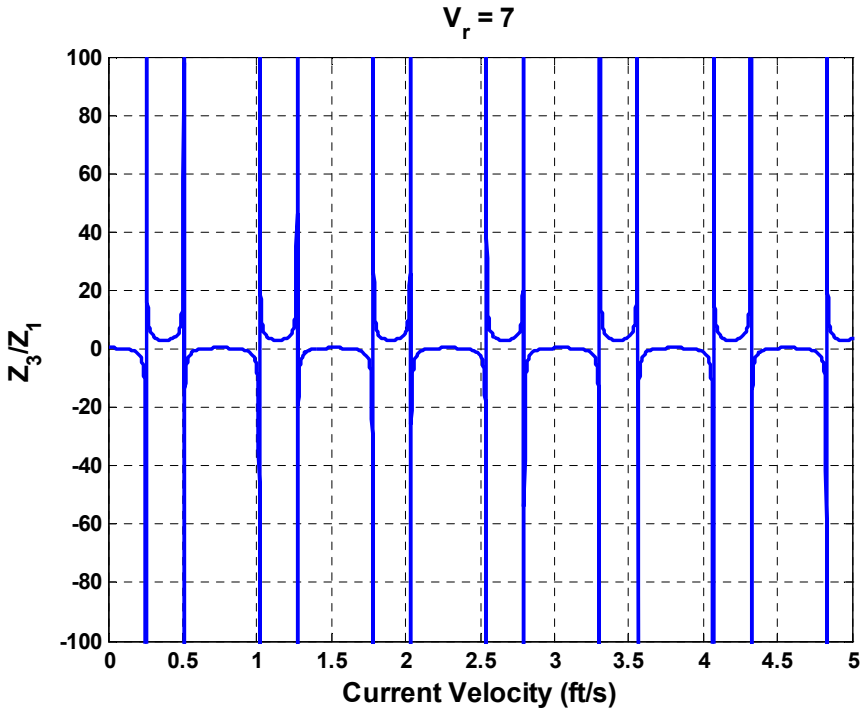

Figure 99 – Ratio of the first harmonic and the third harmonic mechanical impedance

The ratio of the impedance of the third harmonic to the impedance of the first harmonic varies from approximately three to approximately one-third. When the impedance of the third harmonic is three times the impedance of the first harmonic, the third harmonic is disadvantaged, it is still possibly for the third harmonic to exist, but

three times the force is needed to create the same velocity as the velocity of the first harmonic. When the impedance of the third harmonic is one-third of the impedance of the first harmonic, the force needed is significantly less to create the same velocity at the third harmonic.

Using the same parameters as Figure 99, but fixing the current velocity at 2 ft/s and varying the reduced velocity from 0 to 10 in increments of 0.001, Figure 100 shows that for the same current speed, the reduced velocity can largely impact the existence of higher harmonics.

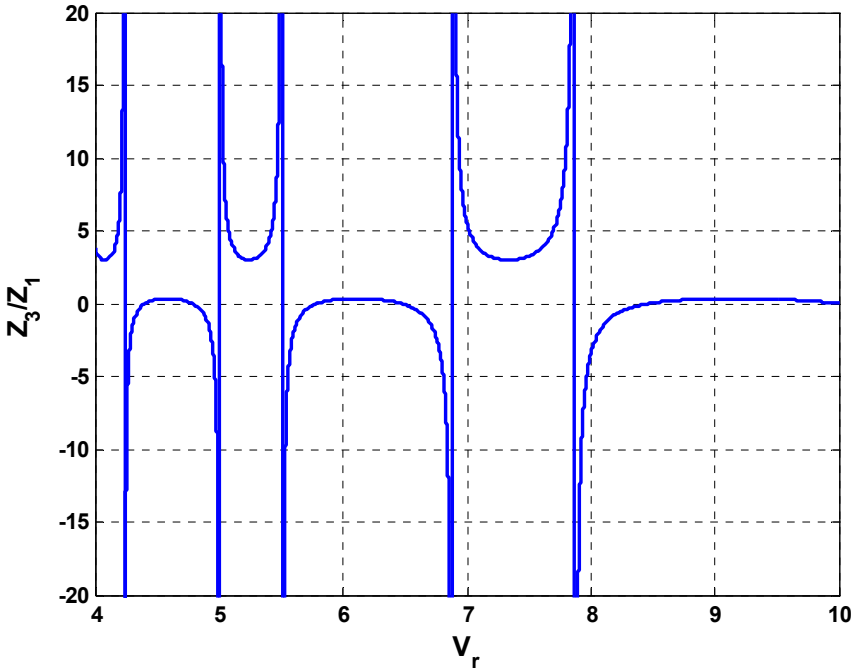

Figure 100 – The ratio of the impedance of the third harmonic to the first harmonic plotted versus the reduced velocity

Since any power-in region can have a range of reduced velocities that is controlled by the reduced velocity bandwidth for any given power-in region, there may be a subset of regions which favor or disadvantage the higher harmonic components.

Jauvtis and Williamson presented results that showed a large third harmonic response for reduced velocity, (V_{rn}), from 5 to 8 on a rigid cylinder. These two results are not mutually exclusive. Jautvis and Williamson's results show that the third harmonic forcing function exists over a particular reduced velocity range. These results show that for any given current speed, there are a set of reduced velocities for which the presence of

the third harmonic is favored, and a set of reduced velocities for which the creation of the third harmonic is disadvantaged.

Conclusions

This section demonstrated the derivation of the cases of finite and infinite string lengths with standing waves. The Lake Seneca and Gulf Stream tests fit neither the infinite string nor the finite string with standing waves cases. Instead, the test results were in between the infinite and finite string cases.

These models were also built without damping, which is an intrinsic property of the riser. The two cases derived here represent the two extreme cases, whereas the Lake Seneca and Gulf Stream tests are in between. The ratio of the two impedances will not be a constant ratio of one third, but will not have the extreme characteristics of the standing wave case either.

With the addition of damping, which is an inherent characteristic of the system, the tendency for the ratio to go to infinity and negative infinity will disappear. Instead the system will have a smoother ratio of the impedances.

Thus the Lake Seneca and the Gulf Stream tests will not exactly follow either of these extreme cases, and will instead be a combination of the two extremes. There will be regions of the reduced velocity that will favor or disadvantage the creation of strong higher harmonic components.

Appendix G: High Mode-Number Test Design

Introduction

One of the goals of this thesis was to design and execute a high mode-number experiment in VIV. Three different aspects of the test design are discussed here: sensor placement to maximize potential post-processing techniques, rotation methods for finding in-line and crossflow vibrations, and the integration of acceleration to displacement for looking at the data in post-processing.

Sensor-Placement Theory

The placement of instrumentation on a riser can be crucial to later analysis of the data. If the instruments are not placed correctly, certain types of analysis such as modal analysis are impossible. With incorrectly placed instruments, the modes could be misidentified through aliasing as other modes or could be missed entirely. The purpose of this algorithm is to find the optimal placement for instrumentation on a riser, in order to avoid these problems.

This algorithm for placement of the sensors uses assumed mode shapes. Since mode shapes are orthogonal, the dot product of any two different modes should be zero. In the case of an instrumented riser, the mode shapes are discretely sampled only at the locations of the instrumentation. If the sampling of the mode shapes is poorly chosen, then the dot product of two different modes will not be zero. This algorithm considers the dot product of all the mode shapes when discretely sampled at the specified sensor locations and tries to minimize the dot products by locating the sensors in the optimal position.

This algorithm was first shown by Karl Erik Kaasen of Marintek in Trondheim, Norway, but it further developed an analyzed below.

Mathematical Derivation

This analysis assumes that the mode shapes of the riser are known. These mode shapes can be theoretically derived or found using finite-element analysis software. The [Ω] matrix, the modal matrix, is defined such that each column represents the discrete values of a mode shape. The points at which the mode shape is sampled are determined by the

placement of the accelerometers. [Ω] is defined as an n by m matrix, where n is the number of accelerometers and m is the number of modes considered in the analysis. Taking [Ω] and pre-multiplying by the transpose of the mode shape creates the [A] matrix.

$$[A] = [\Omega]^T [\Omega] \tag{17.1}$$

In an ideal case where the orthogonal mode shapes are densely sampled and represent nearly continuous functions, the diagonal terms would be the integral of the mode shape squared; the off-diagonal terms should be approximately zero.

In practical cases, the sampling of the mode shape may not be dense enough to guarantee that the off-diagonal terms are zero. The density of the sampling of the mode shape is determined by the number and placement of the accelerometers in the pipe. When limited accelerometers are available, then the method described here seeks to minimize the off-diagonal terms of [A]. The off-diagonal terms will never be equal to zero in a practical case, because of numerical inaccuracies.

For ease of analysis, the [A] matrix can be normalized such that the diagonal terms equal one. This normalization allows for the easy comparison between the modes. [B] is a diagonal matrix, where the diagonal terms are equal to the square root of the diagonal terms of [A]; all other entries in [B] are zero. The matrix [C] defined in equation (3) is a normalized version of [A].

$$[B] = \begin{bmatrix} \sqrt{A_{11}} & & & \\ & \sqrt{A_{22}} & & \\ & & \searrow & \\ & & & \sqrt{A_{nn}} \end{bmatrix} \tag{17.2}$$

$$[C] = [B]^{-1} [A] [B]^{-1} \tag{17.3}$$

The off-diagonal terms of the [C] matrix indicate whether the accelerometer configuration is appropriate for the number of modes and the mode shapes that were used. The diagonal terms are equal to one. The diagonal terms represent the approximate integrals of the original mode shapes squared, and then normalized to one. The off-

diagonal terms represent the dot product of every possible combination of two different mode shapes.

For sinusoidal mode shapes, if the accelerometers are evenly spaced and the mode shapes are orthogonal, then little spatial aliasing occurs for mode numbers less than or equal to the number of accelerometers. The [C] matrix would approximately equal the identity matrix, with off-diagonal terms equaling numeric errors. The off-diagonal terms in this case are numerical errors caused by using a discrete sampling of a continuous function.

When using this methodology for the accelerometer placement, all modes less than the greatest mode of interest must be included in the calculation. Even if the lower modes are not considered to be of great importance to the testing, they must be included. The reasoning behind the inclusion is the higher-order modes could be confused for the lower-order modes if spatial aliasing occurs. If the lower-order modes were not included then the aliasing would go undetected by this method.

Examples of Accelerometer Placement

Three examples are shown below which exemplify three potential problems that can be found using this analysis, the ideal case, a case of aliasing and a case of double roots. The riser used in the following examples was modeled after the pipe used in the Lake Seneca Experiment. The pipe is 400 ft. long with a diameter of 1.31 inches with 401 nodes; therefore the nodes were located one foot apart. For further information about the structure, refer to the Shear7 data file in Appendix B.

Figure 101 shows the assumed mode shapes that were generated by Shear7. Modes 1 to 5 are plotted.

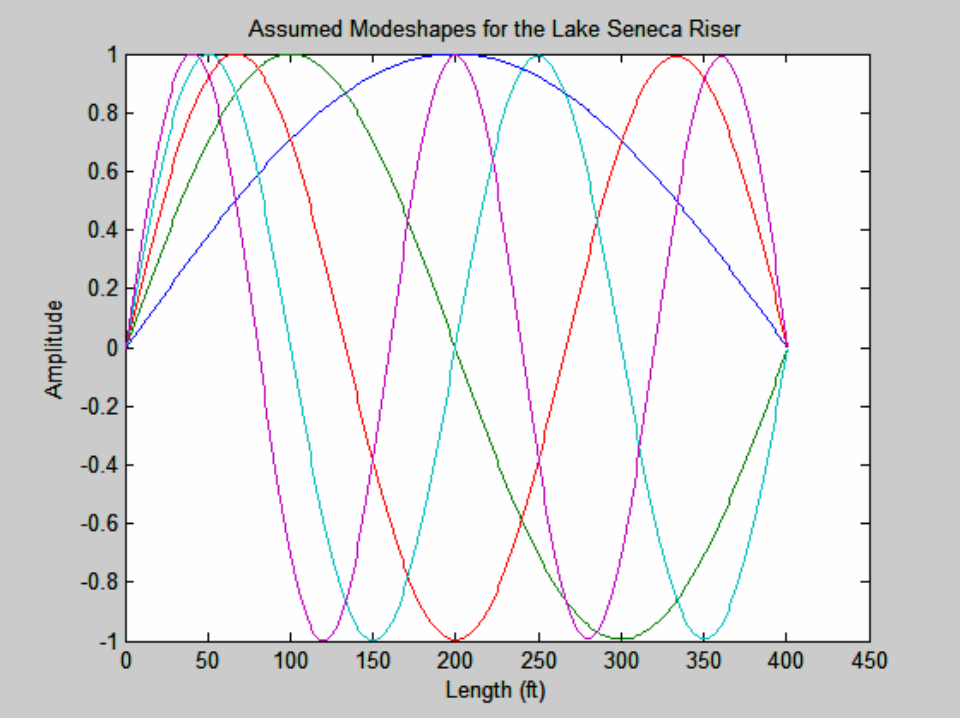

Figure 101 – 1st to 5th modes created by SHEAR7

An Ideal Case

In this case twenty-four accelerometers were evenly spaced, with an additional two virtual accelerometers at each end, which report zero response due to the boundary condition. In the non-dimensional coordinate x/L, the accelerometers are located at integer multiples of 0.04 for n equal to 0 to 25.

This case is ideal, because the number of modes is less than the number of accelerometers. This layout should capture the first twenty-four modes accurately. This is illustrated in Figure 102. Figure 102(a) is a three dimensional plot of the matrix [C]. The horizontal axes are mode numbers from 1 to 24 and the vertical axis is the value [C]. The off-diagonal terms are near zero. Figure 102(b) is a contour plot of the information in [C]. The off diagonal terms are less than 1.0% of the diagonal. The axes in the figure are the mode numbers.

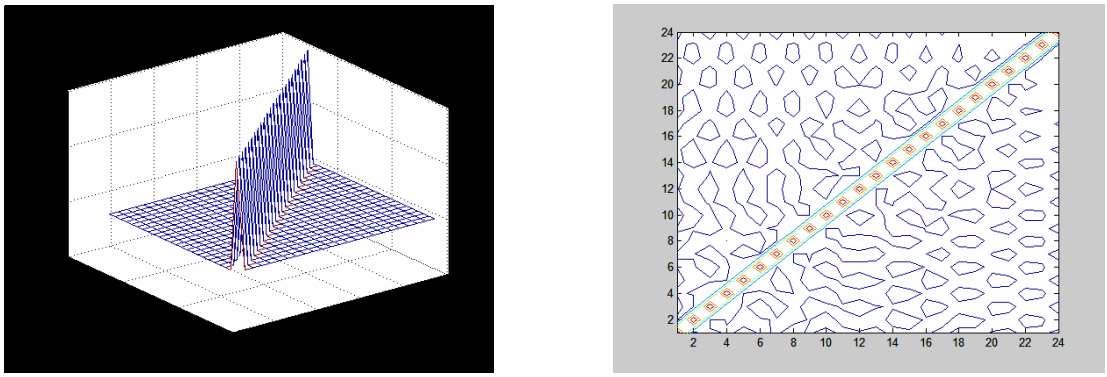

Figure 102 - Visualization of the [C] matrix for the ideal case (a) 3D-plot; (b) contour view

A Case Where Modes Can Be Spatially Aliased:

The exact same placement used in the ideal case was used in a case where the modes that were included were from 1 to 30. Spatial aliasing occurs when two modes can be mistaken for each other. This manifests itself as a transpose diagonal, with a magnitude sometimes greater than ninety percent of the diagonal values. In this case, two modes appear similar with the accelerometer located as described above, allowing spatial aliasing to occur.

Mathematically, aliasing is when one sampled mode shape appears very close to another mode shape when sampled at a discrete number of points. This leads to a significant dot product and a large corresponding off-diagonal term.

When the [C] matrix is calculated, the transverse diagonal can be seen. In this example the largest off-diagonal term occurs at the dot product of modes 25 and 26 (Figure 103).

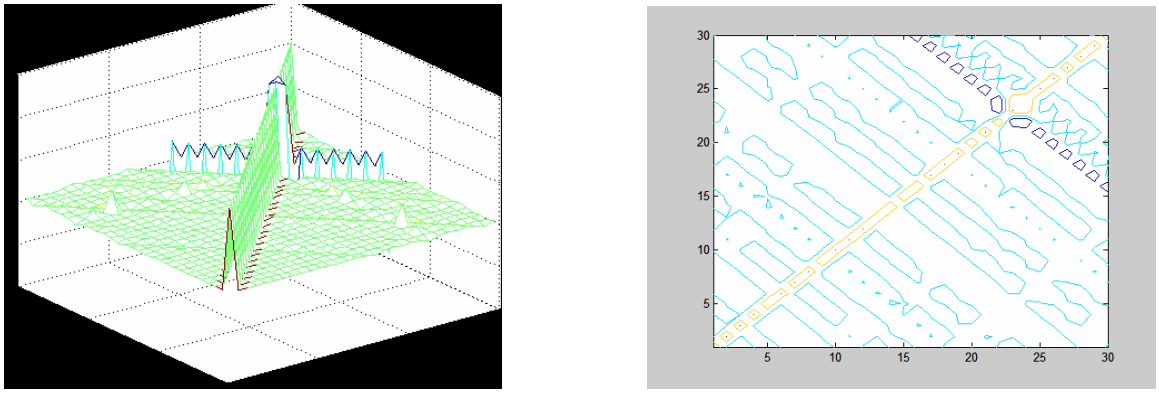

Figure 103 - Visualization of a case with spatial aliasing (a) 3-D plot; (b) contour plot

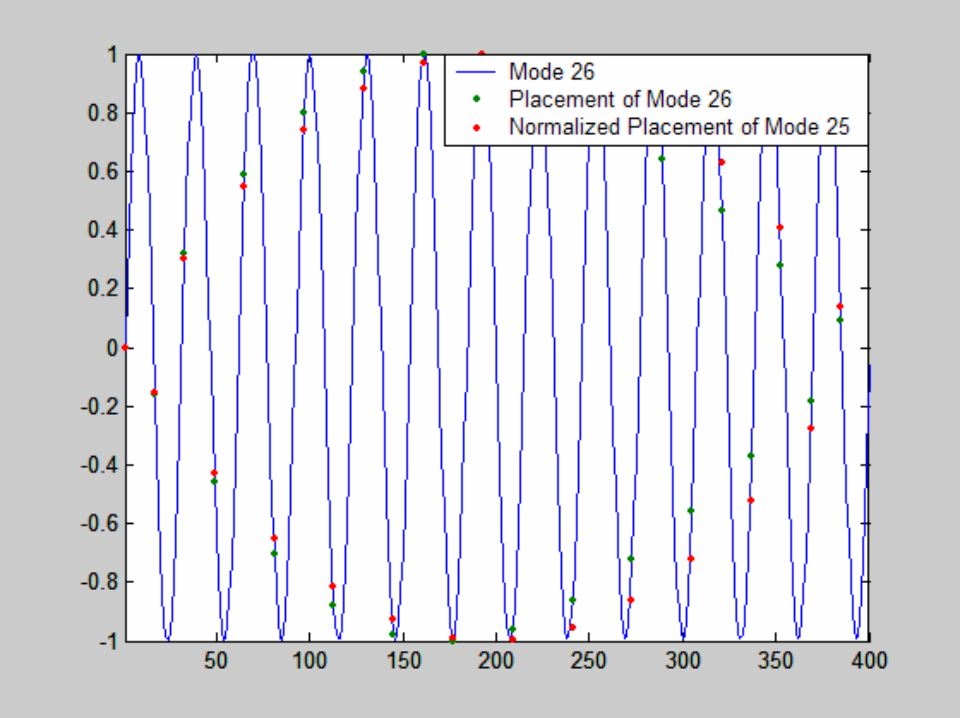

Figure 104 – Mode shape overlaid with accelerometer spacing

In Figure 104, Mode 26 is plotted. The green dots represent the locations of the accelerometers for mode 26. The red dots represent the placement of the accelerometers for mode 25. The dot product of the two modes shown will always be a positive number. Therefore, when the [C] matrix is calculated, there will be off-diagonal terms associated with mode 26 that will not be zero. These two modes could be confused for one another if this accelerometer placement were used.

A Case of Double Roots

For the Lake Seneca experiment, a dynamics model was created with a 400 ft pipe with a cylindrical weight on the end. [Vandiver et al. 2005] The solution to this dynamic model is a transcendental function. In a transcendental natural frequency equation, the two sides of the equation are equal only at the natural frequencies of the system.

For this case, the fifth and sixth modes of the solution, the natural frequencies, are very close. This results in two nearly identical mode shapes. In Figure 105, the two sides of the transcendental function are plotted. The intersections are shown by the red circles, which indicate natural frequencies. Also the mode shapes, drawn in the figure on the right, show that the fifth and sixth modes appear to be identical.

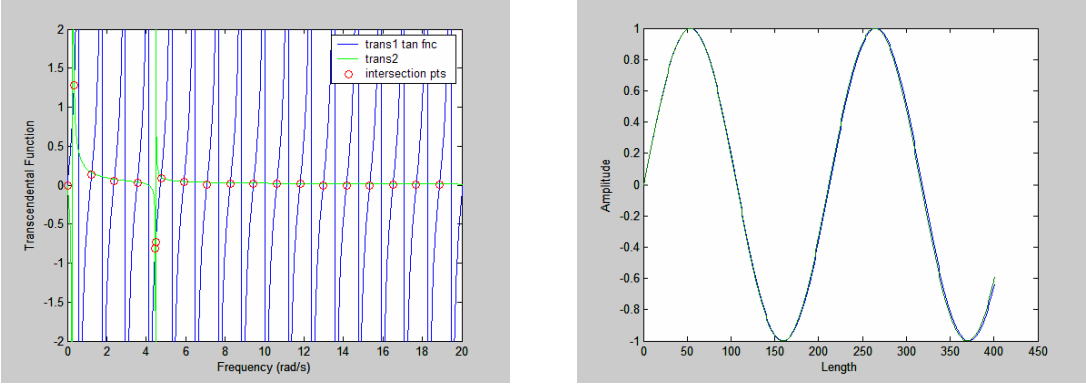

Figure 105 – (a) Results of the transcendental function; (b) Resulting mode shapes for the double root

If two natural frequencies are similar, as is the case when a double root occurs, then the two mode shapes are linearly dependent and will be indistinguishable. Instead of a transposed diagonal event in the [C] matrix, only the two modes involved in the double root will be affected. This will cause only two off-diagonal points to be raised. Since mode shapes with double roots have consecutive mode numbers, the off-diagonal terms will be next to the diagonal terms. In the contour plot below, this looks as if there is a plateau on the contour plot. (Figure 106)

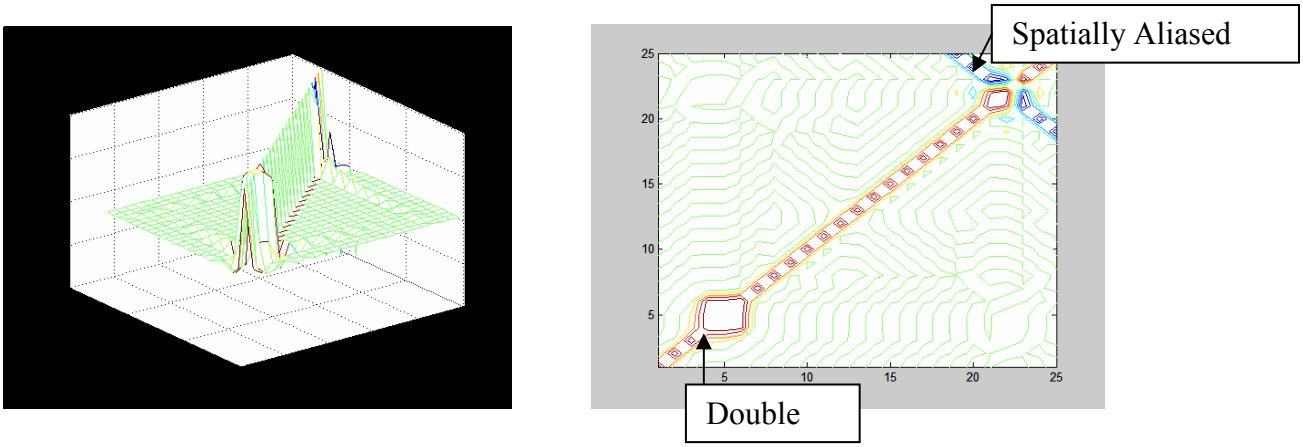

Figure 106 - The [C] matrix for the case of the double root (a) 3-D plot; (b) contour plot

No practical solution exists for the case of the double root, because the two mode shapes are virtually indistinguishable. The same case was run with 401 uniformly spaced accelerometers. The results, still had an off-diagonal term of 99.9% and a similar plateau in the figure. (Figure 107)

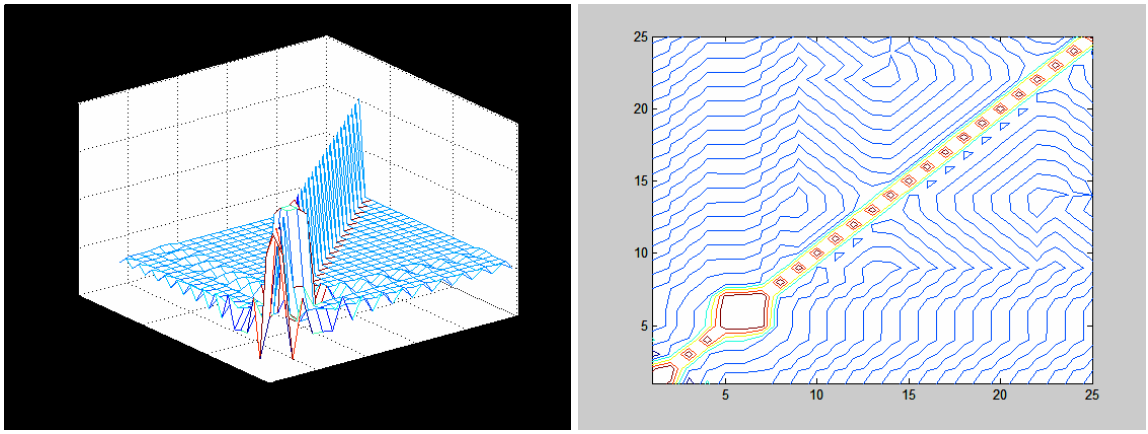

Figure 107 - Visualization of the [C] matrix showing the double root with 401 nodes

Accelerometer Placement for the Lake Seneca Test

In the case of the Lake Seneca test, twenty-four tri-axial accelerometers were to be placed in the pipe, with two additional sets: one at the top to measure tilt, and the other at the bottom to measure the movement of the weight. The pipe is 401 ft long with a weight at the bottom. The top end was fixed to the boat, and can be considered fixed. The weight at the bottom tensions the pipe; the weight responds dynamically and affects the natural frequencies. The mode shapes used in this analysis were derived from the transcendental model that took the dynamics of the bottom weight into consideration. The pitching motion of the bottom weight is especially important to model correctly.

Finding the natural frequencies of this system in which the lower boundary is not fixed requires the solution of a transcendental function. Once the natural frequencies have been found, then the mode shapes follow. In this system, the mode shapes are approximately sinusoidal with one end fixed and one end matching the moving boundary condition created by the weight. In the limit of very high mode numbers, the inertia of the weight is great enough as to make the lower end fixed, resulting in fixed-fixed sinusoidal mode shapes.

In choosing the placement of the accelerometers the pendulum modes and the first twenty-four spatial modes were considered. An additional constraint was placed on the accelerometer placement: one accelerometer was required to be within the last seven to ten feet of the lower pipe end. This was desirable, so as to be able to estimate the location of the node nearest to the weight at the bottom.

An optimization algorithm was used to identify the accelerometer layout with the lowest off-diagonal terms. To optimize the accelerometer placement, the accelerometers were laid out evenly along the pipe. Then each accelerometer was moved individually to all possible locations between the starting positions of the accelerometers above and below it. At each position the [C] matrix and the off-diagonal terms were calculated. If a better fit was found, then that accelerometer was moved to the new position and the next another accelerometer was moved. This iteration algorithm was run a number of times to ensure optimal placement. Usually, the optimal placement was determined within four iterations of the initial guess.

This algorithm is dependent upon the initial guess. If a poor initial guess is given, then the results are potentially poor. For the Lake Seneca test, more than 30 different initial conditions were given. Also, the order in which the accelerometers are moved can give different results, though the resultant accelerometer placement and the off-diagonal terms tend to have very small differences.

Additionally in the case of the double root, this optimization algorithm attempts to place the accelerometers as close together as possible so that it can distinguish the two modes. This is far from the optimal solution since these two modes are almost identical and this placement is done at the expense of larger errors in distinguishing other modes. The strategy used for this experiment design is to vary the configuration of the bottom weight to avoid double roots.

An example solution which includes modes one to twenty-four is shown below. The number of accelerometers was equal to the number of modes, and a nearly linear spacing was found. This ensures good quality of mode identification for cross-flow modes between 1 and 24. The spacing, which was found, is shown below.

Accelerometer Placement:

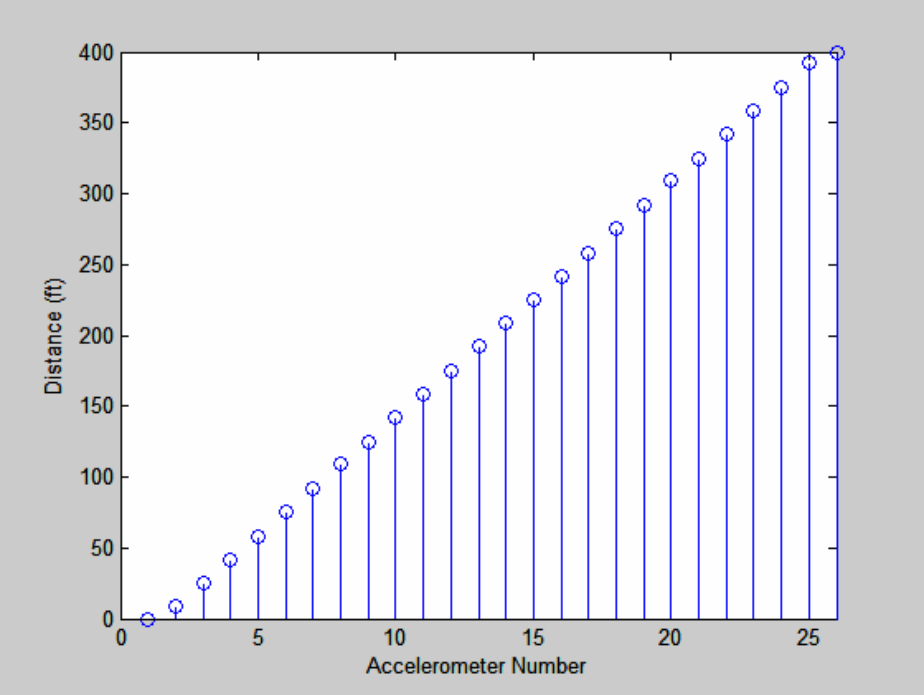

Figure 108 - Accelerometer placement for the Lake Seneca experiement

The placement of the accelerometers is as follows (given in feet from one end):

x = 0, 9, 25, 42, 58, 75, 92, 109, 125, 142, 158, 175, 192,

209, 225, 242, 258, 275, 292, 309, 325, 342, 358, 375, 392, 400 ft.

Using the above placement, the following visualization of the [C] matrix can be seen in Figure 109. Using modes 1 through 24, the maximum off-diagonal term is 4.6% of the normalized center values.

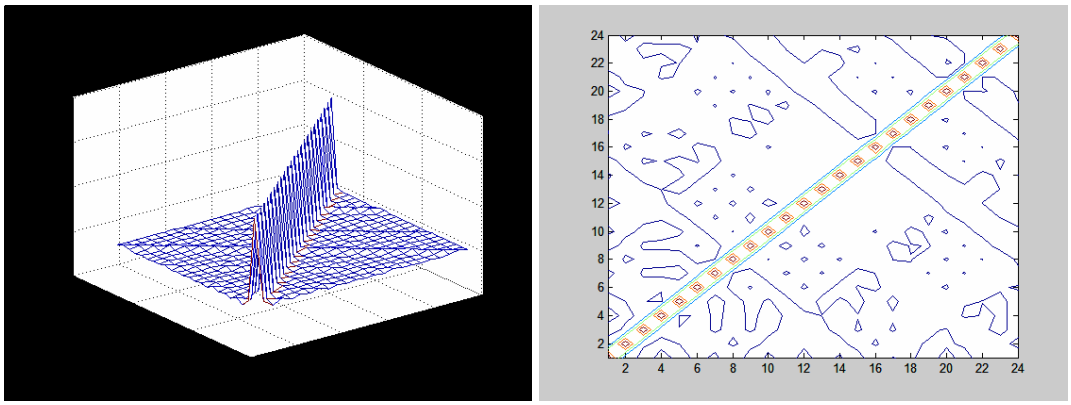

Figure 109 - The [C] matrix for the Lake Seneca experiment using modes 1 to 24 (a) 3-D plot; (b) contour plot

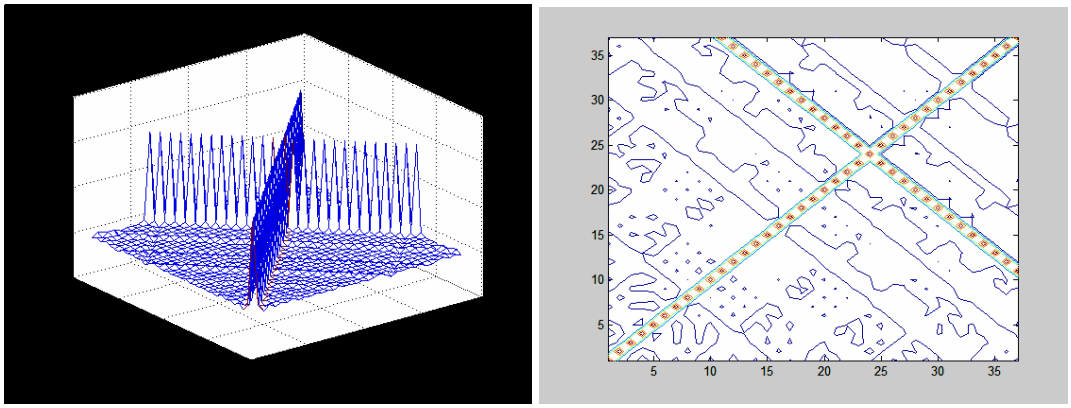

Figure 110 - The [C] matrix for the Lake Seneca experiment using modes 1 to 27 (a) 3-D plot; (b) contour plot

Attempts to identify higher modes than the number of sensors can introduce additional error. Figure 9 shows an example that used the same spacing as in the previous case. The [C] matrix values are shown for modes 1 through 37. Mode 25 is shown to be especially problematic for this particular accelerometer spacing. The maximum off-diagonal value is 99.6% of the normalized center values. In this case, mode twenty-five could potentially be mistaken for another mode if the assumed mode shapes are correct.

Other than the potential aliasing of the twenty-fifth mode, the accelerometer placement produces good results for all other modes. The smallest spacing between any two accelerometers is sixteen feet. The half wavelength of the twenty-fifth mode is sixteen feet. Therefore for mode 25, many of the accelerometers are located at nodes,

which leads to considerable error and would make mode twenty-five very difficult to detect. Though it should be noted that for modes above the twenty-fifth mode, no two accelerometers are located in any one wavelength and yet the off diagonal terms are still quite small.

Modal Participation

One method to determine whether the accelerometer placement will be effective in later analysis is to use each placement to compute a trial set of modal participation factors. Modal participation is a methodology that expresses the response, y, as the superposition of the systems mode shapes, [Ω].

$$y(x,t) = \sum_{r=1}^{\infty} \left(\Omega_r(x) P_r(t) \right) \tag{17.4}$$

In actuality, there will be other factors influencing y(x,t) such as noise in the system and error.

$$y(x_j,t) = \sum_{i=m}^{N} P(t) * \Omega(x_j) + E(x_j) \tag{17.5}$$

Therefore in Matrix form:

$$\{y\} = [\Omega] * [P] + \{E\} \tag{17.6}$$

Using minimization of least-squares error, it is possible to determine the modal participation factors from the measured responses, by applying the following equation. [Jong and Vandiver 1981]

$$[P] = \left[[\Omega]^T * [\Omega] \right]^{-1} * [\Omega]^T * [y] \tag{17.7}$$

Low-Frequency Mode Case

SHEAR7 is a program that predicts VIV response and fatigue life for risers. Given the pipe properties, SHEAR7 will calculate the natural frequencies and orthogonal mode shapes used in this analysis. SHEAR7 will also create an animation output file that will show the predicted motions on the pipe for a given current profile.

For this example, data was synthesized from the SHEAR7 animation output file. The data had 401 nodes placed along the pipe at one-foot intervals. A sheared current was used to create this example. The case indicated single-mode dominance at the 17th mode.

The total solution consisted of resonant response of the 17th mode added to the non-resonant response of all other modes from the 14th to the 20th.

Modal participation factors were computed using three different sets of accelerometer placements:

The first accelerometer placement had an accelerometer at every node. With 401 accelerometers, the closest possible solution is given. This placement results in the closest solution to true. The largest off-diagonal term was 0.2%. The Figure 111 (a) and (b) below show the [C] matrix.

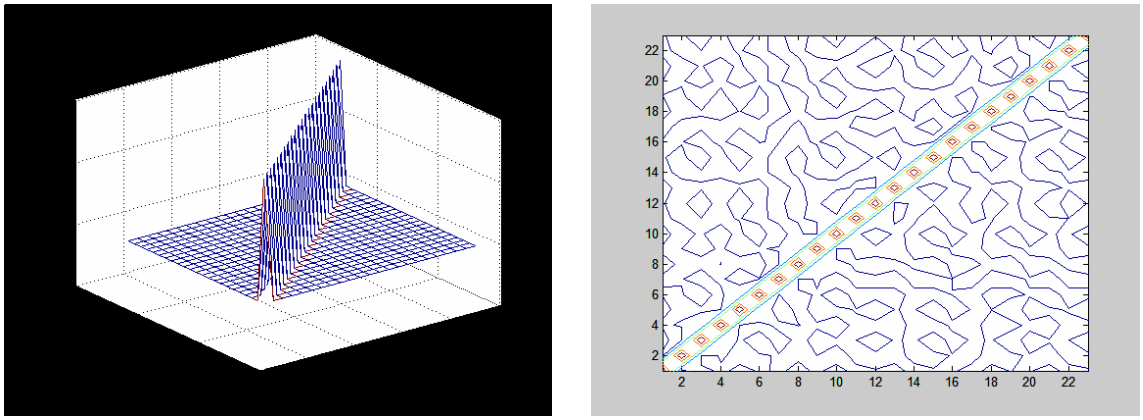

Figure 111 - The [C] matrix for the first accelerometer placement (a) 3-D plot; (b) contour plot

The second accelerometer placement that was used is the optimized solution shown in the previous section (refer to Accelerometer Placement for Lake Seneca Test), with twenty-four approximately equally spaced accelerometers and two accelerometers at the ends. This resulted in the same mode participation factors as in the case with an accelerometer at every node, even though the largest off-diagonal term of [C] was 3.9%.

Lastly, the placement of accelerometers in the third case was to show that certain accelerometer placements could create poor results even if the number of accelerometers is greater than the number of modes. For this case a non-even distribution of accelerometers was created that would spatially alias mode 16. The largest off-diagonal term was 69.7%. Figure 112 (a) and (b) below show the [C] matrix for this placement. The accelerometers were located at: 0, 9, 19, 25, 29, 39, 49, 50, 59, 69, 75, 79, 89, 100, 125, 150, 175, 200, 225, 250, 275, 300, 325, 350, 375, 400 ft.

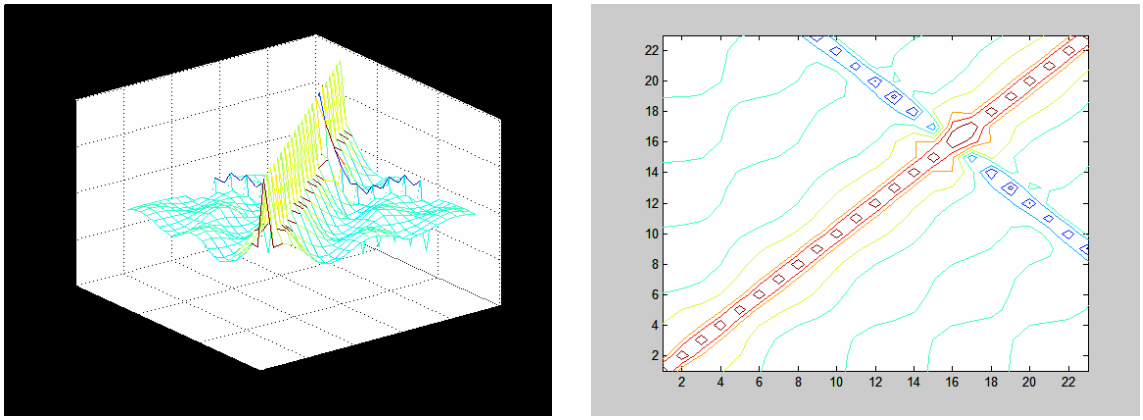

Figure 112 - The [C] matrix for the third accelerometer placement (a) 3-D plot; (b) contour plot

The first two-accelerometer placements yielded the same results for the modal participation factors with the correct dominant and participating modes. The third accelerometer placement produced dominant modes of 17th and 16th, and participation factors from 10th to 22nd. The correct dominant mode was 17th.

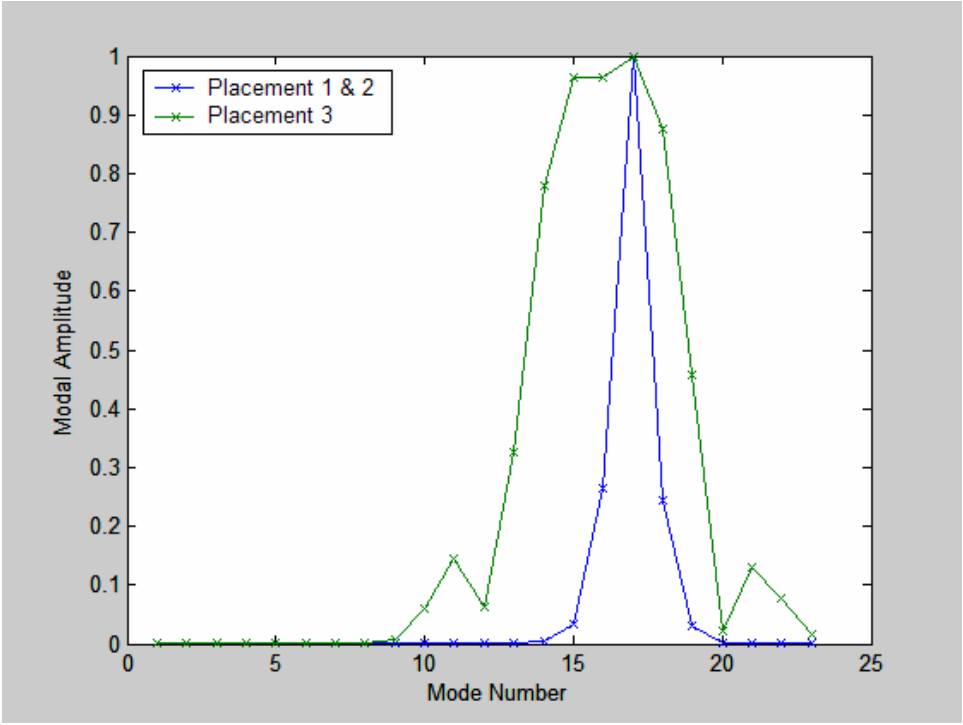

Figure 113 - The mode participation factors for all three placements

A High-Frequency Mode Case

A second test case was used to see the effect of these accelerometer placements on higher-frequency modes. The second test was identical to the first except a higher velocity sheared current was used. This case was also a single mode dominant case, with

a dominant, resonant 33rd mode, and non-resonant participating modes from 30 to 36. For the modal participation calculations only modes 18 to 41 were used. This is because the number of modes used in the modal participation must be less than number of accelerometers.

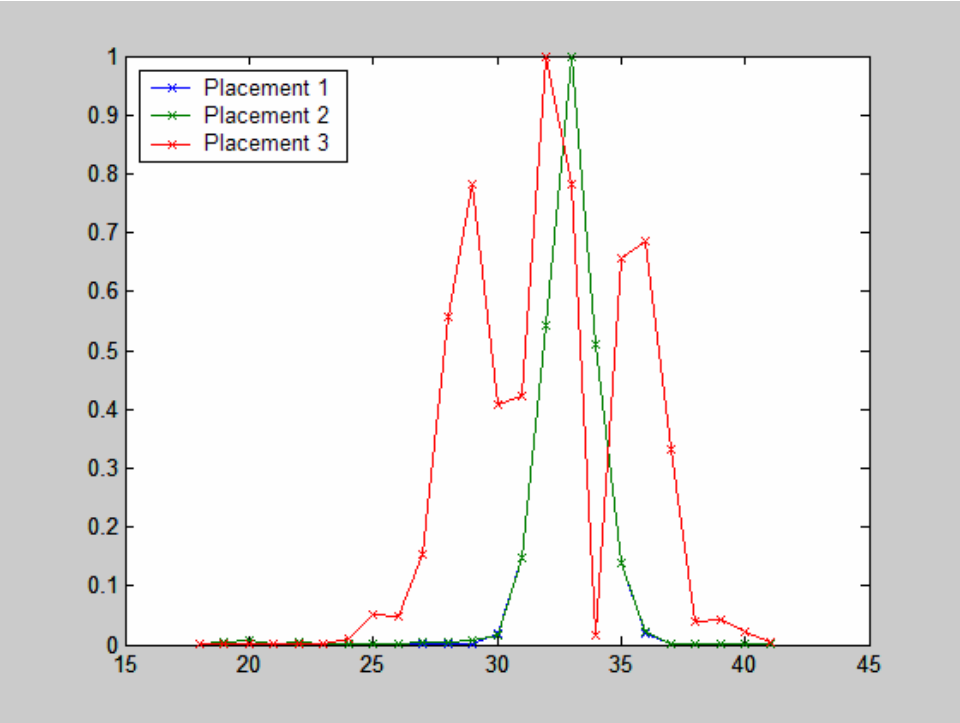

Figure 114 - The mode participation factors for all three placements of the high mode number case

As can be seen in Figure 114, the first and second placements gave approximately the same modal participation factors. The third placement predicted the wrong dominant mode and exhibited large and erroneous values for several additional participating modes.

A Low-Frequency Multi-Mode Case

The same case was run again with the lower sheared velocity, but with a lower modal cut-off to allow for a multi-mode solution. In this case modes 15, 16, and 17 were resonant and had power-in regions. In the prediction, there were contributing non-resonant modes from 12 to 20. Again, the first two placements yielded virtually identical solutions, while the third placement did not predict the resonant and non-resonant modes or amplitudes correctly.

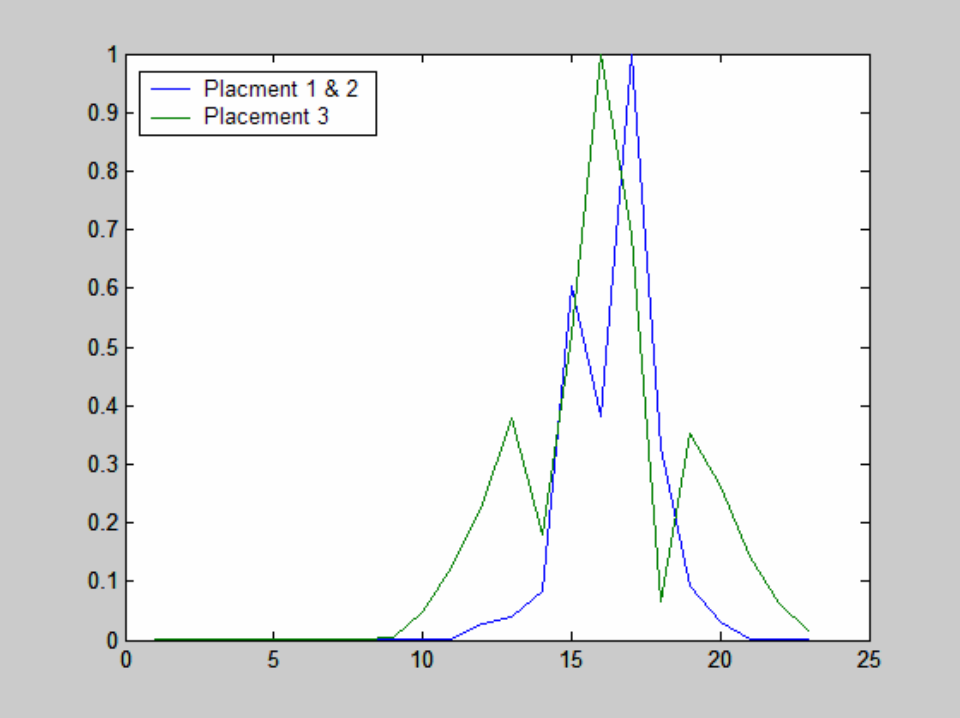

Figure 115 - The mode participation factors for the low-frequency multi-mode case

A High-Frequency Multi-Mode Case

The same case was run with the higher velocity sheared flow, but with a modal cut-off that allowed for multiple modes. In this case, modes 29 to 34 were contributing resonant modes, and modes 26 to 37 were the contributing non-resonant modes.

For the high frequency case with multi-modes, the first and second placement yielded similar results for the participating resonant and non-resonant modes. The third solution predicted similar modes, but different values for the participation factors.

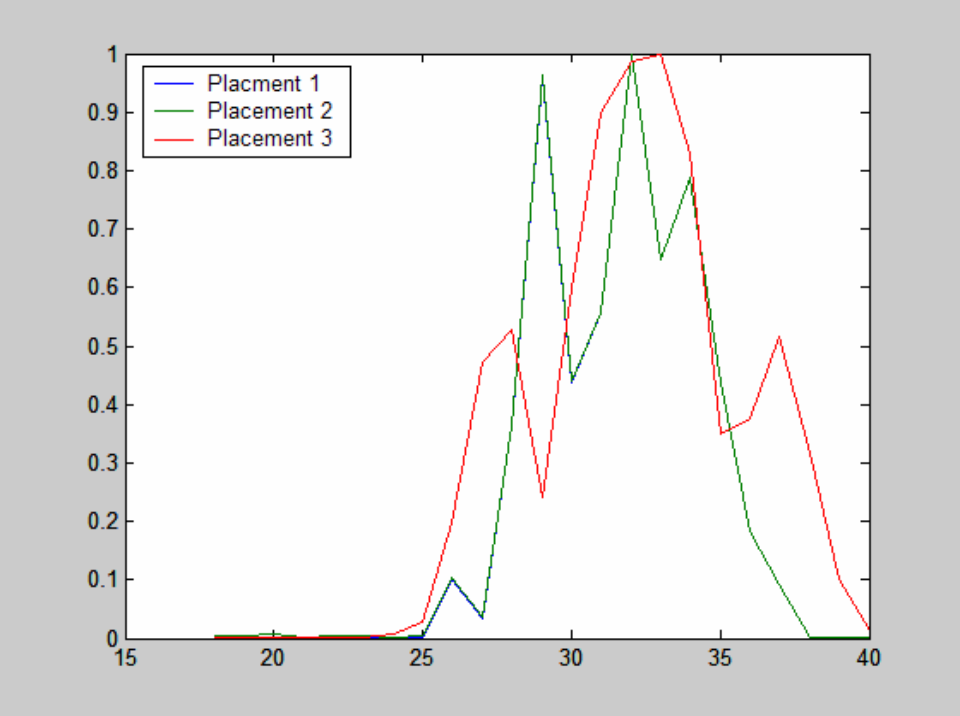

Figure 116 - The mode participation factors for high-frequency multi-mode cases

Accelerometer Placement Conclusions

Using this methodology can be a good indication of problematic accelerometer placements, but common sense must also be applied when choosing the accelerometer placements.

The first thing that must be determined is the application of the data. If the data is being used for modal participation with mode numbers higher than the number of accelerometers, then a different optimization algorithm or further constraints in the algorithm may need to be used to ensure optimum resolution.

Any attempt to optimize the placement of a limited number of accelerometers requires precise knowledge of the expected mode shapes. Differences between predicted and actual mode shapes will lead to errors in the results. For the Lake Seneca Test, the accelerometer placement that was chosen is a distribution that seems to be robust and relatively insensitive to the expected range of variation of the first twenty-four mode shapes that we expect to see.

A weakness of this algorithm is that is does not detect if there are at least two accelerometers in a wavelength. If the data is going to be used for modal participation or

other further research, then having two accelerometers located within a wavelength may be needed to satisfy the spatial Nyquist requirement.

Standard modal participation factor analysis will be sensitive to the off-diagonal terms in the [C] matrix. The method of choosing accelerometer placement shown here should lead to reasonably good results for the first 24 modes for the Lake Seneca Test and potentially useable results for some higher modes.

Appendix H: Further Investigation in Finding the Power-In Region

Introduction

Chapter 6 introduced the reduced velocity and coherence mesh methods to finding the power-in region. This appendix shows further evaluation of this methodology using uniform flow cases, cases with multiple power-in regions, and the effects of strakes on this methodology.

Results

Figure 26(a) shows the current profile for a run from the Gulf Stream test with both speed (blue+green) and direction (red). The likely power-in region found from the reduced is overlaid on the current profile (green). The current profile is sheared from 1.5 ft/s to 3.0 ft/s. Figure 26(b) shows the total RMS strain (blue) and the RMS strain filtered to only contain the dominant VIV frequency (green).

Figure 27(a) shows the same current profiles as Figure 26. Figure 27(b) shows the dominant VIV frequencies for each location. The frequency that dominates for the most time is shown with the blue vertical line. The error bars show the variation of the dominant VIV frequency during the total record. In the power-in region, the variation in the frequency is seen to be similar and fairly constant.

As the frequencies change with time sharing, the reduced velocities change at each location. This power-in region takes into account the reduced velocities for a three minute time window, as the frequencies shift the power-in region may move as well. This is the power-in region of all frequencies during this run. When looking at a smaller amount of time, the power-in region would be smaller.

Outside the power-in region, the variation is larger. In these areas, traveling waves from the power-in region will sometimes dominate, which would cause the frequency to appear to be the same as the power-in region. At other times locally generated small amplitude waves that are caused by local currents will dominate. This causes for much greater variation in the frequency, because the two current speeds can because the current speeds can be very different from the power-in region to the local current.

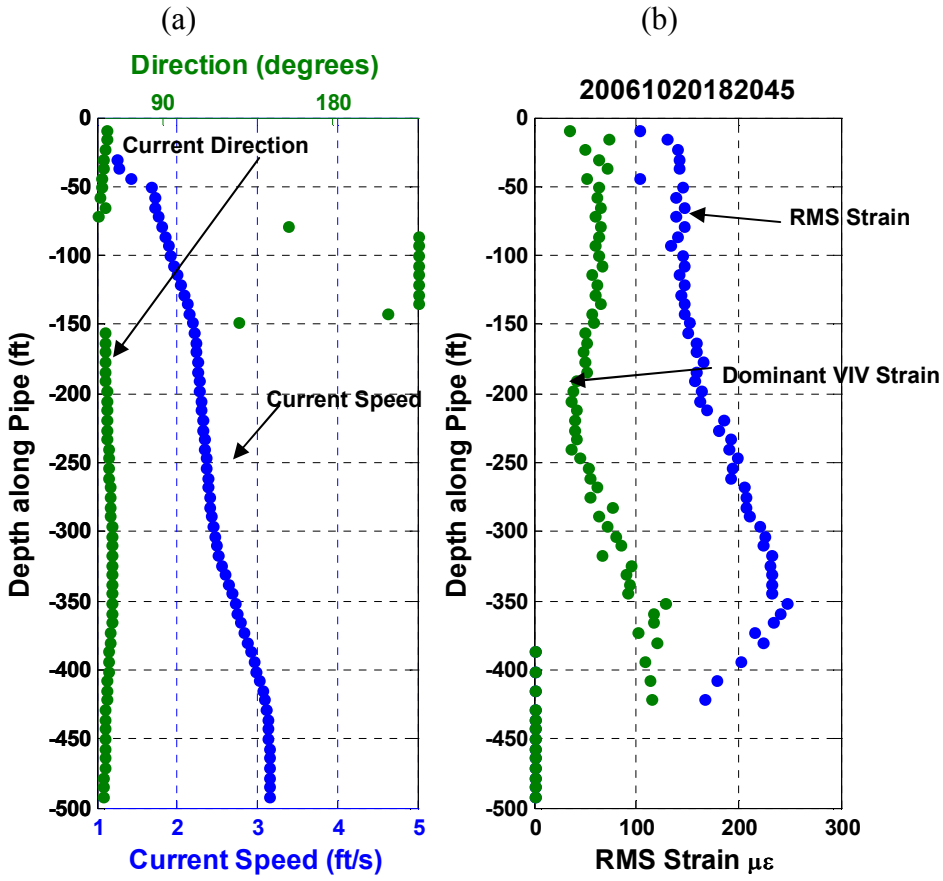

Figure 117 – Gulf Stream bare case (a) Current Speed (blue) and current direction (green); (b) RMS strain (blue) and RMS strain filtered to only show the contribution of the dominant VIV frequency.

Figure 27(c) shows the reduced velocity, calculated using the frequency of vibration. In the power-in region the reduced velocity is between 5 and 6, with the largest amount of time spent at about 5. The power-in, shown on the current profile, was calculated using the reduced velocities that ranged between 5 and 8. Because of time sharing the reduced velocities vary with time.

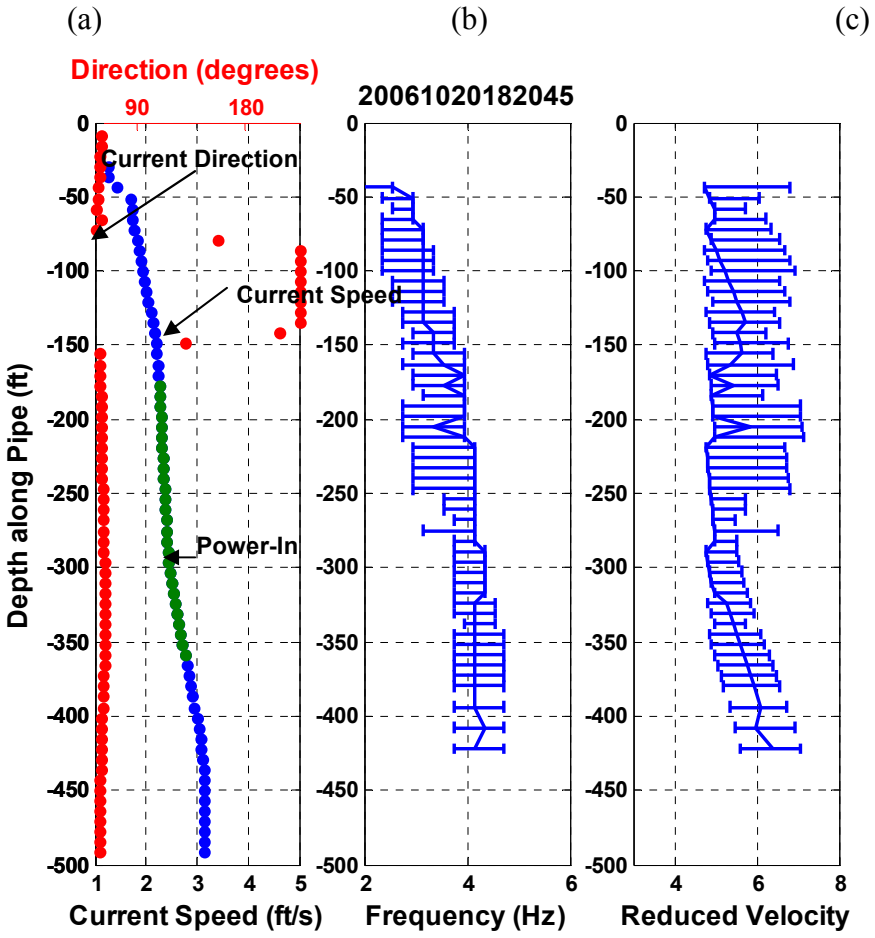

Figure 118 – Gulf Stream bare case (a) Current speed (blue), current direction (red), and power-in region (green); (b) Dominant VIV frequency, showing the most common frequency with the vertical line and the varying frequencies due to time sharing; (c) the reduced velocity, using dominant VIV frequency, the variance is due to the variation in frequency with time shifting.

Figure 28 shows an example of the distance ranges from each sensor for an example from the Gulf Stream test (20041029170336). The bliue colors represent sensors and frequencies that are coherent over less than 50 ft. Therefore, these waves have little energy and do not travel much distance. The yellow and red tones represent waves that are traveling up to 200 ft. By looking at the frequency 4.2 Hz, it shows that at that frequency waves are traveling over a significant distance. The sensors from 175 ft to 375 ft all show significant coherence over a large distance.

Similar phenomena can be seen at approximately twice the frequency, this would represent the power-in region for the in-line. Due to a sample rate issue with the data [See Appendix A], the coherence is not as good at this frequency and can not be seen as

clearly. Additionally the orientation of this fiber is not known with respect to the flow, and the sensor may be oriented in the cross-flow direction.

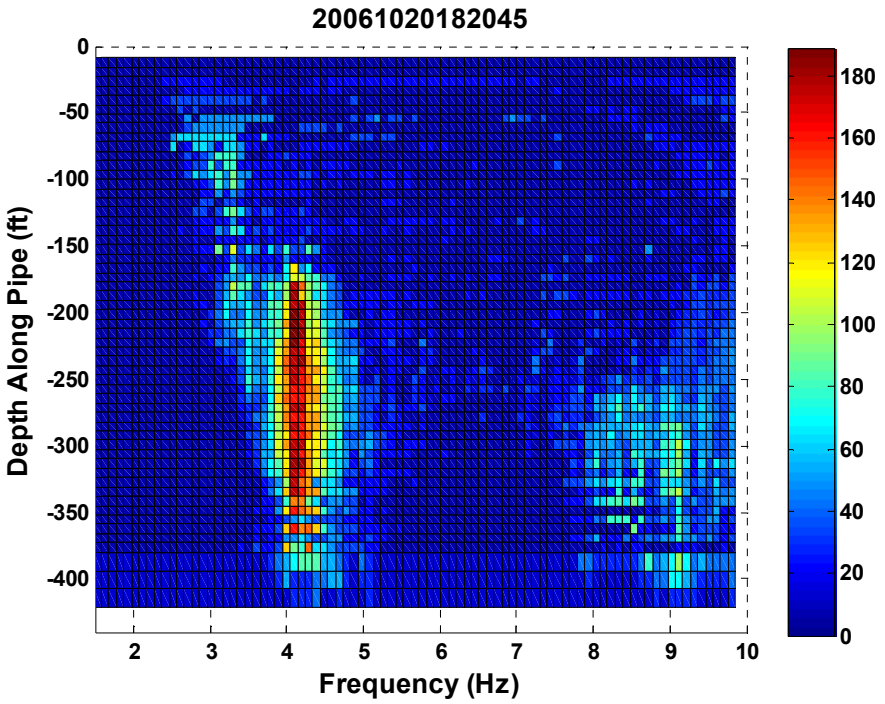

Figure 119 – Gulf Stream bare case coherence mesh showing the distance range from every point over which there is coherence of greater than 0.7

More than one frequency can be seen to be coherent; this is because of time sharing. For the coherence calculation to be accurate, a number of averages must be taken. Each average contains 10 seconds of data with 50% overlap between averages. For this coherence mesh 60 seconds of data was used, indicating approximately 10 averages were used in the mesh. The more averages used the better to reduce error from noise. Unfortunately because of time sharing, the frequencies were not constant and shifted in the 60 second window used for this example.

Figure 120 shows the waterfall spectra for the same case. This waterfall was done using Maximum Entropy Method (MEM) analysis with the Burg method [Burg 1968]. A window length of 5 seconds was used with 80% overlap between the spectra. For the MEM analysis, 30 poles were used. This waterfall plot of spectra clearly shows the time-sharing theory. Over the course of the entire run, the dominant VIV frequency varies from 4 Hz to 5.5 Hz. The in-line component at twice the frequency can faintly be seen.

Between 12Hz and 14 Hz, a third harmonic can also be seen which correlates to the cross-flow component.

Each of these frequencies can have a different power-in region. These different power-in regions could be seen more clearly in a coherence mesh by reducing the amount of time that the coherence mesh is calculated over to prevent the shifting frequencies from reducing the coherence. Unfortunately, reducing the amount of times reduces the number of averages in the coherence calculation, which will increase the error caused by noise.

When looking at the coherence mesh in Figure 28, more frequencies can be seen around the 4.2 Hz dominant frequency. At approximately 5 Hz, a power-in region can be seen from approximately 300 ft to 400 ft. This most likely correlates to the last 10 seconds of the run when a 5 Hz signal can be seen in the waterfall in Figure 120.

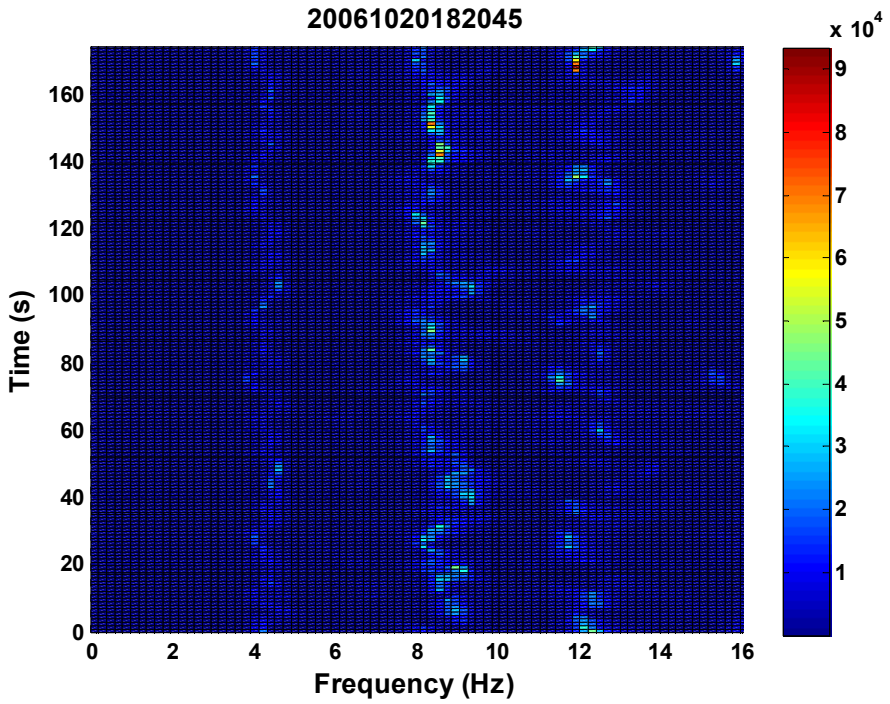

Figure 120 – Gulf Stream bare case waterfall spectra of a strain gauge sensor in the middle of the power-in region at 281 ft. found using the coherence method. Each spectrum was calculated using MEM analysis with a 5 second window and 80% overlap.

Since the coherence is calculated over all time, the 5 Hz signal would only be coherent over the last few averages. This would lead to the lower coherence seen in the coherence mesh since that is the average over all time.

Figure 121 shows the same coherence mesh as Figure 28, except the distance ranges have been normalized to the wavelength for each frequency. Effectively, this mesh shows the number of wavelengths that the vibration is traveling out in the sum of the up and down the pipe. Interestingly, the three-time harmonic is more prominent when the graph is shown in this manner. This shows that the three-time harmonic travels a similar number of wavelengths as the cross-flow direction, but the wavelength of the three-time harmonic is one-third that of the cross-flow direction.

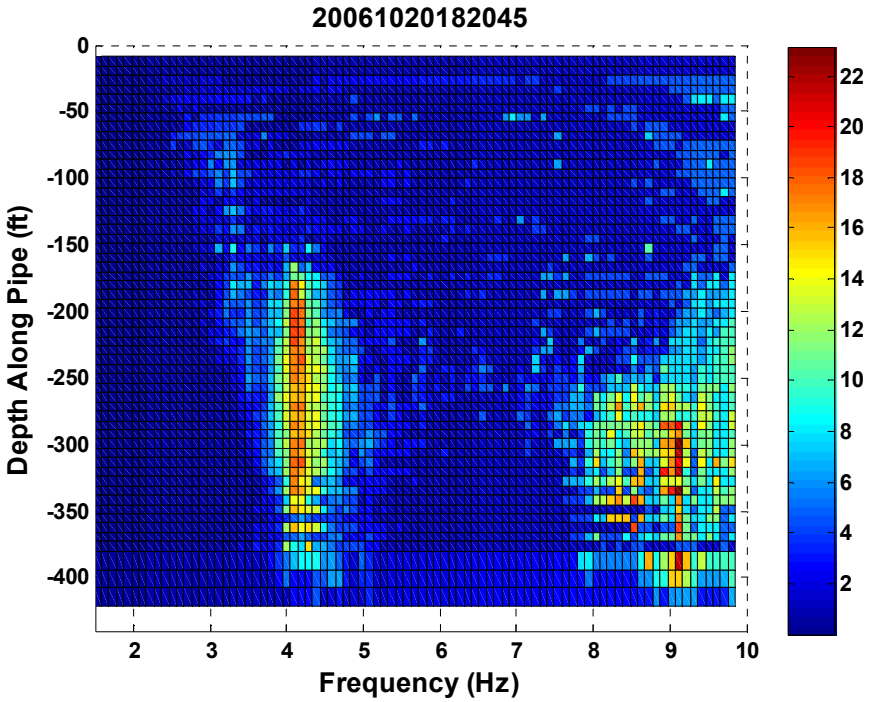

Figure 121 – Gulf Stream bare case coherence mesh showing the distance ranges with greater than 0.7 coherence normalized by wavelength at each freqeuncy

Further Investigation

Another example using the coherence mesh is shown in Figure 122. The dominant power-in region is shown to be from 275 ft to 325 ft from 3.5 Hz to 4.5 Hz.

The second and third harmonics are not as prevalent in this example as in the first example. The absence of the second harmonic may be due to the orientation of the sensor with respect to in-line and cross-flow motion. This can also be seen in the waterfall spectra plot, Figure 123.

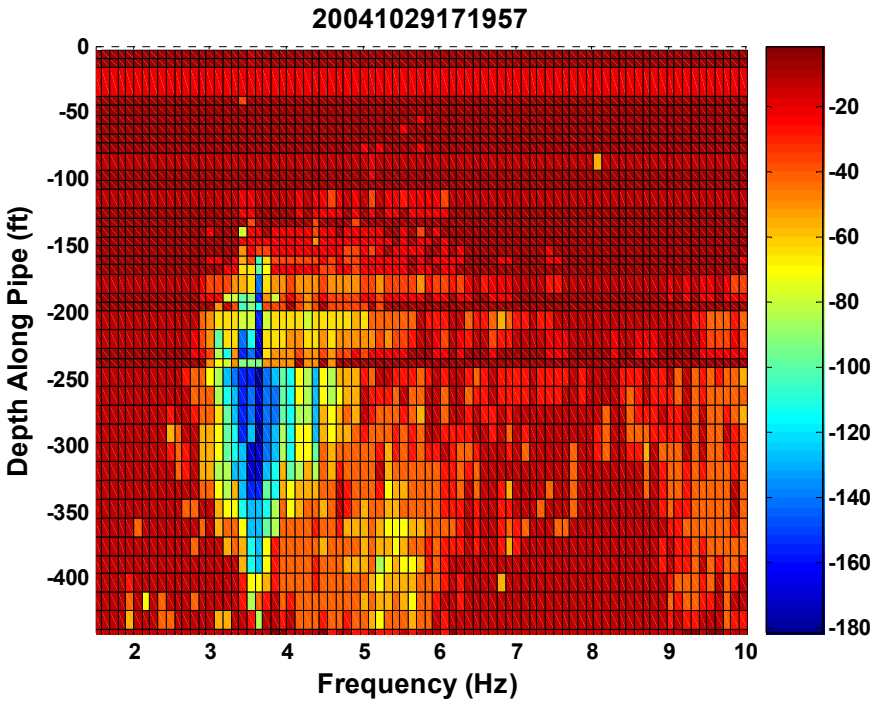

Figure 122 – Gulf Stream bare case coherence mesh showing the distance range from every point over which there is coherence of greater than 0.7

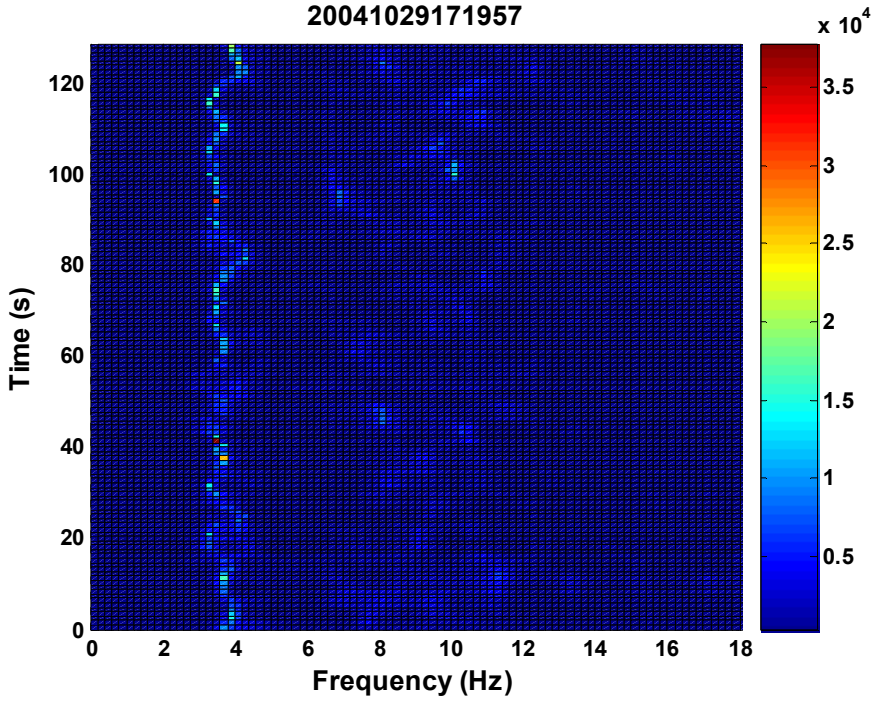

Figure 123 – Gulf Stream bare case waterfall spectra of a strain gauge sensor in the middle of the power-in region found using the coherence method. Each spectrum was calculated using MEM analysis with a 5 second window and 80% overlap.

The third harmonic appears to be less stable; the third harmonic can be a very powerful component of the spectra, but appears over shorter regions of the pipe and because it has a shorter wavelength, and damps in a shorter distance. From laboratory testing [Williamson and Jautvis], the third harmonic appears most prominently when the reduced velocity is approximately 7.

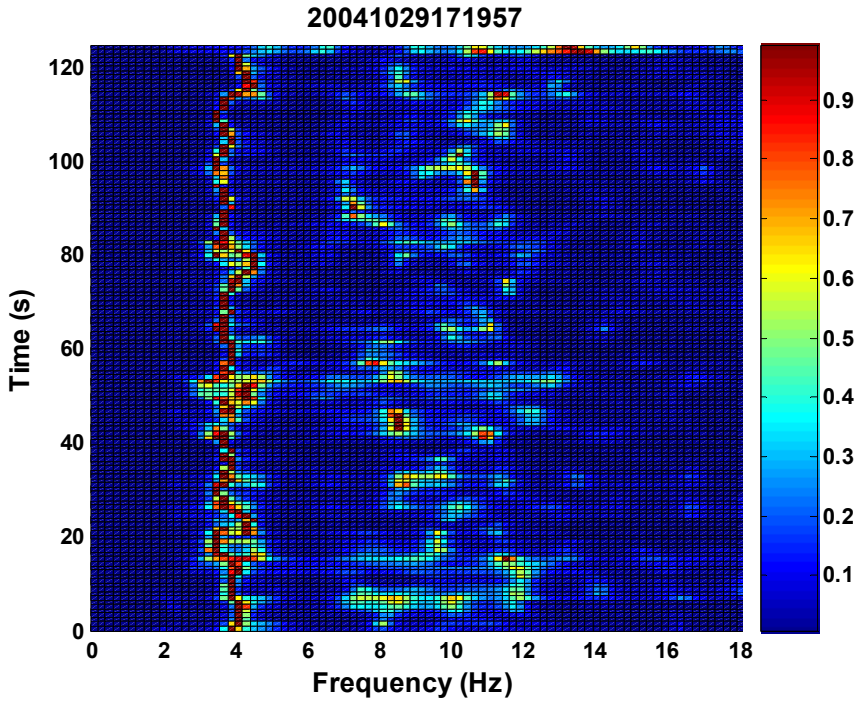

Figure 124 – Gulf Stream bare case waterfall spectra normalized to the maximum for each time step

Figure 32(b) shows the RMS strain for the same case with the power-in region overlaid. The power-in region is in the area of highest strain response. This logically makes sense that the region with the highest response would be the power-in region, where outside the power-in region the vibrations are damped and the response is lower.

In Figure 126(b), the dominant VIV frequencies are seen; this can be compared to Figure 123 where the dominant VIV frequency is mostly seen as just less than 4 Hz, but the frequency can spike to higher frequencies for small lengths of time. Figure 126(c) shows the reduced velocity for each location. In the power-in region identified the dominant reduced velocities range between 4 and 6.

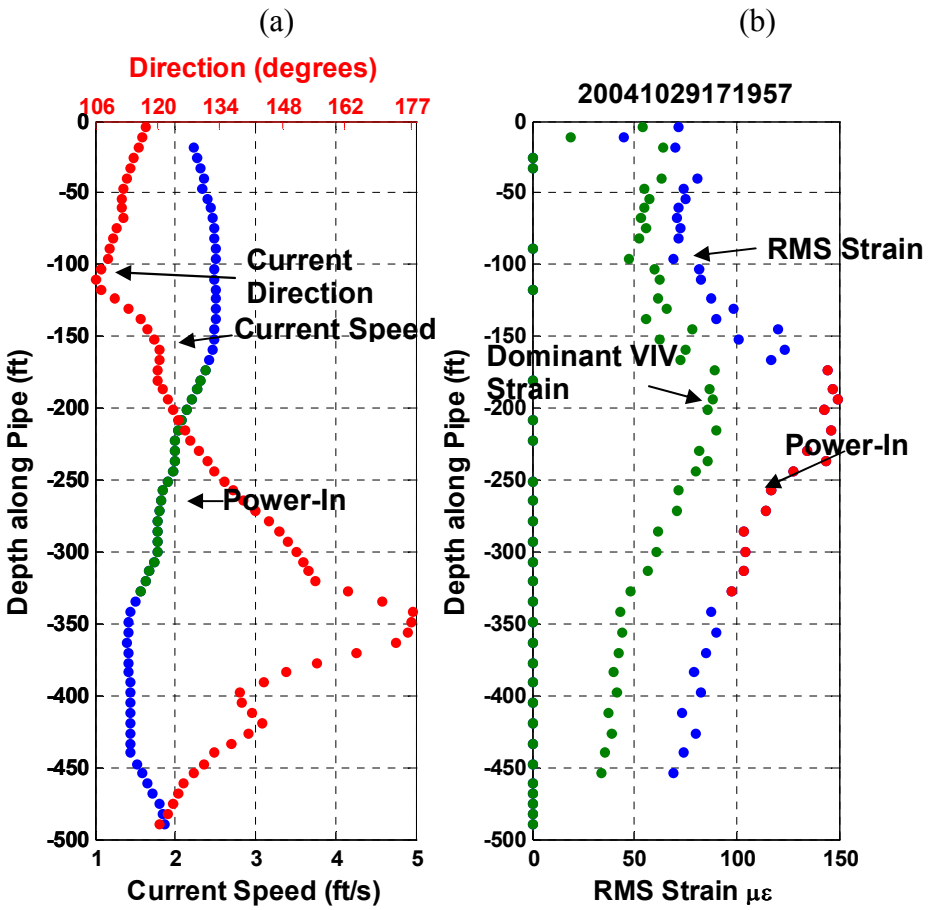

Figure 125 – Gulf Stream bare case (a) Current speed (blue), current direction (red), and power-in region (green); (b) RMS strain (blue) and RMS strain filtered to only show the contribution of the dominant VIV frequency. The power-in region found using the coherence method is shown on both graphs; (a) green and (b) red.

For the example shown in Figure 126, the highest velocity region is near the top of the pipe. Traditional theories of VIV would suggest that a steady high velocity region would be the most likely power-in region. The static curvature of the pipe and therefore the incidence angle of the current at the top is the largest. The large incidence angle of the current may prevent a dominant power-in region from forming in this area. The area above the power-in region found using the coherence mesh had tilt angles that varied from 47 to 60 degrees. The power-in region found here is possibly in the highest velocity region which is unaffected by the incident angle of the current.

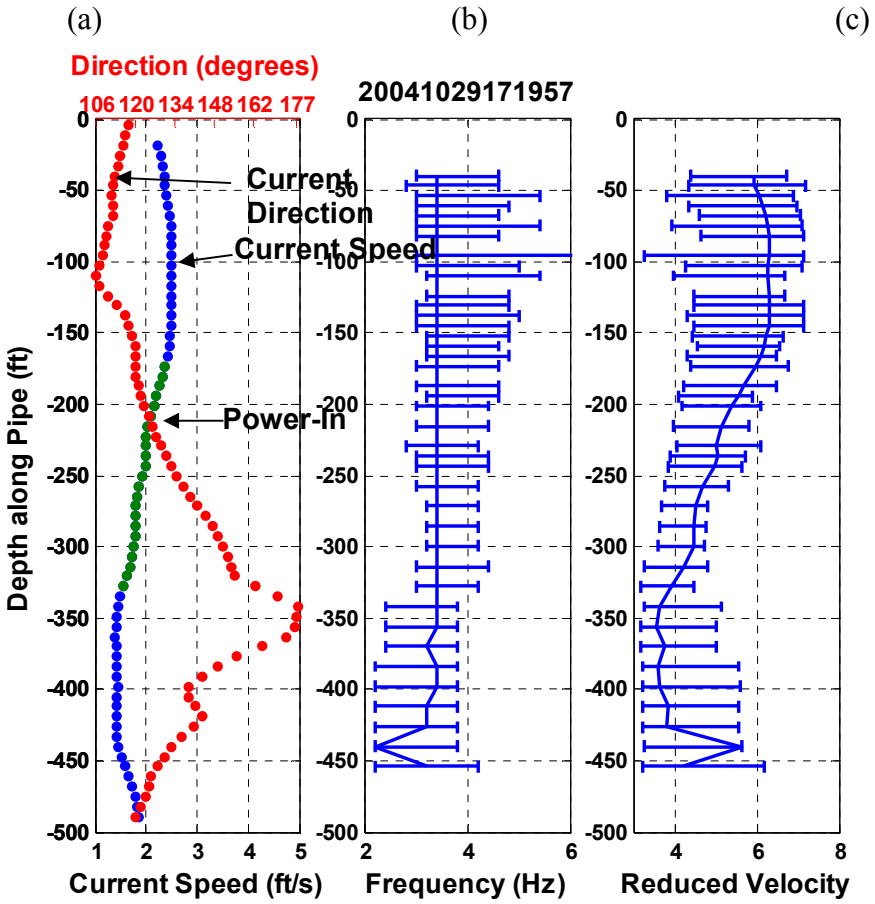

Figure 126 – Gulf Stream bare case (a) Current speed (blue), current direction (red), and power-in region (green); (b) Dominant VIV frequency, showing the most common frequency with the vertical line and the varying frequencies due to time sharing; (c) the reduced velocity, using dominant VIV frequency, the variance is due to the variation in frequency with time shifting.

Multiple Power-In Regions

Looking at another example from the Gulf Stream test, by looking at the RMS strain in Figure 30(b), the RMS strain from significant vibration can be seen in the lower portion where the primary power-in region is from 275 ft to 400 ft.

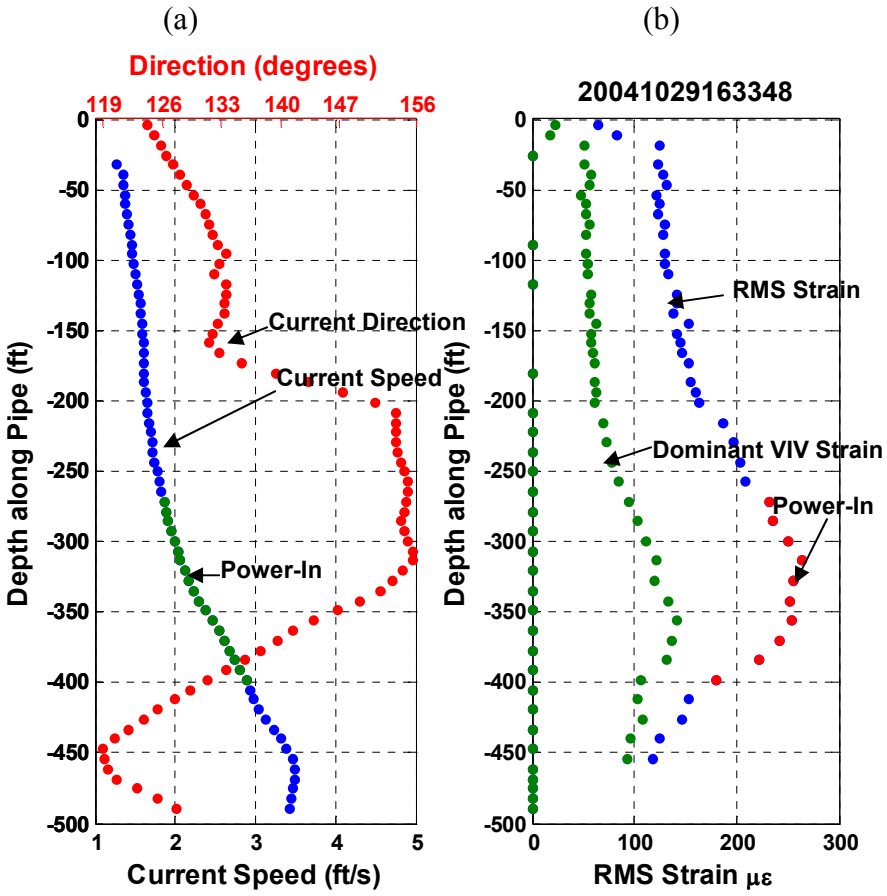

Figure 127 – Gulf Stream bare case (a) Current speed (blue), current direction (red), and power-in region (green); (b) RMS strain (blue) and RMS strain filtered to only show the contribution of the dominant VIV frequency. The power-in region found using the coherence method is shown on both graphs; (a) green and (b) red.

In Figure 128(a), the dominant power-in is shown in green. A secondary power-in region can be seen by looking at the frequency plot in Figure 128(b). The frequency of the dominant power-in region is most prominent from the bottom up to 200 ft. In the upper portion of the pipe, a completely different frequency dominates; this is the secondary power-in region. Figure 128(c) shows the reduced velocity associated with this case. In the dominant power-in region the reduced velocity is between 4.0 and 5.75. In the secondary power-in region the reduced velocity is between 4.0 and 5.5.

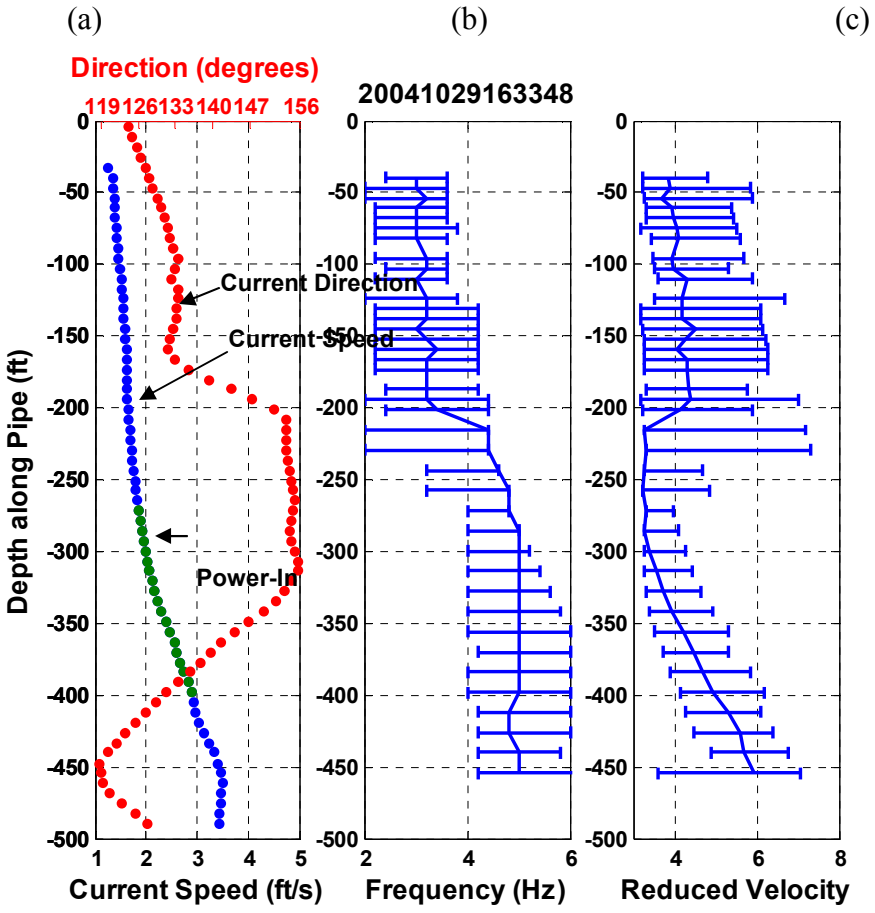

Figure 128 – Gulf Stream bare case (a) Current speed (blue), current direction (red), and power-in region (green); (b) Dominant VIV frequency, showing the most common frequency with the vertical line and the varying frequencies due to time sharing; (c) the reduced velocity, using dominant VIV frequency, the variance is due to the variation in frequency with time shifting.

In the Gulf Stream data, there are multiple instances where more than one power-in region is evident. By using the coherence mesh, it can be found where each set of frequencies is originating from. In Figure 129, a coherence mesh is shown for Gulf Stream Test. In this case there were two power-in regions which contributed vibrations at different frequencies. In this case one power-in region extends from 275 ft to 400 ft. with a frequency of approximately 5 Hz. Another power-in region can be seen from 50 ft to 150 ft at approximately 3 Hz. The vibrations in the upper power-in region can be seen to dominate in the frequency over a large portion of the pipe, but not contribute much to the RMS strain.

The two power-in regions need to be separated by some minimum distance for the two to exist simultaneously. If the two power-in regions are closer than X, then the

dominant power-in region will prevent the other power-in region from existing. This goes back to the concept of time sharing, that in a finite space only one frequency can dominate at one time. Far enough from the dominant frequency's power-in region where the dominant frequency has been significantly damped, a second power-in region can exist.

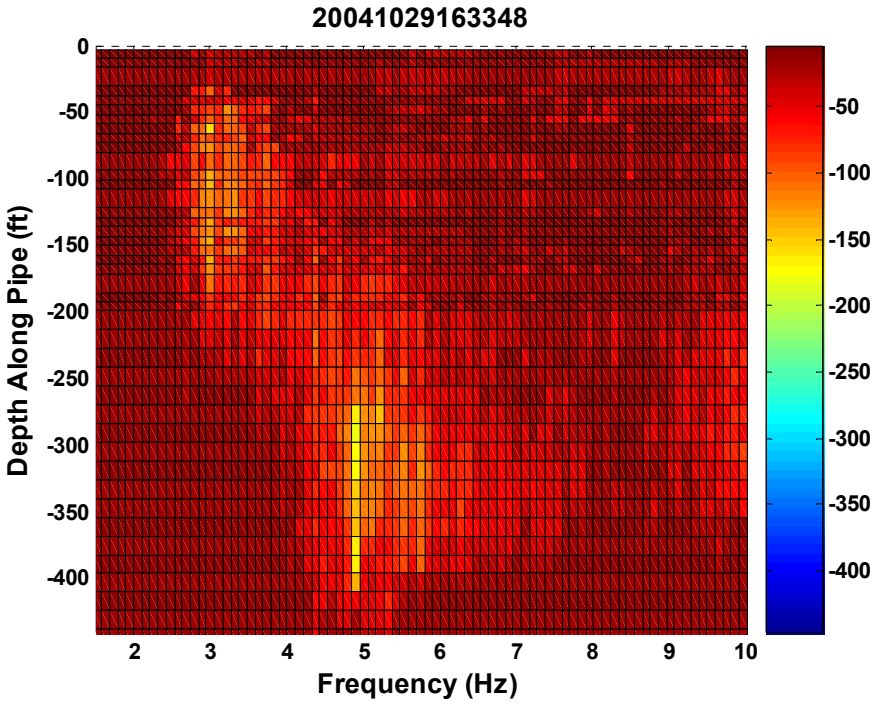

Figure 129 – Gulf Stream bare case coherence mesh showing the distance range from every point over which there is coherence of greater than 0.7 for multiple power-in regions.

In Figure 130, the same coherence mesh as in Figure 129 is shown but the distance ranges are normalized to the wavelength. This shows that though the secondary power-in region exists, the waves are traveling less than 10 wavelengths, whereas the dominant power-in region in both in-line and cross-flow, the waves travel 20 wavelengths.

By comparing Figure 131 and Figure 132, which show the MEM waterfall spectra for a strain gauge in the dominant power-in region and the secondary power-in region respectively, the different dominant frequencies are evident.

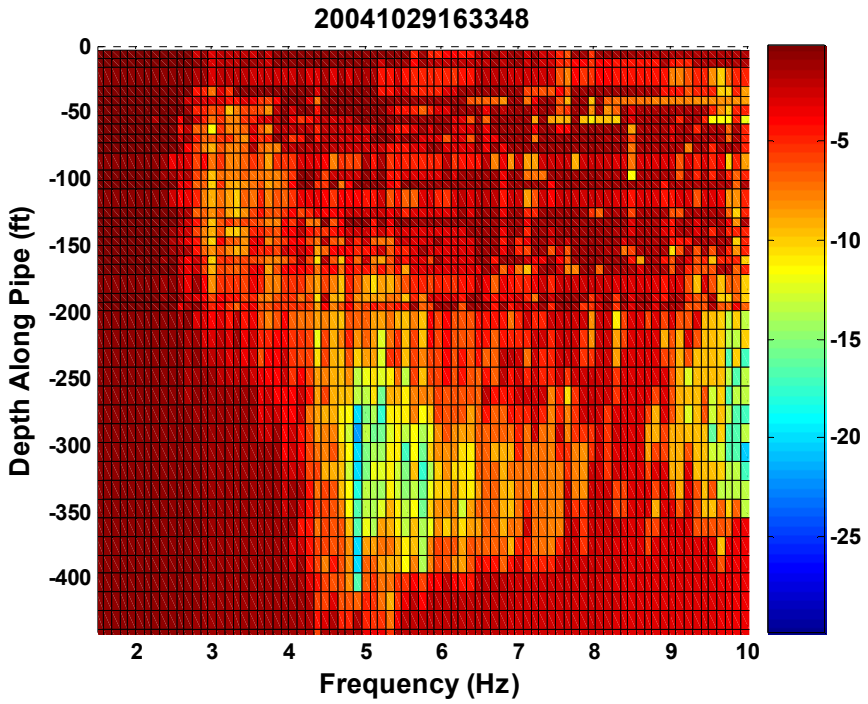

Figure 130 – Gulf Stream bare case Coherence Mesh showing the Distance Ranges with Greater than 0.7 Coherence Normalized by Wavelength at each Freqeuncy

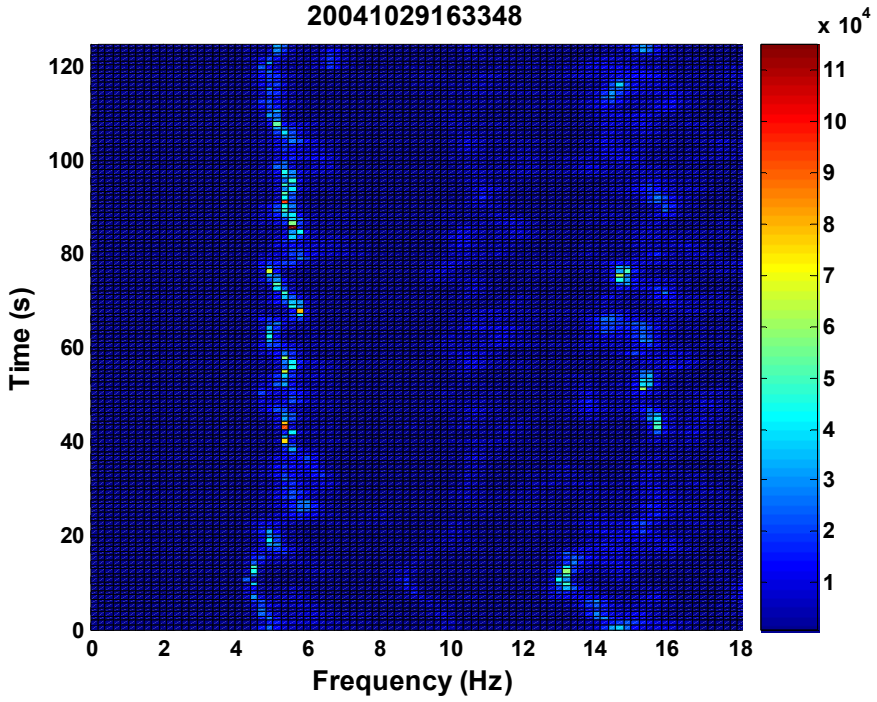

Figure 131 – Gulf Stream bare case waterfall spectra of a strain gauge sensor in the middle of the dominant power-in region found using the coherence method. Each spectrum was calculated using MEM analysis with a 5 second window and 80% overlap.

For Figure 131, the dominant VIV frequency is between 4 Hz. and 6 Hz; whereas for Figure 132, the dominant frequency is between 2 and 4 Hz. In both Figure 131 and Figure 132 the dominant frequency from the other figure can not be seen; thus the 2 to 4 Hz frequency seen in the top of the pipe can not be seen in the lower power-in region. This means that the vibration from one power-in region is effectively damped before traveling to the other power-in region and does not interfere with the creation of a second power-in region.

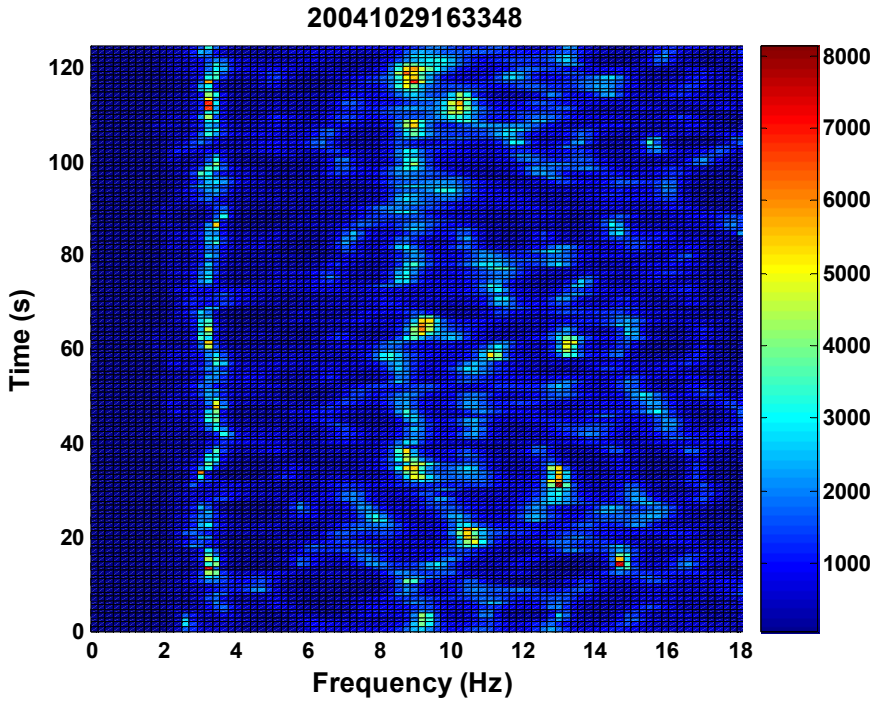

Figure 132 – Gulf Stream bare case waterfall spectra of a strain gauge sensor in the middle of the secondary power-in region found using the coherence method. Each spectrum was calculated using MEM analysis with a 5 second window and 80% overlap.

By looking at the magnitude of the two waterfall spectra (Figure 131 and Figure 132) it can be seen which power-in region is dominant. The spectra in Figure 131 are an order of magnitude larger than the spectra in Figure 132.

Lake Seneca Data

The same analysis techniques can be used on the Lake Seneca Data. The pipe at Lake Seneca was 401 ft long and subject to a uniform flow [Vandiver et al. 2005]. The sensors at Lake Seneca where nominally placed 16.6 ft apart, but due to a large number of sensor failures, the spacing was much further apart.

In Figure 133, a coherence mesh for a Lake Seneca steady state example. Only thirteen sensors were active over the 401 ft pipe. The length of the power-in region can be seen to span much of the pipe, as is expected for uniform flow. The current speed was 1.5 ft/s and the top angle for this case was 17.1 degrees.

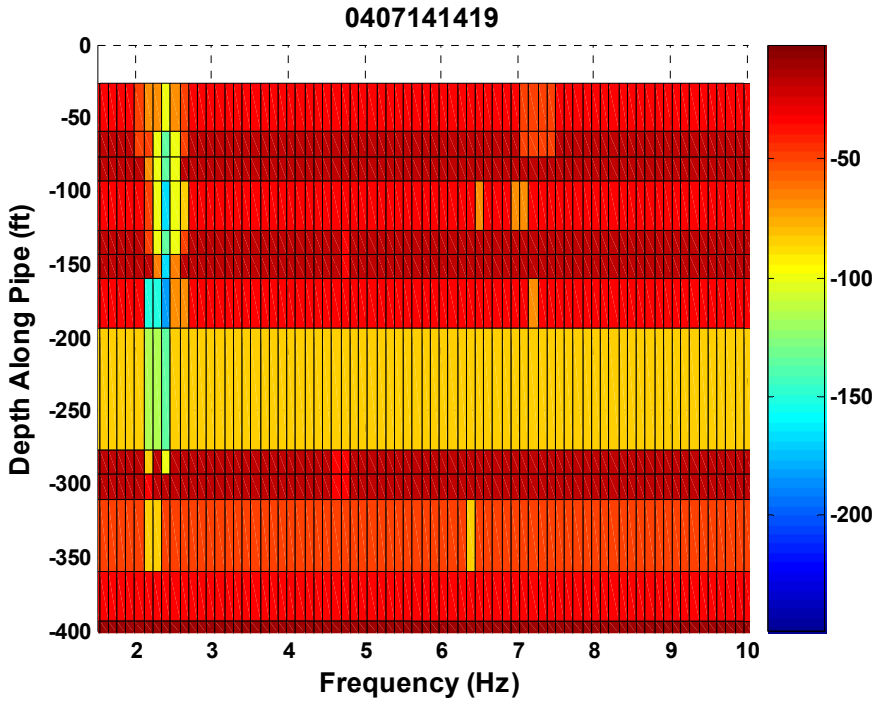

Figure 133 – Lake Seneca bare case coherence mesh showing the distance ranges with greater than 0.7 coherence normalized by wavelength at each freqeuncy for the Lake Seneca test

The curvature of the pipe at the top end is less than 18 degrees; therefore the variation in pipe due to incidence angle varies by less than 5%. This change in velocity is unlikely to effect the location of the power-in region, as seen in Figure 133. Larger inclination angles make areas less likely to be the power-in region, as seen in the Gulf Stream data, power-in regions are possible to an inclination angle of 47 degrees.

The coherence mesh does not work as well with the low density of sensors. Since the coherence mesh is dependant upon the length over which the signal is coherent, if the sensors are far apart, then the actual distance over which the sensor is coherent cannot be seen. The coherence mesh is not as useful a tool for finding the power-in region of the third harmonic without densely spaced sensors because the third harmonic attenuates more quickly in space because of the shorter wave length.

Figure 134 shows the waterfall plot for this case at a depth of 193 ft. Only one dominant VIV frequency is present at any time supporting the concept of time sharing and the dominant VIV frequency varies little over the 3 minute run and it stable at a single frequency for long periods of time.

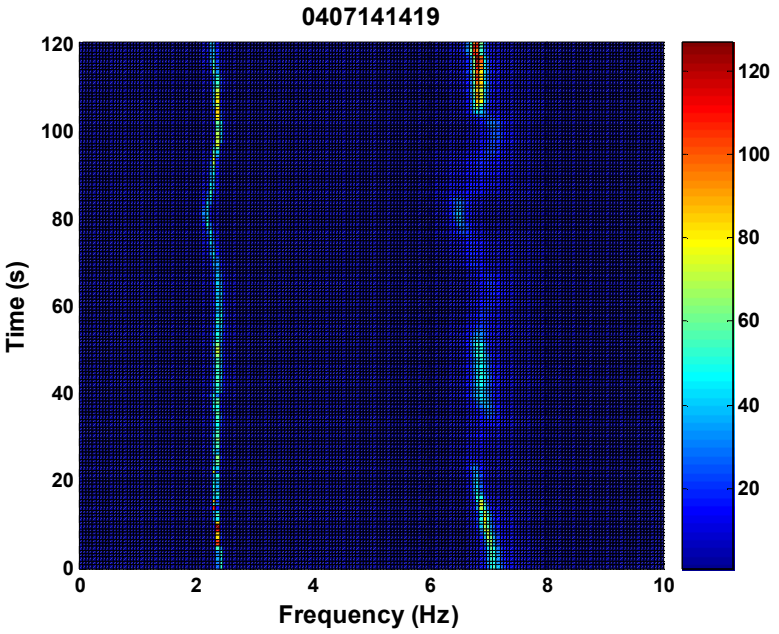

Figure 134 – Lake Seneca bare case waterfall spectra of a strain gauge sensor in the middle of the secondary power-in region found using the coherence method. Each spectrum was calculated using MEM analysis with a 17 second window and 95% overlap.

The coherence mesh shows that the entire pipe is not the power-in region. The area shown to be the power-in region by the coherence mesh is also the area of high RMS acceleration response which can be seen in Figure 135(a).

Figure 135(a) shows the RMS acceleration in the cross-flow and in-line directions. Figure 135(b) has the dominant VIV frequency. The variation in frequency is less than in the Gulf Stream test, as is expected because the variation in current was significantly less. Figure 135(c) shows the reduced velocity for the case based upon the current speed and dominant VIV frequency.

The reduced velocity is centered on 6. This is higher than the average reduced velocity seen for the Gulf Stream tests. In the tests of Williamson [Jauvtis and Williamson 2004], the third harmonic was more prominent at higher reduced velocities, and was most prominent around a reduced velocity of 7. The third harmonic is clearly

visible in the waterfall spectrum in Figure 134. The third harmonic is stable over multiple time spans in this example.

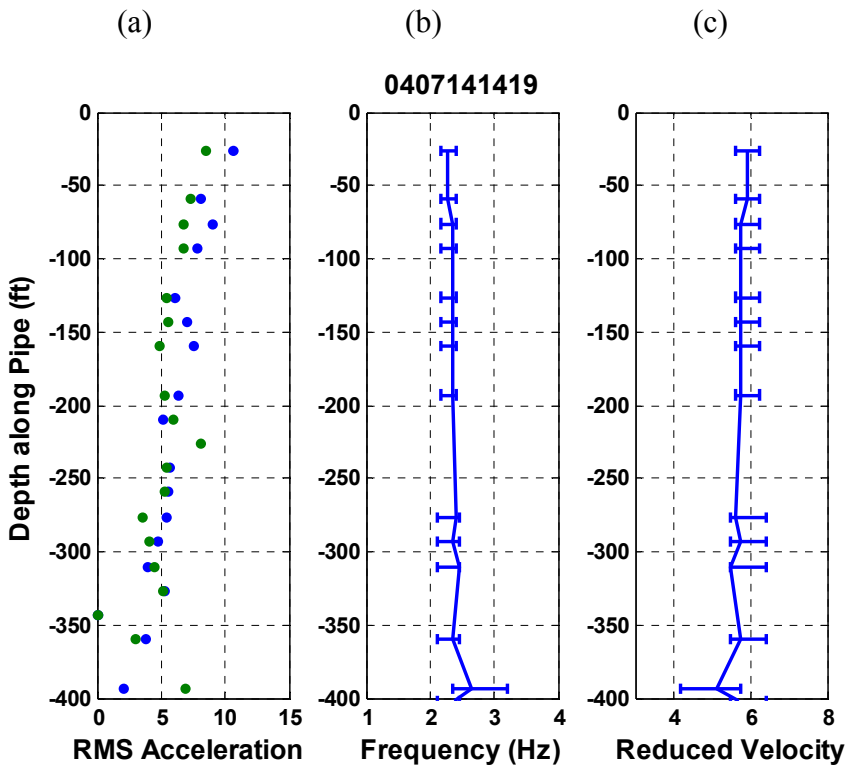

Figure 135 – Lake Seneca bare case with current speed of 1.5 ft/s (a) RMS acceleration in the cross-flow (blue) and in-line (green) directions; (b) Dominant VIV frequency, showing the most common frequency with the vertical line and the varying frequencies due to time sharing; (c) the reduced velocity, using dominant VIV frequency, the variance is due to the variation in frequency with time shifting.

Figure 136 shows the coherence mesh for a case with 19 out of 25 sensors working. The power-in region is located near the bottom of the pipe for this example. Some third harmonic coherence can be seen in this case because of the higher density of sensors especially in the power-in region.

In previous uniform flow tests, standing wave behavior was apparent in the RMS data. This behavior is not seen in the Lake Seneca data. At low mode numbers, the pipe reacts as a pinned-pinned tensioned string and standing wave behavior is common. In both the Gulf Stream test and the Lake Seneca test the mode number is high and the pipe reacts more like an infinite string than a pinned-pinned string. When evaluating whether the pipe will react as a pinned-pinned tensioned string or an infinite string the parameter

nξ is useful. When the nξ is greater than 1, the structure will react as an infinite string. When nξ is small, the pipe will react as a pinned-pinned string.

When structural damping on the pipe is approximately 0.003, and when the hydrodynamic damping is outside the power-in region, the damping can be 0.03 to 0.04. The dominant VIV frequency for both the Lake Seneca test and the Gulf Stream is between 20th and 30th, which leads to nξ from 0.6 to 1.2.

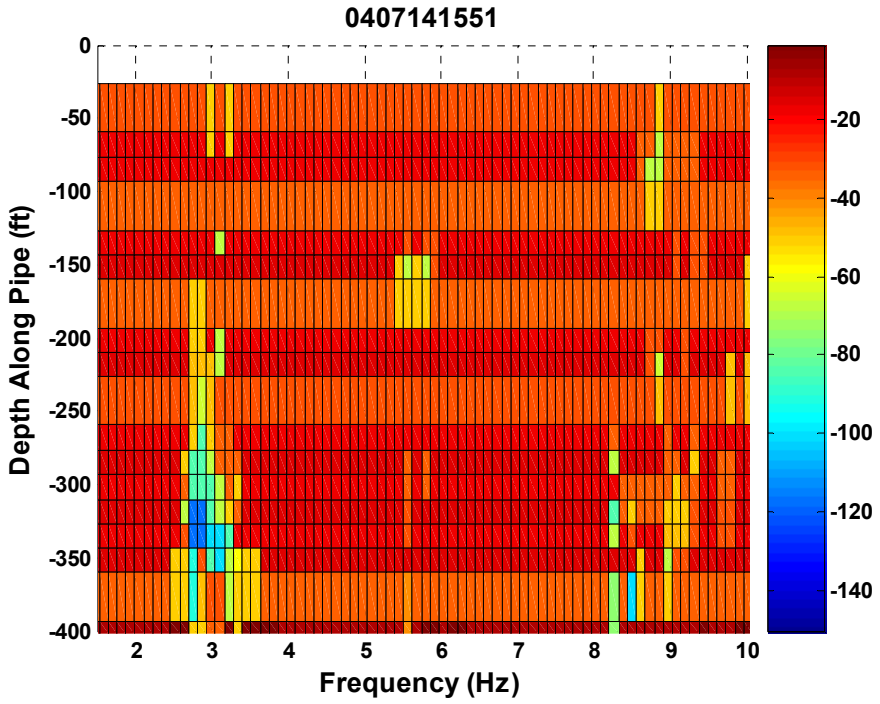

Figure 136 – Lake Seneca bare case coherence mesh showing the distance ranges with greater than 0.7 coherence normalized by wavelength at each freqeuncy for the Lake Seneca test

For this example, the current speed was 2.1 ft/s, and the top tilt angle was 28.7 degrees. The variation in current speed due to incidence angle is less than 15% at the top end. As in the previous example, the highest RMS acceleration response, shown in Figure 138, is at the bottom of the pipe, in the area that the coherence mesh predicted as the power-in region.

Figure 137 shows the waterfall spectrum at a depth of 343.5 ft, which is in the power-in region found by the coherence mesh. The third harmonic is prominent in the waterfall spectrum. Though waterfall spectrum, outside the power-in region, shows the dominant VIV, but the third harmonic is not prominent.

Figure 138(a) shows the RMS acceleration response. The frequency variation, shown in Figure 138(b), is less than 12%, which is about the same variation as the current. The reduced velocity is similar to the other Lake Seneca cases averaging around 6.

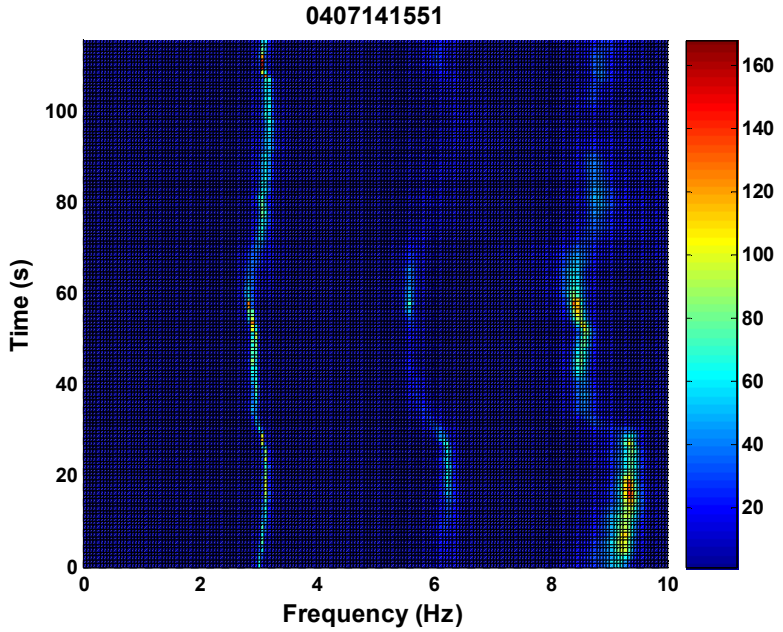

Figure 137 – Lake Seneca bare case in the lower power-in region; waterfall spectra of a strain gauge sensor in the middle of the secondary power-in region found using the coherence method. Each spectrum was calculated using MEM analysis with a 17 second window and 95% overlap.

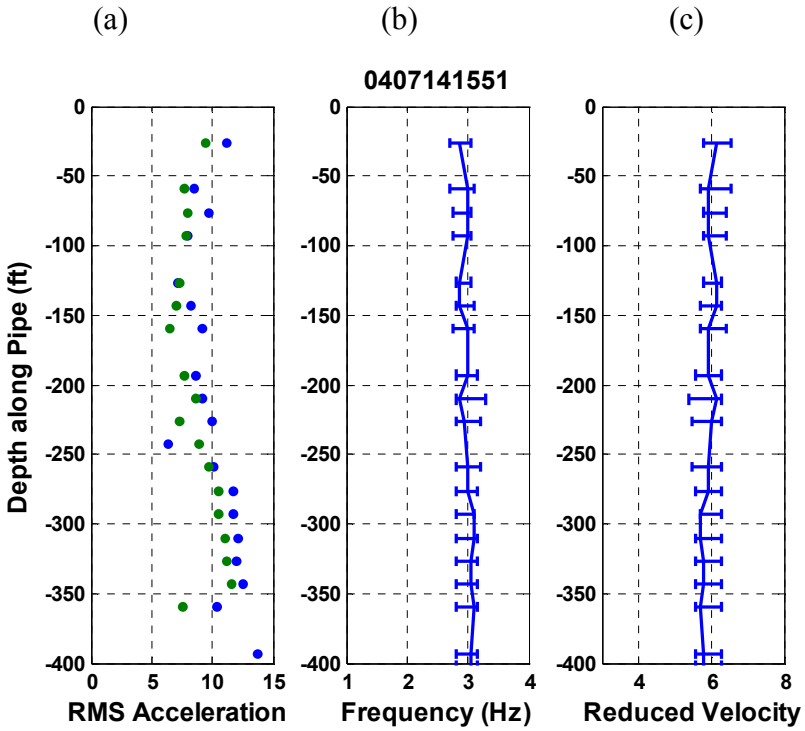

Figure 138 – Lake Seneca bare case with current speed of 2.1 ft/s (a) RMS acceleration in the cross-flow (blue) and in-line (green) directions; (b) Dominant VIV Frequency, showing the most common frequency with the vertical line and the varying frequencies due to time sharing; (c) the reduced velocity, using dominant VIV frequency, the variance is due to the variation in frequency with time shifting.

Data with Strakes

The same type of analysis can be done on the straked pipe. Two different strake configurations were used [Vandiver et al 2005]: one with 40% strake coverage at the bottom, and the other with 70% coverage distributed in five sections over the length of the pipe. Below is an example from both of these tests.

Figure 139 shows the coherence mesh of the 40% coverage case. The strakes are from 300 ft down. The power-in region appears to start above the straked region and continue well into the straked region. The power-in region is unlikely to be in the straked region. The coherence calculation merely shows how well a frequency corresponds at two different locations.

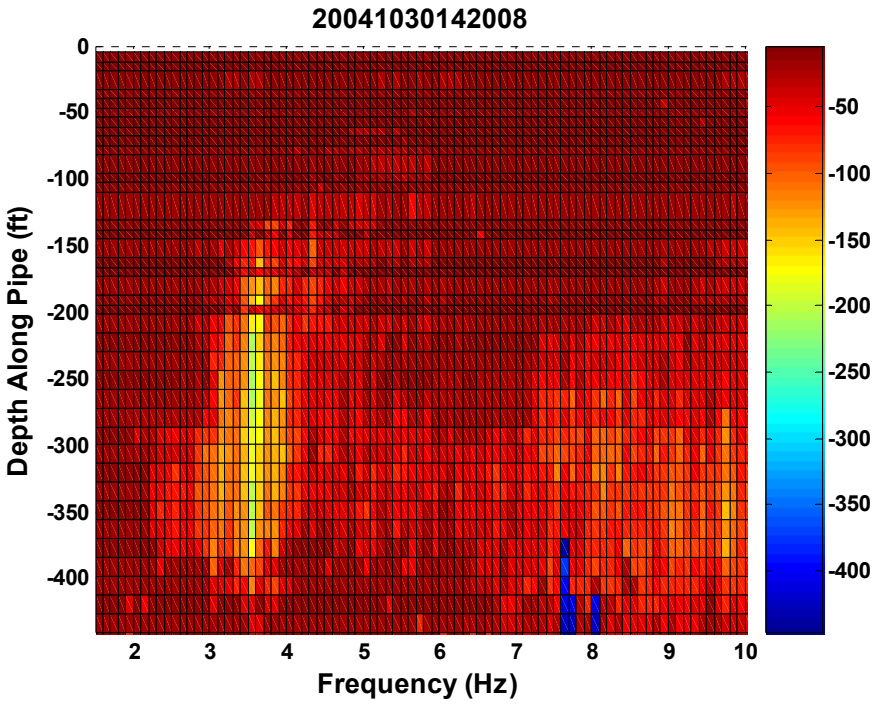

Figure 139 – Gulf Steam 40% coverage case coherence mesh of the 40% strake case showing the distance ranges with greater than 0.7 coherence normalized by wavelength at each freqeuncy

In the straked region, the amplitude of the response decays, but the signals do not appear to decay as there is good correspondence. This is an indication that the noise that decays the signal is caused by locally generated waves. Hydrodynamic forces cause these other waves that degrade the signal, whereas in the straked region these hydrodynamic forces are much smaller because they are uncorrelated due to the strakes. With the small forces, there is no introduction of other vibrations or noise to degrade the signal.

Figure 140 shows a waterfall spectrum from the straked region. Though the magnitude of the spectrum is significantly lower than a normal VIV spectrum as seen in Figure 131, the features are similar. A single dominant VIV frequency dominates the spectra with scattered higher harmonic components.

Figure 141(a) shows the current profile and direction for the 40% strake coverage example. Through the potential power-in region, the profile is fairly uniform and current direction does not change significantly. Figure 141(b) shows the RMS strain with the power-in region found using the coherence mesh overlaid.

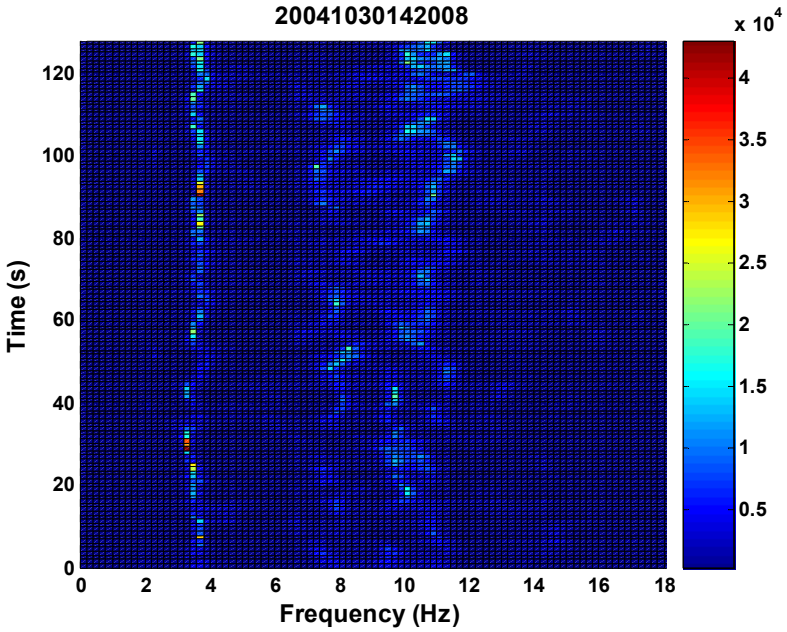

Figure 140 - Gulf Steam 40% coverage case waterfall spectra of a strain gauge sensor in the middle of the secondary power-in region found using the coherence method. Each spectrum was calculated using MEM analysis with a 5 second window and 80% overlap.

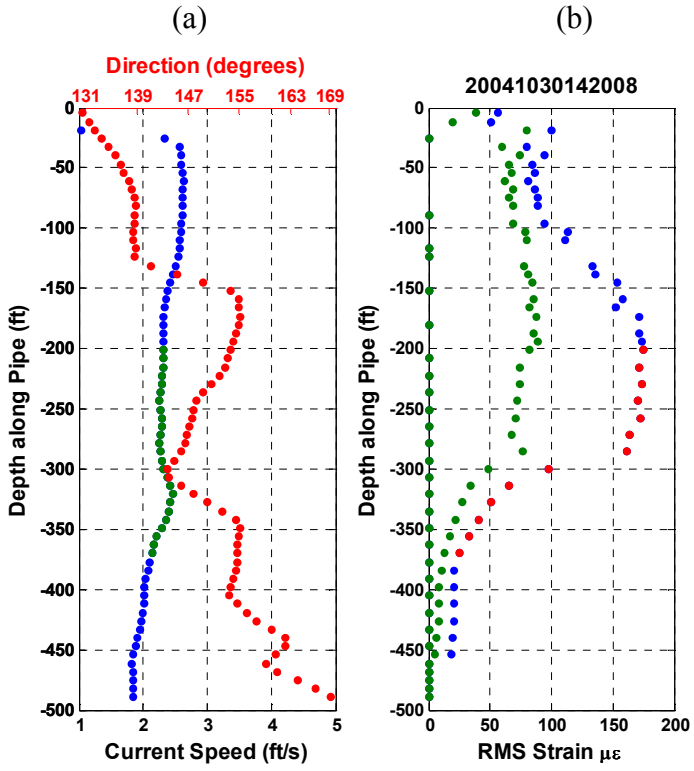

Figure 141 - Gulf Steam 40% coverage case (a) Current speed (blue), current direction (red), and power-in region (green); (b) RMS strain (blue) and RMS strain filtered to only show the contribution of the dominant VIV frequency. The power-in region found using the coherence method is shown on both graphs; (a) green and (b) red.

The power-in region extends over the area with highest RMS response, which is directly above the straked region, and into the straked region. The straked region can be easily identified because the RMS strain exponentially decays.

Figure 142 shows the dominant VIV frequency and the corresponding reduced velocity for the 40% straked example. As expected the range of frequencies seen in the power-in region is small and the reduced velocity is most often between 5 and 6.

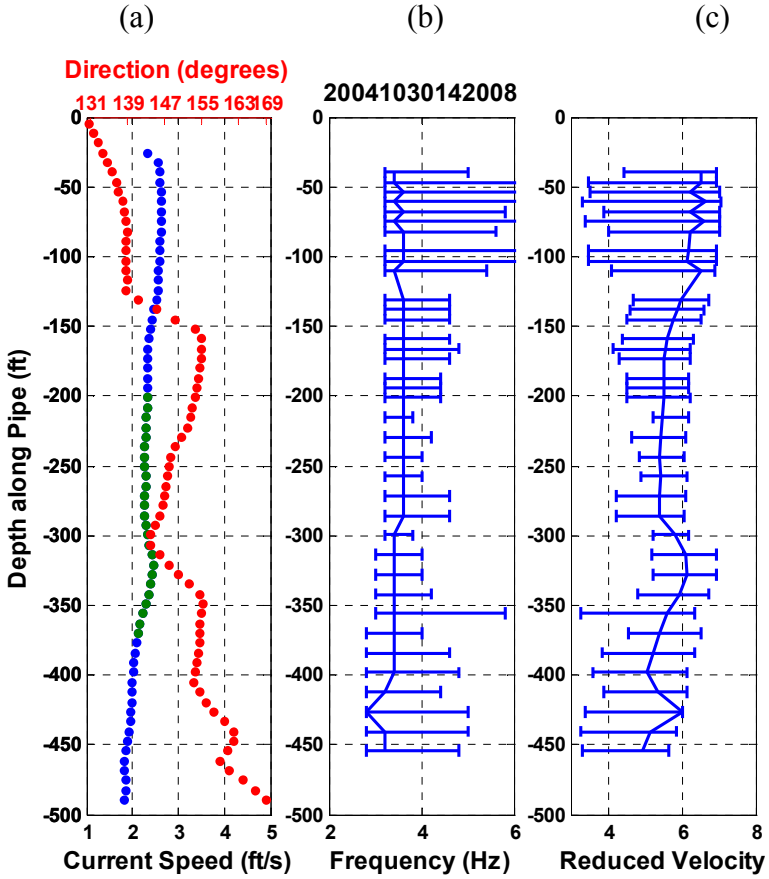

Figure 142 - Gulf Steam 40% coverage case (a) Current speed (blue), current direction (red), and power-in region (green); (b) Dominant VIV frequency, showing the most common frequency with the vertical line and the varying frequencies due to time sharing; (c) the reduced velocity, using dominant VIV frequency, the variance is due to the variation in frequency with time shifting.

A similar analysis can be done for the 70% straked cases. The power-in regions are very limited in this case because such finite lengths of pipe are bare. The example shown in Figure 143 appears to have two separate power-in regions. The first is a power-in region at the dominant VIV frequency. The second power-in region appears to be at approximately three times the frequency. The three-time component is seen because of the high density of sensors.

When looking at the reduced velocity for this case, shown in Figure 146, the reduced velocity in the lower region is approximately 6. The reduced velocity in the upper power-in region is 7. In tests by Williamson and Jauvtis, [Jauvtis and Williamson 2004], they found at a reduced velocity of 7, the largest three-time component existed. This example exemplifies those findings.

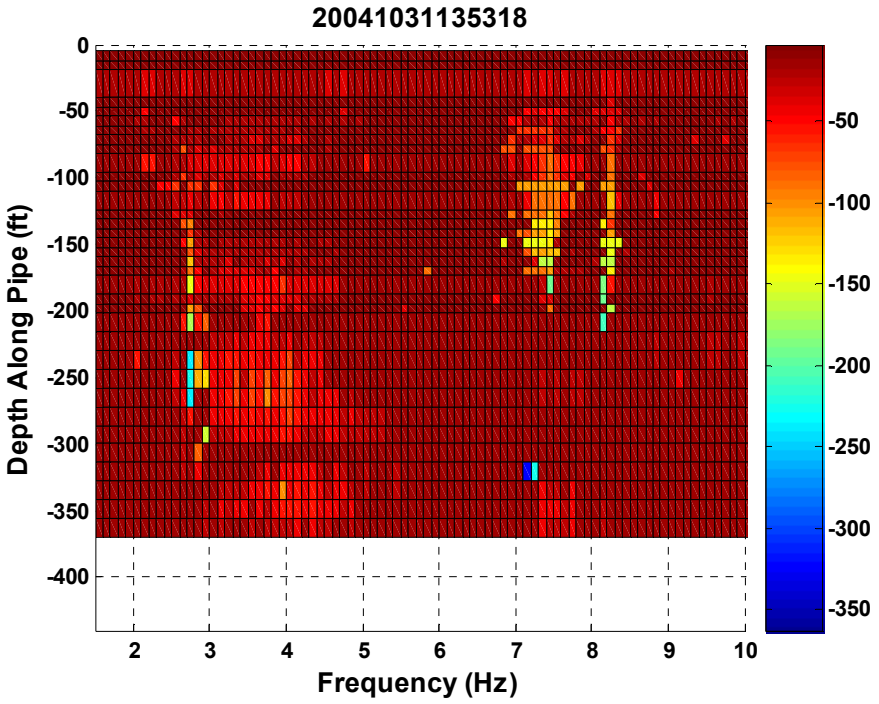

Figure 143 - Gulf Steam 70% coverage case Coherence Mesh showing the Distance Ranges with Greater than 0.7 Coherence Normalized by Wavelength at each Freqeuncy

Figure 144 shows the waterfall spectrum for the 70% coverage case in the dominant power-in region for the VIV frequency. A single frequency is seen to dominate the power-in region. A secondary higher frequency can also be seen when the dominant VIV frequency. This frequency can be seen faintly in the coherence mesh at 350 ft. depth. This is another power-in region in a different bare region. The different regions were separated by sections of strakes. Almost no three-time component is present in the waterfall spectrum.

Figure 145 shows the waterfall spectrum for the 70% case in the high-frequency power-in region. The third harmonic does not show a large spectral component, yet the waves, though small, are traveling. This could be considered a non-dominant power-in region, where vibrations are coherent, but little power is input to the system.

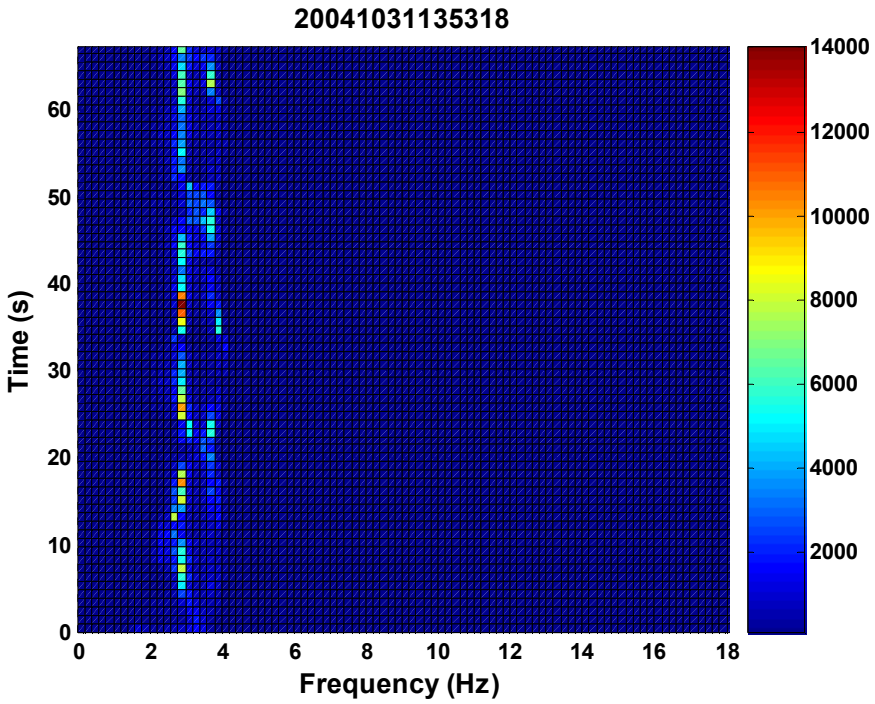

Figure 144 - Gulf Steam 70% coverage case waterfall spectra of a strain gauge sensor in the middle of the secondary power-in region found using the coherence method. Each spectrum was calculated using MEM analysis with a 5 second window and 80% overlap.

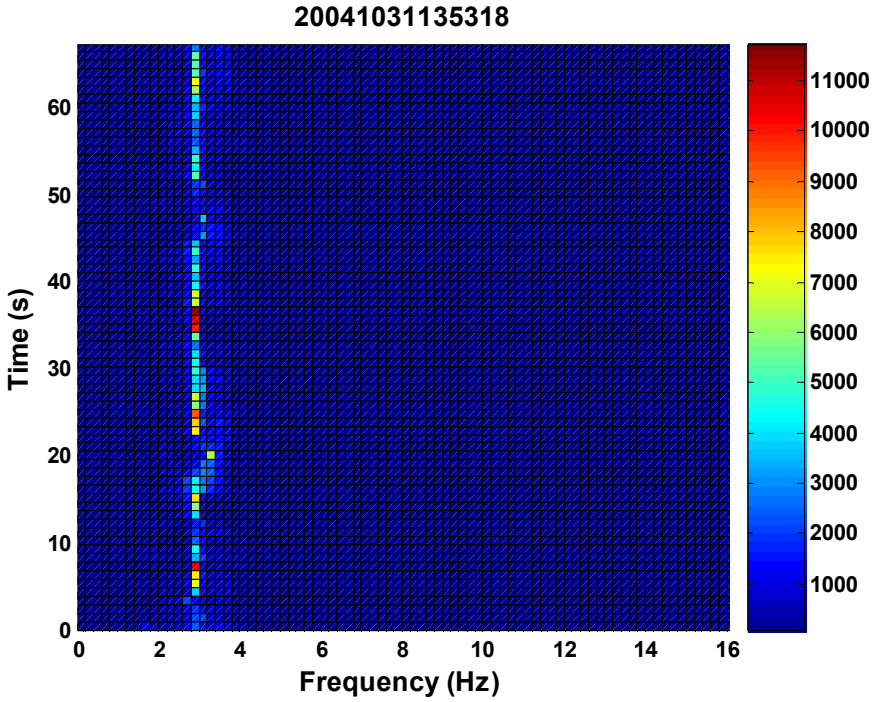

Figure 145 - – Lake Seneca bare case in the upper power-in region; waterfall spectra of a strain gauge sensor in the middle of the secondary power-in region found using the coherence method. Each spectrum was calculated using MEM analysis with a 17 second window and 95% overlap.

Figure 146(a) is the current profile and the current direction for the 70% strake coverage case. Figure 146(b) shows the RMS strain. The magnitude of the strain is less than one fourth of the RMS strain for a bare case with similar current profile. The power-in regions are limited to the bare sections of the pipe; therefore the power-in regions have finite length and can not lock-in over a large length. The amount of vibrations created by these abbreviated power-in regions is less than the bare case.

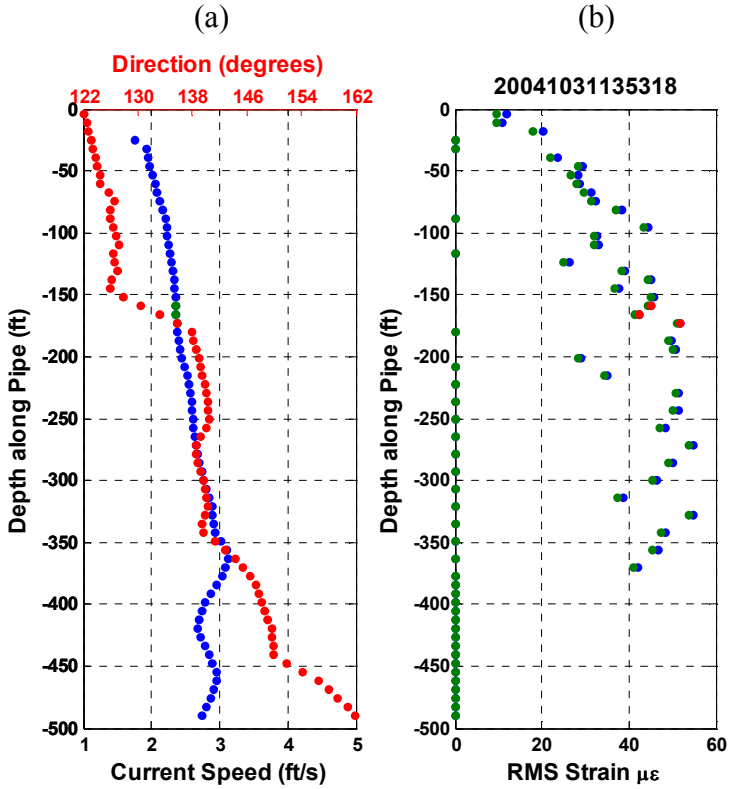

Figure 146 - Gulf Steam 70% coverage case (a) Current speed (blue), current direction (red), and power-in region (green); (b) RMS strain (blue) and RMS strain filtered to only show the contribution of the dominant VIV frequency. The power-in region found using the coherence method is shown on both graphs; (a) green and (b) red.

In Figure 147(b) the dominant VIV frequency for each location is shown. The length of the error bars for the frequency is similar to that of the bare cases. The dominant frequency at each sensor changes more in the 70% straked case than in other cases. This is because each bare region will have locally generated waves that are damped in the straked regions between.

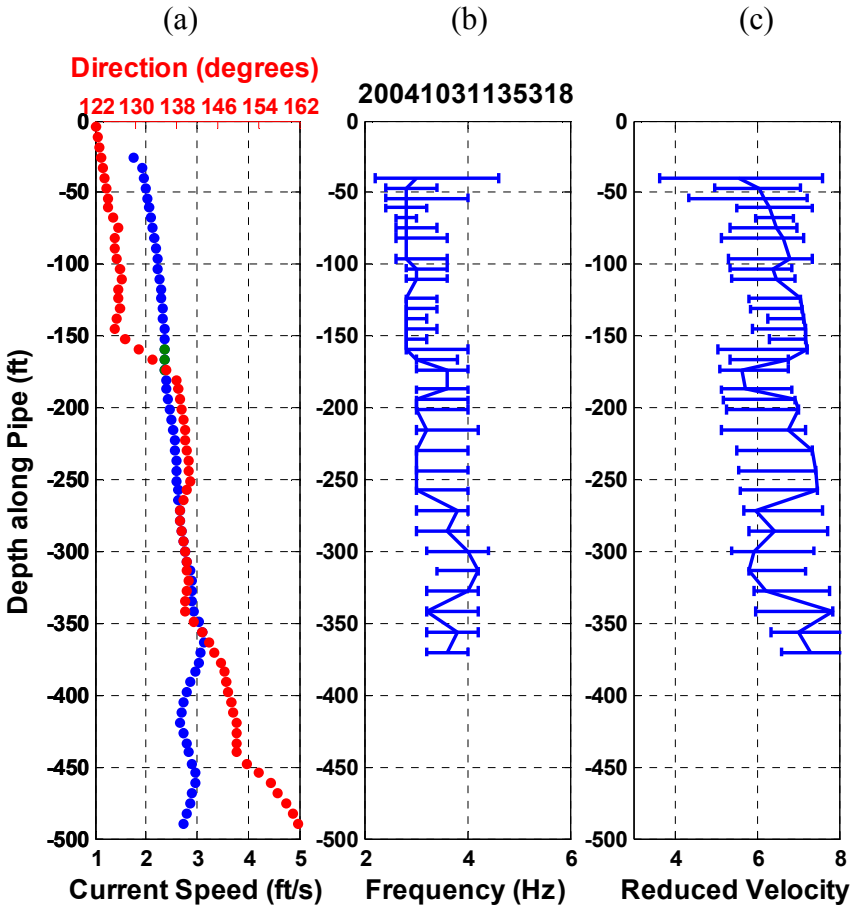

Figure 147 - Gulf Steam 70% coverage case (a) Current speed (blue), Current direction (red), and power-in region (green); (b) Dominant VIV frequency, showing the most common frequency with the vertical line and the varying frequencies due to time sharing; (c) the reduced velocity, using dominant VIV frequency, the variance is due to the variation in frequency with time shifting.

Limitations

The coherence mesh is a useful tool when trying to locate the power-in region. One limitation of the method is when analyzing a test with standing wave behavior. If standing wave behaviors is found, usually at modes less than twentieth, the entire pipe responses coherently and this methodology will break down. Power-in regions will be found all down the pipe. Therefore the coherence mesh only works when standing wave behavior is not observed.

Conclusions

This methodology will not give the exact location of the power-in region; instead it is an indicator as to where the waves are generated. The exact location of the power-in region shifts fairly quickly with the shifting in frequency. The spacing of the sensors can also

affect the error in power-in length. The coherence mesh will only give an estimate of the length of the power-in region.

To use this methodology the density of the sensors must be fairly close together with at least two sensors in the power-in region. This methodology would work best on data that is stationary for larger lengths of time, but can be effective in indicating the frequencies and area of origin of the waves in non-stationary cases. With a larger length of time with a stationary power-in region and frequency, a better coherence average could be done and a more exact power-in region found.

Due to the sample rate problems when taking the Gulf Stream data, [See Appendix A], the coherence meshes are not as accurate at the higher harmonic components. Another similar test without the sample rate issues could resolve the issue of whether or not the coherence mesh is effective at the higher harmonics.